Nanofabrication and its application in plasmonic chemical and bio-sensors

by

Jian Zhang

A thesis

presented to the University of Waterloo

in fulfillment of the

thesis requirement for the degree of

Doctor of Philosophy

in

Electrical and Computer Engineering

Waterloo, Ontario, Canada, 2014

© Jian Zhang 2014

Author's Declaration

This thesis consists of material all of which I authored or co-authored: see Statement of Contribution included in the thesis. This is a true copy of the thesis, including any required final revisions, as accepted by my examiners.

I understand that my thesis may be made electronically available to the public.

Statement of Contribution

This thesis contains materials from several published or submitted papers, some of which resulted from collaboration with my colleagues in the group.

For the work on high molecular weight polystyrene as sensitive electron beam resist, covered in Chapter 3, Section 3.2, Celal Con is the first author of the published paper and my contribution is on resist film preparation and electron beam lithography.

For the work on high sensitive ZEP resist developed by MEK:MIBK developer, covered in Chapter 3, Section 3.3, Babak Shokouhi is the first author of the published paper and my contribution is on electron beam lithography and the comparison with amyl acetate developer.

For the work on tapered nano-hole array for extraordinary optical transmission, covered in Chapter 5 Section 4.4, Dr. Mehrdad Irannejad is the first author of the published paper responsible for the numerical simulation, and my contribution is on the nanofabrication, characterization and optical measurement.

Abstract

This thesis is focused on nanofabrication and its application in plasmonic chemical and bio-sensors. The contribution thus is the development of novel nanofabrication techniques and nano-structures for the sensors based on surface plasmon (SP).

Part I (Chapter 1-3) is about novel nanofabrication techniques, especially nanoimprint lithography (NIL) and electron beam lithography (EBL). For NIL, the four major aspects of NIL were discussed, including the resist, mold, imprint process and equipment for NIL. Combined with NIL and soft lithography, hybrid nanoimprint-soft lithography was investigated. To overcome the difficulty of mold fabrication, a more robust solution of mold fabrication through a sacrificial poly(dimethyl glutarimide) (PMGI) master mold was designed in this work. Based on this method, the mold was fabricated without structure distortion, and pattern replication with sub-10 nm resolution was demonstrated. For EBL, several aspects were discussed to improve the performance of EBL, including the resist, development, and exposure condition. The charging effect to the pattern distortion was studied systemically for the electron beam exposure in large area with high current (>nA). Tilted periodic nanostructure was achieved by electron beam scanning on tilted sample with dynamic focus mode. EBL on irregular surface was realized by the exposure on evaporated polystyrene.

Part II (Chapter 4-6) is the application in surface plasmonic chemical and bio-sensors. The first type of sensors is surface enhanced Raman scattering (SERS) sensor based on localized SP. Bowtie-shape nano-antenna structures of sub-10 nm gap were fabricated with the breakthrough of EBL resolution to 3 nm by exposing resist on Si_3N_4 membrane. By controlling the gap size during lithography, the surface plasmon enhancement was tuned accurately. High sensitivity of Au bowties antenna with sub-10 nm gap was achieved at low concentration of the target

molecule (10^{-7} mM, 1,2-di(4-pyridyl)ethylene in ethanol solution) and high enhancement of 10^7 resulting from the corresponding bowtie structure.

The second type of sensors is extraordinary optical transmission (EOT) sensor based on propagating SP. The process of double liftoff was developed for the fabrication of nano-hole arrays on 100 nm-thick Au film utilizing EBL. This technique is versatile for the fabrication of many kinds of high-aspect-ratio noble metal structures. Additionally, annealing method was employed in this work to improve the smoothness of Au film. It was found that the RMS roughness of the deposited film was reduced by 72 % and the sensitivity was increased by 32 nm/RIU as a result of annealing. It was also found that the optical transmission intensity of the annealed NHA of similar hole diameter was increased more than twice which is due to the smaller absorption/scattering of the incident light and surface waves from the Au film surface. Besides the double liftoff process, several techniques were developed for EOT structures, including electroplating, imprint method, and deposition on membrane.

Acknowledgements

In this thesis, I would like to thank gratefully for the contributions from many people. First, there are many thanks to my wife for her selfless supports to my work. During my Ph. D. study, I got my most cherished gift in my life from her-our Cynthia. I would also thank my parents for supporting my study oversea.

I would like to thank my supervisor, Dr. Bo Cui, for his guidance, encouragement and patience throughout my Ph. D. study. I am grateful to Dr. Mustafa Yavuz, Dr. Omar M. Ramahi, Dr. Chris Backhouse, Dr. David Klymyshyn, who agreed to be my committee members and gave me many suggestions. I would also thank to the following professors in University of Waterloo, Dr. Ting Tsui, Dr. William Wong, Dr. Hany Aziz, Dr. Dayan Ban, Dr. Simarjeet Saini, Dr. Siva Sivoththaman, for their help in my research. I would like to thank the lab managers in cleanroom, Richard Barber, and Vito Logiudice, for their friendly supports in these years.

I feel fortunate to have worked in Waterloo nanofabrication group, especially with my group mates Celal Con, Dr. Mehrdad Irannejad and Dr. Xiangcheng Sun. Thanks a lot for Dr. Mehrdad Irannejad's theoretical and computing contribution on the part of surface plasmonic devices. I would also thank to my friends working together in cleanroom, Qi Wang, Bin Sun, Graeme Williams, Yingjie Zhang, Chang Guo, Minoli Pathirane, Ruifeng Yang, Jaspreet Walia, Mina Fouad, Mark Ferguson, Brandon Seo, Baolin Tian, Dr. Kai Wang, Dr. Ying Liu, Dr. Yipu Song, Dr. Nathan Nelson-Fitzpatrick for their kind support during working. Best wishes for their development in research and carrer.

The work is partly supported by the NSERC-Industrial Postgraduate Scholarships.

This is dedicated to my wife and my Cynthia:

Love is giving; love is enough.

Table of Contents

Part I: Nanofabrication

Chapter 1 Introduction to nanofabrication 1
1.1. Introduction to nanotechnology 1
1.2. Introduction to nanofabrication 2
1.3. The work in this thesis 4

Chapter 2 Imprint methods for nanofabrication 5
2.1. Background of imprint methods in nanoscale 5
2.2. Traditional nanoimprint lithography and its principle 8
2.2.1 NIL resist. 9
2.2.4 Equipment for NIL. 11
2.3. Alternative NIL 12
2.3.1. Laser-assisted direct imprint (LADI) lithography 12
2.3.2. Step and flash imprint lithography (S-FIL) 13
2.3.3. UV-NIL. 14
2.4. Soft lithography based on poly(dimethysiloxane) (PDMS) 16
2.4.1. Introduction 16
2.4.2. Microcontact printing (μCP) 17
2.4.3. Hybrid nanoimprint-soft lithography 18
2.5. Hybrid nanoimprint-soft lithography using sacrificial PMGI master mold 20
2.5.1 The advantage of the hybrid mold fabricated by sacrificial PMGI master mold 20
2.5.2 Three types of fabrication processes 21
2.5.3 Results and discussion 23
2.5.3.1 Sacrificial PMGI mold fabrication by imprint (method-A&B) 23
2.5.3.2 Sacrificial PMGI mold fabrication by EBL (method-C) 25

2.5.3.3 The effect from the lifetime of the anti-adhesive layer on the hybrid mold............. 26
2.6. Conclusion.. 27

Chapter 3 Nanofabrication by electron beam lithography 29
3.1. Introduction 29
3.2. The most popular resists: PMMA and ZEP 31
3.2.1. Poly(methylmethacrylate) (PMMA) and its developer 32
3.2.2. ZEP-520A and its developer.. 34
3.3. Novel resist and its development 35
3.3.1. Self-developing aluminum fluoride resist 35
3.3.2. High sensitive EBL using high molecular weight polystyrene (PS) resist................. 36
3.3.3. High sensitivity EBL using MEK:MIBK developer for ZEP resist 38
3.4. Charging effect reduction in electron beam lithography with nA beam current........... 41
3.5. Periodic tilted structure fabrication by electron beam lithography 46
3.6. Electron beam lithography on irregular surfaces with evaporated resist 50
3.7. Conclusion.. 58

Part II: Surface plasmonic sensors

Chapter 4 Surface plasmon fundamentals and applications 60
4.1. Introduction to bulk plasmon 60
4.2. Introduction to surface plasmon... 62
4.3. Dispersion relation 63
4.4. Spatial extension of the SP field 65
4.5. Types of surface plasmonic sensors 66
4.6. Basis introduction to FDTD simulation method 68

Chapter 5 Surface enhanced Raman spectroscopy (SERS) for chemical sensors 70
5.1. Introduction to Raman spectroscopy... 70
5.2. Introduction to surface-enhanced Raman spectroscopy (SERS).................................. 71
5.2.1. Electromagnetic Enhancement Mechanism (EEM) 72

5.2.2. Numerical methods for calculating electromagnetic enhancement factors 72
5.2.3. Metals for SERS 76
5.3. Nano-fabrication technologies for SERS chemical sensors 78
5.4. Proximity effect in EBL and Monte Carlo method for dose optimization 81
5.5. High-resolution electron beam lithography on Si_3N_4 membrane 84
5.5.1. Dose simulation 84
5.5.2. Bowtie nano-antenna fabrication 86
5.6. Bowtie-shape nano-antenna for SERS sensors 89
5.6.1. The advantages of bowtie-shape nano-antenna in SERS 89
5.6.2. Numerical modeling 90
5.6.3. Surface enhanced Raman spectroscopy (SERS) measurement 91
5.7. Results and discussion 92
5.7.1. Numerical analysis 92
5.7.2. SERS chemical sensors 93
5.8. Conclusion 98

Chapter 6 Extraordinary optical transmission (EOT) for chemical and bio-sensors 99
6.1. Introduction to existing sensors based on propagating SP 99
6.1.1. Kretschmann configuration of attenuated total reflection (ATR) 99
6.1.2. Grating coupling 102
6.1.3. Surface plasmonic waveguide 103
6.2. Extraordinary optical transmission (EOT) 104
6.3. Nanofabrication techniques for EOT structures 106
6.3.1. Nano-hole array (NHA) fabrication through double liftoff process and its characterization 107
6.3.1.1. Fabrication process 107
6.3.1.2. Comparison to single liftoff process 109
6.3.1.3. The effect of exposure dose 111
6.3.1.4. The effect of facing-up and facing-down during the second liftoff 112
6.3.1.5. The effect of low-temperature development 112
6.3.2. Methods to improve the smoothness of Au films 114

6.3.3. Other fabrication methods for EOT structures 119
6.3.3.1. Fabrication of EOT structure on Si_3N_4 membrane 119
6.3.3.2. Fabrication of EOT structures by electroplating of Au 122
6.3.3.3. Fabrication of EOT structure using nanoimprint lithography (NIL) 125
6.4. Numerical analysis 127
6.4.1. Effect of hole diameter 128
6.4.2. Effect of Au film thickness 129
6.4.3. Effect of hole array period 131
6.4.4. Effect of tapered angle 132
6.5. Optical Characterization 133
6.5.1. Transmission measurement 133
6.5.2. The effect of nano-hole array period and diameter on EOT result 134
6.5.3. The effect of tapered angle on EOT performance 136
6.5.4. The effect of annealing on Au EOT sample 137
6.5.5. Transmission of the hole array structure in free-standing gold film 138
6.6. Application of annealed nano-hole array in bio-sensing 139
6.7. Conclusion 140

Chapter 7 Conclusions of Completed Works 142

Appendix A: List of publication 144

Appendix B: Conference presentations 146

Reference 148

List of Figures

Figure 1.1 The Lycurgus cup, kept in the British Museum, is made in about 290-325 AD. The cup shows green color when illuminated from outside and red color when illuminated from inside. Copyright 2014 by the British Museum. ……..1

Figure 1.2 Schematic diagram of (a) the top-down and (b)&(c) the bottom up approaches. In the top-down approaches, (1) the resist is patterned by lithography, and then the pattern is transferred by (2) deposition followed by (3) liftoff, or the pattern is transferred by (4)&(5) direct etch. In the bottom-up approaches, method (b) is coating synthesized nano- particles or SAM layer; (c) is block-copolymer annealing lithography. ………………………………………………………………………….……………3

Figure 2.1 Schematic diagram of the optics of the projection lithography system. 5

Figure 2.2 Schematic of X-ray lithography. 6

Figure 2.3 Patterns with high resolution by e-beam lithography. (a) Ring array with the line width of 60 nm on PMMA. (b) Grating pattern with the period of ~150 nm and the line width of 22 nm on ZEP-520A. 7

Figure 2.4 Schematic of the originally proposed NIL process. 8

Figure 2.5 Peeling off the resist onto an untreated mold. 9

Figure 2.6 Formation of a monolayer of crosslinked fluoroalkyltrichlorosilane on oxide surface. 9

Figure 2.7 Scheme of the NIL. 10

Figure 2.8 Viscosity of 110 kg/mol PMMA vs. temperature. 10

Figure 2.9 Moiré pattern used for alignment in NIL process. Copyright 2007 by the Elsevier. 11

Figure 2.10 A miniaturized camera between the stamp and substrate before pressing down. 12

Figure 2.11 (a-e) Schematic of laser-assisted direct imprint (LADI) of nanostructures in silicon; (f) The reflectivity of a He-Ne laser beam from the silicon surface versus the time, which proves the imprint process lasts about 220 ns; SEM image of the cross-section of (g) quartz mold and (h) imprinted silicon. Copyright 2002 by Nature Publishing Group. 13

Figure 2.12 Schematic of (a) thermal NIL and (b) UV-curing S-FILS processes. Copyright 2007 by the Springer-Verlag. 14

Figure 2.13 Schematic of UV-assistant NIL. 15

Figure 2.14 SEM images of UV-NIL result imprinted by (a) the original master mold, (b) the imprinted polymer replica, (c) the tenth replica mold. Copyright 2005 by the American Chemical Society. 16

Figure 2.15 Schematic of microcontact printing process. 17

Figure 2.16 Schematic illustration of possible deformations and distortions of microstructures in PDMS. Copyright 1998 by the John Wiley and Sons. 18

Figure 2.17 Schematic of the fabrication process of the hybrid mold and the hybrid nanoimprint-soft lithography. Copyright 2009 by the American Chemical Society. 19

Figure 2.18 SEM images of 200 nm pitch grating on the surface of 125 μm diameter optical fiber array with the direction (a) parallel and (b) perpendicular to the fiber axis. Copyright 2009 by the American Chemical Society. 19

Figure 2.19 Optical images of (a) stable liquid resist film, (b) unstable liquid resist film, which shrank after 30sec. 20

Figure 2.20 Schematic of the fabrication process of the hybrid UV-resist/PDMS mold. 22

Figure 2.21 Three methods for the fabrication of sacrificial mold in PMGI (or LOR-5A that is based on PMGI). A) Direct imprint into PMGI at high temperature; B) Imprint into PVPK at reduced temperature, then RIE transfer the pattern into LOR-5A; C) Electron beam lithography using PMGI as positive resist. 23

Figure 2.22 SEM images of (a) hybrid mold containing UV-cured resist on PDMS duplicated from a sacrificial PMGI mold that was patterned using the method as shown in Fig. 2.21A; (b) grating with a crack imprinted into UV-curable resist using this mold. 24

Figure 2.23 SEM image of a grating imprinted into UV-curable resist using a mold in UV-cured resist on PDMS, which was duplicated from a sacrificial PMGI mold that was patterned using the method as shown in Fig. 2.21B. a) Overview; b) Zoom-in image. 24

Figure 2.24 SEM image of a grating imprinted into UV-curable resist using a mold duplicated from a sacrificial PMGI mold that was patterned using the method as shown in Fig. 2.21C. Grating patterns with the periods of 150 nm, 100 nm, 80 nm were exposed with the line dose 5, 6, 7, 8 nC/cm, respectively. ..25

Figure 2.25 SEM image of a grating imprinted into UV-curable resist using a mold duplicated from a PMGI sacrificial mold that was patterned using the method as shown in Fig. 2.21C. a) Grating of 100 nm period with a trench-width ~17 nm; b) A collapsed grating shows features down to 8 nm. 26

Figure 2.26 SEM image of (left) the first and (right) the third imprint results by the same hybrid mold. 27

Figure 3.1 Schematic of an electron beam lithography system. 30

Figure 3.2 Contrast curves of resist A, B, and C. 31

Figure 3.3 Pillar array on PMMA resist with the exposure dose 10-time higher than normal one. 33

Figure 3.4 SEM image of a trench with high aspect ratio on ZEP-520A, done by ELIONIX INC. 34

Figure 3.5 The process of self-development of AlF_3 during e-beam exposure. 35

Figure 3.6 SEM image of lines with 16 nm period in $AlCl_3$. 36

Figure 3.7 SEM images of 90 kg/mol polystyrene line array exposed at 5 keV with line dose of 0.54 nC/cm, and developed by tetrahydrofuran for 2 min. (a) 150 nm period, (b) 200 nm period. 37

Figure 3.8 Contrast curves for 90 kg/mol polystyrene exposed at (a) 20 keV and (b) 5 keV, and developed by tetrahydrofuran for 2 min. 37

Figure 3.9 (a-b) Contrast curves for ZEP-520A resist exposed at 5 keV and 20 keV, and developed by MEK : MIBK = 40 : 60 for 30 sec at room temperature. (c-d) Contrast curves for ZEP-520A resist exposed at 5 keV and 20 keV, and developed by amyl acetate for 1 min at room temperature. The thickness is normalized to the original film thickness. For (a-b), the unexposed area (dose = 0 $\mu C/cm^2$) has normalized thickness <1.0 because the first developer dissolves slowly the unexposed resist. 39

Figure 3.10 Line array pattern poorly defined in ZEP-520A that was spun on bare silicon wafer. The resist was exposed at 5 keV and developed by MEK : MIBK for 30 sec. The array periods are 140 nm and 170 nm, which cannot be resolved due to resist's poor adhesion to the substrate. 40

Figure 3.11 Line array pattern in ZEP-520A with periods of 70, 80 and 90 nm. The resist was spun on oxygen plasma treated ARC film, and exposed at 5 keV and developed by MEK : MIBK for 30 sec. 40

Figure 3.12 The four different pattern designs that all give a 200 nm period dot array. a) Large square where array periodicity is defined by the exposure step size along the x- and y-direction; b) Line array with offset at the beginning, where the "nodes" on each line indicate the position of exposed dots. The resulted 200 nm period dot array is rotated by 45°; c) Similar to b) but the step size and line-spacing is set such that the resulted 200 nm period dot array is rotated by 26.6^o; d) Dot array with 200 nm period along both directions. 43

Figure 3.13 Hole array with 200 nm period developed in PMMA coated on a heavily doped n-type Si substrate with resistivity 0.01-0.02 Ω·cm. (a-d) are exposed using the pattern design as shown in Fig. 3.12 a-d, respectively. 43

Figure 3.14 Hole array with 200 nm period developed in PMMA coated on: (a-b) a lightly doped n-type Si substrate with resistivity 1-10 Ω·cm, exposed using the pattern design as shown in Figure 2.13(a-b), respectively; (c-d) a quartz substrate with 20 nm Cr conductive layer coated on the resist, exposed using the pattern design as shown in Fig. 3.12(c-d), respectively. 44

Figure 3.15 Hole array with 200 nm period. (a) Developed in PMGI resist using pattern design as shown in Fig. 3.12a; (b-c) Developed in ZEP-520A resist using pattern design as shown in Fig. 3.12a and Fig. 3.12d, respectively. The exposure doses are 48 fC/dot for PMGI, and 2.4 fC/dot for ZEP-520A. 45

Figure 3.16 SEM images of 45° tilted hole array in (left) 100 nm-thick ZEP-520A with the hole diameter of 150 nm, and (right) 645 nm-thick ZEP-520A with the hole diameter of 250 nm. 49

Figure 3.17 Top view SEM images of 45° tilted hole array in 645 nm-thick ZEP-520A showing hole-size uniformity across the pattern area of ~1 mm. The images were taken on the bottom-left corner (a), center (b), and top-right corner (c) of the scanning area. 49

Figure 3.18 SEM images of 45°-tilted pillar array in 500 nm-thick SU-8 resist (left) and 1000 nm-thick 260 kg/mol polystyrene resist (right). The array period is about 1 μm for SU-8 and 2 μm for polystyrene. 49

Figure 3.19 SEM images of 45° tilted Au pillar arrays with 1.2 μm periodicity by electroplating into tilted hole arrays in ZEP-520A resist. (a) Tilted pillars of ~300 nm diameter and ~750 nm length without Au over-plating. (b) Mushroom shaped Au pillar array due to over-plating. The images were taken at 45 degree viewing angle. 50

Figure 3.20 Changes of PS structures from thermal evaporation to electron beam exposure. 52

Figure 3.21 Microscope images of spin-coating defects. (a) Films shrink and form droplets on the substrate with low surface energy. (b) Under layer swells and cracks caused by the solvent from spin-coating. (c) A dust causes un-uniform resist film. (d) Edge beads occur regardless in spin-coating method. 52

Figure 3.22 AFM images of PS films prepared by spin-coating method (left) and thermal evaporation (right). 54

Figure 3.23 Contrast curves for 1.2 kg/mol polystyrene by spin-coating and evaporation. Both were exposed at 5keV and developed by xylenes for 30 seconds. The sensitivity (dose for 100 % remaining thickness) and contrast are 1920μC/cm^2 and 4.3 for spin-coated PS, and 4500μC/cm^2 and 2.6 for evaporated PS. 55

Figure 3.24 Line array patterns with 60 nm period exposed by16.3, 18.4, 20.8 nC/cm, respectively. 55

Figure 3.25 SEM images of patterned PS on an AFM cantilever by EBL. AFM cantilever written with WIN (Waterloo Institute for Nanotechnology). 56

Figure 3.26 SEM images of (a) Al pattern of starline to demonstrate the exposure uniformity along the all directions. (b) Al circuit with line width of 36 nm, (c) transferred to Si substrate by deep RIE of 1 minute with the depth of 180 nm. (d) High-aspect-ratio pattern of the name of our institute and group was etched by deep RIE of 10 minute with the depth of 2 μm. 57

Figure 3.27 SEM images of nanostructures on an optical fiber with height/depth of 270 nm. (a) 2D grating array with line-width of 167 nm; (b) dot array with diameter of 200 nm; (c) crossbar array with line-width of 167 nm; and (d) starline pattern. The inserts show top view and/or zoom-in view of the structures. 58

Figure 4.1 In a metal the nucleus and core electrons retain their configuration in the free atom, but the valence electrons leave the atom to form the electron gas. 61

Figure 4.2 Simple model of a plasmon oscillation caused by a time-dependent electric field. 61

Figure 4.3 SPs at the interface have a combined electromagnetic wave and surface charge character. This combined character also leads to the field component perpendicular to the surface being enhanced near the surface and decaying exponentially with increasing distance from the surface. 63

Figure 4.4 (a) The relationship between the charges and the electromagnetic field of SPs propagating on metal/dielectric interface in x direction. (b) The field E_z decreases exponentially away from the interface. 64

Figure 4.5 Dispersion curve for surface plasmons. At low *k*, the surface plasmon curve approaches the free-space photon curve. ……………………………………………………………………………66

Figure 4.6 Localized surface plasmon on metal nanoparticles excited by free-space light. 67

Figure 4.7 Surface plasmon coupling schemes: (a) Schematic prism-coupled SPR bio-sensor (Kretschmann configuration); (b) Grating-coupled SPR sensor. Here Au is deposited on a polymer as a 600nm-period grating created by nano-imprinting/hot embossing; (c) EOT-based SPR biosensor. Here a 600 nm period hole array in 120nm-thick Au is fabricated by e-beam lithography and liftoff. 68

Figure 4.8 In FDTD method, the object is separated to a series of discrete units. 69

Figure 5.1 (a) Diagram of energy levels involving Rayleigh scattering, Stokes scattering and Anti-Stokes scattering. (b) Schematic of inelastic scattering on a small particle. 71

Figure 5.2 Schematic of localized surface plasmon. 72

Figure 5.3 Schematic of a sphere of radius *a* and dielectric constant ε_2, immersed in a dielectric extending to infinity, with dielectric constant ε_1. 74

Figure 5.4 The relationship between the wavelength and (a) the real part ε_1; (b) the imaginary part ε_2 of dielectric constant of the most popular metals. 78

Figure 5.5 SEM images of (a) open gold nanofingers with 68 nm radius and (b) closed nanofingers after molecule trapping; (c) simulated distribution of electric field intensity $|E(r)|^2$ on the (b) structure at 750 nm laser, the hotspots exist at the nano gap. Copyright 2010 by the American Chemical Society. SEM image of (d) 200 nm period nanostar array of 5 nm Ti/15 nm Au on silicon, and (e) zoom-in view of nanostars with sub-10 nm apex and gap between adjacent stars; (f) simulated distribution of electromagnetic near field at 750 nm wavelength, the hotspots exist at the nano tip. Copyright 2010 by the AIP Publishing LLC. 79

Figure 5.6 (a) SEM image of typical bowtie structure fabricated by EBL on membrane with 8 nm gap; (b) The FDTD simulated $|E|^2$ profile of the same bowtie structure, which shows the extremely high electrometric field in the gap area (hotspots). 80

Figure 5.7 (a) Spin-coating the solution of polymer nano-sphere and Au deposition; (b) Formation of a close-packed hexagonal array of Au nano-prisms after lift-off. 81

Figure 5.8 Simulation of the electron scattering trajectories in silicon substrate with 100 nm PMMA layer, with the incident beam energy: (a) 5 keV, (b) 10 keV, (c) 15keV, and (d) 20 keV. (e) Distribution of the backscattering electrons dependent on depth. 84

Figure 5.9 Simulation of the electron scattering trajectories with 20 keV on (a) 100 nm PMMA layer on silicon substrate, (b) 100 nm PMMA layer, 150 nm Si_3N_4 layer on silicon substrate, (c) 100 nm PMMA layer on 150 nm Si_3N_4 membrane. 85

Figure 5.10 Top view of dose distribution of bowtie patterns on bulk wafer with the gap size of (a) 25 nm, (b) 6 nm. Cross-sectional view of proximity effects on bowtie with the gap size of (c) 25 nm, (d) 6 nm. 87

Figure 5.11 Schematic of the fabrication process of bowtie nano-antenna on Si_3N_4 membrane: (a) photolithography on backside Si_3N_4 and CF_4 reactive ion etching to remove the unpatterned Si_3N_4; (b) Si wet etch in KOH solution to form Si_3N_4 membrane; (c) spin-coating 100 nm PMMA layer and deposition 10 nm Cr for EBL; (d) e-beam lithography of bowtie array and development; (e) evaporation of 1nm Cr and 25nm Au or Ag; (f) liftoff in anisole and rinse the surface; (g) illustration of the final bowtie structure on Si_3N_4 membrane and SEM image of fabricated bowtie structure with gap size of 8 nm as an example of the fabricated structure. 88

Figure 5.12 (a) SEM image of bowtie array exposed on Si wafer; (b) SEM image of bowtie array exposed on Si_3N_4 membrane, with the varied gap size from 3 nm to 24 nm. d) SEM image of gold bowtie array with 6 nm gap. (e) SEM image of silver bowtie array with 6 nm gap. 89

Figure 5.13 Corresponding electric field in bowtie pattern with (a) nano-gap and (b) connection. 90

Figure 5.14 Schematic of the simulated bowtie structure with 25 nm thickness on 150 nm Si_3N_4 membrane in (a) 3D view and (b) cross-sectional view at bowtie center on x/z plane. 91

Figure 5.15 Molecular structure of 1,2-di(4-pyridyl)ethylene (BPE) and its Raman spectroscopy. 93

Figure 5.16 FDTD calculated electric field intensity , $|E|^2$, on gold bowtie structure with 8 nm gap illuminated by excitation wavelength of (a) 632.8 nm and (b) 785 nm. 94

Figure 5.17 FDTD simulations of the electrical field intensity $|E|^2$ on the (a) gold and (b) silver bowtie. 94

Figure 5.18 (a) Recorded SERS Raman signal of 0.1 mM BPE from bowtie array of a) gap size of 6 nm and different period in the range of 550 nm to 1000 nm, (b)The relationship between recorded Raman intensity of C=N bond and the bowtie period. 95

Figure 5.19 Recorded SERS Raman signal of 0.1 mM BPE from bowtie array of (a) period of 550 nm, excitation wavelength of 785 nm and different gap size, and (b) period of 550 nm, excitation wavelength of 632.8 nm and different gap sizes. 96

Figure 5.20 Recorded Raman intensity of C=N bond from gold and silver bowtie nano-antenna with 8 nm gap, period of 550 and excitation wavelength of 785 nm for gold and silver bowtie nano-antenna. 97

Figure 5.21 Comparison of SERS spectra of BPE with varied concentration from 10^{-1} mM to 10^{-6} mM on bowtie array with (a) 6 nm gap and (b) 25 nm gap. 99

Figure 6.1 Prism coupling to surface plasmon polarizations (SPPs) using attenuated total internal reflection in the Kretshmann (left) and Otto (right) configuration. 102

Figure 6.2 Prism coupling and SPP dispersion. 102

Figure 6.3 (left) Schematic of the commercial SPR device with Kretschmann configuration; (right) surface plasma resonance curves of silver film and the same film coated with a monolayer of p-4-BCMU. Copyright 2007 by the Springer. 103

Figure 6.4 Phase-matching of light to SPPs using a grating. 104

Figure 6.5 Schematic of a symmetric waveguide with width *w*, thickness *t* and length *l*, where *l*>>*w*, *t*. 106

Figure 6.6 SEM image of EOT-based SPR biosensor. Here 500 nm period hole array with the diameter of 150 nm in 100nm-thick Au film is fabricated by EBL and liftoff. 106

Figure 6.7 (A) SEM image of an array of nano-holes in a gold film. (B) EOT spectra for three hoe arrays with different periodicities. (C) Schematic of EOT device. Copyright 2008 by the American Chemical Society. 107

Figure 6.8 Schematic diagram of the nano-hole array fabrication process which includes (a) EBL process, (b) resist development, (c) Cr deposition, (d) first liftoff, (e) RIE, (f) gold deposition and (g) second liftoff process, and (h) final structure. 108

Figure 6.9 AFM images of fabrication of EOT structure after three intermediate steps: (a) after first lift-off; (b) after CF_4 and O_2 RIE to silica; (c) after second liftoff. 110

Figure 6.10 (a)-(c) The schematic of fabrication process through single liftoff step. In (c) the mechanism of three types of defects are described: 1. pattern covered by metal blocking dissolution; 2. chimney-shape holes; 3. collapse of structures. (d) SEM image of final EOT pattern through double liftoff process. (e) SEM image of final EOT pattern through single liftoff process. 112

Figure 6.11 SEM images of final EOT hole array with the dot dose of (a) 10 fc/dot, (b) 20 fc/dot, (c) 30 fc/dot, (d) 40 fc/dot, (e) 50 fc/dot, (f) 60 fc/dot, (g) 80 fc/dot, (h)100 fc/dot. Fewer pillars fall with increasing exposure dose of 10-30 fc/dot. Higher exposure dose over 60 fc/dot leads to obvious noise. After 100 fc/dot, central area was over exposed totally because of dose overlap. 113

Figure 6.12 SEM images of final EOT hole array by facing up position during the second liftoff step. The patterns were exposed with the dot dose of (a) 40 fc/dot, (b) 50 fc/dot, (c) 60 fc/dot, respectively. 114

Figure 6.13 (a)-(g) SEM images of EOT hole array with the dot dose of 30, 40, 50, 60, 70, 80, 90 and 100 fc/dot, developed in low temperature, respectively. (h) The relationship between exposure dose and the diameter of holes with the development at room temperature and low temperature (5 ^{o}C). 116

Figure 6.14 (a) Schematic of mechanism for reduced transmission by random scattering on rough surface and gaps of grains and particles within the noble metal film. (b) Cross-sectional SEM image of the rough surface of the evaporated Au film contained nano-hole array. 117

Figure 6.15 Comparison of the roughness of (a) 1 nm Cr/100 nm Au, (b) 1 nm Ge/100 nm Au, and (c) MPTMS/100 nm Au by AFM (left) and SEM (right). The RMS roughness for the three types of Au films is 6.4 nm, 6.9 nm and 7.4 nm, respectively. (d) Chemical structure of MPTMS. 119

Figure 6.16 Schematic of "Template stripping" method: (a) film deposition or pattering; (b) resin casting; (c) template stripping. 120

Figure 6.17 Comparison of the same EOT samples (a) before and (b) after annealing with the exposure dose of 40 and 60 fc/dot, respectively. 120

Figure 6.18 Schematic of the fabrication process of EOT pattern on Si_3N_4 membrane: (1) coating 15 nm Al/100 nm ZEP-520A on cleaned Si_3N_4 membrane and EBL; (2) development in amyl acetate; (3) etching through by BCl_3 and CF_4 RIE; (4) deposition of 1 nm Cr and 100 nm Au. 122

Figure 6.19 (a) The relationship between dot dose and the diameter of the final hole array. (b) Top-view by microscope of the Au nano-hole array patterns. SEM images of the nano-hole arrays with varied diameters exposed by (c)&(f) 10 pC/dot, (d)&(g) 40 pC/dot, (e)&(h) 70 pC/dot...................................123

Figure 6.20 Top-view SEM images of (a) bare Si_3N_4 membrane with etched-through nano-hole array, (b) the same membrane with 100nm-thick Au by electron beam evaporation. 124

Figure 6.21 Schematic of the fabrication process of EOT pattern by electroplating: (a) coating 20 nm ARC/300 nm ma-N 2403 on cleaned ITO and EBL; (b) development in MF-319; (c) electroplating of Au film; (d) resist removal by O_2 RIE. 125

Figure 6.22 AFM imaging of Au film by electroplating current of (a) 2.8 mA and (b) 3.6 mA. (c) SEM cross-sectional view of Au film by electroplating current of 2.8 – 3.6 mA. 126

Figure 6.23 SEM image of (a) electroplating result without ARC adhesive layer; (b) electroplating result with ARC adhesive layer; (c) final EOT pattern after resist removal; (d) uniform resist pillar array after EBL in large area; (e) uniform final EOT pattern in large area. 127

Figure 6.24 Schematic of the fabrication process of EOT pattern by hybrid nanoimprint-soft lithography: (a) coating 200 nm PMMA/140 nm UV-curable resist on cleaned silica and imprinting by hybrid mold; (b) CF_4/O_2 RIE to bottom; (c) electron beam evaporation of 1 nm Cr and 100 nm Au, followed by liftoff. (d) SEM image of final EOT hole array. 128

Figure 6.25 Simulated optical transmission spectrum of the EOT hole array fabricated on silica with varied diameter from 140 nm to 300 nm, Au film thickness of 100 nm, and periodicity of 500 nm. …..130

Figure 6.26 Simulated optical transmission spectrum of the EOT hole array fabricated on silica with varied film thickness from 60 nm to 200 nm, diameter of 140 nm, and periodicity of 500 nm. ………..131

Figure 6.27 Effects of film thickness on EOT transmission intensity at the first peak (1,0) and the second peak (1,1). 132

Figure 6.28 (a) Simulated optical transmission spectrum of the EOT hole array fabricated on silica with varied period from 400 nm to 600 nm, diameter of 140 nm, and 100 nm Au film. (b) The position of the first and second peaks impacted by changing period from 400 nm to 600 nm. 133

Figure 6.29 Schematic of a periodic array of tapered nan-hole array in Au film fabricate by (a) double lift-off process and (b) evaporation of Au onto the hole array patterned on a free standing membrane. The structures are illuminated by TM polarized light from glass side. 134

Figure 6.30 (a) FDTD simulated near filed transmission spectrum of non-vertical profile of nano-hole structure at different tapered angle of nano-hole array with radius of 100 nm, hole depth of 100 nm, and structural periodicity of 500nm. (b) Effect of tapered angle on the normalized electric field of the nano-hole array with radius of 100 nm, hole depth of 100 nm, and period of 500 nm at wavelength of 820 and 200 nm away from the air/Au interface. (c) The FDTD calculated $|E|^2$ profile of the $(1,0)_{film/glass}$ resonance mode. The raw shows the cross section across middle of the tapered nano-holes of period 500 nm at wavelength of λ= 807 nm and α=0, λ= 810 nm and α=4, λ= 814 nm and α=8, λ= 817 nm and α=12, and λ= 820 nm and α=16, respectively. The hole radius and hole depth were 100 nm. Light incident from the substrate medium through the nano-hole array. 135

Figure 6.31 Transmission spectrum of nano-hole arrays with varied periods and diameters. The thickness f Au film is 100 nm. The diameters are 153.6 nm, 174.9 nm, 184.2 nm, 198.2 nm, 209.3 nm, and 234.5 nm, with the changing period from 400 nm to 550 nm with step of 25 nm. 137

Figure 6.32 (a) SEM micrograph of the positive profile NHA before annealing. The inset shows the positive profile NHA after annealing. (b) FDTD simulated transmission spectrum of the positive profile NHA and measured one before and after annealing at 600 °C. 138

Figure 6.33 Comparison of optical transmission spectrum of NHAs with the diameters of (a) —148.9 nm after annealing, —174.9 nm before annealing, —153.5 nm as-fabricated, —150 nm in simulation; (b) —208.4 nm after annealing, —235.5 nm before annealing, —209.3 nm as-fabricated, —209 nm in simulation. 140

Figure 6.34 Recorded and FDTD simulated far field transmission spectrum of the nano-hole array patterned on free-standing Au film. The hole diameter, hole depth and period is 178 nm, 100 nm, and 500 nm respectively. 141

Figure 6.35 Measured transmission spectrum of a) annealed hole array of diameter of 149 nm; b) as-fabricated hole array of diameter of 153 nm; c) annealed hole array of diameter of 208nm and d)as-fabricated hole array of diameter of 209 nm. 142

List of Tables

Table 3.1 Influence of developer concentration on resist resolution. 32

Table 3.2 Typical exposure dose of PMMA with different accelerate voltage. 33

Table 3.3 Different developer systems for ZEP-520A. 34

Table 6.1 Positions for the first and second peaks with varied radius. 131

Table 6.2 Positions for the first and second peaks with varied thickness. 132

Table 6.3 Positions for the first and second peaks with varied period. 133

Chapter 1

Introduction to nanofabrication

1.1. Introduction to nanotechnology

Human beings have utilized nano-materials and structures for a long history. A most cited example is the Lycurgus cup, which is made of dichroic glass by the ancient Romans in about 290-325 AD. Because of the surface plasmon generated by the gold and silver nano-particles dispersed within the glass, more blue light is scattered during light transmission. By these ~70 nm particles, the cup shows different color in transmission and reflection (as shown in Fig. 1.1). Another example is handmade gold leaf, of which the thickness is achieved below 120 nm within large area. The manufacturing process is systemically recorded in an ancient Chinese encyclopedia: *Tiangong Kaiwu*, by Yingxing Song, published in 1673 AD. Last, activated charcoal has been used to detoxicate and purify water throughout human's history, because its micro-/nano-porous structure can absorb organic small molecules. However, all these applications do not involve the recognition in nano-scale.

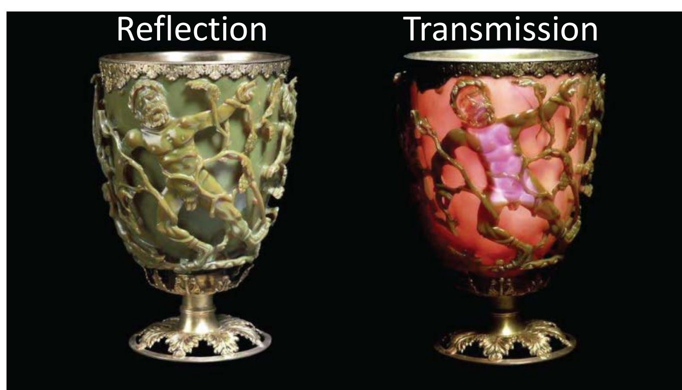

Figure 1.1 The Lycurgus cup, kept in the British Museum, is made in about 290-325 AD. The cup shows green color when illuminated from outside and red color when illuminated from inside. Copyright 2014 by the British Museum.

Nanotechnology, as the fast developing technology in this century, means the recognition and manipulation in the nano-scale. Nanotechnology includes the systemic study of observation, characterization, synthesis, fabrication and application in nanoscale. The first transmission electron microscope (TEM) was setup by Max Knoll and Ernst Ruska in Berlin in 1931. The first well-focused scanning electron microscope (SEM) with high magnification was set up by Baron Manfred von Ardenne in 1937. The first scanning tunneling microscope (STEM) was developed by Gerd Binnig and Heinrich Rohrer in IBM in 1981. These techniques of electron microscopes and other characterization techniques, such as atomic force microscope (AFM), X-ray diffraction (XRD), Raman spectroscopy, and so on, improve the characterization and manipulation in the nano-scale greatly. As Prof. Richard Feynman envisioned in 1956, “there is plenty of room at the bottom”.[1] Nowadays, nanotechnology has been applied in many research fields, such as nanomaterials, nanoelectronics, nanophotonics, and nanobiology.

1.2. Introduction to nanofabrication

Nanofabrication means fabrication technologies in nano-scale. Though film with nano-thickness can be fabricated easily through deposition techniques, e.g. evaporation, and molecular beam epitaxy (MBE), nanofabrication refers to patterning in three dimensions. From microfabrication to nanofabrication, fabrication technology has been continually pushed by the main driving force from semiconductor industry. As predicted in Moore’s law, “the number of transistors on integrated circuits doubles approximately every 18 months”.[2] When the semiconductor manufacturing technology was set up in the 1970s, the original critical dimension of integrated circuits was 1 µm. By the invention of deep UV photolithography in 1982, this feature size has shrunk to 500 nm in 1990s and to sub-100 nm in 2000s.[3] In 2008, the 45 nm generation was developed by Intel using immersion lithography, and then in 2009 the 32 nm generation was achieved using 193 nm deep UV lithography (White Paper Introducing the 45nm Next-Generation Intel® Core™ Microarchitecture). In April 2012, the 22 nm CMOS process

following the 32 nm process was started for CPU products. The 14 nm process was introduced by the semiconductor industry in the 2014 timeframe.

Different from the standard nanofabrication process in the semiconductor industry, various nanofabrication techniques are being developed in academic research, which can be classified into two kinds: the top-down approaches and bottom-up approaches. For the top-down approaches, the resist is patterned firstly by lithography (Fig. 1.2a-1), e.g. photolithography, electron beam lithography (EBL), and nanoimprint lithography (NIL), then the pattern is transferred by either metal deposition followed by liftoff (Fig. 1.2a-2&3), or direct etching (Fig. 1.2a-4&5). This process is very similar to the nano-manufacturing in semiconductor industry and is mostly a physical process. For bottom-up approaches, the substrate is coated by chemically synthesized nano-particles, or chemically grafted self-assembly monolayer (SAM layer), as shown in Fig. 1.2b. Another popular bottom-up method is annealing the block-copolymer (BCP) film on substrate to form nano-holes or pillars by phase separation, named as block-copolymer annealing lithography (Fig. 1.2c).

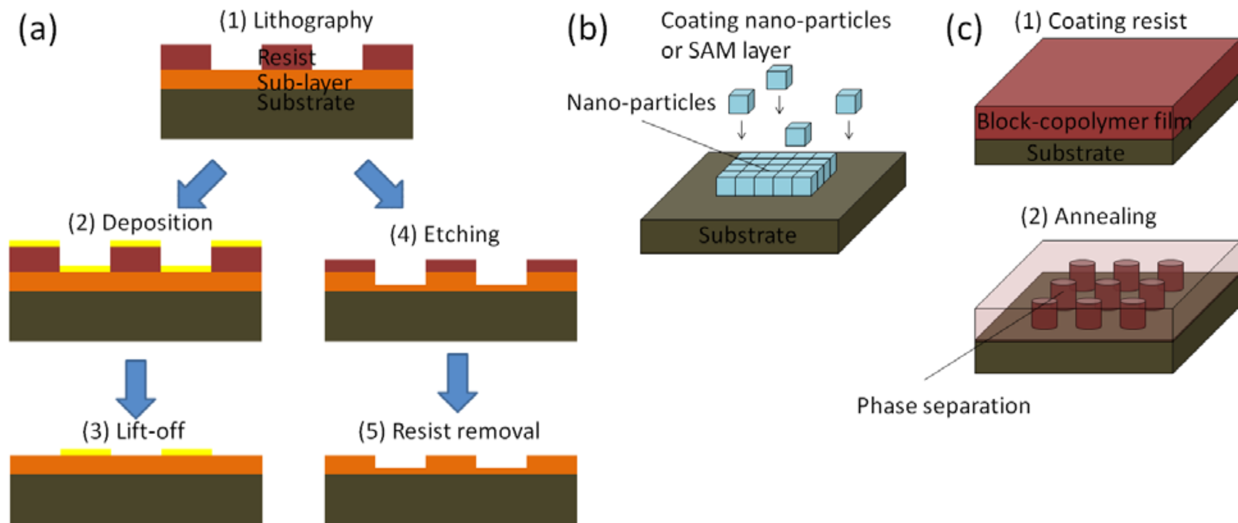

Figure 1.2 Schematic diagram of (a) the top-down and (b)&(c) the bottom up approaches. In the top-down approaches, (1) the resist is patterned by lithography, and then the pattern is transferred by (2) deposition followed by (3) liftoff, or the pattern is transferred by (4)&(5) direct etch. In the bottom-up approaches, method (b) is coating synthesized nano-particles or SAM layer; (c) is block-copolymer annealing lithography.

1.3. The work in this thesis

In this thesis, several nanofabrication techniques were investigated, developed and applied in the nanostructures for surface plasmonic chemical/bio-sensors. Chapter 2 and 3 described the experimental study in nanofabrication techniques of nanoimprint methods and electron beam lithography, respectively. Chapter 4 described briefly the mechanism of surface plasmon. In Chapter 5, the work was focused on the breakthrough of the EBL resolution limited by the proximity effect and the application in surface enhanced Raman scattering (SERS). In Chapter 6, structures of nano-hole arrays (NHAs) were achieved by several nanofabrication techniques and applied in extraordinary optical transmission (EOT). The applications in chemical and bio-sensors were discussed in Chapter 5 and 6.

Chapter 2

Imprint methods for nanofabrication

2.1. Background of imprint methods in nanoscale

Design and fabrication of sub-wavelength structures are important for surface plasmonic (SP) and other applications. The most popular patterning technique in micro- and nanofabrication is optical lithography (see Fig. 2.1). During the process a photomask (also called reticle) is imaged onto a flat substrate surface coated with a thin layer of polymer material called a photoresist. The deposited photonic energy will cause either chemical reaction/polymer chain breaking (positive tone) or cross-linking (negative tone).

Based on Rayleigh Criterion:[4]

$$R = {k_1 \lambda}/{NA} \qquad (2.1)$$

The resolution (R) of optical lithography is determined by the wavelength (λ) and the numerical aperture (NA) of the lens, while k_1 factor has no well-defined physical meaning. In an effort to get smaller feature sizes, light sources with smaller wavelengths (using 193 nm exposure) were introduced as the semiconductor industry developed. At the same time, various techniques of resolution enhancement are developed, such as immersion lithography, optical proximity correction, off-axis

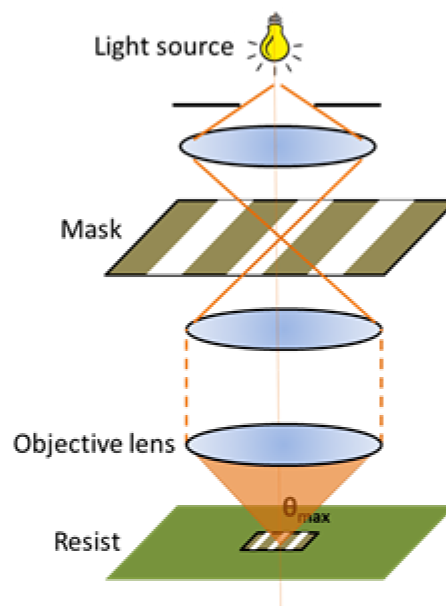

Figure 2.1 Schematic diagram of the optics of the projection lithography system.

illumination, phase-shift mask, double patterning, and so on.

Since semiconductor manufacturing technology was set up in 1970s, the critical dimension of integrated circuits has shrunk from 1 μm to 10s nm by industrial photolithography.[3] In 2008, the 45 nm generation was developed by Intel using immersion lithography, and then in 2009 the 32 nm generation was achieved using 193 nm deep UV lithography (White Paper Introducing the 45nm Next-Generation Intel® Core™ Microarchitecture). In April 2012, the 22-nm CMOS process following the 32-nm process was started for CPU products.

While extreme UV (EUV) lithography at λ=13.5 nm can fabricate sub-20 nm structures, there are still many challenging problems. The photomask needs special Mo–Si layers and the cost of fabrication is expensive.[5] What's more important, the Rayleigh Criterion still limits the achievable feature size. A deep ultraviolet (DUV) lithography system costs about $20M USD and an industrial EUV lithography system can cost up to $50M USD. High maintenance costs are also expected.

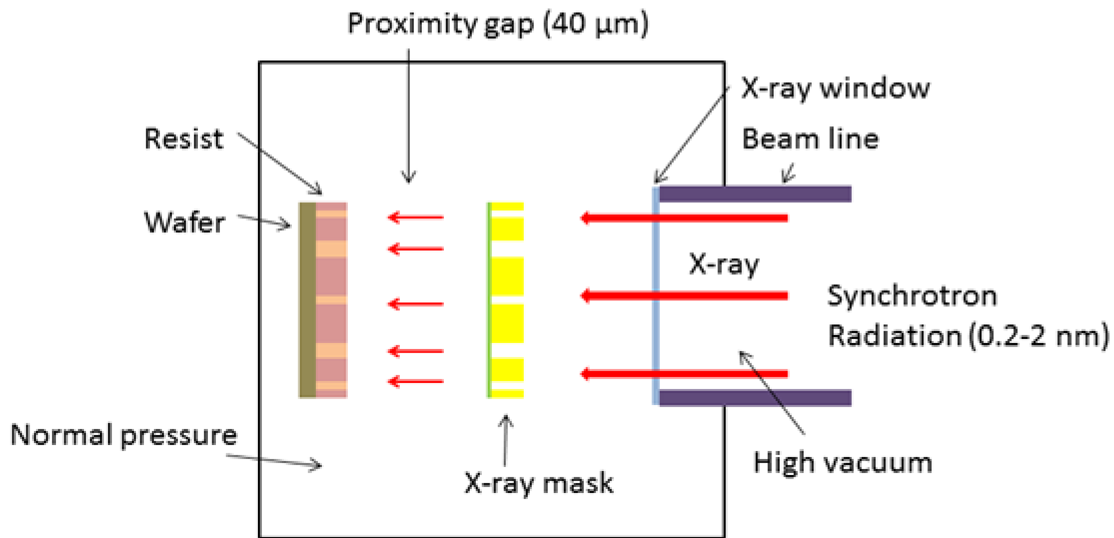

Figure 2.2 Schematic of X-ray lithography.

Several other lithographies can be used to achieve sub-micron structures. X-ray lithography can achieve high resolution (as shown in Fig. 2.2). The source wavelength spans from 1 nm ('soft' X-rays) to 0.1 nm ('hard' X-rays). However, since no materials can diffract X-rays (the refractive index is very close to 1.0), no lens exists and all pattern transfers are 1:1. Furthermore, local stress caused by heavy metal absorption and internal stress of the supporting membrane can have influences on the pattern resolution. The cost of setting up and maintaining the X-ray light source is also not affordable in most labs.

Electron beam lithography (EBL) and focused-ion beam lithography (FIBL) employ particle beams to pattern resists. EBL at 30 kV acceleration voltage has a beam wavelength of 0.007 nm. Theoretically, the limit of EBL resolution is as low as 10 nm because of secondary electron diffusion. As the examples, ring array and grating patterns with the line widths of ~60 nm and ~20 nm were achieved on poly(methyl methacrylate) (PMMA) and ZEP-520A, respectively (see Fig. 2.3). It's also reported that a 10 nm pitch has been achieved using hydrogen silsesquioxane (HSQ).[6] EBL and FIBL write on resist point by point, and are useful to pattern in nano-scale, but hours or days will be needed to expose over large area.

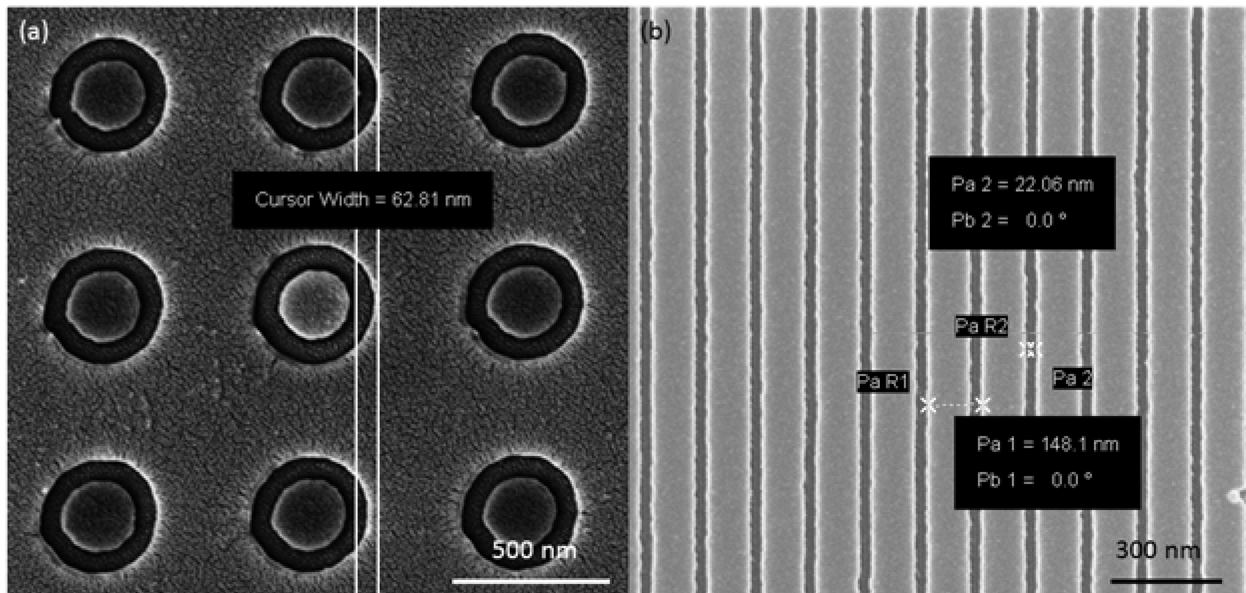

Figure 2.3 Patterns with high resolution by e-beam lithography. (a) Ring array with the line width of 60 nm on PMMA. (b) Grating pattern with the period of ~150 nm and the line width of 22 nm on ZEP-520A.

One simple way of making sub-100 nm structures is by precise duplication of existing structures. In 1995, nanoimprint lithography (NIL) with sub-25 nm resolution was first demonstrated by Prof. S. Y. Chou.[7] The principle of traditional NIL is quite simple and is shown in Fig. 2.4. A hard mold that contains nanostructures is imprinted by pressure into a softened polymer layer coated on a substrate, thereby duplicating a thickness contrast in the polymer resist. A thin residual layer on the resist is left underneath the mold protrusions, and acts as a buffer layer to avoid scratching between the hard mold and the substrate. Typically, the residual layer needs to be removed by oxygen reactive ion etching (RIE) then transferred into an under layer.

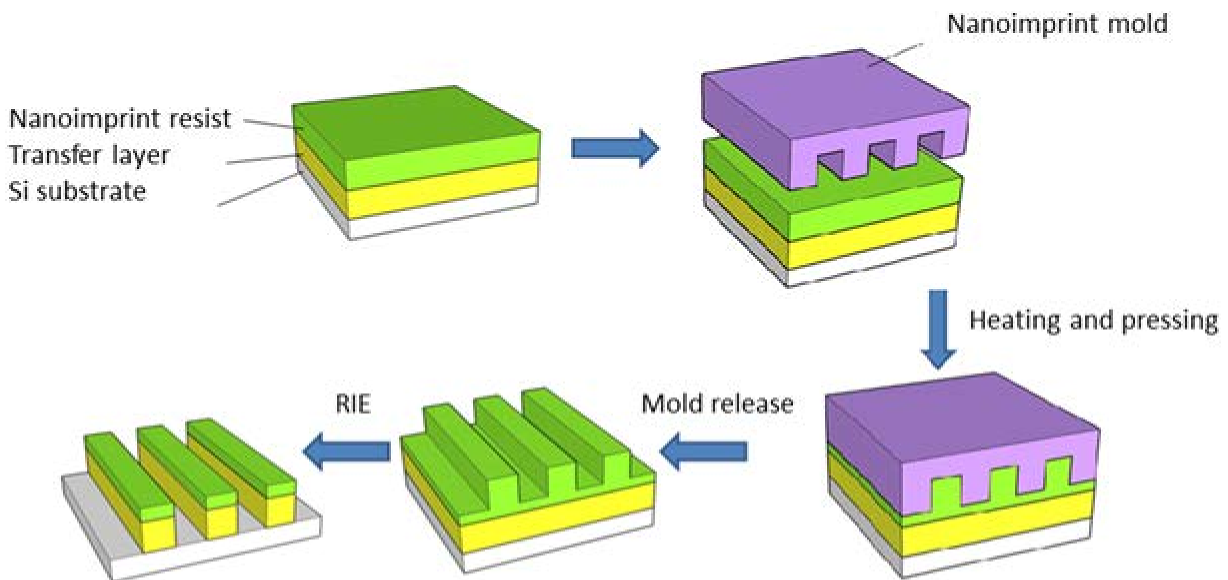

Figure 2.4 Schematic of the originally proposed NIL process.

2.2. Traditional nanoimprint lithography and its principle

Thermal NIL was firstly proposed by Prof. S. Y. Chou in 1995.[7] In this process high temperature (above the glass transition temperature (T_g)) and pressure are employed to imprint the mold into a softened polymer layer.

There are four key issues in thermal NIL:

2.2.1 NIL resist. In the imprint process, mechanical embossing makes a direct replica from the mold to the resist surface; this means the materials for NIL resist should be deformable easily under a reasonable pressure and above its T_g. The basic requirements of NIL resist are (a) low T_g to enable low imprinting temperature; (b) low viscosity to allow easy flow of polymer during the process of filling mold cavity, and (c) low shrinkage after demolding to maintain pattern fidelity. For example, as a NIL resist, PMMA with molecular weight of 15,000 $g \cdot mol^{-1}$ can be imprinted beyond 110 ^{o}C, as its T_g is 95~105 ^{o}C. Polystyrene (PS) has a T_g of 120 ^{o}C, but its viscosity is much lower than PMMA for the same temperature.[8]

Figure 2.5 Peeling off the resist onto an untreated mold.

2.2.2 NIL mold. In thermal NIL, the pattern can only be duplicated by a 1:1 ratio. The NIL mold plays a key role in replicating nanostructures into the polymer, because the duplication cannot be finer than the master. Due to the high-temperature/pressure imprint process, the mold should be made of a hard materials with a low thermal expansion coefficient, such as Si, quartz, SiC and Ni. One noticeable issue is that the surface area of the mold, owning nanoscale protrusions, is much larger than the flat area of the resist. This large contact area with the imprinted polymer promotes strong adhesion of the imprinted resist to the mold. During demolding, this effect can be seen as the sticking of the resist on a mold without any special treatment (shown in Fig. 2.5).[9] An anti-adhesive layer is

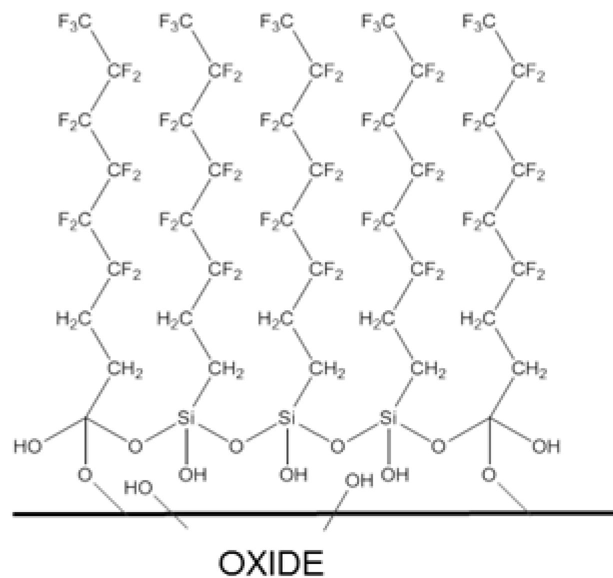

Figure 2.6 Formation of a monolayer of crosslinked fluoroalkyltrichlorosilane on oxide surface.

coated for better mold release after the imprint.[10,11] Typically, a fluoroalkyltrichlorosilane release agent is applied to silicon, silica, or quartz molds via chemical reaction with silanol groups (shown in Fig. 2.6).[12] The mold needs to be firstly treated with O_2 RIE to form –OH group on its surface, then fluoroalkyltrichlorosilane can react with the –OH group and form a fluorinated self-assembled monolayer on the mold surface, which provides a low surface energy.

2.2.3 Imprint process. The thermal NIL process involves heating the resist past its T_g, imprinting, and cooling. A high pressure is needed to overcome the viscosity and surface energy of the resist to fully fill in the protrusions. Based on classic hydrodynamics, the force F needed for squeezing resist flow can be expressed by Equation 2.2:[13]

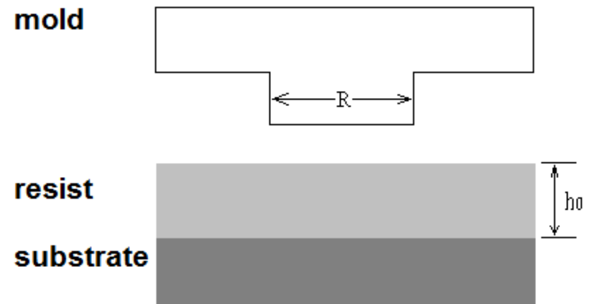

Figure 2.7 Scheme of the NIL.

$$F = \left(\frac{3\pi R^4}{4h_0^3}\right)\left(\frac{dh}{dt}\right)\eta_0 \qquad (2.2)$$

where R is the radial flow distance, h_0 is the initial thickness of polymer layer, dh/dt is the ideal speed of polymer layer being pressed in depth direction, and η_0 is the viscosity of the polymer (see Fig. 2.7). Higher process temperature can decrease the viscosity, permitting lower pressure (Fig. 2.8), but this will also increase the thermal expansion between the mold and resist layer. Increased initial thickness of the resist layer can be useful as well, but sometimes it will affect the following O_2 RIE to remove the residual layer.

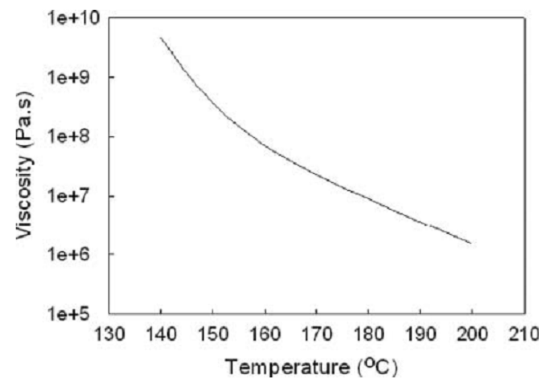

Figure 2.8 Viscosity of 110 kg/mol PMMA vs. temperature.

2.2.4 Equipment for NIL. The whole NIL process needs to be executed in vacuum to avoid air bubble formation. Uniform heating and pressure is essential for uniform results. For single-level patterning in large area NIL is more efficient than other lithography techniques, but for multilevel patterning alignment becomes crucial. One way to solve this issue is to use the Moiré method for high accuracy alignment (as shown in Fig. 2.9).[14] The Moiré method can amplify the misalignment between the mold and patterned substrate. The Moiré pattern period P_M can be expressed as:

$$P_M = \frac{P_2}{1 - \frac{P_2}{P_1}} \qquad (2.3)$$

where the periods of the alignment gratings on the substrate and mold are P_1 and P_2, respectively.

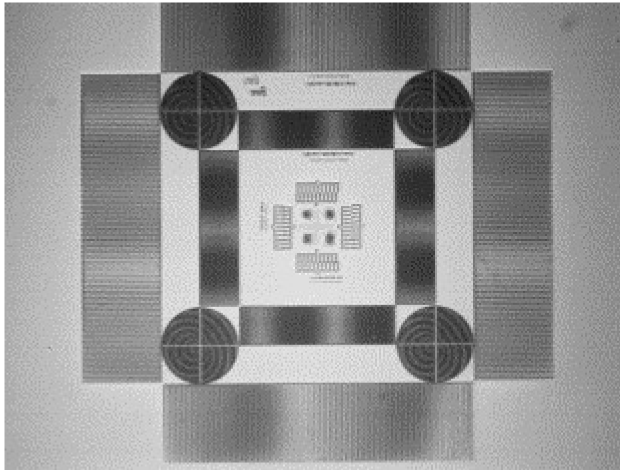

Figure 2.9 Moiré pattern used for alignment in NIL process. Copyright 2007 by the Elsevier.

For example, if the periods of the grating on the mold and substrate are 1.96 μm and 2 μm respectively, the period of the formed Moiré pattern will be 98 μm. Using the above formula a shift misalignment of 150 nm corresponds to a movement of the large Moire pattern by 7.35 μm, which can be observed readily by an optical microscope. Another way for NIL alignment with nontransparent imprint mold is to insert a miniaturized camera between the stamp and substrate before pressing down (as shown in Fig. 2.10).

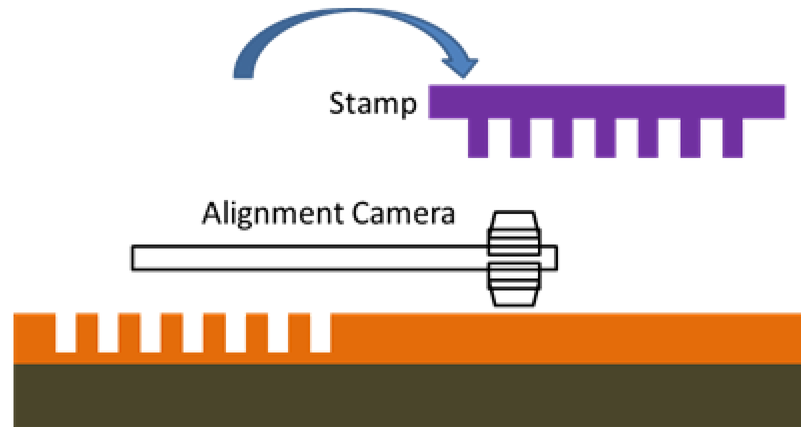

Figure 2.10 A miniaturized camera between the stamp and substrate before pressing down.

2.3. Alternative NIL

2.3.1. Laser-assisted direct imprint (LADI) lithography was reported by Prof. S. Y. Chou in 2002, where nanostructures were transferred directly from quartz into silicon (the scheme is shown in Fig. 2.11).[15] The method does not use resist and the process is very fast. A single XeCl excimer laser pulse melts the top surface of a silicon wafer (within nanoseconds the melted depth of the silicon surface can be about 300nm), and a mold is embossed into the melted liquid layer by pressure. Features with resolution below 10 nm have been imprinted into silicon using LADI, and the embossing time is less than 250 ns.

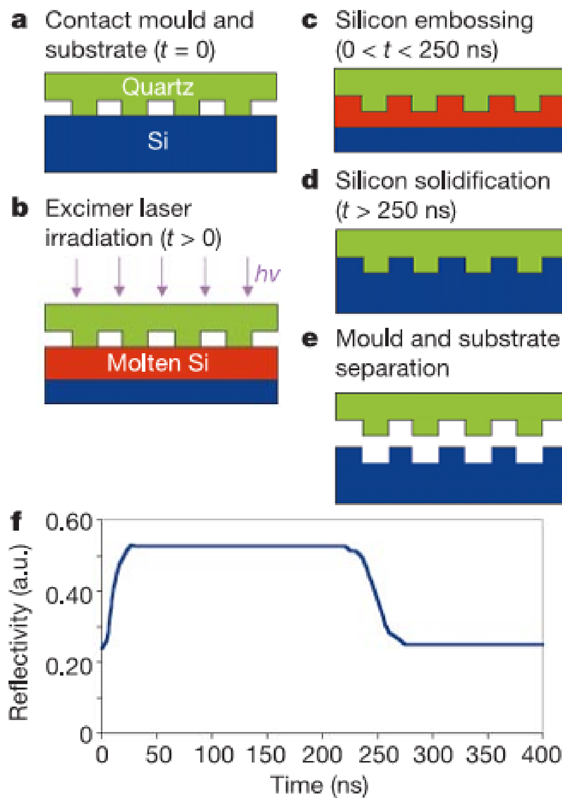

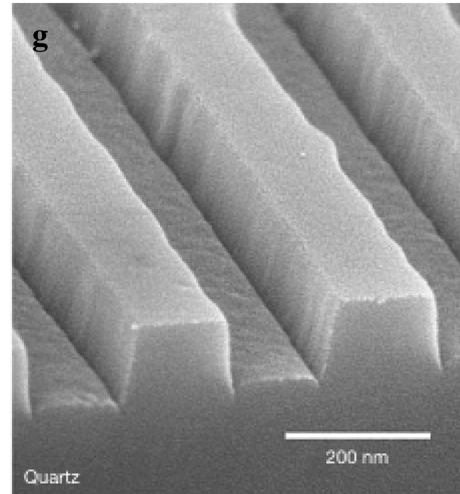

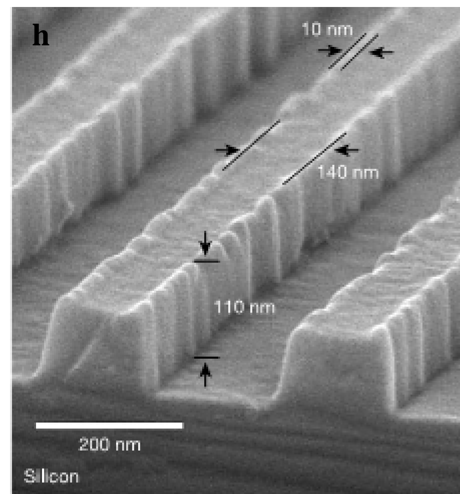

Figure 2.11 (a-e) Schematic of laser-assisted direct imprint (LADI) of nanostructures in silicon; (f) The reflectivity of a He-Ne laser beam from the silicon surface versus the time, which proves the imprint process lasts about 220 ns; SEM image of the cross-section of (g) quartz mold and (h) imprinted silicon. Copyright 2002 by Nature Publishing Group.

2.3.2. Step and flash imprint lithography (S-FIL) was developed by Prof. C. G. Willson in 1999.[16] The process is quite similar to thermal NIL with the comparison shown in Fig. 2.12.[17,18] A low-viscosity solution containing photo-curable resist and organosilicon precursors is dropped into the gap between the template and substrate. The low viscous resist automatically fills the recessed feature on the mold due to the capillary effect. The solution trapped between the surfaces is photopolymerized by UV-exposure through the quartz template. After exposure the template is separated from the substrate, leaving a UV-cured replica on the substrate. Grating structures with 60 nm resolution has been achieved over large area (6 in. × 6 in.). A quartz mold

is required for S-FIL. To fabricate a quartz mold, chromium is deposited and patterned by nanolithography method. During dry etching, Cr acts as etching mask and the pattern is transferred into quartz.

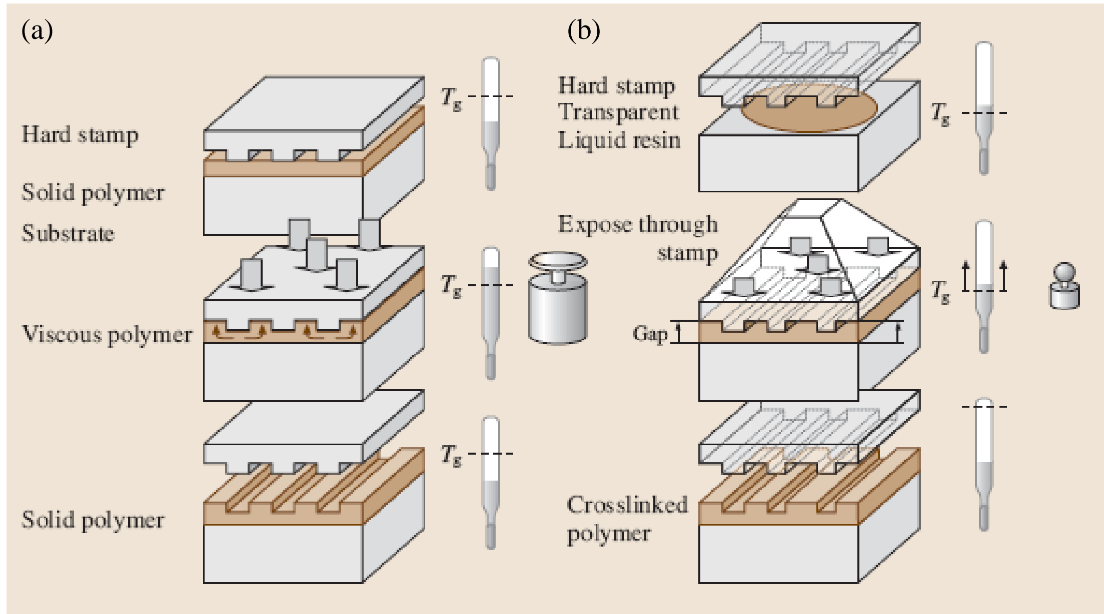

Figure 2.12 Schematic of (a) thermal NIL and (b) UV-curing S-FILS processes. Copyright 2007 by the Springer-Verlag.

2.3.3. UV-NIL. Thermal NIL uses high temperature to melt a polymer resist and high pressure to imprint structures into this viscous resist. This process may damage the samples. As an alternative, the aforementioned UV-curing S-FIL utilizes liquid resist drops and allows imprinting performed at low pressure and low temperature. But merging liquid droplets into a thin film by capillary force may cause a non-uniform thickness of the residue layer under the imprinted patterns, with residual thickness varying from about 10s nm to 100s nm. Moreover, such variation of film thickness is undesirable for pattern transferring from solid polymeric material to the substrate, thereby significantly limiting the applicability of this method for device fabrication.

Chou's group proposed a novel low-viscous and photo-curable liquid resist system for spin coating.[19] Contrary to S-FIL resists, which employ small and volatile monomers, this resist is a UV-curable acrylated oligomer formulation with a low viscosity around 100 mPa·s, which was able to meet the requirements both for formation of a thin uniform liquid film by spin-coating and low imprint pressure and temperature. They demonstrated that their photo-curable resist was capable of 14 nm pitch lines, 5 nm critical dimension features, and could be uniformly patterned over an entire 4 in. wafer in a single imprint step. This UV-NIL process was performed at room temperature and requires less than 15 psi of pressure, thus allowing for a wide range of temperature- and pressure-sensitive applications.

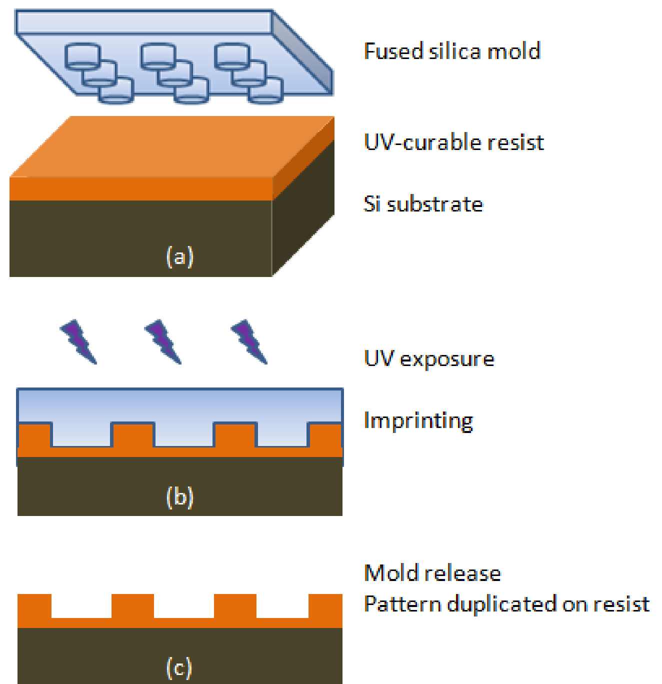

Figure 2.13 Schematic of UV-assistant NIL.

One of the most popular applications of UV-NIL is mold duplication. Since the resist includes siloxane its surface can form silanol (Si-OH) groups by O_2 RIE and is thus capable of receiving anti-adhesive treatment. This cross-linked polymer substrate provides good release properties and can be applied as a repeated mold for imprint. Thermal and UV imprinting tests demonstrated the quality of the resulting molds.[19] The typical fabrication process of a NIL mold requires patterning by other lithographic techniques and RIE for pattern transfer. Compared with the above time-consuming and expensive process, mold duplication by UV-curable resist is a quite high-throughput and low-cost technique (as shown in Fig. 2.14). Another application is reverse-contact UV nanoimprint lithography (RUVNIL). The first-layer resist is cured after first NIL so it cannot be deformed by subsequent imprint processes. Hence, this resist can be imprinted layer by layer. In 2007, N. Kehagias reported 3-layer grating structures through RUNIL.[20]

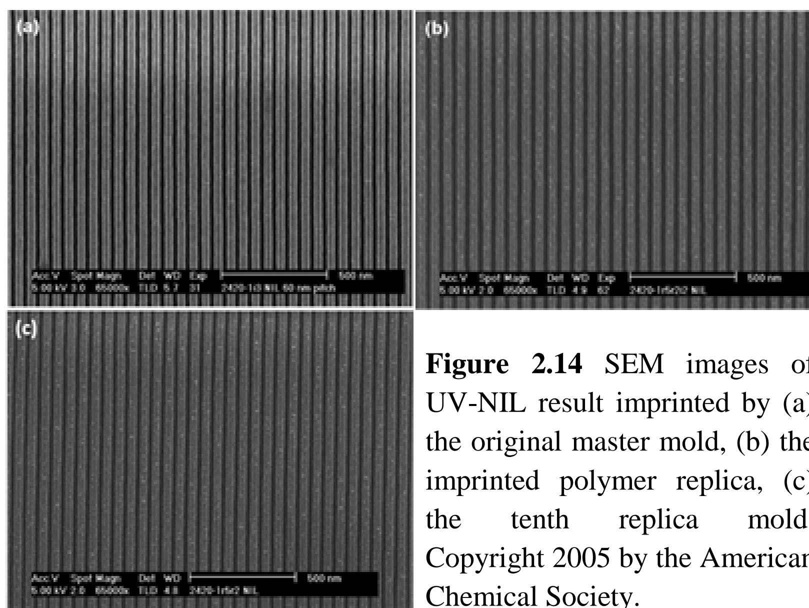

Figure 2.14 SEM images of UV-NIL result imprinted by (a) the original master mold, (b) the imprinted polymer replica, (c) the tenth replica mold. Copyright 2005 by the American Chemical Society.

2.4. Soft lithography based on poly(dimethysiloxane) (PDMS)

2.4.1. Introduction

The imprint techniques introduced previously are based on hard mold or stamp, such as silicon, quartz and nickel. High pressure, normally higher than 1 bar, is applied on the mold. The low-viscosity UV-curable resist reduces the required pressure, and facilitates the embossing by capillary force. This wetting process is more important in soft lithography, which can be used to transfer ‘‘ink’’ (as liquid resist in NIL) from the stamp to substrate. In fact, this concept of stamping ink onto a surface was proposed before the advent of nanoimprint. Soft lithography was demonstrated in 1993 by A. Kumar and G. M. Whitesides,[21] while thermal NIL appeared in 1994.

This silicone polymer (PDMS), consisting of repeating chemical structures of $-OSi(CH_3)_2O-$, is commercially available from Dow Corning Corp. under the trade name Sylgard 184. To form solid PDMS, the oligmer is mixed with the curing agent in a 10:1 volume ratio and cured by baking. PDMS has several advantages for microfluidics and biological applications. It is non-

toxic, chemically inert and friendly for living environment. It is optically transparent between ~240 nm and 1000 nm, non-fluorescent, and therefore allows standard optical measurement. It has a high bulk electrical resistivity which is important for electrokinetic applications. Moreover, its surface chemical properties can be modified for anti-adhesive treatment.

2.4.2. Microcontact printing (μCP)

The first replica technique in soft lithography was μCP. In 1993, A. Kumar and G. M. Whitesides reported using an elastomer stamp, made by casting PDMS on a master mold, to transfer alkanethiol ink to a substrate coated with thin gold film.[21] The alkanethiol ink pattern then acts as a gold wet etching mask to transfer the ink pattern into the thin gold film pattern on a substrate. The process is schematically illustrated in Fig. 2.15.

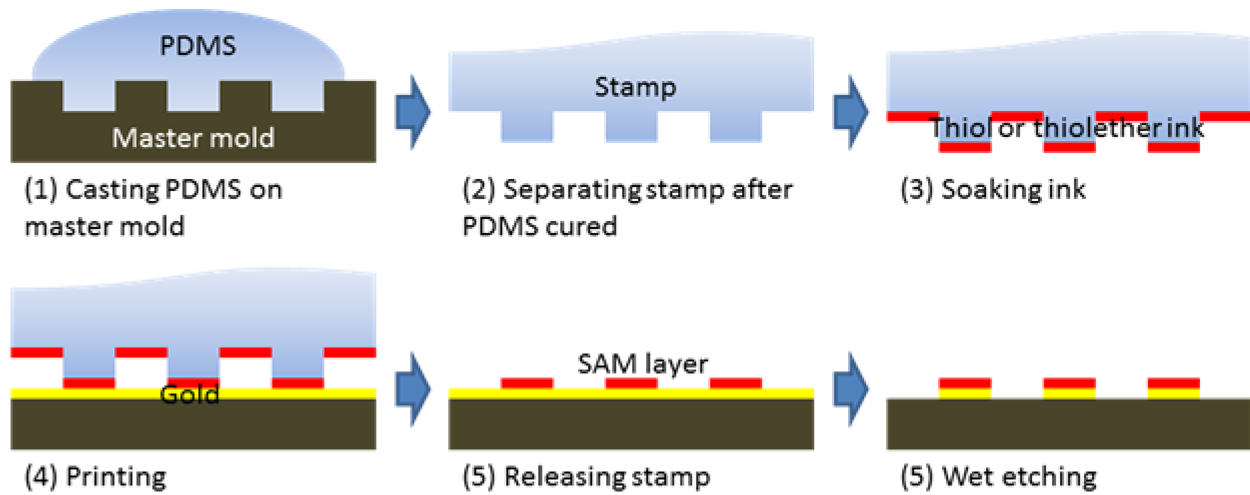

Figure 2.15 Schematic of microcontact printing process.

Soft lithography allows for patterning on a curved surface, which is desirable in many fields such as MEMS, electronic devices, and optics. But because of its low Young's modulus, a PDMS pattern will be distorted when the aspect ratio increases or the feature size is below order of 1 μm (as shown in Fig. 2.16).[22] The feature size of soft lithography should be above 100 nm and the ideal aspect ratio is around 1:1,

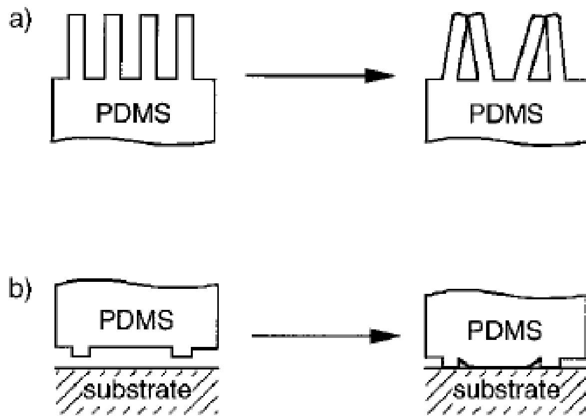

Figure 2.16 Schematic illustration of possible deformations and distortions of microstructures in PDMS. Copyright 1998 by the John Wiley and Sons.

2.4.3. Hybrid nanoimprint-soft lithography

Dr. Z. W. Li in Nanjing University developed hybrid nanoimprint-soft lithography in 2008. The process is shown in Fig. 2.17.[23] To fabricate this hybrid mold consisting of a rigid UV-cured resist layer on top of a cured soft PDMS, an elastic PDMS support was prepared by casting and thermal curing of Sylgard 184. UV-curable resist is spin-coated on a bare wafer, and a PDMS support is then placed against the resist-covered wafer. PDMS absorbs the liquid resist, and repetition for 3 total steps forms a uniform absorption film. The UV-resist-absorbed PDMS support is then placed against the resist-covered master mold and is UV-exposed in ambient nitrogen. During curing, the resist absorbed in the PDMS and the resist on the master mold forms an interpenetrating polymer network and links to the PDMS surface firmly. Consequently, after separation the pattern is transferred onto the PDMS support. After O_2 RIE and anti-adhesive treatment, the hybrid mold was fabricated and applied in the following imprint process.

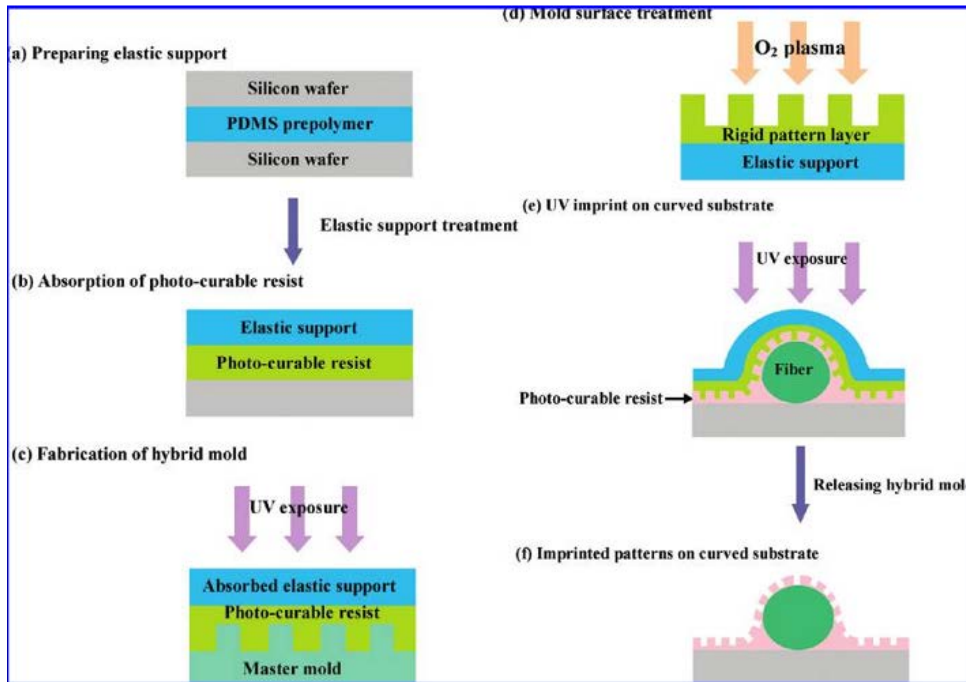

Figure 2.17 Schematic of the fabrication process of the hybrid mold and the hybrid nanoimprint-soft lithography. Copyright 2009 by the American Chemical Society.

As a demonstration, the hybrid mold was imprinted on a segment of a cylindrical single-mode optical fiber (125 μm in diameter) placed on the surface of a Si wafer. A 200 nm grating pattern was achieved over large area, as shown in Fig. 2.18.

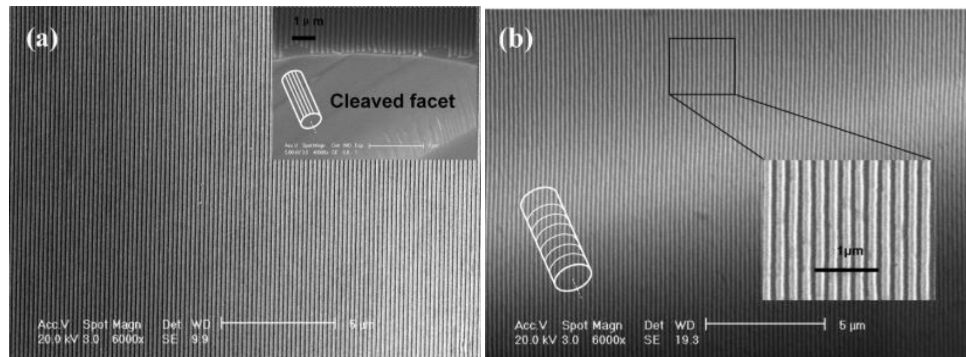

Figure 2.18 SEM images of 200 nm pitch grating on the surface of 125 μm diameter optical fiber array with the direction (a) parallel and (b) perpendicular to the fiber axis. Copyright 2009 by the American Chemical Society.

The above parts introduced briefly the various nanoimprint techniques. In the following, I will cover my contribution to this field.

2.5. Hybrid nanoimprint-soft lithography using sacrificial PMGI master mold

2.5.1 The advantage of the hybrid mold fabricated by sacrificial PMGI master mold

Hybrid nanoimprint-soft lithography using molds of a rigid UV-cured resist layer on a soft PDMS support allows intimate contact with non-flat surface during imprinting. It has achieved sub-15 nm resolutions, as compared to soft lithography using PDMS mold with >100 nm resolution. For the fabrication of the hybrid molds from a master mold, one remaining critical issue is the surface energy of the master mold relative to the liquid UV resist: if it is too high, the resist will wet the mold and thus the demolding will be difficult; if it is too low, the liquid UV resist will dewet and cannot fully fill the trenches and holes in the master mold. In order for a perfect wetting condition, the spreading coefficient $S_{liquid/solid}$ should satisfy:[24]

$$S_{liquid/solid} = \gamma_{solid} - (\gamma_{liquid} + \gamma_{liquid/solid}) > 0 \qquad (2.4)$$

where Υ_{solid} is the surface tension of the solid, Υ_{liquid} is the surface tension of the liquid, and $\Upsilon_{solid/solid}$ is the interfacial tension between the liquid and the solid. Only when $S_{liquid/solid}$ is positive, can the liquid wet the surface well (Fig. 2.19(a)). Distinct from other resists, UV imprint resist contains Si, which makes its surface tension too low to yield a uniform film (Fig. 2.19(b)).

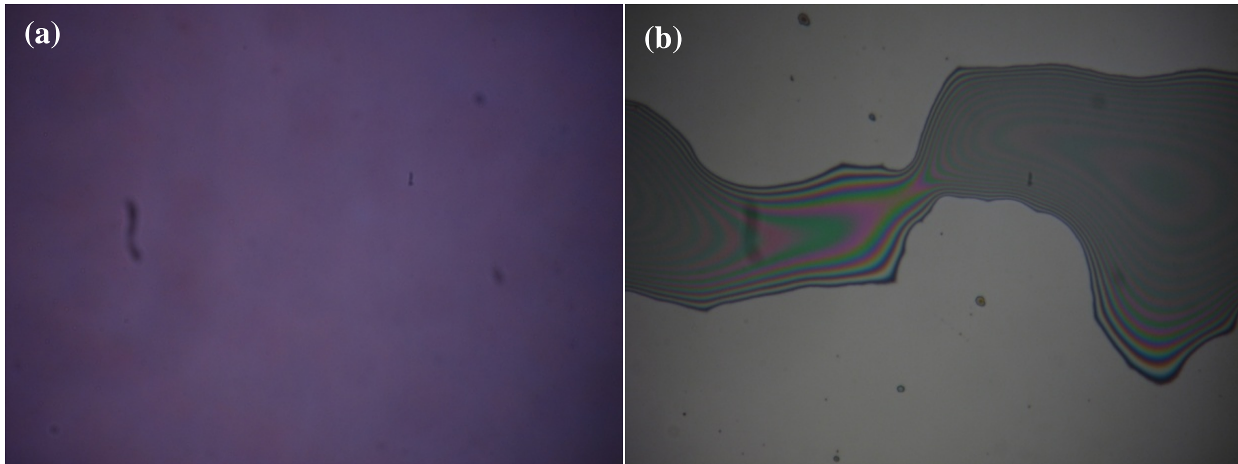

Figure 2.19 Optical images of (a) stable liquid resist film, (b) unstable liquid resist film, which shrank after 30sec.

The solution to this dilemma has been a partial treatments of the master mold surface by exposing it for a shorter time in (1H,1H,2H,2H)-perfluorooctyltrichlorosilane (FOTS) to form *sub*-monolayer, but narrow process windows and low yields have resulted. A more robust solution designed here is to use a sacrificial organic master mold that the resist wets well, and dissolve the master mold after the resist is UV-cured. We proposed to duplicate the mold from a sacrificial mold fabricated in poly(dimethyl glutarimide) (PMGI, MicroChem Corp.). The UV-curable resist wets the PMGI and can thus fully fill the trenches and holes in it. After UV curing of the resist, PMGI can be dissolved in an aqueous basic solution that, unlike most organic solvents, does not swell and deform the PDMS.[25] More importantly, PMGI is resistant to most of the solvents, so the pattern will not be affected (dissolved or swelled) by the solvent of the UV-curable resist.

2.5.2 Three types of fabrication processes

The fabrication process is described in Fig. 2.20 and is very similar to the original hybrid nanoimprint-soft lithography. Instead of silicon master mold, pattern on PMGI is fabricated and used as master mold. Briefly, to fabricate the mold for hybrid nanoimprint-soft lithography, the UV-curable resist was absorbed into the PDMS elastic support several times, as well as spin-coated onto the master mold. The elastic support was then placed against the resist-covered PMGI master mold and exposed to UV radiation. The PMGI was subsequently dissolved by AZ-300 developer containing 0.22 M tetra-methyl ammonium hydroxide (TMAH). After O_2 plasma treatment, the hybrid mold was coated with FOTS anti-adhesive layer. For hybrid nanoimprint-soft lithography, a silicon substrate was first coated with PMMA as an adhesive and liftoff layer, and then with UV-curable resist layer, upon which the mold was laid down. Next, the mold-substrate stack was placed in a plastic bag that was flushed with nitrogen gas, and the stack was exposed to UV light of 365 nm wavelength until the resist was fully cured.

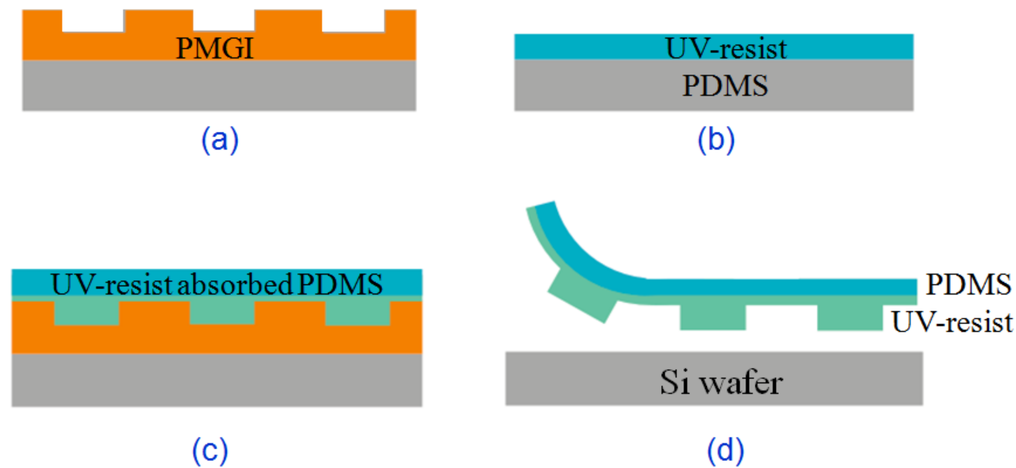

Figure 2.20 Schematic of the fabrication process of the hybrid UV-resist/PDMS mold.

To fabricate the sacrificial PMGI master mold, we developed three methods as shown in Fig. 2.21. (A) In the first method, we imprinted directly into a thick PMGI layer (spun three times to attain 200 nm thickness) with 1.2 MPa and 230°C (41°C above the T_g of PMGI). (B) In the second method, to avoid the use of high temperature of >200 °C ,which is unachievable for some commercial imprint tools, we carried out imprint on poly(vinyl phenyl ketone) (PVPK) at 90°C and 1.2 MPa. The pattern in PVPK was then transferred into the underlying 700 nm-thick LOR-5A (similar product based on PMGI, MicroChem Corp.) using low-pressure oxygen RIE that etched LOR-5A approximately twice as fast as PVPK. To further improve the adhesion of PMGI/LOR-5A to the silicon substrate, an anti-reflection coating (ARC, Brewer Science) may be coated and baked before spinning PMGI/LOR-5A. (C) In the third method, as PMGI is a high resolution resist for electron beam lithography (EBL), it can be patterned readily by EBL. A silicon wafer was first coated with a thick LOR-5A layer that dissolves faster than a thin PMGI layer with AZ-300, followed by a 20 nm conduction layer of Cr deposited by e-beam evaporation that separates the LOR-5A and PMGI layer, and finally a 70 nm PMGI layer (thin PMGI layer reduces pattern collapse due to capillary force during developer drying). After exposure using Raith 150^{TWO} at 30 kV acceleration voltage and 1.3 nA beam current, the pattern was developed using methyl isobutyl ketone (MIBK) : 2-propanol = 1 : 3 for 1 min.

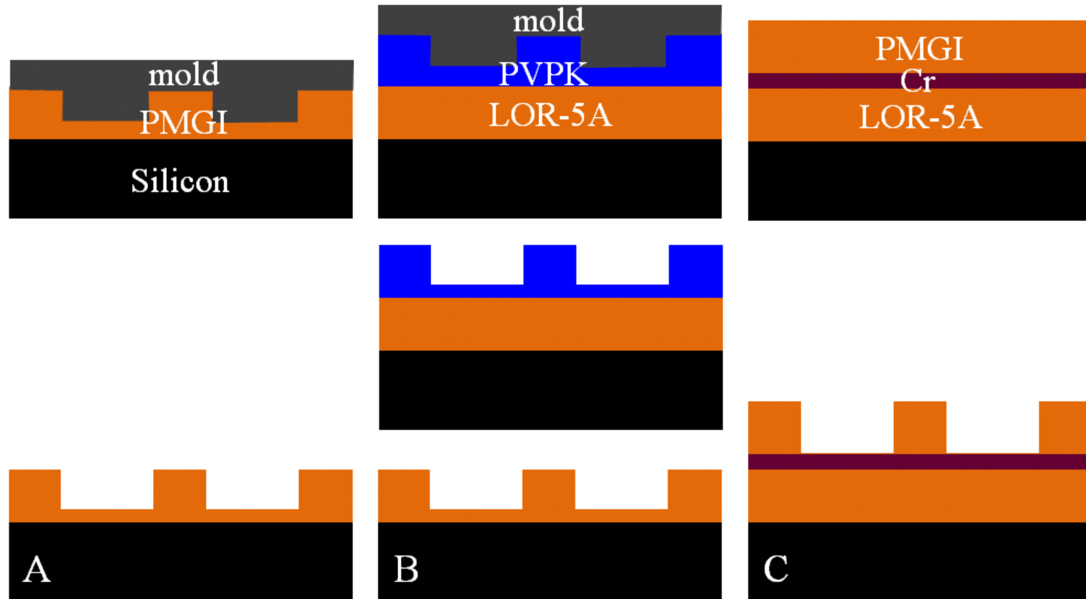

Figure 2.21 Three methods for the fabrication of sacrificial mold in PMGI (or LOR-5A that is based on PMGI). A) Direct imprint into PMGI at high temperature; B) Imprint into PVPK at reduced temperature, then RIE transfer the pattern into LOR-5A; C) Electron beam lithography using PMGI as positive resist.

2.5.3 Results and discussion

2.5.3.1 Sacrificial PMGI mold fabrication by imprint (method-A&B)

Fig. 2.22 shows (a) the SEM image of a mold duplicated from a sacrificial PMGI mold that was fabricated by the first method, and (b) an image of the 200 nm period grating in UV-curable resist imprinted using this mold. As can be seen, the line width of the mold matches well with the trench width of the imprinted resist. It was also found that the high imprint temperature of 230°C made PMGI less soluble in the AZ 300 developer, so the dissolution of the sacrificial mold took hours and some cracks resulted from mechanical separation. The crack on the imprinted result shown in Fig. 2.22b was copied from the cracked hybrid mold which was released from sacrificial PMGI mold assisted by mechanical separation.

The imprint result using the 200 nm period grating mold duplicated from the PMGI master mold that was fabricated by the second method is shown in Fig. 2.23. Due to the low imprint

temperature of only 90°C for PVPK, LOR-5A was not hardened and could be dissolved quickly by AZ-300.

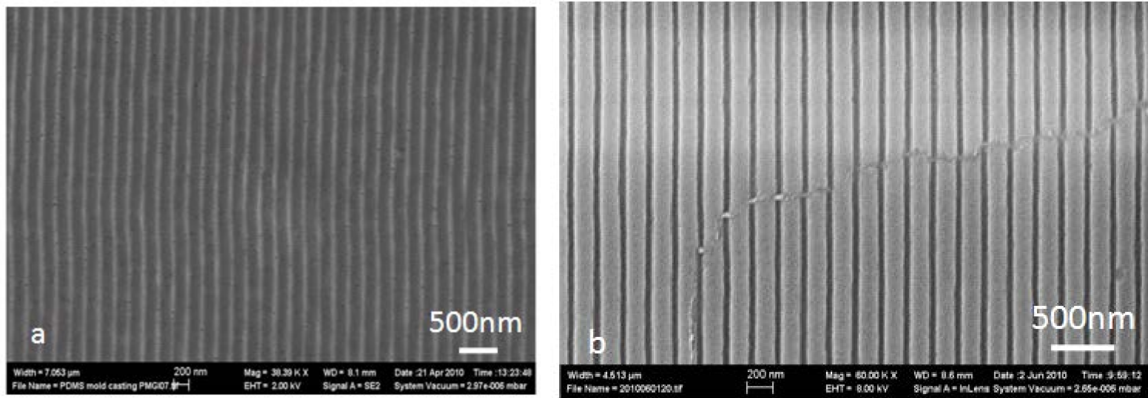

Figure 2.22 SEM images of (a) hybrid mold containing UV-cured resist on PDMS duplicated from a sacrificial PMGI mold that was patterned using the method as shown in Fig. 2.21A; (b) grating with a crack imprinted into UV-curable resist using this mold.

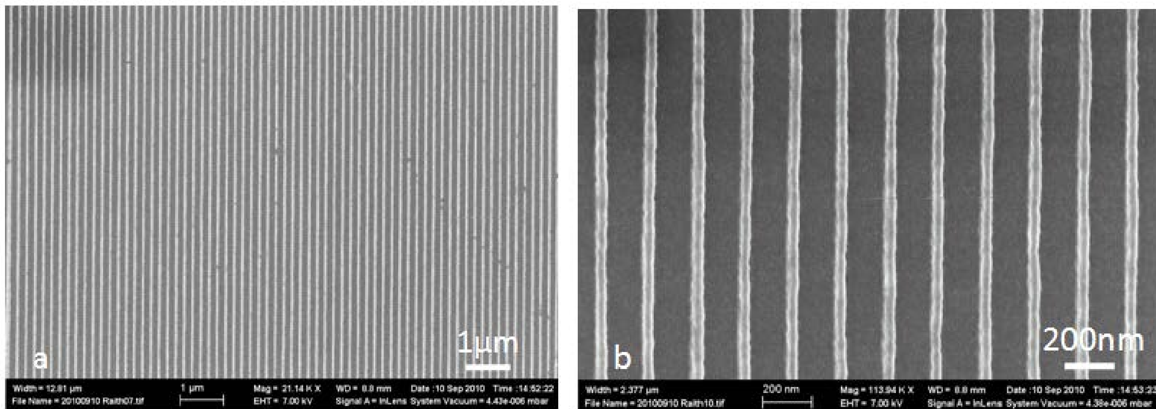

Figure 2.23 SEM image of a grating imprinted into UV-curable resist using a mold in UV-cured resist on PDMS, which was duplicated from a sacrificial PMGI mold that was patterned using the method as shown in Fig. 2.21B. a) Overview; b) Zoom-in image.

2.5.3.2 Sacrificial PMGI mold fabrication by EBL (method-C)

To test the capability of the imprint resolution using hybrid mold, line arrays with different doses and periods were patterned on PMGI layer by electron beam lithography, which was applied as the sacrificial master mold for the fabrication of the hybrid UV-resist/PDMS mold. The final result imprinted by the hybrid mold was shown in Fig. 2.24. The distorted line arrays shown in the right side of the Fig. 2.24 was caused by the capillary force during PMGI development for the minimum period of 80 nm here.

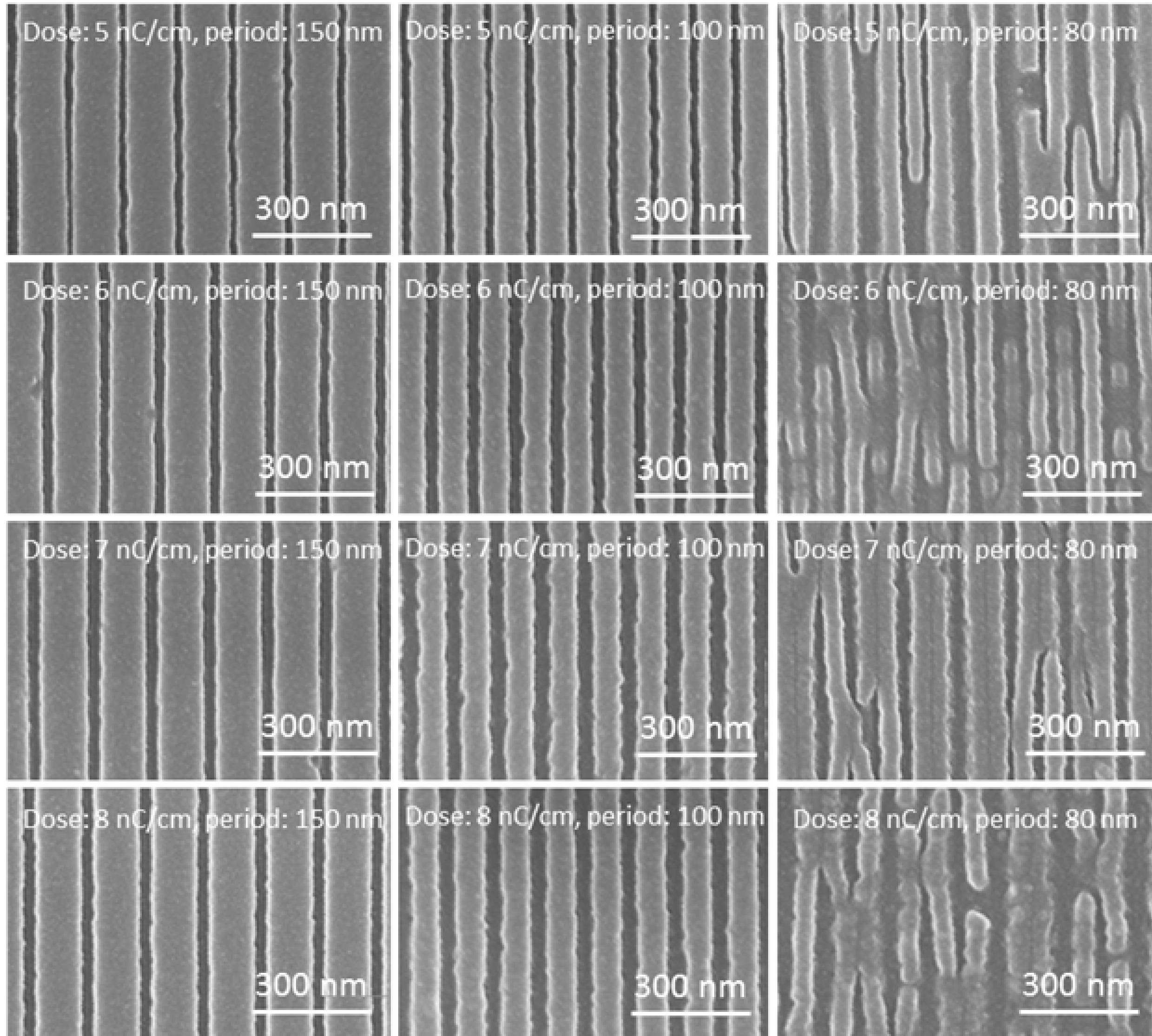

Figure 2.24 SEM image of a grating imprinted into UV-curable resist using a mold duplicated from a sacrificial PMGI mold that was patterned using the method as shown in Fig. 2.21C. Grating patterns with the periods of 150 nm, 100 nm, 80 nm were exposed with the line dose 5, 6, 7, 8 nC/cm, respectively.

As can be seen in Fig. 2.25, high resolution features of 17 nm width can be created readily. Moreover, the narrow trenches of ~8 nm in PMGI (due to PMGI pattern collapse by capillary force during developer drying) were faithfully duplicated, indicating that the resolution of the current process is below 10 nm. This is not possible for imprint process with soft mold materials like PDMS.

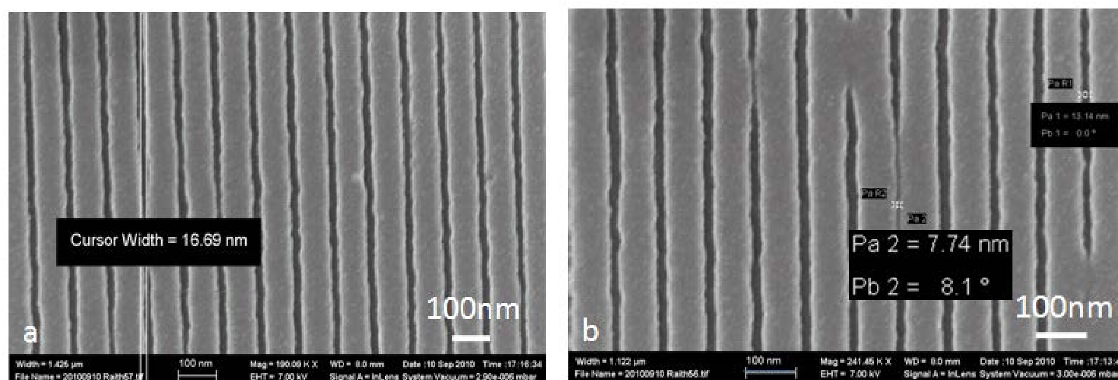

Figure 2.25 SEM image of a grating imprinted into UV-curable resist using a mold duplicated from a PMGI sacrificial mold that was patterned using the method as shown in Fig. 2.21C. a) Grating of 100 nm period with a trench-width ~17 nm; b) A collapsed grating shows features down to 8 nm.

2.5.3.3 The effect from the lifetime of the anti-adhesive layer on the hybrid mold

Lastly, we want to point out that, despite the ultra-high resolution and ease of fabrication (without the need of vacuum, applied pressure and thermal cycle), there are still some critical issues to be addressed before the hybrid nanoimprint-soft lithography can be employed for commercial application.

One issue is the lifetime of the anti-adhesive layer that may be degraded by the UV-curable resist. Since both of the pattern layer on the hybrid mold and the imprinted resist layer are made of the same UV-resist, the anti-adhesive layer is important for separation. After being imprinted for more than three times, the anti-adhesive layer was degraded partly leading to the peeling off of the pattern layer in the mold, shown in Fig. 2.26.

Another issue is the cracking of the brittle UV-cured resist on the soft PDMS, which is also a major concern for the hard PDMS/regular PDMS combination.[26] Because of this strength mismatch between the rigid UV-resist layer and the soft PDMS stamp, cracking usually happens during mold separation. For the hybrid mold achieved by the traditional method, the cracking appears on the hybrid mold during the separation from the master mold. By the method of sacrificial PMGI mater mold we developed here, a crack-free hybrid mold can be achieved easily. But it still happens in the following imprinting process (see in Fig. 2.26). One needs to be very careful during the fabrication of the hybrid mold and the separation after imprint.

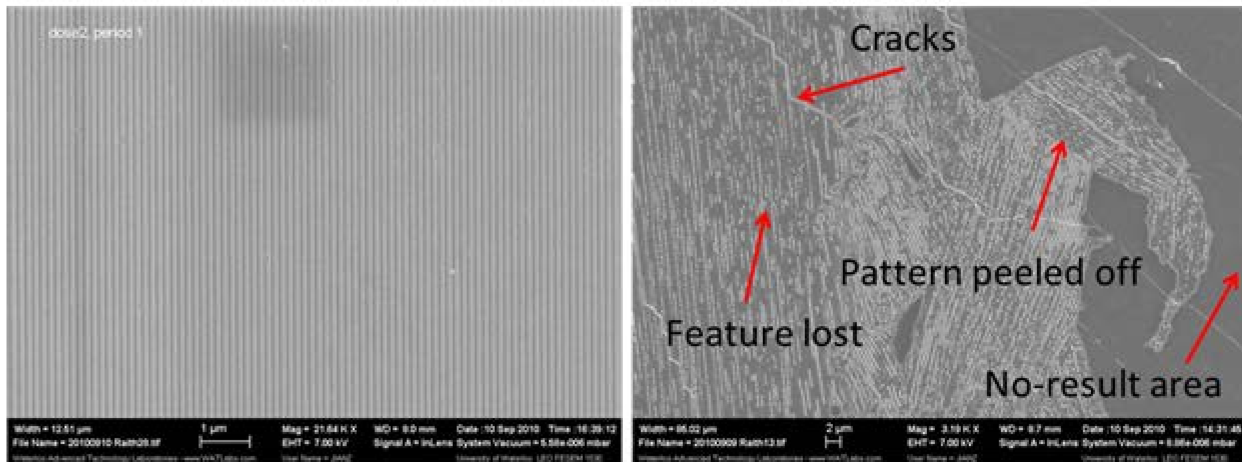

Figure 2.26 SEM image of (left) the first and (right) the third imprint results using the same hybrid mold.

2.6. Conclusion

In conclusion, imprint methods especially by soft molds were discussed in this chapter. Hybrid nanoimprint-soft lithography is capable of high resolution patterning without the need of vacuum, applied pressure or high temperature. As a more robust process, hybrid molds consisting of features in rigid UV-cured resist on an elastic PDMS support were fabricated through using a sacrificial PMGI master mold. PMGI was chosen because it can be dissolved using an aqueous basic solution that did not swell the PDMS support, and it is resistant to the solvent in the UV-curable resist. Three methods were developed to fabricate the sacrificial PMGI

mold: direct imprint into it at >200 ^{o}C, imprint into another polymer layer at sub-100 ^{o}C and then RIE transfer the pattern into PMGI, and direct writing by e-beam lithography. The third method is the most flexible, but also the most time-consuming. Using the hybrid nanoimprint-soft lithography process, we demonstrated pattern replication with sub-10 nm resolution.

Chapter 3

Nanofabrication by electron beam lithography

3.1. Introduction

In electron beam lithography (EBL), resist is exposed with electrons, analogous to photolithography's use of photons. The energetic electrons fragment or cross-link the molecular chains in the resist, decreasing or increasing its molecular weight respectively, thus adjusting the dissolvability of the exposed resist in a developer. The wavelength of the electrons λ_e can be expressed based on wave-particle duality:

$$\lambda_e = \frac{h}{p} = \frac{h}{\sqrt{2mE}} = \frac{h}{\sqrt{2meV}} = \frac{1.226}{\sqrt{V}}\ (nm) \qquad (3.1)$$

where p is the momentum of the electron, V is the voltage. For example, at a 30 kV acceleration voltage the wavelength of the electrons is 0.007 nm, and at 100 kV it is 0.004 nm. It indicates that EBL provides much higher resolution than optical lithography.

EBL evolved from scanning electron microscope (SEM), and the systems for e-beam generation are quite similar to SEM. The first popular electron-sensitive polymer material is poly(methylmethacrylate) (PMMA) developed in the 1960's.[27] EBL demonstrated nanofabrication much earlier than photolithography at that time. Because of the fine beam enabled by electron optics, EBL using PMMA resist immediately demonstrated much higher resolution capability than optical lithography. In the early 1970's EBL was already able to pattern features as small as 60 nm.[28] The modern EBL system, combined with special e-beam resist materials and processes, can fabricate structures below 10 nm.[29]

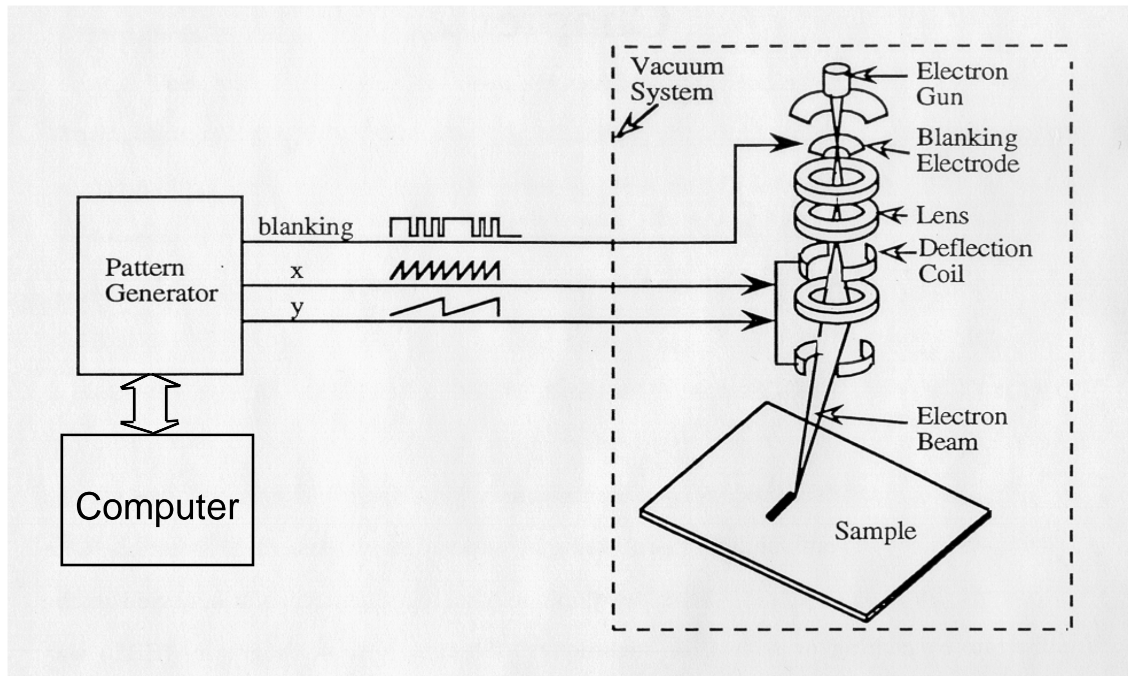

Figure 3.1 Schematic of an electron beam lithography system.

Fig. 3.1 shows a schematic of an electron beam lithography system. Generally, the electron beam is generated from an electron gun by applied acceleration voltage. The astigmatism and focus distance of the beam are adjusted through the lens. The pattern generator controls the deflection of the beam to write on the resist within the write field; it also blanks the beam during shifting between write fields or patterns. A laser detects the stage movement in X, Y and Z directions; all these signals are collected and analyzed by a computer to make sure that exposure is executed precisely. The writing process can be analogous to drawing pictures on a piece of paper (silicon wafer or other substrate) with an extremely sharp pen (sub-10 nm resolution).

In this chapter, several kinds of resists and their different development methods are introduced. The next section discusses novel resists and developments for high sensitivity electron beam lithography and resist for *in situ* development without the proximity effect. Ways for reducing the charging effect in EBL with a nano-Ampere beam current are discussed. This is used for patterning large-area dot arrays with an area dose to save exposure time and memory. The final

part shows the development of non-traditional EBL methods including tilted exposure and patterning on non-flat surface using evaporated resist.

3.2. The most popular resists: PMMA and ZEP

In electron beam lithography, electron-sensitive materials are used as resists. Due to the exposure of electron beam the molecular chains of some resists are broken into shorter chains, which can be dissolved by solvent developer. The exposed area can thus be removed by a developer. Similar in photolithography, this is termed a positive resist. Conversely, if polymerization happens by electronic energy, the exposed area becomes less soluble. This is termed a negative resist.

Contrast and sensitivity are important resist parameters which directly decide the resist's resolution capability. To calculate the contrast and sensitivity, the development curves, also called contrast curves, are obtained by measurements of the remaining resist thickness after exposure and development of a series of large-square patterns with increasing doses. The sensitivity is defined as the lowest dose needed for full development, such that a lower dose for full exposure implies a higher sensitivity. For example, in Fig. 3.2, the necessary dose (D_1) is lower for positive resist A than B, which means that A is more sensitive than B. Resist contrast is defined by the slope of its development curve and it can be calculated by:

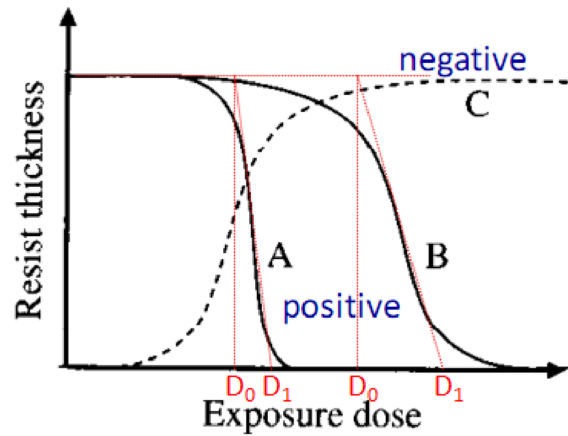

Figure 3.2 Contrast curves of resist A, B, and C.

$$\gamma \equiv \frac{1}{log_{10}(D_1/D_0)} \qquad (2.2)$$

where D_0 is the dose at which resist dissolution by developer begins, and D_1 is the lowest dose at which the resist is fully dissolved. The steeper the slope, the higher the contrast. For example, the resist A in Fig. 3.2 has higher contrast than resist B. An ideal resist gives a sharp transition with $D_1 \approx D_0$, thus its contrast is infinity according to Eqn. 2.2. Typical high-resolution resist has a contrast of $\gamma > 2$.

3.2.1. Poly(methylmethacrylate) (PMMA) and its developer

PMMA is one of the most popular resists for EBL, and was the first one used. Solid PMMA is a white powder, and normally it is dissolved in chlorobenzene for spin-coating. Concentration and spin-coating speed will affect the thickness of the resist layer. For example, at 2,500 rpm a 2 μm thickness was achieved with 9% PMMA in chlorobenzene, but a thickness of only 0.5 μm results from using 4% PMMA at the same rpm. Chlorobenzene is very inflammable and harmful to health, so in our experiment 2.5% PMMA (Mw. 950kg/mol) dissolved in anisole was normally used. A 100 nm thickness is achieved at 3,000 rpm.

The mixture of methyl isobutyl ketone (MIBK) and isopropyl alcohol (IPA) is used as the PMMA developer. The concentration of the developer mixture affects the sensitivity and resolution. As shown in Tab. 3.1, higher fractions of MIBK make the PMMA more sensitive, but with lower resolution.[30] The most popular conditions for high-resolution patterning are MIBK: IPA=1:3 for 1 minute with the typical resist thickness of 100~200 nm. The exposure dose is shown in Tab. 3.2.

Developer concentration MIBK:IPA	Sensitivity	Resolution
1:3 (MIBK: methyl isobutyl ketone)	Low	Extremely high
1:2	Medium	Very high
1:1	High	High
Pure MIBK	Very high	Low

Table 3.1 Influence of developer concentration on resist resolution.

	10 kV	20 kV	30 kV
Area dose (μC/cm^2)	100	180	250
Line dose (nC/cm)	0.5	0.9	1.3
Dot dose (fC/dot)			1.5

Table 3.2 Typical exposure dose of PMMA with different accelerate voltage.

In some reports, development in Cellosolve (2-ethoxyethanol): methanol=3:7 for 7-10 seconds is claimed to have slightly higher contrast than MIBK system.[31] In another study, MEK (methyl ethyl ketone): ethanol=53:147 for 2-5 seconds also works well.[32] One report by Shazia Yasin suggests that water/IPA solution can also develop PMMA even though neither of these agents can dissolve PMMA individually.[33] PMMA in this developer has even higher contrast than 1:3 MIBK/IPA. In addition, PMMA has been found to reverse to a negative tone when the exposure dose is very high (around 10 times of normal dose[34]), as shown in Fig. 3.3.

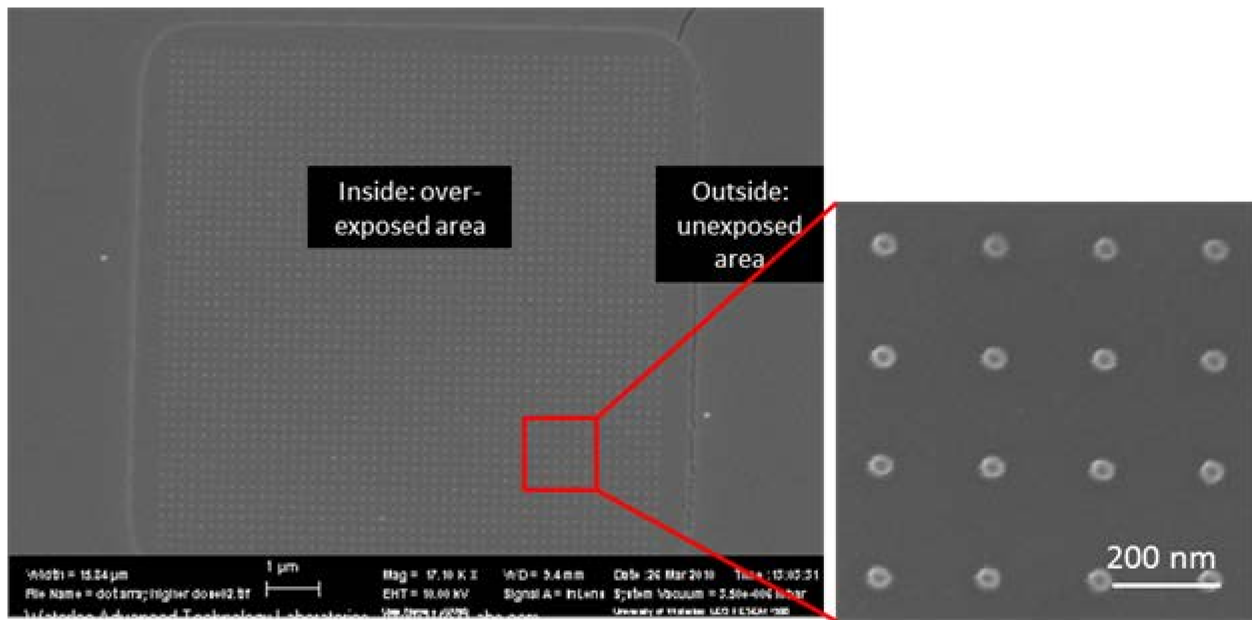

Figure 3.3 Pillar array on PMMA resist with the exposure dose 10-time higher than normal one.

In summary, PMMA resist is cheap and yields a high contrast. Its downsides are low sensitivity (50-500 μC/cm^2, as shown in Tab. 3.2), and poor dry etch resistance relative to photoresist.

3.2.2. ZEP-520A and its developer

ZEP-520, developed by ZEON Inc. in Japan, is the most popular commercially positive resist for EBL. Its sensitivity is 3-5 times higher than PMMA. The dry etch resistance of ZEP is 5 times higher than PMMA.

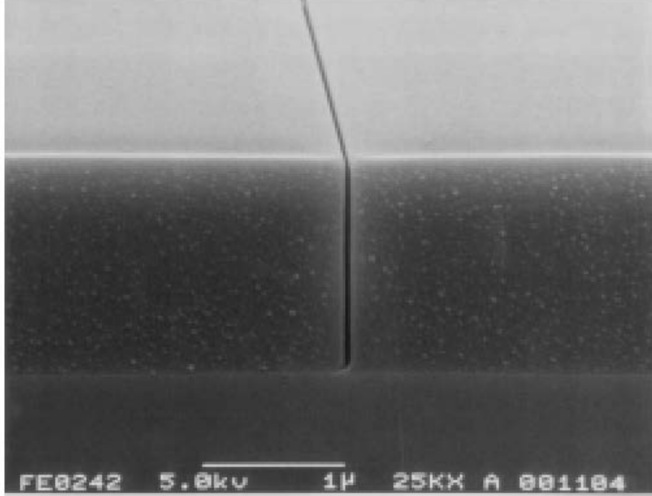

Figure 3.4 SEM image of a trench with high aspect ratio on ZEP-520A, done by ELIONIX INC.

ZED-N50 (100% amyl acetate), ZEP-RD (xylenes, o-, m-, p- mixed) and ZEP-SD (40 % 2-butanone, 60% methyl isobutyl ketone) can be used as the developer for ZEP (shown in Table 3.3). Anisole can be used for a liftoff process or diluting the resist for a thinner film.

Item	Composition	Remarks
ZEP-RD	Xylene(o-, m-, p- mixed)	standard
ZED-N50	n-Amyl acetate	high resolution
ZEP-SD	2-Butanone 40% Methyl isobutyl ketone 60%	high sensitivity

Table 3.3 Different developer systems for ZEP-520A.

ZEP-520A only has a one-year shelf life and it costs > $20/ml, much more expensive than PMMA.

In the following sections I will show my work in EBL.

3.3. Novel resist and its development

3.3.1. Self-developing aluminum fluoride resist

All of the popular resists introduced previously are organic resists. After electron beam exposure the resists need to be developed in organic solvent as an additional step before the pattern can be examined. Another problem arises from the fact that the primary electrons do not directly interact with the resists. The energy of the primary electrons is between thousands and hundreds of thousands of electron volts, too high to match the bond energy of resists. Only the generated secondary electrons with energy below 400 eV can affect the bonds of the resist. These secondary electrons diffuse laterally in the resist away from the small spot of incident electron beam and thus limit the resolution of EBL.

Inorganic halides could potentially be suitable materials for extremely high resolution, since only the primary, high energy electrons are responsible for exposure. As shown in Fig. 3.5, during electron beam exposure, AlF_3 undergoes a self-developing process. The irradiation by primary electrons causes dissociation of the metallic state. After ionic bonds are broken floride becomes gas and is removed. The aluminium self-assembles on the surface, making the resist layer thinner. This "milling" phenomenon proceeds until the layer is broken through.

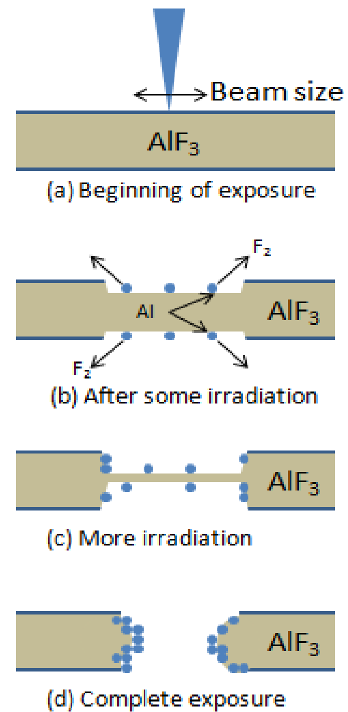

Figure 3.5 The process of self-development of AlF_3 during e-beam exposure.

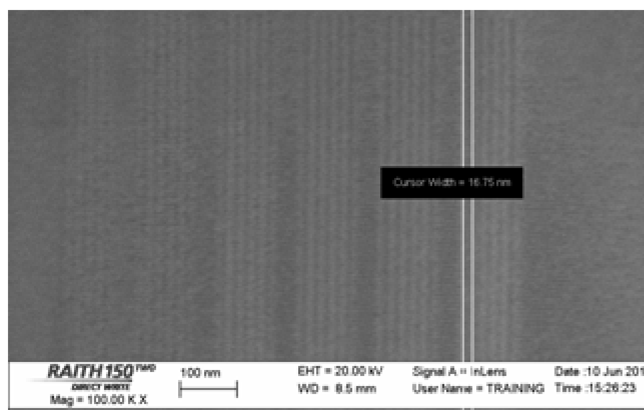

Figure 3.6 SEM image of lines with 16 nm period in $AlCl_3$.

In our work, the patterning of 16 nm period lines is achieved by a line dose of 1C/cm at 20kV. The AlF_3 film is prepared by thermal evaporation and the thickness is controlled at 20 nm. However, only line and dot array can be achieved by AlF_3 resist.

3.3.2. High sensitive EBL using high molecular weight polystyrene (PS) resist

PMMA and ZEP-520A are the most popular positive resists. Negative resists are preferred for some applications, such as fabrication of hole arrays in a metal film via liftoff. HSQ and SU-8 are common negative resists, but they are expensive and unstable, and have limited shelf lives. It is therefore desirable to have a simple and inexpensive negative resist analogous to PMMA. Previously, our group demonstrated ultra-dense patterning using 2 kg/mol polystyrene negative electron beam resist that has low sensitivity.[35]

To drastically improve its sensitivity, the exposure behavior of polystyrene with molecular weight of 90 and 900 kg/mol was studied here. Very high sensitivity of 1 μC/cm2 was obtained for 900 kg/mol when exposed at 2 keV. The sensitivity for 90 kg/mol polystyrene is about one order lower. The resist has a contrast around 1.5 that is nearly independent of molecular weight for the current range of molecular weight. It can achieve fairly well-defined patterns of 150–200 nm period line arrays (as shown in Fig. 3.7). Fig. 3.8 shows the contrast curves for 90 kg/mol polystyrene resist exposed at 20 and 5 keV. The contrast for exposure at 20 keV, defined as:

$\gamma = [lg\left(\frac{D_1}{D_0}\right)]^{-1}$, is calculated to be 1.5, which is very close to the contrast at 5 keV exposure. The contrast is much lower than the popular chain-scission positive resist PMMA and ZEP-520A.

Polystyrene is a simple and low-cost resist with easy process control and practically unlimited shelf life. It is also considerably more resistant to drying etching than PMMA. Therefore, the current high molecular weight polystyrene could be employed for applications that need moderate resolution but high sensitivity for a reasonable exposure time.

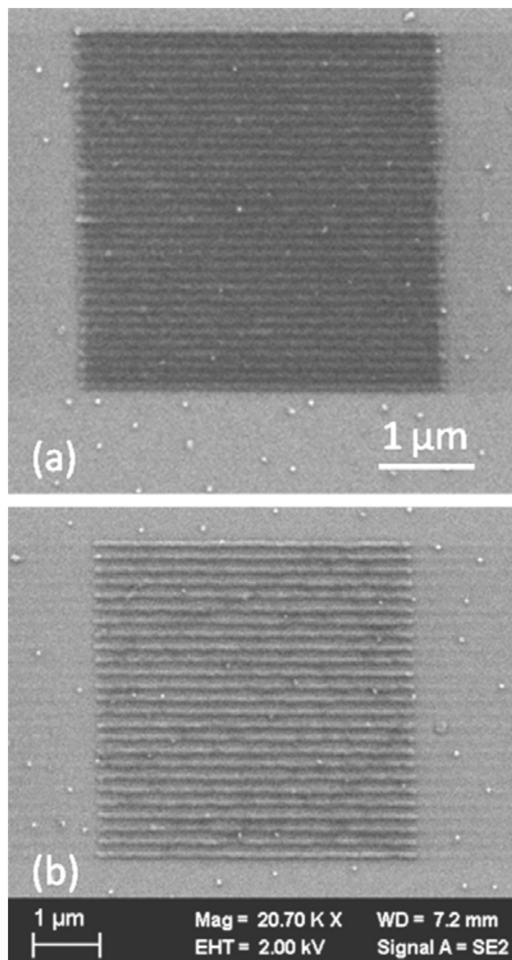

Figure 3.7 SEM images of 90 kg/mol polystyrene line array exposed at 5 keV with line dose of 0.54 nC/cm, and developed by tetrahydrofuran for 2 min. (a) 150 nm period, (b) 200 nm period.

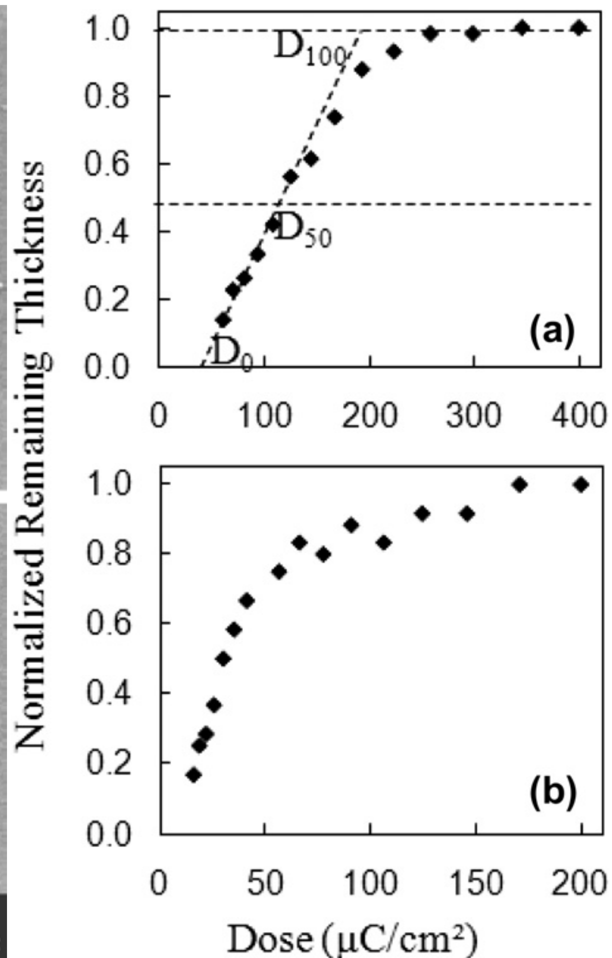

Figure 3.8 Contrast curves for 90 kg/mol polystyrene exposed at (a) 20 keV and (b) 5 keV, and developed by tetrahydrofuran for 2 min.

3.3.3. High sensitivity EBL using MEK:MIBK developer for ZEP resist

Low throughput is the major drawback for electron beam lithography (EBL). ZEP as the popular non-chemically amplified electron beam resist, though ~3× more sensitive than PMMA, it is still very insensitive when using high resolution developers such as amyl/hexyl acetate or xylene (e.g. sensitivity ~100 μC/cm^2 at 30 keV).[36]

In our work, we found that the sensitivity for ZEP (520A) resist can be substantially increased from 10 μC/cm^2 to 2.6 μC/cm^2 at 5 keV beam energy and from 41.9 μC/cm^2 to 9.2 μC/cm^2 at 20 keV beam energy by using MEK (methyl ethyl ketone) : MIBK (methyl isobutyl ketone) = 2:3 developer, though at the cost of reduced contrast compared to standard developers xylene, amyl acetate or hexyl acetate, as compared in Fig 3.9. The achievable resolution was found to depend strongly on the resist's adhesion to the substrate or under-layer; and we obtained the resolution of 40 nm half pitch using ZEP resist spun on a layer of anti-reflection coating that was treated by oxygen plasma.

In experiment, as-purchased ZEP-520A was further diluted with anisole with a ratio of 1:2, which gave the film a thickness of 45 nm when spun at 2000 rpm. After spin-coating, the film was baked on a hotplate at 180°C for 10 minutes. Exposure was performed using Raith 150^{TWO} system at acceleration voltages of 20 kV and 5 kV. For high-resolution study, we exposed periodic line arrays with the lines defined as single-pass lines with beam step size of 15 nm. After exposure, the samples were developed using MEK : MIBK = 40 : 60 for 30 seconds, followed by rinsing with 2-propanol and nitrogen drying.

Fig. 3.9a-b shows the contrast curves for ZEP-520A exposed at 5 keV and 20 keV, and developed using MEK : MIBK = 40 : 60 for 30 sec. Atomic force microscope (AFM) was used to obtain the contrast curves. The resist sensitivity was found to be 9.2 μC/cm^2 and 2.6 μC/cm^2 for 20 keV and 5 keV exposure, respectively. The dependence of sensitivity on electron beam energy is fair in agreement with the fact that sensitivity is expected to be roughly inversely

proportional to the beam energy (E) as predicted by the Bethe equation for electron energy loss (E_{loss}) in the resist: $E_{loss} \propto 1/E \cdot \log(\alpha E)$ with α being a constant. As shown in Fig. 3.13, the contrast of ZEP resist using the current developer is 2.6 and 9.2 for 5 keV and 20 keV exposure, respectively; these values are lower than the contrast by normal developer using amyl acetate (shown in Fig. 3.9 c-d).

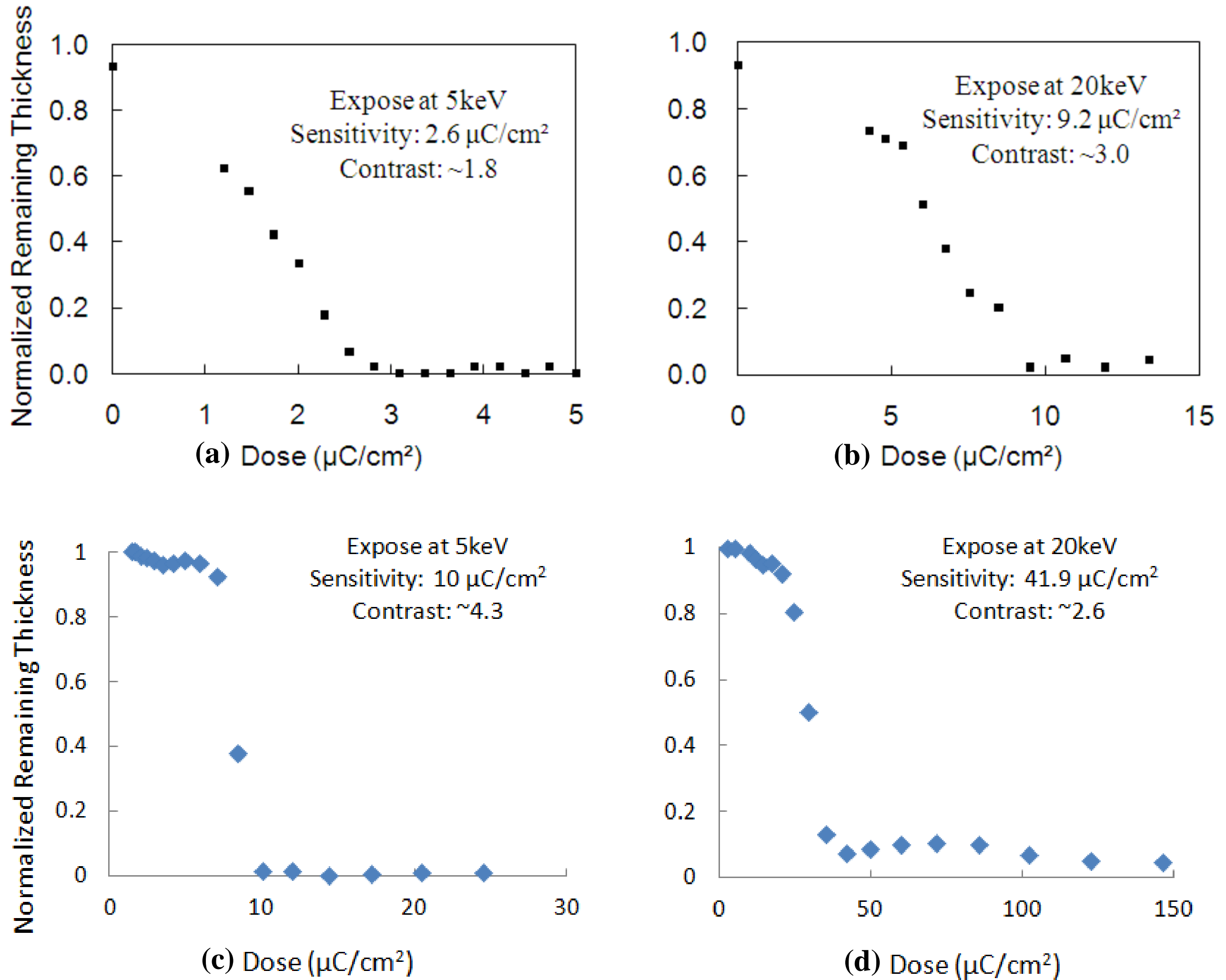

Figure 3.9 (a-b) Contrast curves for ZEP-520A resist exposed at 5 keV and 20 keV, and developed by MEK : MIBK = 40 : 60 for 30 sec at room temperature. (c-d) Contrast curves for ZEP-520A resist exposed at 5 keV and 20 keV, and developed by amyl acetate for 1 min at room temperature. The thickness is normalized to the original film thickness. For (a-b), the unexposed area (dose = 0 $\mu C/cm^2$) has normalized thickness <1.0 because the first developer dissolves slowly the unexposed resist.

In addition, even the un-exposed resist was found to be developed by ~4 nm within the development time of 30 sec, which is due to the presence of the relatively strong solvent MEK. In principle, increasing the development time can increase resist sensitivity to an infinitely high value. However, we fixed the development time to be 30 sec for the current film thickness of 45 nm, because longer development time was found to lead to poorer pattern definition.

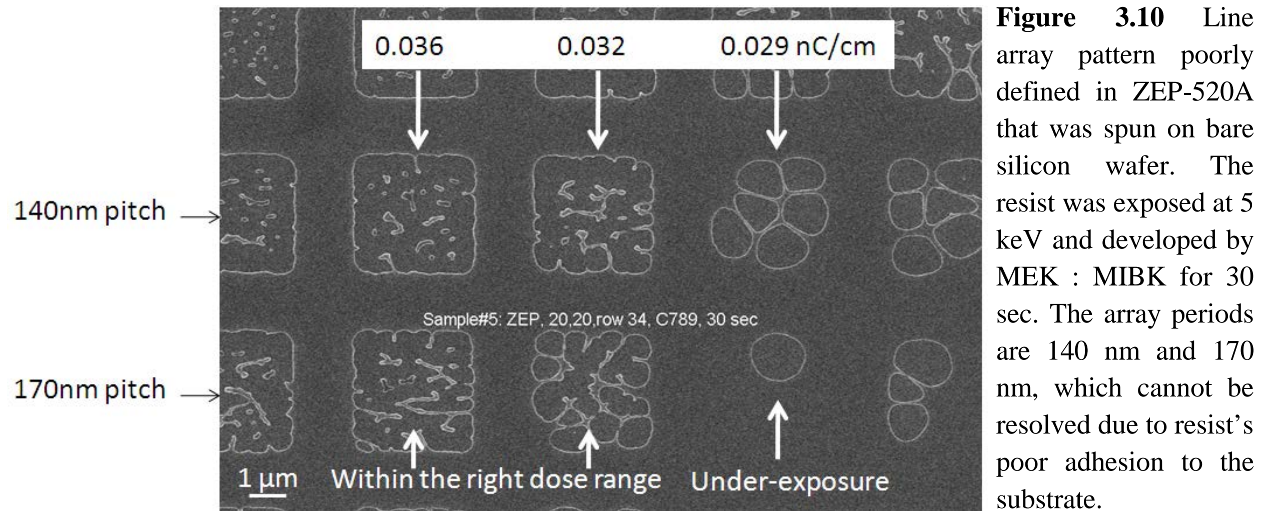

Figure 3.10 Line array pattern poorly defined in ZEP-520A that was spun on bare silicon wafer. The resist was exposed at 5 keV and developed by MEK : MIBK for 30 sec. The array periods are 140 nm and 170 nm, which cannot be resolved due to resist's poor adhesion to the substrate.

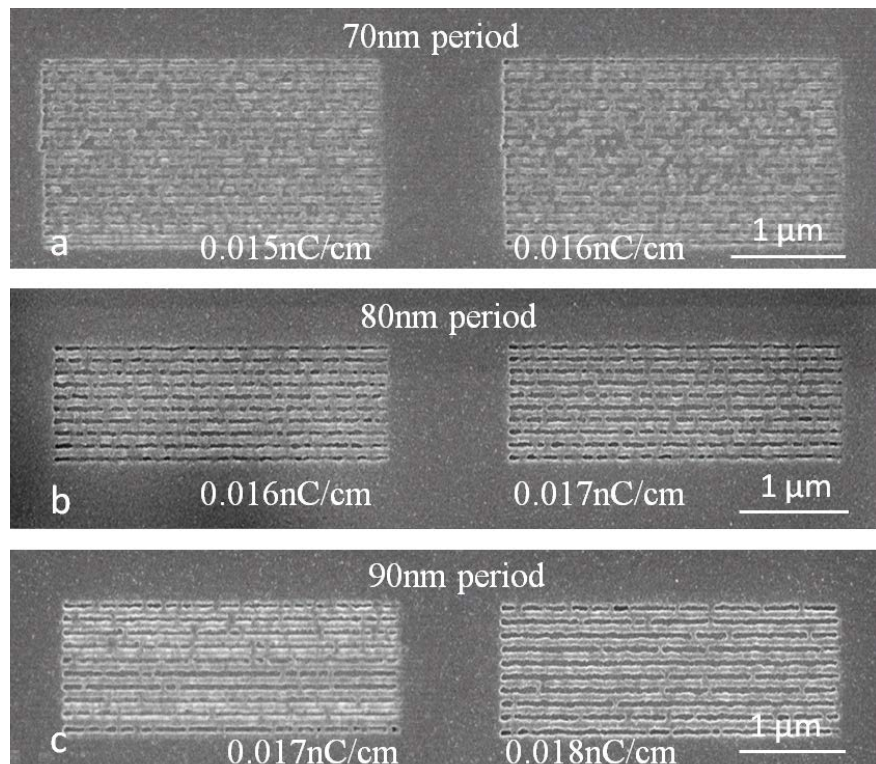

Figure 3.11 Line array pattern in ZEP-520A with periods of 70, 80 and 90 nm. The resist was spun on oxygen plasma treated ARC film, and exposed at 5 keV and developed by MEK : MIBK for 30 sec.

To study the achievable resolution (half-pitch) of this resist, we exposed dense line arrays at 5 keV since low e-beam energy increases resist sensitivity. We first coated the ZEP resist on a bare silicon wafer that was cleaned by solvents (acetone and 2-propanol) and oxygen plasma. However, no well defined pattern was obtained as seen in Fig. 3.10. Evidently once the resist was developed to the bottom at certain spots, the spots expanded quickly in an uncontrolled way possibly due to the lack of adhesion to the substrate. Alternatively, an ARC layer was spin coated on a clean wafer and then thinned to 10~20 nm thickness by O_2 RIE, which can modify its surface energy and thus resist's adhesion to it. The exposure performance is shown in Fig. 3.11. We claim that the current process can achieve a resolution of 40 nm half pitch. This resolution is slightly lower than SU-8 resist (34 nm half pitch) as demonstrated by Bonam et al.[37] However, in that study the authors did not mention the pattern area as compared to the range of proximity effect for 100 keV exposure. In addition to proximity effect (backscattering range is about 200 nm for 5 keV e-beam into silicon), the noticeable defects for the 35 nm half pitch pattern may be due to inadequate adhesion of the film to the substrate and agglomeration or phase separation of additives in the resist film.

3.4. Charging effect reduction in electron beam lithography with nA beam current

Sub-wavelength hole/pillar arrays are very important for EOT-based SPR biosensors (EOT means "Extraordinary Optical Transmission", which will be discussed in Chapter 5). EBL can pattern nanostructures easily with 10-100 nm feature size. However, with a necessarily large sensor area, semi-infinite nano-hole/pillar arrays are needed. For example, if a 200 nm-period dot array within 2 cm^2 is needed for one sensor, there will be 10^{10} dots on the wafer. If one dot needs 10 μs for exposure, the whole exposure time will be 27.7 hours. The total time includes two parts. The first part is dwelling time, which is the real time of exposure. The second part, setting time, partly aims to reduce the charging effect from previously exposed dots. If the beam needs to wait 5 μs for the charge electrons from the previous dots to completely disperse into the wafer, the

total setting time will be 13.9 hours for the same example. The charging effect becomes a more serious issue when performing EBL in large area with high beam current.

In our work, we studied three methods to minimize the charging effect with a pattern of 200 nm period hole array on PMMA, PMGI and ZEP-520A resists. EBL was carried out using Raith 150^{TWO} system with 30 kV acceleration voltage and 60 µm beam aperture for fast exposure, resulting in a beam current of 1.2-1.5 nA (typical currents for EBL are sub-100 pA).

Firstly, charging effects can be reduced by increasing the spacing between adjacent dots. The periodic dot arrays were exposed using four different pattern designs, as shown in Fig. 3.12: (a) a large 100 µm square with the exposure step size set to 200 nm in both x- and y-direction (we name it the (100) lattice); (b) parallel horizontal lines with offset of $100\times\sqrt{2}$ nm (that is the spacing between adjacent dots is increased by $\sqrt{2}$) at the beginning, step size of $200\times\sqrt{2}$ nm, and spacing between two adjacent lines of $200/\sqrt{2}$ nm ((110) lattice); (c) same as (b) but replacing $\sqrt{2}$ with $\sqrt{5}$ ((120) lattice); d) periodic dot array, which leads to a very large CAD file (we name it dot array). The area, line and dot doses are set such that the exposure dose for each dot is the same: 12 fC/dot for PMMA. All four designs will result in the same pattern, except that the b array is rotated by 45°, and the c array by $\tan^{-1}(1/2)=26.6^o$. However, the total writing time, including both dwelling time and setting time (the pause before exposing each element, 0 for a-c, finite for (d)), is much longer for d than for a-c. Fig. 3.13 shows the SEM images of a 200 nm period hole array in 100 nm thick PMMA developed using methyl isobutyl ketone (MIBK): 2-propanol (IPA) = 1: 3 for 30 seconds. Because of the charging effect it was found that the holes were noticeably elongated along the beam scanning (horizontal) direction. The direction of elongation is consistent with the direction of electrostatic force between deposited electrons from the previous exposure and incoming electrons. The elongation is highest (hole-width 86 nm) for the (100) lattice pattern design, followed by the (110) lattice pattern design (hole-width 68 nm), and the lowest (hole-width 53 nm) occurred in the (120) lattice pattern design. This indicates that pattern distortion due to charging effect can be greatly reduced simply by re-arranging the exposure sequence. The pattern elongation (hole-width 60 nm) for the dot array pattern design is

also much lower than that for the (100) lattice pattern design, because of the longer charge dissipation time. However, this means a longer writing time (28 μs per dot, including a dwelling time of 8.2 μs and a setting time of 19.8 μs) when using the dot array pattern design, as compared to that of the (100) lattice pattern design (8.2 μs per dot for beam a current of 1.46 nA).

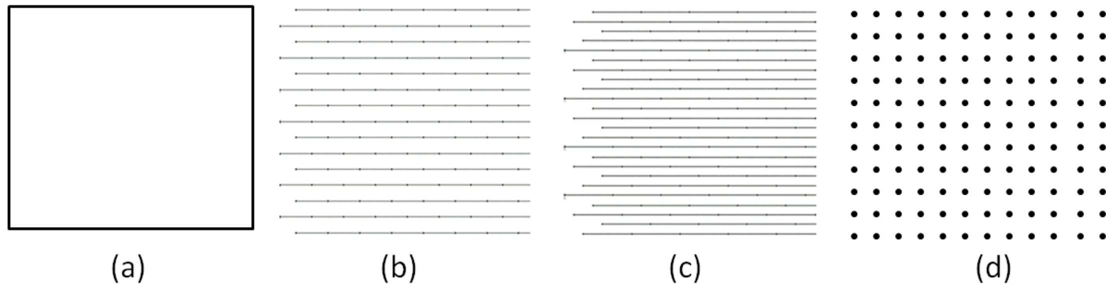

Figure 3.12 The four different pattern designs that all give a 200 nm period dot array. a) Large square where array periodicity is defined by the exposure step size along the x- and y-direction; b) Line array with offset at the beginning, where the "nodes" on each line indicate the position of exposed dots. The resulted 200 nm period dot array is rotated by 45°; c) Similar to b) but the step size and line-spacing is set such that the resulted 200 nm period dot array is rotated by 26.6^{o}; d) Dot array with 200 nm period along both directions.

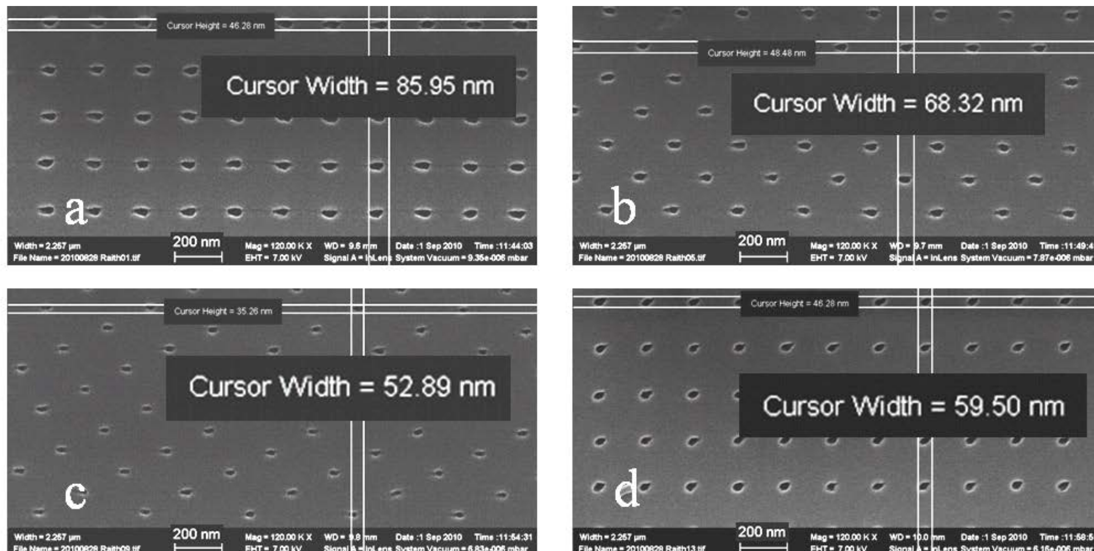

Figure 3.13 Hole array with 200 nm period developed in PMMA coated on a heavily doped n-type Si substrate with resistivity 0.01-0.02 Ω·cm. (a-d) are exposed using the pattern design as shown in Fig. 3.12 a-d, respectively.

The substrate conductivity also affects the rate of charge dissipation/screening, and higher conductivity can offset the effects more obviously. For the (100) lattice pattern design as shown in Fig. 3.13a that used a lightly doped n-type wafer with a relatively high resistivity of 1-10 Ω·cm, the pattern distortion and positioning error is much more severe than that shown in Figure 3.11a, made with a low-resistivity wafer. As expected, the hole array is better defined for the (110) lattice pattern design as shown in Fig. 3.14b. For a quartz substrate, even with a 20 nm Cr layer on the resist, the hole array is not defined for the (100) lattice and (110) lattice pattern design (not shown), and very poorly defined for the (120) lattice pattern design (Fig. 3.14c). The "traces" that link the holes along the horizontal direction due to partial development when under-exposed are clearly seen. Here we want to mention that the traces are not because of exposure by the un-blanked beam between exposing two adjacent holes, since the patterning speed of the tool is 20 MHz, indicating only ~0.05 μs of transfer time. The hole array is reasonably well-defined for the dot array pattern design, implying that the characteristic charge screening time through the Cr layer is of the same order as the writing time of each hole (28 μs, including dwelling and setting time). We can also conclude that, for the current experimental parameters, the charge dissipation through the lightly doped substrate is more efficient than charge screening through the Cr layer.

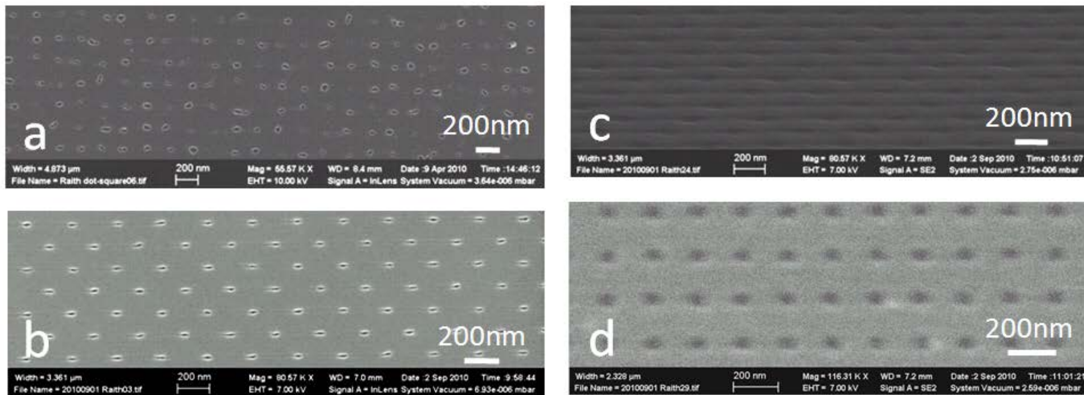

Figure 3.14 Hole array with 200 nm period developed in PMMA coated on: (a-b) a lightly doped n-type Si substrate with resistivity 1-10 Ω·cm, exposed using the pattern design as shown in Figure 2.13(a-b), respectively; (c-d) a quartz substrate with 20 nm Cr conductive layer coated on the resist, exposed using the pattern design as shown in Fig. 3.12(c-d), respectively.

Besides PMMA, we also studied poly(dimethyl glutarimide) (PMGI, MicroChem Corp.) resist, which is ~4× less sensitive than PMMA when using the same developer (MIBK:IPA) for 30 sec;[38] and ZEP-520A resist, which is ~5× more sensitive than PMMA when using amyl acetate

developer for 1 min. As shown in Fig. 3.15a for PMGI resist, contrary to general intuition, it is found that the charging effect is negligible even for the (100) lattice pattern design and high-resistivity wafer. This is because even though the deposited charge is significantly higher than that for PMMA resist, the charge dissipation/screening time is also higher to balance this out; and as the resist is less sensitive, the exposure due to scattered electrons will not result in noticeable development. However, for the same beam current, the writing time is longer when using less sensitive resists. The exactly opposite holds for the ZEP-520A resist, where the hole array is not well defined for the (100) lattice pattern design (except for the first hole along each writing line - see Fig. 3.15b - though the array is clearly defined for the dot array pattern design due to the long setting time (Fig. 3.15c).

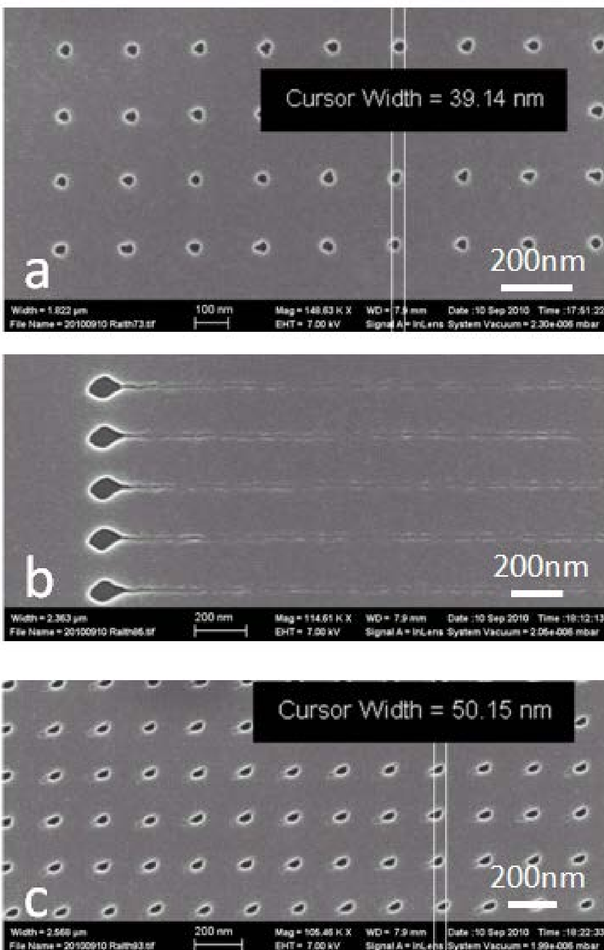

Figure 3.15 Hole array with 200 nm period. (a) Developed in PMGI resist using pattern design as shown in Fig. 3.12a; (b-c) Developed in ZEP-520A resist using pattern design as shown in Fig. 3.12a and Fig. 3.12d, respectively. The exposure doses are 48 fC/dot for PMGI, and 2.4 fC/dot for ZEP-520A.

3.5. Periodic tilted structure fabrication by electron beam lithography

Tilted micro- and nano-structures have various applications. For example, tilted periodic pillars in soft materials like PDMS is important for the study of directional cell movement,[39] and surface enhanced Raman spectroscopy,[40] as well as artificial surface mimicking gecko feet for dry adhesive pads application.[41-43] Tilted nanostructures can also be employed for directional adhesion and wetting[44,45] or introduced into photovoltaic device to avoid a short circuit between the two electrode.[46]

Micro-scale tilted structures in polymer resist can be fabricated readily by photolithography with the substrate tilted because the depth of focus for collimated UV light is effectively infinite.[41,47,48] Nanoscale tilted structures have been fabricated by reactive ion etching with tilted substrate; however, modification of the etching system is needed as otherwise the spontaneously generated self-bias field in the plasma (that determines the etching direction) would remain normal to the substrate surface.[49] In principle, one can fabricate tilted nanostructure by electron beam lithography with tilted substrate using laser auto-focus; however, in practice this could be very time consuming because the depth of focus of the electron beam is typically on the order of 10 µm, and thus each write field has to be in the same order for 45 degree tilt in order to maintain focus within each write field, which leads to tens of thousands of write fields over an exposure area of 1 mm^2 and thus very long stage movement and focus adjustment time

In this work, we demonstrated that 2D periodic array of tilted nanostructure can be conveniently fabricated through SEM exposure of an electron beam resist during normal imaging of a tilted resist-coated substrate using the dynamic focus function, which is designed to maintain the focus across a tilted substrate by adjusting the working distance continuously during scanning. Since the exposure is carried out in the normal imaging mode, there is no need of pattern generator or beam blanker. The main limit of the current approach is that only 2D periodic structures can be fabricated, and the number of the fabricated structures is the same as the image resolution (e.g. 1024×768).

ZEP-520A was chosen as positive resist that leads to 2D hole array pattern after exposure and development. The resist (as purchased or diluted by anisole for thinner film) was spin-coated on a silicon wafer and baked at 180°C for 10 min. For negative resist that leads to pillar array pattern, chemically amplified resist SU-8 diluted by cyclopentanone was spin-coated to achieve a film of ~500 nm, and pre-baked at 90°C on a hotplate to drive away the solvent. As well, polystyrene resist with the molecular weight of 260 kg/mol is dissolved in chlorobenzene at 10% concentration to achieve ~800 nm-thick film after spin-coating.[35,50] A LEO 1530 FE-SEM was used to expose the resist at 20 kV acceleration voltage and 0.1~2.5 nA beam current. Pixel average was chosen for noise reduction that is advantageous over line average or frame average because the electron beam was found not to go to the exact pixel location when the scan area is on the order of 1 mm. For the same reason, each exposure was carried out using only one scan. The scan speed was set such that the scanning times per frame was 0.1-1.0 min depending on beam current and resist sensitivity. The substrate was typically mounted on a 45°-tilt sample holder. In the experiment, the imaging frame center was first focused at high magnification by adjusting working distance as usual, then at the target magnification using reduced scanning area on the top or bottom of the frame, the amount of tilt compensation is adjusted until the clearest image was obtained (that is, here the best focus is achieved by adjusting the amount of tilt compensation with the working distance fixed). Exposed ZEP-520A films were developed by n-amyl acetate for 1 min, exposed SU-8 films were post-exposure baked at 90°C on a hotplate for 1 min before development using propylene glycol monomethyl ether acetate (PGMEA) for 2 min, and exposed polystyrene was developed using xylenes for 2.5 min.

One way to transfer the pattern in the resist to another layer or material is electroplating of a metal into the resist template. The wafer was coated with Cr/Au as conduction layer before spin-coating ZEP-520A resist. After exposure and development, the sample was treated with NaOH solution for 1 min to remove possible grease, followed by HCl solution for 3 min to de-passivate the surface. Au electroplating was carried out using a commercial cyanide-free bath at 60°C with 2.0 V constant voltage for ~3 minutes. After electroplating, the sample was rinsed with DI water, followed by soaking in anisole to remove the ZEP-520A resist. Another way of pattern transfer is cast-molding of PDMS onto the resist template.

Fig. 3.16 shows the cross-sectional view of the tilted holes in 100 nm ZEP resist (ZEP-520A diluted with anisole at 1:1 ratio) and 645 nm ZEP resist (undiluted) exposed with the sample tilted by 45 degree at the beam current of 100 pA. The exposure dose per dot is calculated to be on the order of 10 fC/dot. Forward scattering of the electron beam is more serious for tilted incidence than for normal one (partly because of the increased trajectory by 1/cos(tilt angle)), leading to apparent diameter variation along the hole direction for the case of thick (645 nm) resist. As expected, the hole diameter is rather uniform across the entire pattern area of ~1 mm when using the dynamic focus function (see Fig. 3.17). Though ZEP-520A is a high-resolution resist with sub-20 nm resolution readily achievable when using normal electron beam lithography, here the resolution is limited to roughly 100 nm by the beam positioning accuracy and stability when using large scanning field of ~1 mm that is one order larger than that for typical high resolution EBL. It is possible to generate holes larger than 500 nm by using significantly higher dose. In fact, the hole size is ultimately determined by the point spread function of the electron trajectory that predicts an exponential relationship between point dose and hole size. For instance, holes of diameter 600-700 nm (not shown) were formed when using a very high beam current of 2.3 nA.

Tilted nano-pillar array was resulted using negative resist SU-8 (Fig. 3.18a) that is about 20× more sensitive than ZEP-520A. The pillar is larger at the pillar bottom than the top, which is due to strong forward scattering of the incident electron beam and the very low contrast of SU-8 (contrast $\gamma \sim 1$).

To fabricate tilted nano-pillars, as well as to reveal the profile of the holes, we carried out Au electroplating into the hole array in ZEP and subsequently removed the ZEP resist using anisole. The 45 degree tilted Au pillar array with the length of ~750 nm sitting on top of Cr/Au plating base layer is shown in Fig. 3.19. Tilted mushroom-shaped pillars with a “cap” were resulted when the holes were over-filled with Au.

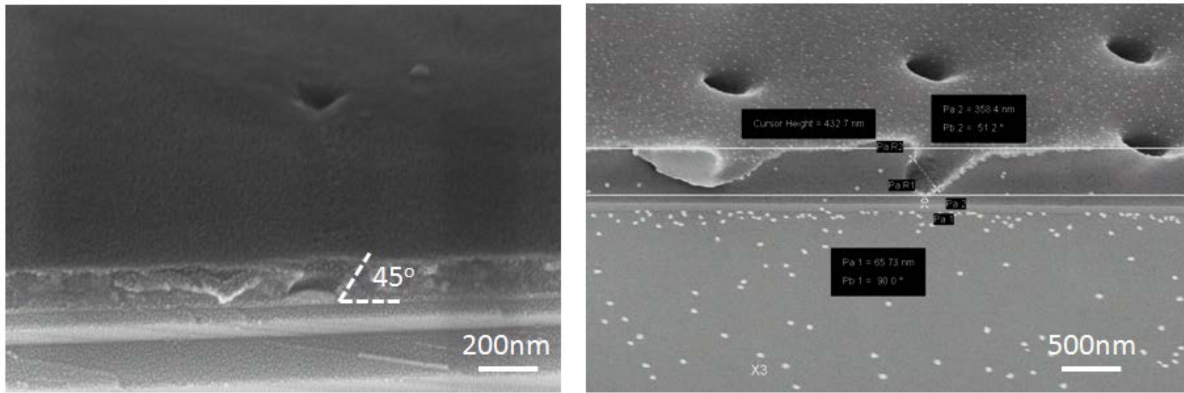

Figure 3.16 SEM images of 45° tilted hole array in (left) 100 nm-thick ZEP-520A with the hole diameter of 150 nm, and (right) 645 nm-thick ZEP-520A with the hole diameter of 250 nm.

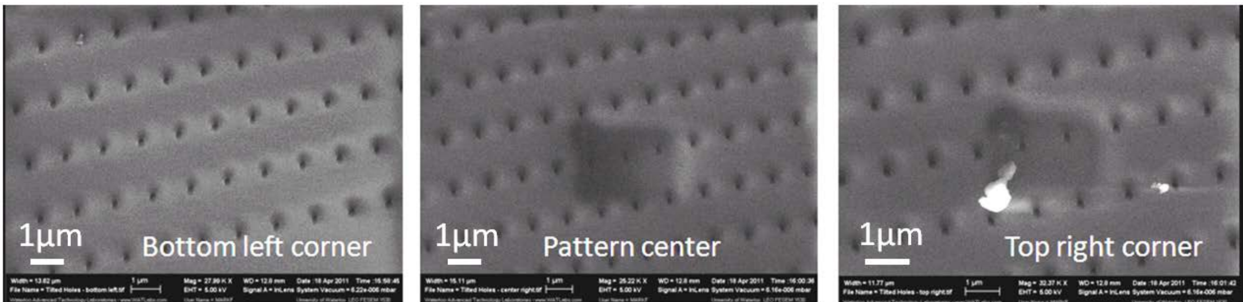

Figure 3.17 Top view SEM images of 45° tilted hole array in 645 nm-thick ZEP-520A showing hole-size uniformity across the pattern area of ~1 mm. The images were taken on the bottom-left corner (a), center (b), and top-right corner (c) of the scanning area.

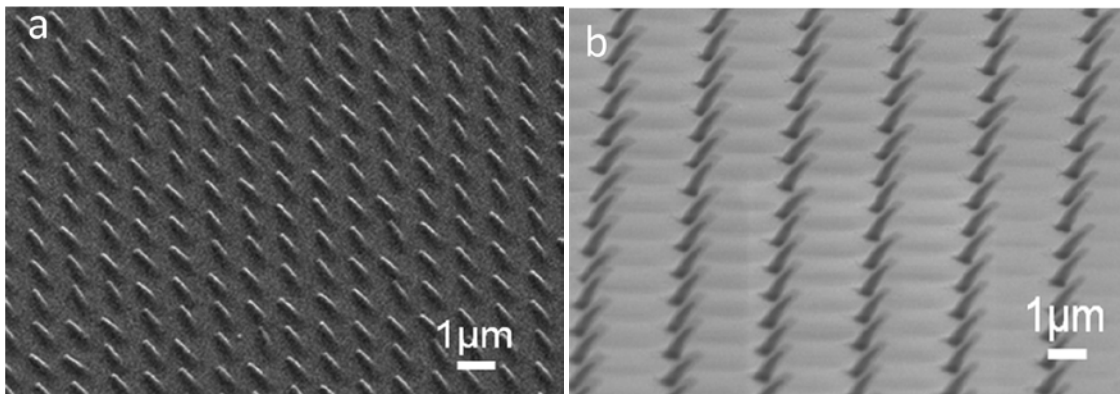

Figure 3.18 SEM images of 45°-tilted pillar array in 500 nm-thick SU-8 resist (left) and 1000 nm-thick 260 kg/mol polystyrene resist (right). The array period is about 1 µm for SU-8 and 2 µm for polystyrene.

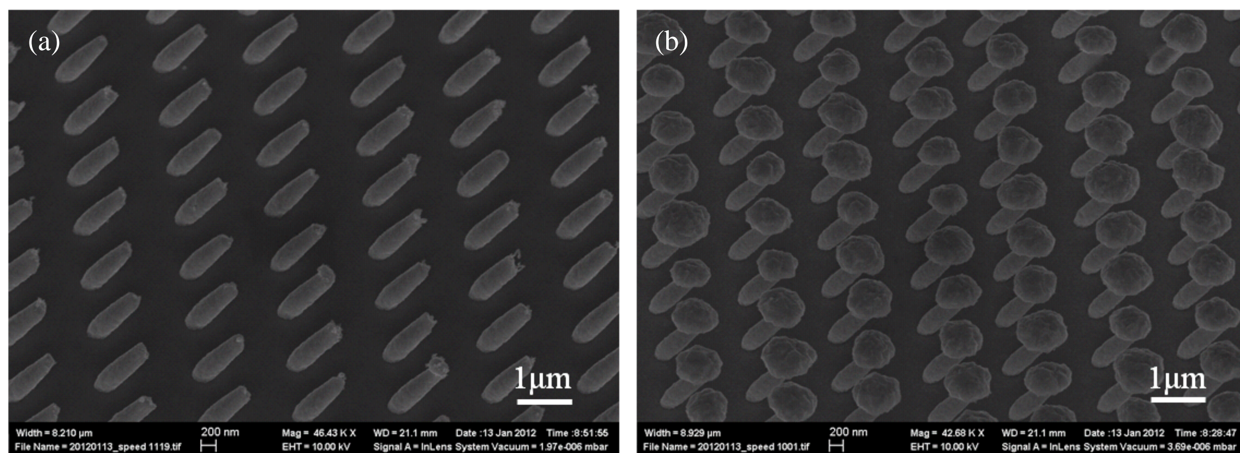

Figure 3.19 SEM images of 45° tilted Au pillar arrays with 1.2 μm periodicity by electroplating into tilted hole arrays in ZEP-520A resist. (a) Tilted pillars of ~300 nm diameter and ~750 nm length without Au over-plating. (b) Mushroom shaped Au pillar array due to over-plating. The images were taken at 45 degree viewing angle.

3.6. Electron beam lithography on irregular surfaces with evaporated resist

One challenge in nano-fabrication is to pattern on non-flat and prestructured surfaces, termed as 3D nanofabrication, which is desired in many fields such as MEMS,[51] electronic devices,[52] super-adhesive surface[53] and optical devices.[54] Imprint method by flexible mold can make a conformal contact on the curved surface.[26] Since 1998, PDMS stamp is reported in soft lithography and in step and flash imprint lithography (S-FIL) for patterning features on non-flat surfaces.[55] But structures were limited on the size scale of 500 nm and larger by this kind of soft mold. Focused ion beam lithography (FIBL) can locate the pattern area accurately.[56] A similar patterning process is available in Helium Ion Microscope by ion milling.[57] But these two techniques are expensive and very slow.

Though electron beam lithography (EBL) is the most available and versatile nano-patterning technology in academic research area, there is still a great challenge in its application in non-flat

surface. This is because the usual film coating method, spin-coating, can form a film only on flat surfaces. Spin-coating on non-flat surface will lead to non-uniform resist thickness. Previously, Pedersen et al. have reported the coating of electron beam resist using plasma polymerized hexane[58]. The resulted hydrocarbon resist presented a negative tone when it was developed in a 1:1 mixture of cyclopentanone and o-xylene for 40 min. However, besides its low sensitivity and poor resolution (demonstrated 150 nm wide sparse line array), this approach is not ideal for a wide range of applications as it needs a special custom-built plasma chamber. Eric Lavallle, et al. have developed a negative evaporated sterol resist, named QSR-5, which was employed to pattern on optical fiber and laser diode facet, as well as on the backside of membranes for the fabrication of the x-ray mask.[59-61] Yet, in addition to its moderate resolution, this specially formulated resist is not commercially available. Daniel et al. introduced water vapor into SEM chamber and formed ice on AFM cantilever or graphene film which was cooled < 120 K. The thin ice layer was patterned by e-beam exposure with low voltage. This novel patterning process is named ice lithography.[62-64] However, for ice lithography the resist has to be kept at very low temperature before pattern transfer by liftoff or dry etching is completed, thus specially designed tool is needed. In addition, the resist sensitivity is very low, three orders lower than PMMA that is already considered as an insensitive resist. Similar to ice, frozen CO_2 might also be used as an electron beam resist, though it would suffer from the same drawbacks as ice resist[65]. Metal halide such as AlF_3, as discussed in Section 3.1, is another type of inorganic evaporated resist, which again suffers from extremely low sensitivity; and it is able to form only line or dot (not areal) patterns.[66,67] Lastly, silicon dioxide, which can be grown or coated by various thin film deposition methods, has been used as a kind of electron beam resist, yet its sensitivity are again extremely low.[68]

Previously, we have demonstrated high-sensitivity patterning using high molecular polystyrene ($[-(CH_2)-CH-(C_6H_5)-]_n$, PS) as a negative electron beam resist (as shown in Fig. 3.7). Here, we introduced thermal evaporation to deposit a high-purity and uniform polystyrene film on substrate for patterning by e-beam lithography (the brief process was shown in Fig. 3.20).

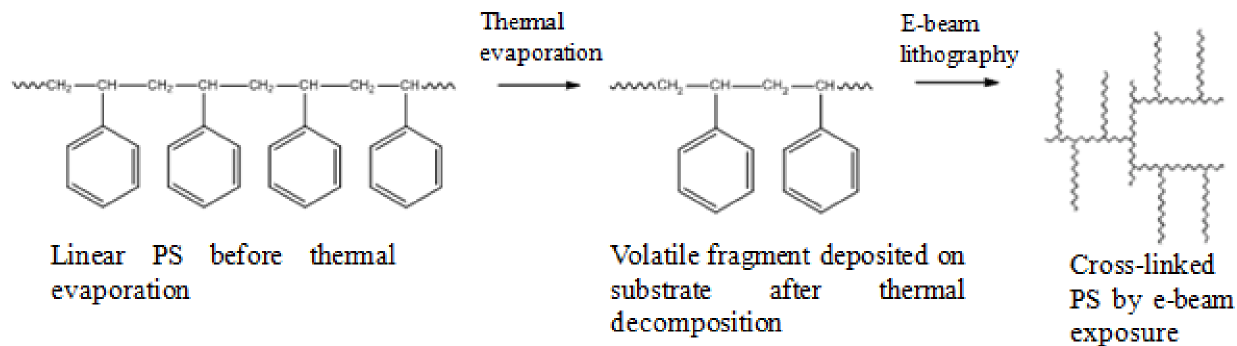

Figure 3.20 Changes of PS structures from thermal evaporation to electron beam exposure.

Compared with spin-coating method, evaporation has many advantages. Firstly, it can form uniform resist film on nearly any types of surface. While in spin-coating, substrate with low surface energy will shrink the resist not to form a flat film (Fig. 3.21a). And organic substrate or sub-layer could be dissolved or swelled by solvent (Fig. 3.21b). Secondly, to prepare the solution for spin-coating, many aspects should be considered to achieve an ideal result, including concentration, viscosity, surface tension, dissolvability and harmfulness to health. Evaporation is a dry process and can be controlled easily. Impurity also will impact the spin-coating process. Normally, spin-coating needs to be carried in cleanroom and the solution needs to be kept carefully. Any dust or particle from the solution and the atmosphere will block the distribution of the resist (Fig. 3.21c). In thermal evaporation, by fixed power, only the material with the relative boil temperature can be evaporated onto the substrate. Moreover, hard baking is not necessary in evaporation. Last, edge beads occur regardless in spin-coating method (Fig. 3.21d). By evaporation, every corner can be covered by a uniform resist film.

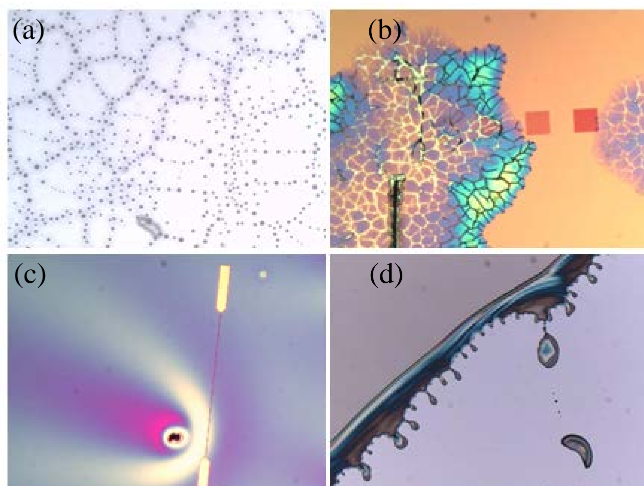

Figure 3.21 Microscope images of spin-coating defects. (a) Films shrink and form droplets on the substrate with low surface energy. (b) Under layer swells and cracks caused by the solvent from spin-coating. (c) A dust causes un-uniform resist film. (d) Edge beads occur regardless in spin-coating method.

To form PS film by thermal evaporation,[69] the tradeoff between evaporation temperature and degradation should be made. For PS with higher molecular weight, higher vaporization temperature is needed, which will lead to fast degradation of the molecule (or oxidation to CO_2 and H_2O gas if vacuum is poor). Here we used 1.2 kg/mol PS for thermal evaporation. The roughness of the PS films prepared by evaporation and spin-coating method on Si wafers is also compared by AFM scanning (Dimension 3100 Scanning Probe Microscope).

Normal low-resistivity wafer (0.01-0.02 Ω·cm) is coated by PS for dose test. AFM tips and optical fibers were used to demonstrate its capability of patterning on non-flat surface. The buffer layer of fibers was removed by soaking in acetone and scratch. Before coating, all the substrates were cleaned using acetone and 2-proponol, followed by short exposure to oxygen plasma. For pattern transfer in the future step and a conductive layer in E-beam exposure, 10 nm Aluminum layer was coated by WLOS Cluster Sputtering System to achieve a uniform coverage on curved surface. The thickness of evaporated PS film is controlled at ~100 nm. E-beam lithography was conducted using Raith 150^{TWO} system with 5 kV acceleration voltage and 0.2 nA beam current. Exposed PS films were developed in xylenes for 1 min and observed by LEO 1530 FE-SEM. The sample of AFM tip was dried carefully in atmosphere without N_2 blow to avoid the tiny tip broken. For pattern transfer, patterns on AFM tip and fiber were etched by O_2 reactive ion etch (RIE, 20sccm, 20 mTorr, RF 20 w) for 3 seconds to clean the residual organic layer, and BCl_3 RIE (50 sccm, 5 mTorr, ICP 800 w, RF 200w) for 15 seconds to remove un-patterned Al. By the etched Al layer as etching mask, deep silicon RIE was carried on the AFM tip to get high aspect-ratio Si structure. Fig. 3.22 shows the comparison of the film roughness prepared through the two methods. Considering the mean roughness (Ra) is 0.223 nm for the evaporated film and 0.239 nm for the spin-coated film, evaporation method can achieve an ideal film as flat as spin-coating method.

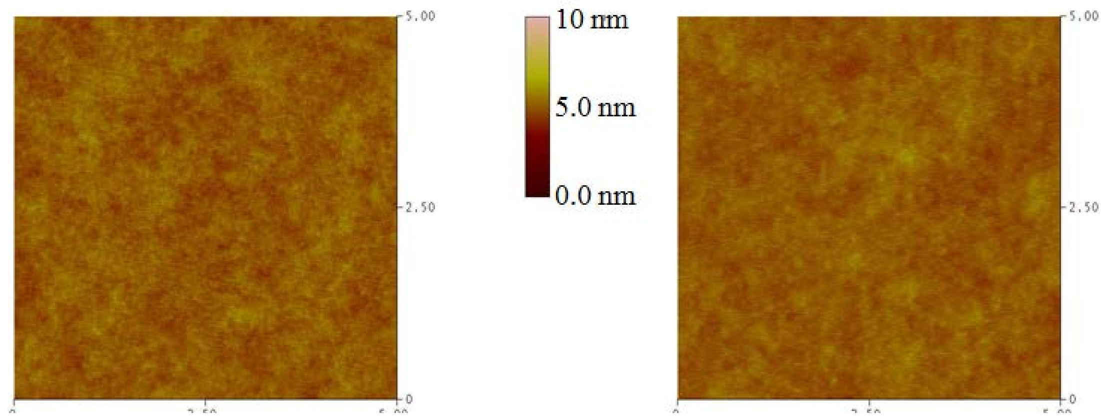

Figure 3.22 AFM images of PS films prepared by spin-coating method (left) and thermal evaporation (right).

Since it is known that for simple cross-linking resist like polystyrene the sensitivity (μC/cm^2) is inversely proportional to molecular weight (kg/mol),[70] we examine the degradation of evaporated film by comparing its sensitivity with the spin-coated film. Polystyrene powder with the same molecular weight of 1.2 kg/mol was dissolved in chlorobenzene with a concentration of 1.3 wt/vol%, which gave a film thickness of 140 nm (measured by Dektak profilometer). After spin coating, the film was baked at 90°C for 5 min on a hotplate.

Fig. 3.23 shows the contrast curves of the PS as EBL resist coated by spin-coating and evaporation. The contrast of the evaporated PS for exposure at 5 keV, defined as $\gamma = [\log(D_{100}/D_0)]^{-1}$, is calculated to be 2.6 with sensitivity at 4500μC/cm^2. The contrast of the spin-coated PS is 4.3 with sensitivity at 1920μC/cm^2. As seen, the sensitivity is lower for evaporated polystyrene, which indicates the evaporated film has lower molecular weight due to partial decomposition during evaporation. PS with higher molecular weight including 13 kg/mol and 260 kg/mol also were applied in evaporation. As mentioned before, PSs with higher molecular weight need higher evaporation temperature which leads the degradation of the organic polymer. The deposition rate was uncontrollable and no film forms on wafer substrate.

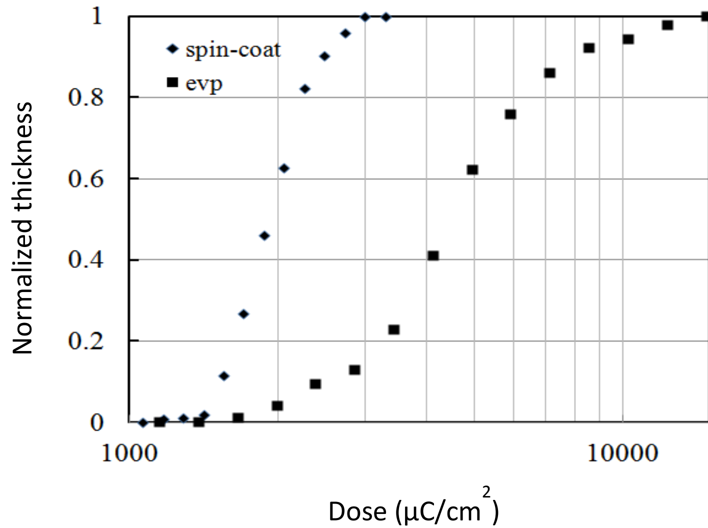

Figure 3.23 Contrast curves for 1.2 kg/mol polystyrene by spin-coating and evaporation. Both were exposed at 5keV and developed by xylenes for 30 seconds. The sensitivity (dose for 100 % remaining thickness) and contrast are 1920μC/cm^2 and 4.3 for spin-coated PS, and 4500μC/cm^2 and 2.6 for evaporated PS.

To study the resolution capability of the polystyrene resist, we exposed periodic dense line arrays with periods 40 nm, 50 nm, 60 nm, 70 nm, and 80 nm, all at 5 keV. Line was written by single-pass exposure with the step size of 6 nm. Fig. 3.24 shows line array patterns of 50 nm and 60 nm periods. Grating with 60 nm period was well defined with the minimum dose of 18.4 nC/cm, whereas the 50 nm one is fairly well defined. Lines with narrower period become cross-linked or fall to each other because of the capillary force. The minimum half pitch of 30 nm is achieved here, which is much higher than the previous reported evaporated resists.

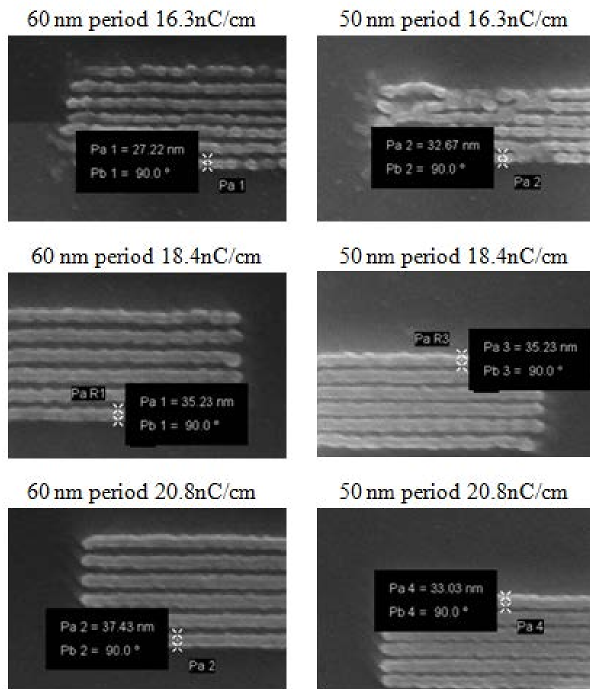

Figure 3.24 Line array patterns with 60 nm period exposed by16.3, 18.4, 20.8 nC/cm, respectively.

To demonstrate its capability of patterning on non-flat surface, evaporated PS on an AFM tip is exposed with same condition here. An array of letters "WIN" (Waterloo Institute for Nanotechnology) with line-width of 28 nm was successfully patterned on an AFM tip using 50 nm evaporated polystyrene, as seen in Fig. 3.25.

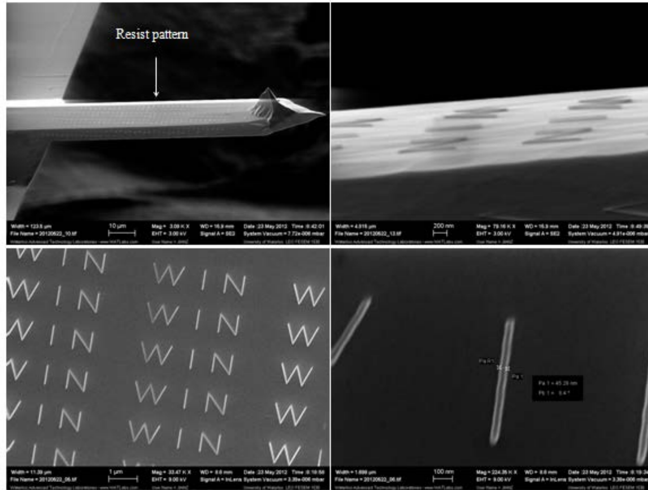

Figure 3.25 SEM images of patterned PS on an AFM cantilever by EBL. AFM cantilever written with WIN (Waterloo Institute for Nanotechnology).

Metal patterns and high aspect-ratio Si patterns were fabricated by deep RIE on patterned AFM tips. 10 nm Al film was deposited on AFM tips before PS evaporation. After e-beam exposure and development, the AFM tips were cleaned by a quick O_2 RIE of 3 seconds to remove the residual organics and followed by BCl_3 RIE to etch Al mask. After this, deep RIE of 10 minutes was carried out to achieve the maximum depth of 2 μm. The etched samples were characterized by microscope (Olympus MX61) and SEM (LEO UltraPlus SEM). Fig. 3.26(a) shows the Al pattern of starline to prove the exposure uniformity along the all directions. Fig. 3.26(b) shows Al circuit with line width of 36nm. The circuit pattern was transferred to Si substrate by deep RIE of 1 minute with the depth of 180 nm, shown in Fig. 3.26(c). High-aspect-ratio pattern of the name of our institute and group was etched by deep RIE of 10 minute with the depth of 2 μm, shown in Fig. 3.26(d).

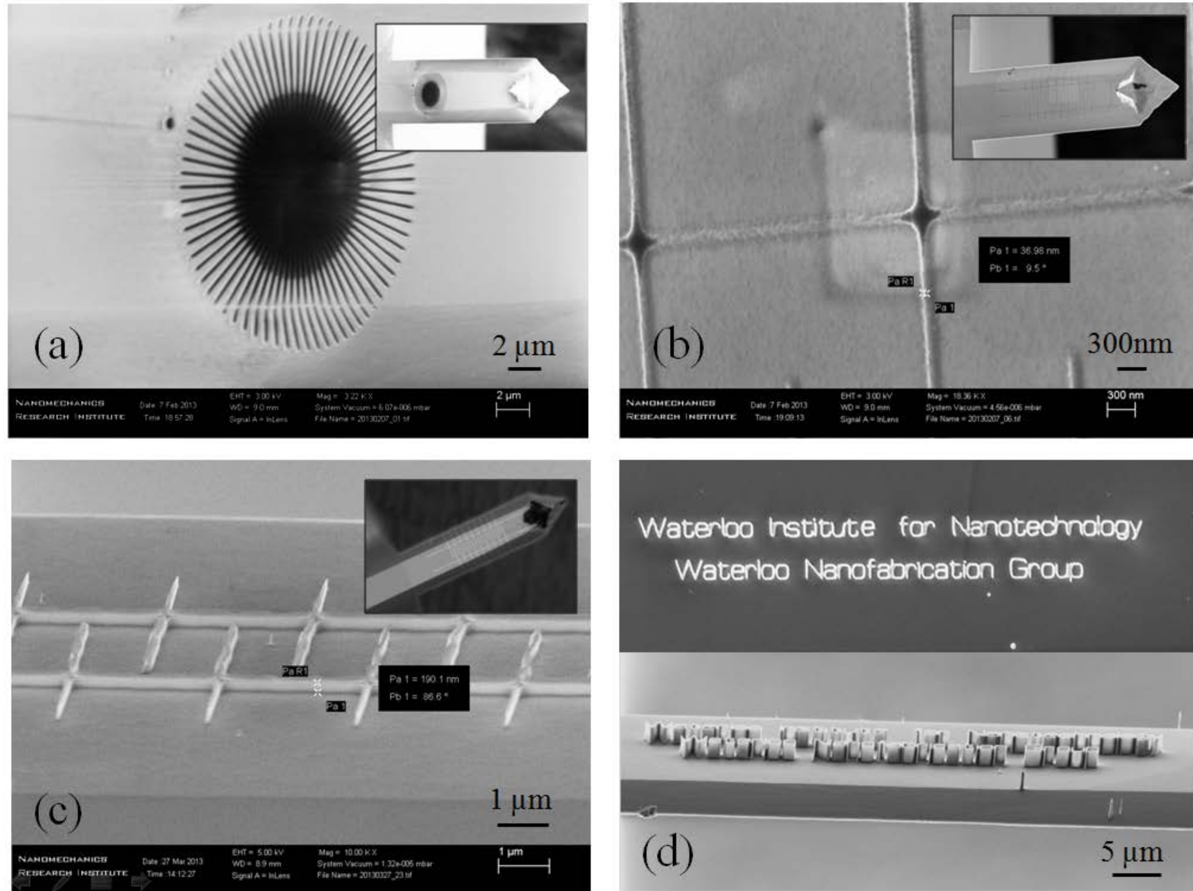

Figure 3.26 SEM images of (a) Al pattern of starline to demonstrate the exposure uniformity along the all directions. (b) Al circuit with line width of 36 nm, (c) transferred to Si substrate by deep RIE of 1 minute with the depth of 180 nm. (d) High-aspect-ratio pattern of the name of our institute and group was etched by deep RIE of 10 minute with the depth of 2 μm.

Not only on AFM tips, The techniques for nano-structured optical fiber attracted growing attention in various aspects, such as the application in Bragg gratings,[71] optical filters,[72,73] SERS sensors,[74,75] plasmonic lens,[76,77] and transmission measurement.[78,79] Our process using evaporated resist can be equally applied to pattern an optical fiber, as shown in Fig. 3.27. Evaporated PS on a fiber (cladding layer removed) was exposed by EBL, then the patterns were transferred to Al layer and fiber (SiO_2) by BCl_3 RIE followed by CF_4 RIE for high-aspect-ratio structures. Fig. 3.27(a) shows the tilted SEM image of the two-dimensional grating array after CF_4 RIE. With the patterned Al structure as etching mask, pattern on fiber having a depth of 270 nm was achieved. Fig. 3.27(b) and (c) show the dot array with diameter of 200 nm and crossbar

array with line-width of 167 nm, both etched into the fiber for 270 nm, respectively. To demonstrate the uniformity along different directions, a pattern of starline was exposed and etched to the fiber as shown in Fig. 3.27(d).

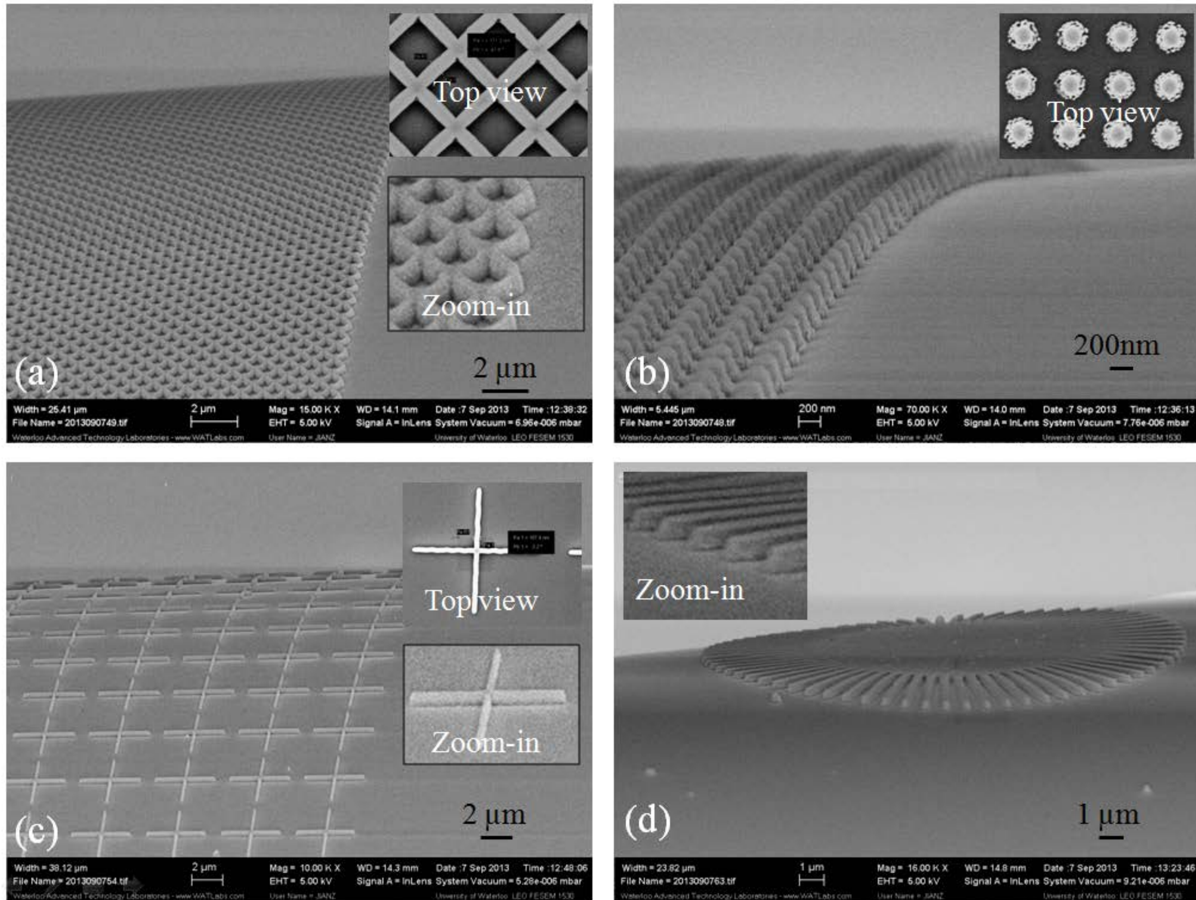

Figure 3.27 SEM images of nanostructures on an optical fiber with height/depth of 270 nm. (a) 2D grating array with line-width of 167 nm; (b) dot array with diameter of 200 nm; (c) crossbar array with line-width of 167 nm; and (d) starline pattern. The inserts show top view and/or zoom-in view of the structures.

3.7. Conclusion

In this Chapter, several aspects were discussed to improve the performance of EBL, including the resist, development, and exposure condition. For the resist, both of the common resists, such as PMMA, ZEP-520A, and PS, and the uncommon resist, such as AlF_3 and evaporated PS, were examined. High sensitivity electron beam lithography can be achieved by using ZEP resist and

MEK:MIBK developer, or using PS with higher molecular weight. The charging effect to the pattern distortion was studied systemically for the electron beam exposure in large area with high current. Two novel exposure methods were developed here. On one hand, tilted periodic nano-structures can be achieved by electron beam scanning on tilted sample with dynamic focus mode. On the other hand, EBL on irregular surface can be achieved by the exposure using evaporated PS.

The breakthrough of EBL resolution by limiting the proximity effect through exposure on membrane substrate was discussed in Chapter 5. This part of the work was applied in SERS sensor. Moreover, EBL method and double liftoff process were utilized in the fabrication of nano-hole array for EOT sensor covered in Chapter 6.

Chapter 4

Surface plasmon fundamentals and applications

4.1. Introduction to bulk plasmon

Plasmon is the collective oscillation of free electrons which can be explained intuitively by the classic Drude model.[80] In Drude model, or free electron model, electrons in metal are divided as two parts. One part is core electrons, which are fixed around positively charged nucleus; the other part is valence electrons. Atoms of a metallic element are brought together to form a solid metal, while the valence electrons become detached and wander freely through the metal (as shown in Fig. 4.1).

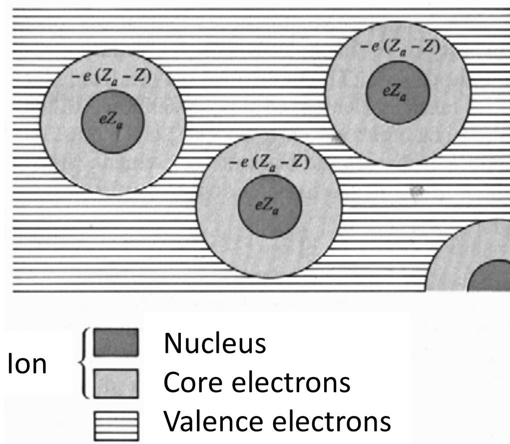

Figure 4.1 In a metal the nucleus and core electrons retain their configuration in the free atom, but the valence electrons leave the atom to form the electron gas.

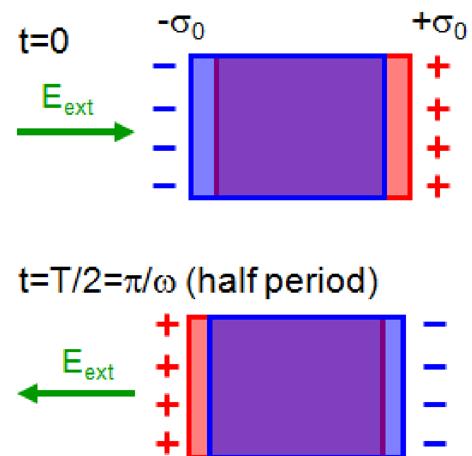

Figure 4.2 Simple model of a plasmon oscillation caused by a time-dependent electric field.

In Drude model, at any time t, the relationship between the momentum of each electron $\boldsymbol{p}_{(t)}$ and external force $\boldsymbol{f}(t)$ can be expressed as:

$$\frac{d\boldsymbol{p}(t)}{dt} = -\frac{\boldsymbol{p}(t)}{\tau} + \boldsymbol{f}(t) \qquad (4.1)$$

When the bulk metal is put in a time-dependent electric field:

$$\boldsymbol{E}(t) = \boldsymbol{E}(\omega)e^{-i\omega t} \qquad (4.2)$$

A rapid oscillation of the valence electron density occurs along the changing electric field, which can be described as an instability in the dielectric function of a free electron gas (as shown in Fig 4.2). The momentum $\boldsymbol{p}(t) = \boldsymbol{p}(\omega)e^{-i\omega t}$ can be expresses in Equation (4.1):

$$-\boldsymbol{i\omega p}(\omega) = -\frac{\boldsymbol{p}(\omega)}{\tau} - e\boldsymbol{E}(\omega) \qquad (4.3)$$

Since the current density $\boldsymbol{j} = -ne\boldsymbol{p}/m$, combined with Equation (4.3), $\boldsymbol{j}$ can be expressed as:

$$\boldsymbol{j}(\omega) = \frac{(ne^2/m)\boldsymbol{E}(\omega)}{(1/\tau) - i\omega} = \sigma(\omega)\boldsymbol{E}(\omega) \qquad (4.4)$$

Supposing $\sigma(\omega)$ as the frequency-dependent conductivity, $\sigma(\omega)$ can be expressed as:

$$\sigma(w) = \frac{\sigma_0}{(1/\tau) - i\omega}, \sigma_0 = \frac{ne^2\tau}{m} \qquad (4.5)$$

To get the dielectric constant $\varepsilon(\omega)$, Maxwell's equations can be rewritten as:

$$\nabla \cdot \boldsymbol{E} = 0;\ \nabla \cdot \boldsymbol{H} = 0;\ \nabla \times \boldsymbol{E} = -\frac{1}{c}\frac{\partial \boldsymbol{H}}{\partial t};\ \nabla \times \boldsymbol{H} = \frac{4\pi}{c}\boldsymbol{j} + \frac{1}{c}\frac{\partial \boldsymbol{E}}{\partial t} \qquad (4.6)$$

Then:

$$\nabla \times (\nabla \times \boldsymbol{E}) = -\nabla^2\boldsymbol{E} = \frac{i\omega}{c}\nabla \times \boldsymbol{H} = \frac{i\omega}{c}\left(\frac{4\pi\sigma}{c}\boldsymbol{E} - \frac{i\omega}{c}\boldsymbol{E}\right) = \frac{\omega^2}{c^2}\left(1 + \frac{4\pi i\sigma}{\omega}\right)\boldsymbol{E} \qquad (4.7)$$

So the complex dielectric constant is given by:

$$\epsilon(\omega) = 1 + \frac{4\pi i\sigma}{\omega} \qquad (4.8)$$

Here, if $\omega\tau \gg 1$, $\varepsilon(\omega)$ can be expressed as:

$$\varepsilon(\omega) = 1 - \frac{\omega_p^2}{\omega^2} \qquad (4.9)$$

where ω_p is known as the frequency for bulk plasmon oscillation. For typical metals, ω_p lies in the visible or UV range.

4.2. Introduction to surface plasmon

A surface plasmon (SP) is a travelling, evanescent surface electromagnetic wave caused by collective and coherent free electron oscillation at a metal-dielectric interface through the interaction between the electromagnetic field and the free electrons of the metal. Fig 4.3 shows that SP is excited by the magnetic field component (H_y in Fig 4.3) of the electromagnetic wave, and as expected the charge oscillates surround the magnetic field lines.[81]

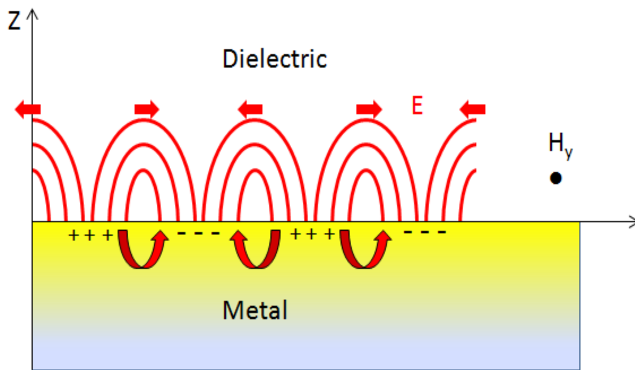

Figure 4.3 SPs at the interface have a combined electromagnetic wave and surface charge character. This combined character also leads to the field component perpendicular to the surface being enhanced near the surface and decaying exponentially with increasing distance from the surface.

Surface plasmon resonance (SPR) refers to the excitation of SP by light or incident electrons. As the SP is confined to the metal-dielectric interface with an extension of only ~200 nm from the interface (as discussed in Chapter 4, Section 4), its resonance frequency is highly sensitive to refractive index changes at the interface. For this, SPR resonance is a sensitive probe for assessment of interfacial compositions and morphologies.

For example, the binding of a monolayer of (bio-) molecules on a metal surface will lead to a detectable shift of resonance wavelength; therefore, SPR can be used as a bio-sensor with high sensitivity to detect, in real time, biological binding events, such as DNA hybridization and antigen-antibody binding.[82] Compared with other types of bio-sensors, like ELISA (Enzyme-linked immunosorbent assay) immune-assays or DNA micro-array based on fluorescent detection, SPR sensors don't involve any labeling process that may be expensive and result in label-induced changes or bleaching.

4.3. Dispersion relation

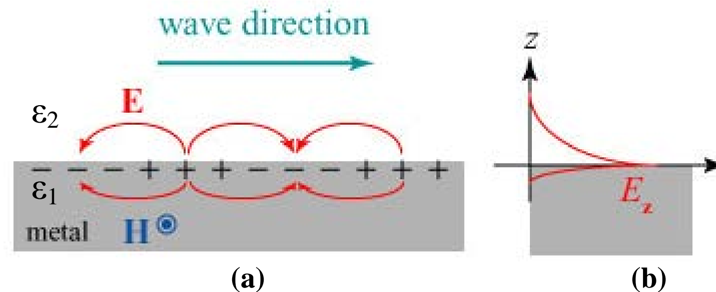

Figure 4.4 (a) The relationship between the charges and the electromagnetic field of SPs propagating on metal/dielectric interface in x direction. (b) The field E_z decreases exponentially away from the interface.

The electric field of a propagating electromagnetic wave (Fig. 4.4a) can be expressed as:

$$E = E_0 \exp[i(k_x x \pm k_z z - \omega t)] \qquad (4.10)$$

where k is the wave number and ω is the angular frequency of the wave.

By solving Maxwell's equations for the electromagnetic wave at an interface between two materials with relative dielectric functions ε_1 and ε_2 with the appropriate continuity relation, the boundary conditions are:

$$D_0 = \frac{k_{z1}}{\varepsilon_1} + \frac{k_{z2}}{\varepsilon_2} = 0 \qquad (4.11)$$

$$\varepsilon_i (\frac{\omega}{c})^2 = k_x^2 + k_{zi}^2 \text{ , } i = 1{,}2. \qquad (4.12)$$

where c is the speed of light in a vacuum, and k_x is the same wave vector for both media at the interface.

Solving these two equations, the dispersion relation for a wave propagating on the surface is:

$$k_x = \frac{\omega}{c} (\frac{\varepsilon_1 \varepsilon_2}{\varepsilon_1 + \varepsilon_2})^{1/2} \qquad (4.13)$$

Here, k_x can be considered as the wave vector along the propagation direction of the SP, which can be renamed as k_{sp}, and $k_0 = \frac{\omega}{c}$, which is the free-space wave vector. For metals and doped semiconductors, $\varepsilon_1 < 0$ and $|\varepsilon_1| > \varepsilon_2$, which makes k_{sp} in Equation 4.13 a real number, though with a finite imaginary part representing attenuation along the propagating direction (x-direction), due to the non-zero imaginary part of metal dielectric function.[83]

From Equation 4.13 we can deduce the dispersion relationship between k_x and ω, as show in Fig. 4.5. The dispersion curve shows the momentum mismatch problem that must be overcome in order to couple light and SP modes together, with the SP mode always lying beyond the light line: it has greater momentum ($\hbar k_{SP}$) than a free space photon ($\hbar k_0$) of the same frequency ω.

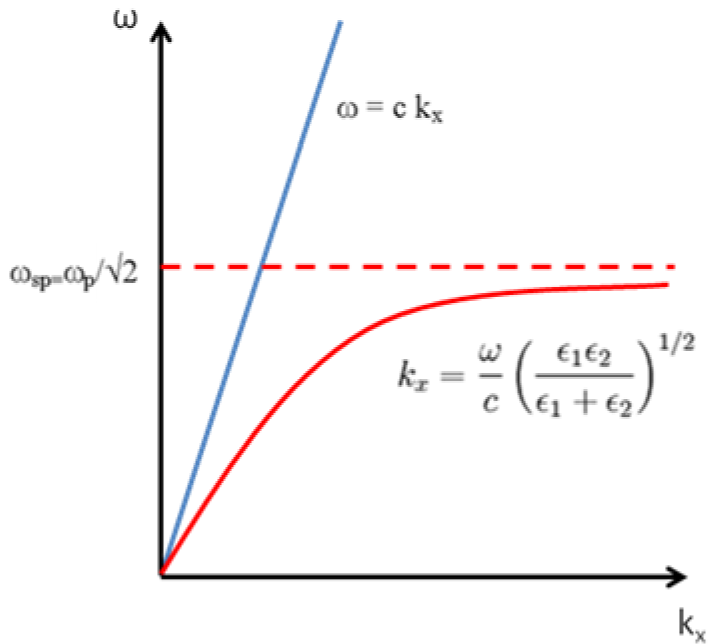

Figure 4.5 Dispersion curve for surface plasmons. At low *k*, the surface plasmon curve approaches the free-space photon curve.

4.4. Spatial extension of the SP field

Wave vectors k_{z1} and k_{z2} will affect the extension depth of SPs. As showed in Equation 4.10, the field amplitude of the SPs decreases exponentially as exp(-$|k_{zi}||z|$) from the boundary. The value of the depth at which the field falls to 1/e, becomes:

$$z = \frac{1}{|k_{zi}|} \qquad (4.14)$$

where K_{Zi} is the imaginary part of K_z.

In the dielectric medium with ε_2: $z_2 = \frac{\lambda}{2\pi}\left|\frac{\varepsilon_1+\varepsilon_2}{\varepsilon_2^2}\right|^{1/2}$ (4.15)

In the metal with ε_1: $z_1 = \frac{\lambda}{2\pi}\left|\frac{\varepsilon_1+\varepsilon_2}{\varepsilon_1^2}\right|^{1/2}$ (4.16)

For $\lambda = 600\ nm$, one can obtain $z_2 = 3900$ Å and $z_1 = 240$ Å for silver; and for gold, 2800 Å and 310 Å, respectively. This shows that SP nearly only occurs at the interface (Fig 4.4b), which also means that SPR can be a very sensitive probe to examine the morphology and composition of the surface.

4.5. Types of surface plasmonic sensors

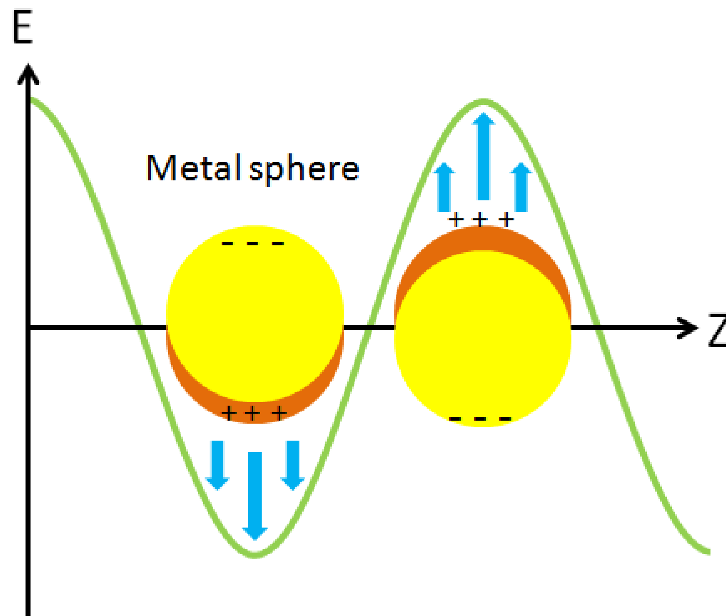

Figure 4.6 Localized surface plasmon on metal nanoparticles excited by free-space light.

Without additional momentum, the momentum mismatch between SPs mode ($\hbar k_{SP}$) and the free-space photon ($\hbar k_0$) leads to confined SPs.[84] It is reported that metal particles (<250 nm in diameter) can interact strongly with light and this leads to localized surface plasmon resonances within 10s nm of the particle surface (as shown in Fig. 4.6).[85] One of the most important applications from localized SPs is for Raman spectroscopy.[86] Raman spectroscopy probes molecular vibration with high selectivity, but it suffers from weak signal intensity due to the extremely small cross section of the inelastic Raman scattering (discussed in Chapter 5, Section 1). However, it was found that the Raman signal can be enhanced by a factor up to 10^{14} when the

molecules are adsorbed on a rough or nano-structured noble metal surface, which is termed as surface enhanced Raman scattering (SERS). In Chapter 5, SERS will be introduced and discussed.

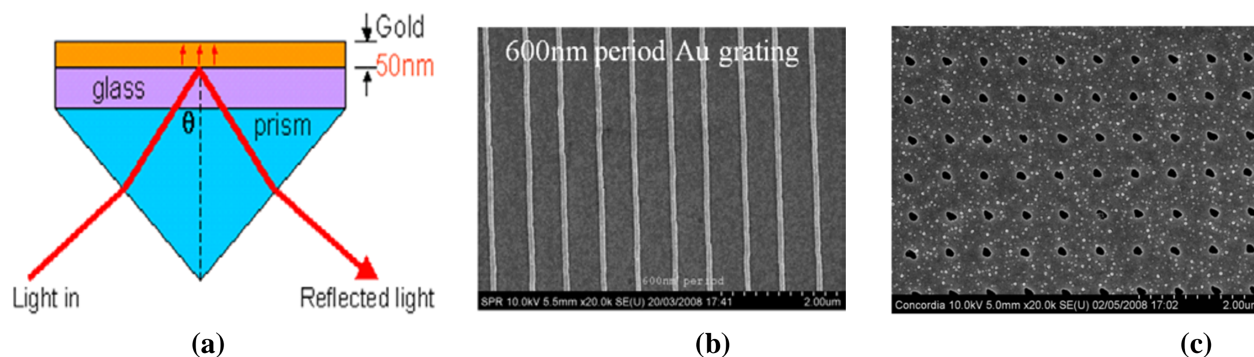

Figure 4.7 Surface plasmon coupling schemes: (a) Schematic prism-coupled SPR bio-sensor (Kretschmann configuration); (b) Grating-coupled SPR sensor. Here Au is deposited on a polymer as a 600nm-period grating created by nano-imprinting/hot embossing; (c) EOT-based SPR biosensor. Here a 600 nm period hole array in 120nm-thick Au is fabricated by e-beam lithography and liftoff.

If additional momentum is provided, SPs will be excited by free-space light and propagate along the surface. Several methods are feasible: this can be achieved by prism coupling (Kretschmann configuration, shown in Fig. 4.7a); by patterning a grating structure on the surface, with the additional momentum being K=2π/period (shown in Fig. 4.7b); or by patterning a 2D grating structure in the metal film (shown in Fig. 4.7c). Recently it was found that light transmission through a hole array (see Fig. 4.7c, hole diameter << wavelength) in optically thick metal films is one order higher than that predicted by Bethe's theory, termed extraordinary optical transmission (EOT).[87] The light has to pass through the holes through "tunneling" with an amplitude that decays exponentially, generally attributed to the coupling of incident light into the holes by SPR. In Chapter 6 EOT sensors will be discussed and compared with prism-coupled SPR sensors, the most popular and commercially available SP sensors.

4.6. Basis introduction to FDTD simulation method

As one of the most popular numerical methods, the finite difference time domain (FDTD) method was introduced in this work to model the distribution of electromagnetic field on metal structures.

Based on Maxwell's differential equations:

$$\nabla \cdot \boldsymbol{E} = \frac{\rho}{\varepsilon_0} \qquad (4.17)$$

$$\nabla \cdot \boldsymbol{B} = 0 \qquad (4.18)$$

$$\nabla \times \boldsymbol{E} = -\frac{\partial \boldsymbol{B}}{\partial t} \qquad (4.19)$$

$$\nabla \times \boldsymbol{B} = \mu_0 \left(\boldsymbol{J} + \frac{\partial \boldsymbol{E}}{\partial t} \right) \qquad (4.20)$$

the change of the ***E*** and ***B*** field in time is dependent on the spatial curl of the ***B*** and ***E*** field, respectively. To calculate the change of electromagnetic field in time, this inter-relationship makes the calculation much complicated. In 1966, Kane S. Yee originally proposed the so-called method of Yee's cell, in which the electromagnetic field and the object is separated to a series of discrete units, shown in Fig. 4.8.[88] For each cell, its EM field is only based on the EM field of the previous cells in time, which simplifies the inter-relationship of the ***E*** and ***B*** field. By this way, the calculation is simplified greatly.

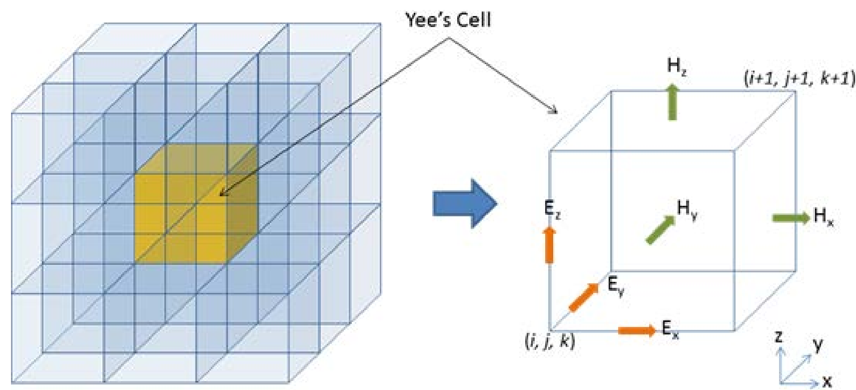

Figure 4.8 In FDTD method, the object is separated to a series of discrete units.

In Chapter 5 and 6, FDTD method was used in the software OptiFDTD10 and Lumerical FDTD Solutions for modeling the SPs in SERS and EOT, respectively. The modeling process and conditions will be discussed in more detail in those chapters.

Chapter 5

Surface enhanced Raman spectroscopy (SERS) for chemical sensors

5.1. Introduction to Raman spectroscopy

Briefly, when the energy of the incident light matches energy level of the electron cloud and the bonds of the small particles such as molecules and atoms, there are mainly three types of scattering occurring: Rayleigh scattering, Stokes scattering and Anti-Stokes scattering. The first scattering is considered as elastic scattering, and the other two are inelastic scattering.

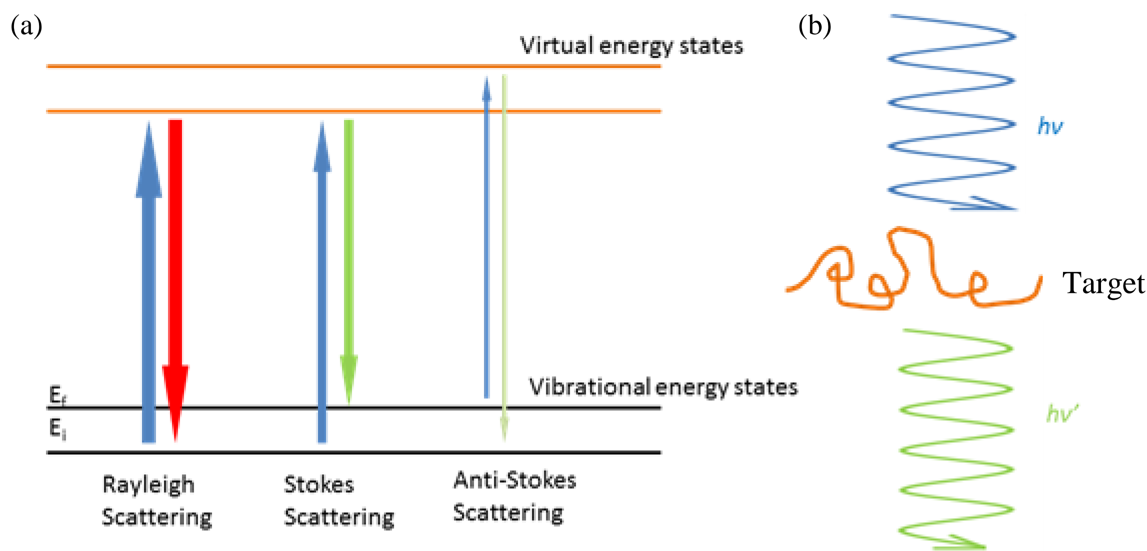

Figure 5.1 (a) Diagram of energy levels involving Rayleigh scattering, Stokes scattering and Anti-Stokes scattering. (b) Schematic of inelastic scattering on a small particle.

As shown in Fig. 5.1b, through Stokes scattering, the relationship between incident light (ν), scattered light (ν'), and the energy shift can be expressed as:

$$\boldsymbol{h}(\boldsymbol{\nu} - \boldsymbol{\nu}') = \hbar\boldsymbol{\omega}_{\mathbf{p}} \qquad (\mathbf{5.1})$$

where $\hbar\boldsymbol{\omega}_{\mathbf{p}}$ is the energy absorption between different energy levels, which is related to the molecular/atomic vibration, rotation, and bonding. Based on this, Raman spectroscopy is a very accurate technique to identify the fingerprint of molecules.[89] However, there is only ~1 photon out of 10^8 incident photons contributing to inelastic scattering, which leads to very weak Raman signal and limits the application of Raman spectroscopy.

5.2. Introduction to surface-enhanced Raman spectroscopy (SERS)

Raman spectroscopy probes molecular vibrations with high selectivity (distinguishing the fingerprint of each type of molecule), but it suffers from weak signal intensity due to the extremely small cross section of inelastic Raman scattering. However, in 1970s it was found that the Raman signal can be enhanced by a nominal factor of $>10^{13}$ when the molecules are adsorbed on rough or nanostructured noble metal surface, which is termed as surface enhanced Raman scattering (SERS).[90-92] Besides spectral specificity, SERS is a label free sensing method capable of single molecule detection. Like SPR sensors, SERS is a powerful tool in the diagnosis of disease and pathogens, as well as detection of chemicals such as explosives and pollutants.

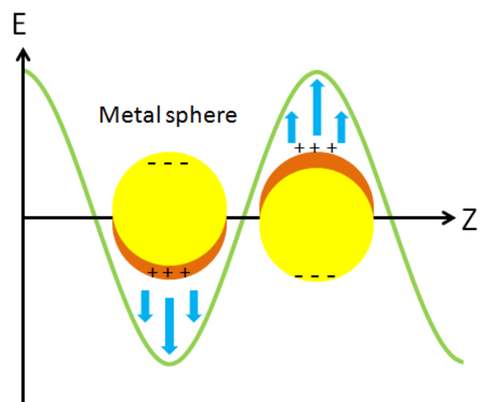

Figure 5.2 Schematic of localized surface plasmon.

5.2.1. Electromagnetic Enhancement Mechanism (EEM)

Since Raman intensities scale as the product of the incident field intensity, the first commonly considered explanation for SERS is the electromagnetic enhancement mechanism.

In EEM theory, the enhancement factor E at each molecule can be approximately given by the equation (5.2):[93]

$$E = |E(\omega)|^2 |E(\omega')|^2 \qquad (5.2)$$

where E(ω) is the enhancement factor for local electric field at the incident frequency ω and E(ω') is the corresponding factor at the Stokes-shifted frequency ω'.

First, the maximum enhancement E_{max} for single-molecule SERS (SMSERS) is more important than the E in equation (5.2), which is averaged over the surface area where molecules can be adsorbed to generate the enhancement factor ‹E›. Since the E_{max} can be orders of magnitude larger than ‹E›, it is necessary to distinguish between these two enhancement estimates. Second, for approximation, E(ω) and E(ω') are usually assumed to be the same, and hence:

$$E = |E(\omega)|^4 \qquad (5.3)$$

This assumption makes sense under some conditions, but in the condition of isolated homogeneous particles it may lead to a noticeable overestimate of the enhancement factor E, by orders of 3 or more.

5.2.2. Numerical methods for calculating electromagnetic enhancement factors

Combined with the electromagnetic enhancement mechanism (EEM) by solving Maxwell's equations, the other mechanism for increased signal intensity involves enhancement in polarizability due to chemical phenomena such as charge-transfer excited states.[94] For example,

an enhancement of the Raman cross section, which is not found on the basis of the gas phase properties of the molecule, appears as a new excited state caused by chemisorptions.[95]

Basic calculations are based on simple models of the roughness or particle structures, such as spheres or spheroids. Taking a sphere as example, as shown in Figure 5.3,[96] a single sphere of radius *a* with a dielectric constant of ε_2 is immersed in an infinite medium with a dielectric constant of ε_1. To determine the relationship between the electric field potential Φ, the general solution of Laplace's equation is represented by:

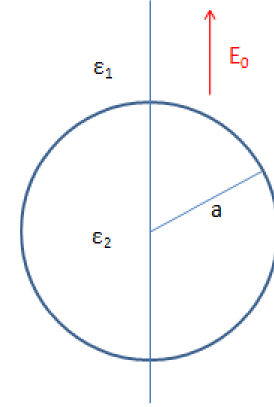

Figure 5.3 Schematic of a sphere of radius *a* and dielectric constant ε_2, immersed in a dielectric extending to infinity, with dielectric constant ε_1.

for outside the sphere:

$$\phi_1 = \sum_{n=0}^{\infty} \left(A_n r^n + \frac{B_n}{r^{n+1}} \right) P_n(\cos\theta) \qquad (5.4)$$

for inside the sphere:

$$\phi_2 = \sum_{n=0}^{\infty} \left(C_n r^n + \frac{D_n}{r^{n+1}} \right) P_n(\cos\theta) \qquad (5.5)$$

The boundary conditions for this system are:

(1) $(\phi_1)_{r\to\infty} = -E_0 z = -E_0 r\cos\theta \qquad (5.6)$

Since far from the origin the field approaches $\mathbf{E}_0$.

(2) $(\phi_1)_{r=a} = (\phi_2)_{r=a} \qquad (5.7)$

Since Φ is continuous across the boundary.

(3) $\varepsilon_1 (\frac{\partial \phi_1}{\partial r})_{r=a} = \varepsilon_2 (\frac{\partial \phi_2}{\partial r})_{r=a} \qquad (5.8)$

Since the normal component of **D** must be continuous at the surface of the sphere.

(4) At the centre of the sphere (when r=0), Φ_2 must not have a singularity.

The solution of equations (5.4) and (5.5) is:

$$\phi_1 = \left(\frac{\varepsilon_2 - \varepsilon_1}{2\varepsilon_1 + \varepsilon_2}\frac{a^3}{r^3} - 1\right)E_0 z \qquad (5.9)$$

$$\phi_2 = -\frac{3\varepsilon_1}{2\varepsilon_1 + \varepsilon_2}E_0 z \qquad (5.10)$$

Since the external potential is given by $\phi = -E_0 z$, equations (5.9) and (5.10) can be rewritten as:

$$\phi_1' = \frac{\varepsilon_2 - \varepsilon_1}{2\varepsilon_1 + \varepsilon_2}\frac{a^3}{r^3}E_0 z \qquad (5.11)$$

$$\phi_2' = \frac{\varepsilon_2 - \varepsilon_1}{2\varepsilon_1 + \varepsilon_2}E_0 z \qquad (5.12)$$

where ϕ_1' and ϕ_2' are contributed from the polarization of the sphere.

For a dipole moment $\boldsymbol{\mu}=\alpha\mathbf{E}_0$, with the metals' dielectric constant set at ε and the dielectric constant of the medium set at ε_0, it can be established that:

$$\alpha_E = \frac{\varepsilon - \varepsilon_0}{\varepsilon + 2\varepsilon_0}a^3 \qquad (5.13)$$

For an ellipsoid particle, the ellipsoid major axis *a* and minor axis *b* dimensions being such that *a, b* << λ, a further simplification can be made:

$$\alpha_E = -\frac{1}{3}ab^2\varepsilon_0\frac{1 - \varepsilon/\varepsilon_0}{1 - (1 - \varepsilon/\varepsilon_0)A} \qquad (5.14)$$

A is a depolarization factor which has been tabulated. For a 3:1 aspect ratio ellipsoid, A=0.1; for a sphere (1:1 aspect ratio), A=1/3.[97]

In recent years, more theoretical work to investigate SERS has considered non-resonant molecules on nano-particle surfaces using computational electrodynamics methods including the discrete dipole approximation (DDA)[98] and the finite difference time-domain (FDTD)[99] method to solve Maxwell's equations for the local fields E(ω). Similar to the basic calculation above, finite elements replace actual particle structures to describe a particle of any shape within a 100 nm scale size. Based on this simplification, many particles can be described together using coupled multi-pole expansions.

Further works also discovered that besides the size and shape of the particles the size of the gap between particles is also a key parameter for predicting the enhancement factor. In the work from Hao and Schatz,[100] E_{max} varies rapidly with different gap size and it is only for gaps on the order of 1-2 nm that one can obtain exceptionally large enhancement values such as $|E_0|^4 = 10^{11}$.

The group of Prof. P. Van Duyne concluded that the governing equation for the electromagnetic field outside the particle in a sphere mode is:[101]

$$E_{out}(x,y,z) = E_0\hat{\boldsymbol{z}} - \left[\frac{\varepsilon_{in} - \varepsilon_{out}}{(\varepsilon_{in} + 2\varepsilon_{out})}\right] a^3 E_0 \left[\frac{\hat{\boldsymbol{z}}}{r^3} - \frac{3z}{r^5}(x\hat{\boldsymbol{x}} + y\hat{\boldsymbol{y}} + z\hat{\boldsymbol{z}})\right] \quad (5.15)$$

where ε_{in} is the dielectric constant of the metal nanoparticle, and ε_{out} is the dielectric constant of the external environment.

The extinction spectrum of the metal particles is expressed as:

$$E_{(\lambda)} = \frac{24\pi^2 N a^3 \varepsilon_{out}^{3/2}}{\lambda \ln(10)} \left[\frac{\varepsilon_i(\lambda)}{\left(\varepsilon_r(\lambda) + \chi\varepsilon_{out}(\lambda)\right)^2 + \varepsilon_i^2(\lambda)}\right] \quad (5.16)$$

Here, $E_{(\lambda)}$ is the enhancement factor; ε_r and ε_i are the real and imaginary components of the metal dielectric function, respectively. χ, which appears in front of ε_{out}, is the shape index equivalent to A in Equation 5.14. For example, the value of χ is 2 for spherical particles, but it takes on values as large as 20 to account for particle shape with high aspect ratios. Noticeable in Equation 5.16 is the wavelength dependences of the metal dielectric function.

5.2.3. Metals for SERS

Based on Equation (5.14), a singularity occurs when $1-\left(1-\frac{\varepsilon}{\varepsilon_0}\right)A$ reaches 0. Solving the suggested function:

$$1-\left(1-\frac{\varepsilon}{\varepsilon_0}\right)A=0 \qquad (5.17)$$

We can conclude that the dielectric constant should satisfy the condition for maximum SERS effect:

$$\varepsilon=\varepsilon_0\left(1-\frac{1}{A}\right) \qquad (5.18)$$

For a sphere, this resonance occurs when $\varepsilon\sim-2\varepsilon_0$. And for a 3:1 aspect-ratio ellipsoid, it occurs when $\varepsilon\sim-8.25\varepsilon_0$. Generally speaking, for strong SERS, the metal should have a large (negative) real and small imaginary electric permittivity. Figure 5.4 (a) and (b) shows the relationship between wavelength (λ) and the real part ε_1/the imaginary part ε_2 of the dielectric constant of most popular metals, respectively, in which silver, gold and copper have the lowest values of ε_1 at the same λ. This means that SERS can mainly be associated with three metals: silver (the most popular one), gold and copper. Other metals which are rarely reported include rhodium[102,103] and platinum[104], and are used only when the experiments are well-characterized for SP enhancement.

(a)

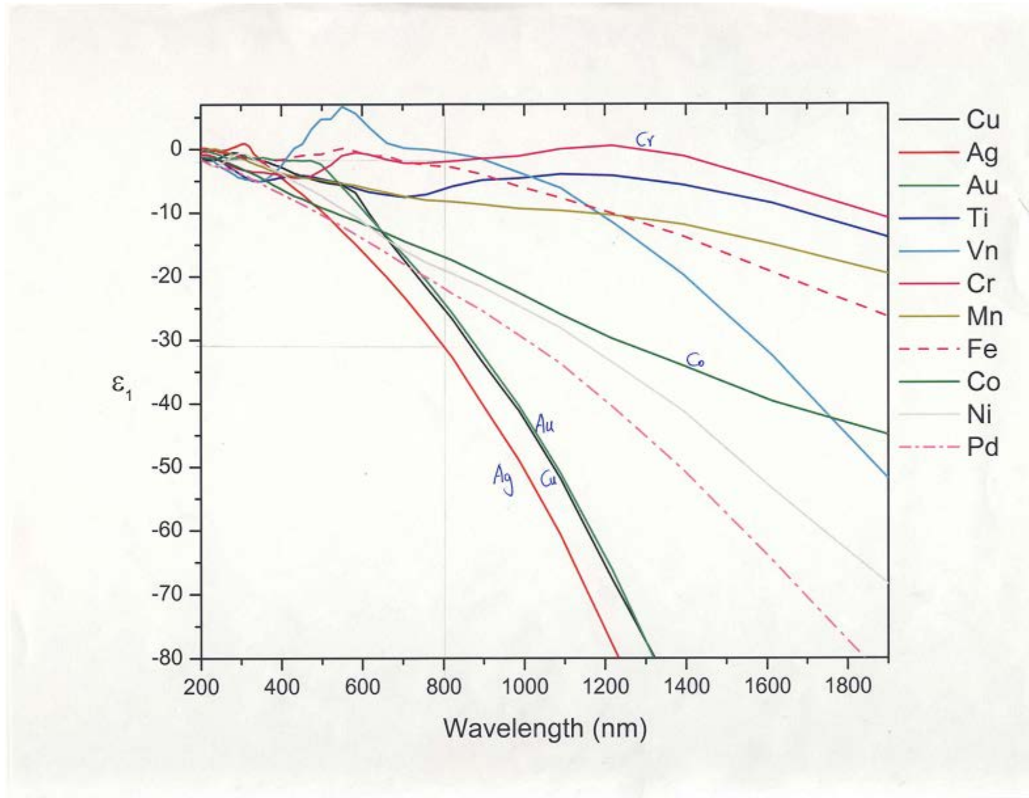

(b)

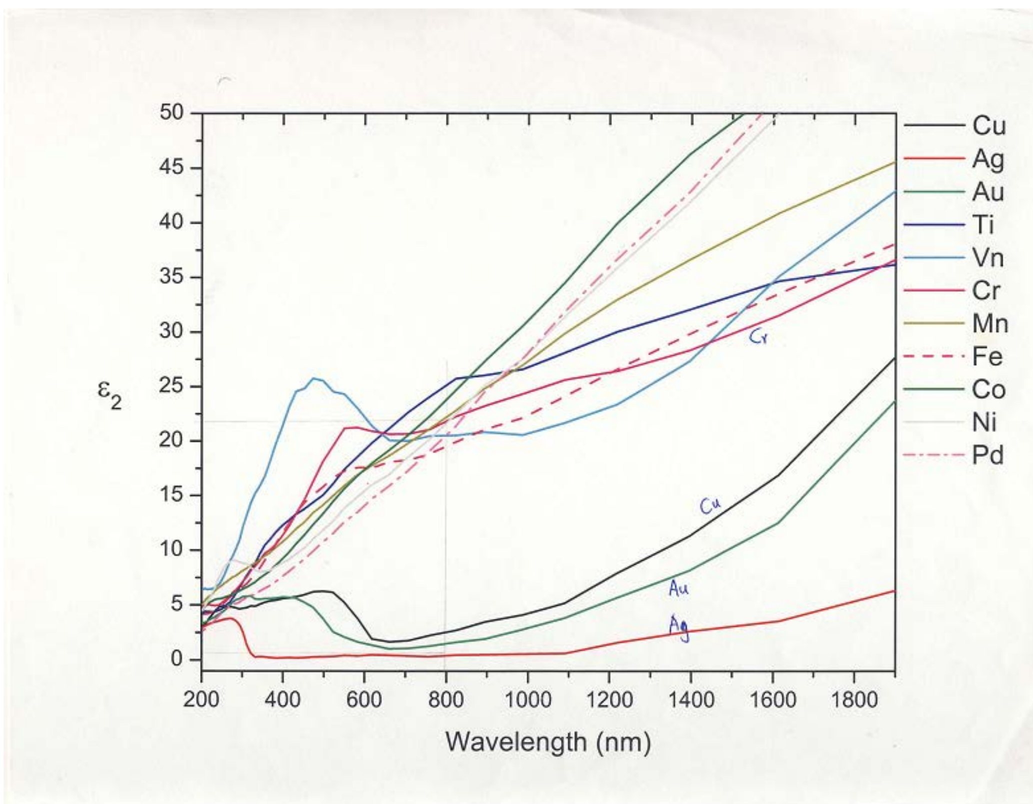

Figure 5.4 The relationship between the wavelength and (a) the real part ε_1; (b) the imaginary part ε_2 of dielectric constant of the most popular metals.

5.3. Nano-fabrication technologies for SERS chemical sensors

SERS owns the importance as a sensitive chemical sensing technique capable of single molecule detection,[105-111] mainly utilizing the LSPR of noble metal nano-particles (NPs) onto which the target molecules adsorb. Since SERS was discovered in 1970s,[112,113] the two factors of great concern exist in the controllable SERS application are: (1) the adsorptivity of the target molecules, and (2) the electromagnetic field enhancement E, which is a function of localized electric field at incident frequency of ω,($E = E(\omega)^4$).

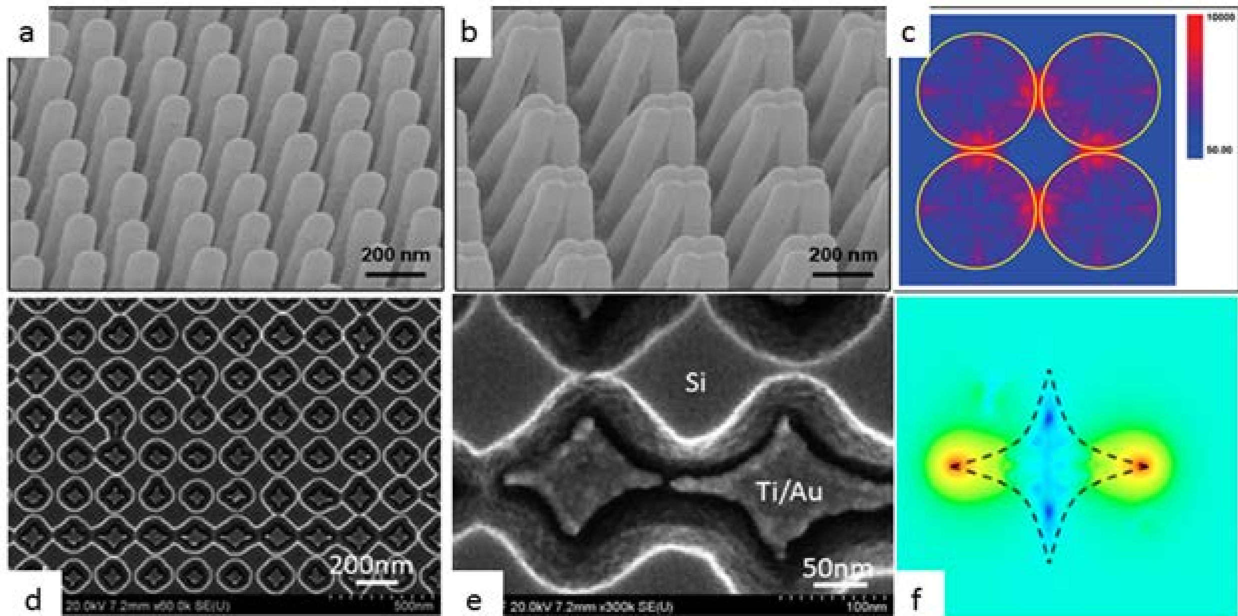

Figure 5.5 SEM images of (a) open gold nanofingers with 68 nm radius and (b) closed nanofingers after molecule trapping; (c) simulated distribution of electric field intensity $|E(r)|^2$ on the (b) structure at 750 nm laser, the hotspots exist at the nano gap. Copyright 2010 by the American Chemical Society. SEM image of (d) 200 nm period nanostar array of 5 nm Ti/15 nm Au on silicon, and (e) zoom-in view of nanostars with sub-10 nm apex and gap between adjacent stars; (f) simulated distribution of electromagnetic near field at 750 nm wavelength, the hotspots exist at the nano tip. Copyright 2010 by the AIP Publishing LLC.

Strong LSPR and consequently strong SERS enhancement occurs at the "hotspots",[111,114,115] such as the sharp tips of the NPs,[116-120] or the tiny gaps between adjacent NPs.[107,121-123] Metallic structures with nanoscale gaps will increase dramatically the local electromagnetic field intensity $E(\omega)$.[124] On the other hand, nano-structured surface can improve the absorption of the target

molecules[86,125] by making the specific surface area much larger than flat metal film. Fig 5.5 shows two examples of patterned nano-structures for SERS sensors.[126,127]

Based on these considerations, artificial antenna through nano-fabrication such as bowtie array (Fig. 5.6a), which is defined as an array of two triangular structures facing each other, with nano-gap is one of the most promising candidate for tunable and reproducible SERS application.[128-130] Here we will show that the hotspots only exist within the gap area, and SERS performance can be controlled by the size, shape, gap distance and period of the array.

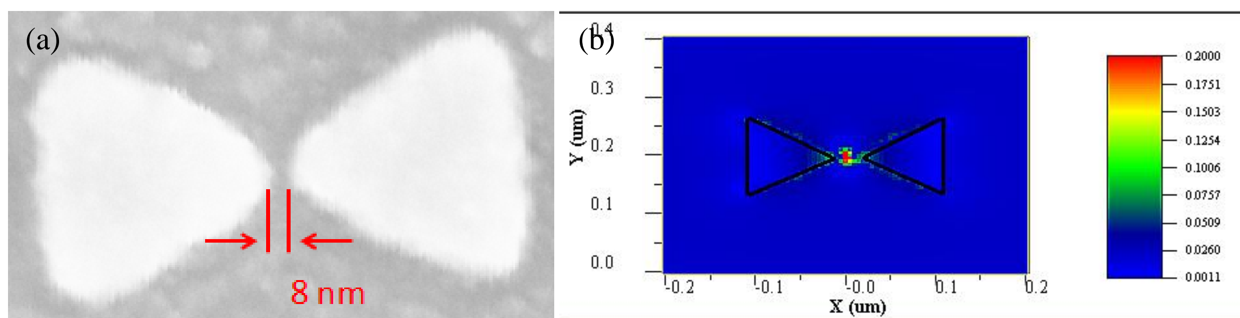

Figure 5.6 (a) SEM image of typical bowtie structure fabricated by EBL on membrane with 8 nm gap; (b) The FDTD simulated $|E|^2$ profile of the same bowtie structure, which shows the extremely high electrometric field in the gap area (hotspots).

Nanofabrication techniques with ultra-high resolution of sub-10 nm are critical in LSPR structures. Simply, the localized electric field intensity is inversely proportional to the separation *d*.[124] Both experiments and numerical studies shows that large enhancement factor occurs for small gap with several nanometers (hotspots).[126,131] A few fabrication methods for sub-10nm feature size are reported:

(1) Fabrication through focused ion beam lithography (FIBL) is utilized in most of literatures.[132-134] Gold structures can be achieved by milling on gold film directly or by pattern transfer in the next step. However, this method is time-consuming for large area patterning and Ga contamination is an issue.[135]

(2) Nanoimprint lithography (NIL) is also applied in SERS patterning by utilizing NIL combined with randomly aggregation of gold particles by evaporation.[125,136] Yet the nano-pattern transfer is challenging due to the residual resist layer.

(3) Nanosphere lithography (NSL) is another way to form triangular particle arrays which can be used for SERS. As shown in Fig. 5.7, after spin-coating and drying of polymer nano-spheres onto substrate, the self-assembly process prompts the nano-spheres to form a close-packed hexagonal array. In the following deposition and lift-off, gold forms triangular patterns in the gaps. However, only one kind of shape can be achieved by this way, which limits the study of SERS structures.

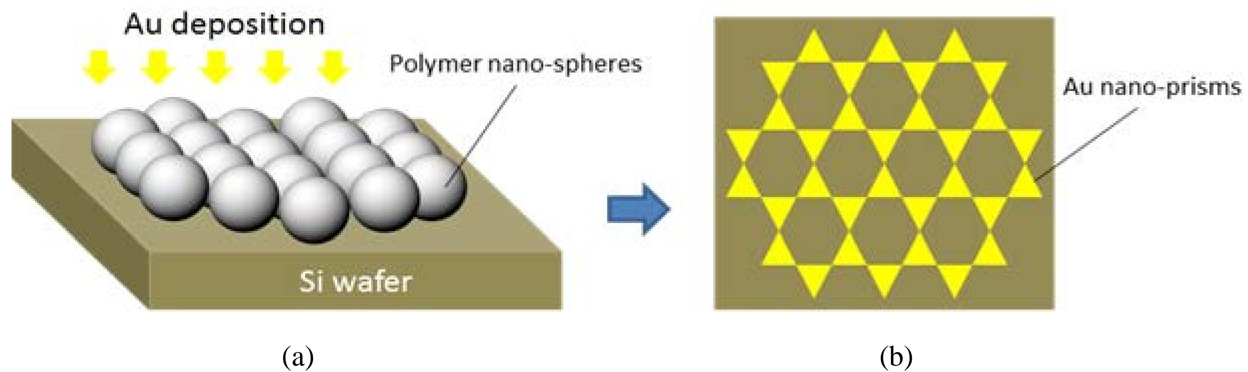

Figure 5.7 (a) Spin-coating the solution of polymer nano-sphere and Au deposition; (b) Formation of a close-packed hexagonal array of Au nano-prisms after lift-off.

Compared with the nanofabrication methods described above, EBL is a more versatile method to achieve nano-patterns with different arrays, shapes, sizes and spacings. Patterns are designed and exposed on resist by EBL to serve as a deposition mask; metal is then deposited through this mask and the resist is removed by lift-off, leaving the tone-reversed metal pattern. By this technique plasmonic coupling between nano-patterns of arbitrary shape with different inter-particle spacing has been investigated.[137-139]

5.4. Proximity effect in EBL and Monte Carlo method for dose optimization

Though electron beam lithography (EBL) is one of the most powerful techniques in nanostructure fabrication, it is still challenging to fabricate sub-10 nm gap due to the proximity effect.[140-142] In typical EBL process, poly(methyl methacrylate) (PMMA) electron beam resist is spin-coated on bulk substrate such as silicon wafer.[143] During electron beam exposure, the incident electron beam generates secondary electrons with the energy of ~10eV, which can react with the polymer chain and change its solubility. Generated secondary electrons are also contributed from back-scattered electrons, which enlarge the feature size.

Four techniques are developed to improve the EBL resolution. First, higher voltage increases the penetration depth of incident electrons and reduces the dispersion of back-scattered electrons on surface.[142,144] Thus all reported EBL patterns of sub-10 nm resolution were exposed by 100 keV system which is extremely expensive. Second, less back-scattered electrons stay within a thinner resist layer, but thin resist layer makes liftoff of a thick metal layer difficult.[145] Third, resists with lower sensitivity such as PMMA and hydrogen silsesquioxane (HSQ) are employed for the feature size with sub-20 nm.[146] The sensitivity of the resist also can be reduced carefully by low-temperature development.[147-149] and different developer.[150,151] Finally, substrate with lower density and higher conductivity reduces the charge accumulation.[152] However, all the methods described above are expensive, difficult or not stable and researchers still need to face the challenge when the feature size is close to sub-10 nm since the proximity effect still exists.

The proximity effect can also be significantly reduced by optimizing exposure dose distribution using numerical computation of electron trajectory and energy loss to generate secondary electrons in the resist and substrate.[153-155] Several numerical packages based on Monte Carlo method are available for dose modification up to around 10 nm, such as Casino and NanoPECS. The principle of Monte Carlo simulation is to approximate the mean energy loss from inelastic

scattering and compute the elastic scattering for the next collision during each electron trajectory. After the position, angle and the energy (eV) of the incident electron is settled, a random distance number D of the electron during two successive collisions within resist is evaluated within the electron elastic cross number and a random scattering angel θ is also generated. So the energy loss ΔE is then calculated as:

$$\Delta E = \frac{dE}{dx} D \qquad (5.19)$$

The mean energy loss $\frac{dE}{dx}$ is calculated based on the incident energy of the electron beam till the incident electron energy drops below threshold energy (can be set manually to reduce unnecessary calculation) or the electron moves out of the materials.

Fig. 5.8 shows the simulation results of electron scattering trajectories during electron beam lithography on 100 nm PMMA as the resist layer on silicon wafer. 2000 electrons are calculated by Casino 2.0 with the incident beam energy of 5, 10, 15, 20 keV, respectively. Two facts are revealed from Fig. 5.8 a-d:

(1) Higher beam energy will increase both of the vertical and lateral dispersion of the primary electrons. While, with the same dose (C/cm^2) in electron beam exposure, which means the same amount of electrons in Monte Carlo calculation, this means more primary electrons disperse deeper into the substrate and less energy contributes to resist layer on the surface. Based on this idea, all reported EBL patterns of sub-10 nm resolution were exposed by 100 keV system which is extremely expensive[54,56]. Fig. 5.8e shows the relationship between the amount of backscattering electrons and the depth at 5, 10, 15, 20 keV. With the increasing e-beam energy, the peak of max backscattering electrons moves to deeper substrate, leading less proximity effect on surface.

(2) Backscattering still happens with high beam energy, which means that proximity effect cannot be eliminated with high-voltage system. Backscattering electrons are mainly generated

during the scattering in substrate, and they can re-enter into resist layer causing unwanted exposure.

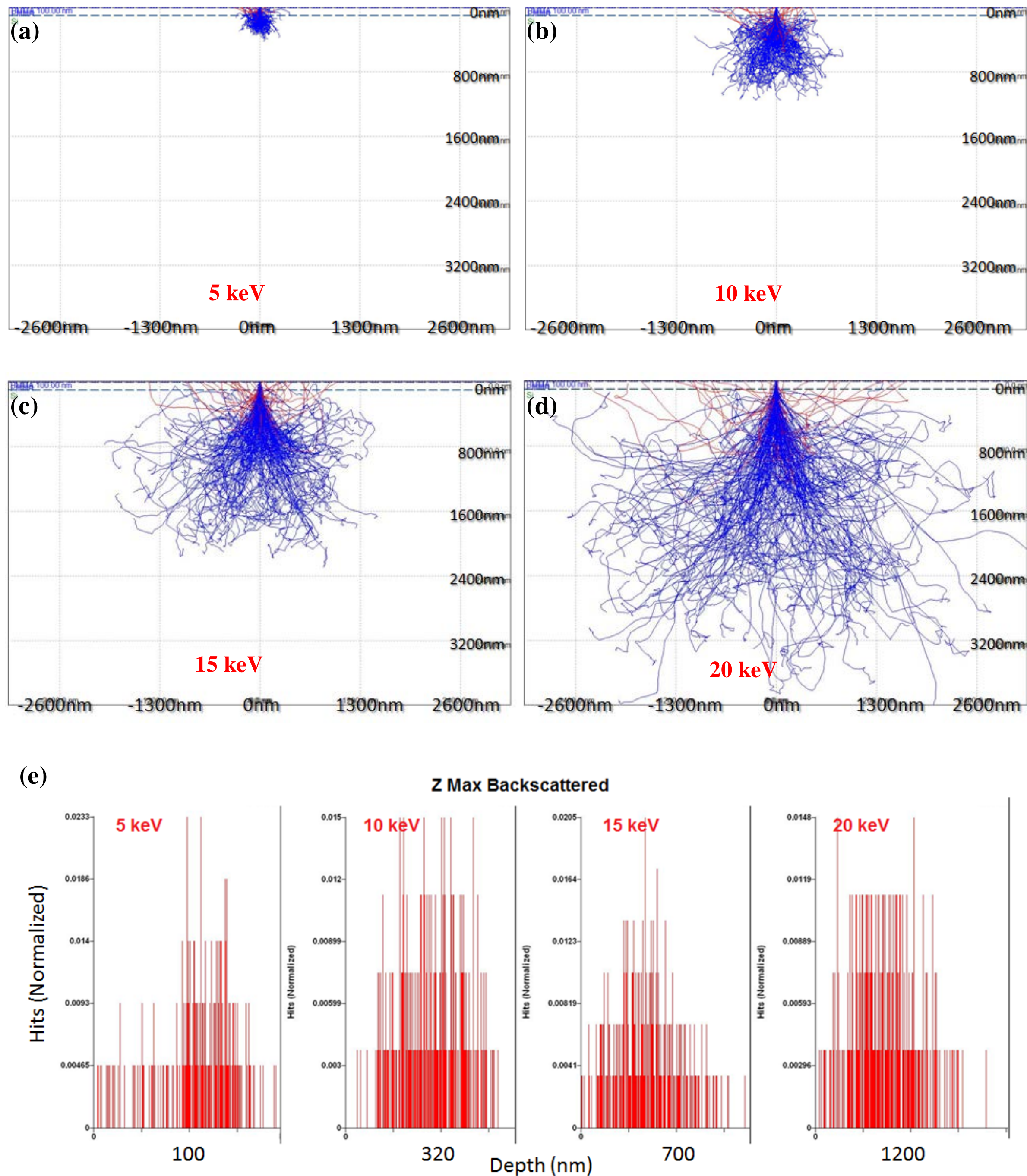

Figure 5.8 Simulation of the electron scattering trajectories in silicon substrate with 100 nm PMMA layer, with the incident beam energy: (a) 5 keV, (b) 10 keV, (c) 15keV, and (d) 20 keV. (e) Distribution of the backscattering electrons dependent on depth.

5.5. High-resolution electron beam lithography on Si_3N_4 membrane

5.5.1. Dose simulation

By optimizing exposure dose distribution using numerical computation of electron trajectory and energy loss in the resist and substrate, the proximity effect can be significantly reduced [153-155]. Several numerical packages based on Monte Carlo method are available for dose modification up to around 10 nm, such as Casino and NanoPECS. However, researchers still need to face the challenge when the feature size is close to sub-10 nm.

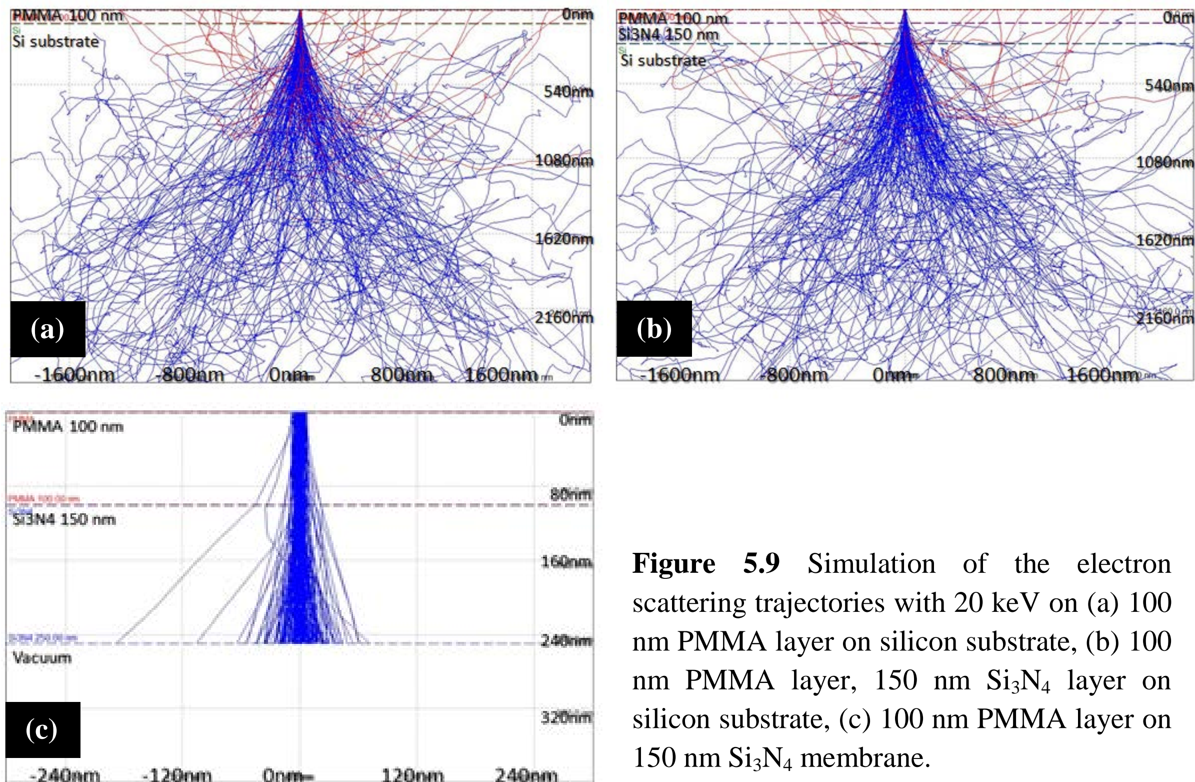

Figure 5.9 Simulation of the electron scattering trajectories with 20 keV on (a) 100 nm PMMA layer on silicon substrate, (b) 100 nm PMMA layer, 150 nm Si_3N_4 layer on silicon substrate, (c) 100 nm PMMA layer on 150 nm Si_3N_4 membrane.

In this work, we prove that using a thin membrane as the EBL substrate, most of incident electrons penetrate the membrane and thus much fewer backscattering electrons are generated. Within the ultra-thin membrane as the substrate, less scattering trajectory reduces backscattering electrons, nearly eliminating the proximity effect. Fig. 5.9 shows the Monte Carlo simulation result of the e-beam exposure with 20 keV on normal silicon wafer, silicon wafer with 150 nm silicon nitride film and free standing silicon nitride membrane with the thickness of 150 nm.

From Fig. 5.9a&b, the dispersion of scattering electrons are slightly increased, because of one more layer of different material (Si_3N_4 here) is inserted which will enhance the reflection of electrons. In contrast, on the Si_3N_4 membrane with the same thickness the dispersion of incident beam is much smaller and nearly no backscattering electron is generated in calculation.

NanoPECS from Raith 150^{TWO} e-beam lithography system can offer more professional calculation for e-beam exposure based on Monte Carlo method. In EBL the typical dose is 1pC~1fC/dot, therefore 500,000 trajectories with the beam energy of 20 keV and a Gaussian beam of radius of 2.5 nm were considered in the numerical calculation. The advantage of NanoPECS is that it can calculate and modify the distribution of exposure dose clearly. Fig. 5.10a&b show the distribution of exposure dose of bowtie pattern with 25 nm and 6 nm gap size on bulk wafer, respectively. And Fig.5.10c&d show the dose distribution on the cross-section of the same pattern. As can be seen from these figures, the gap size of 25 nm could be achieved by dose modification; however, for the gap size of 6 nm, there was overlapped region on the two facing tips of the bowtie even after modification. This overlap was attributed to the electron dispersion length which was larger than the gap size.

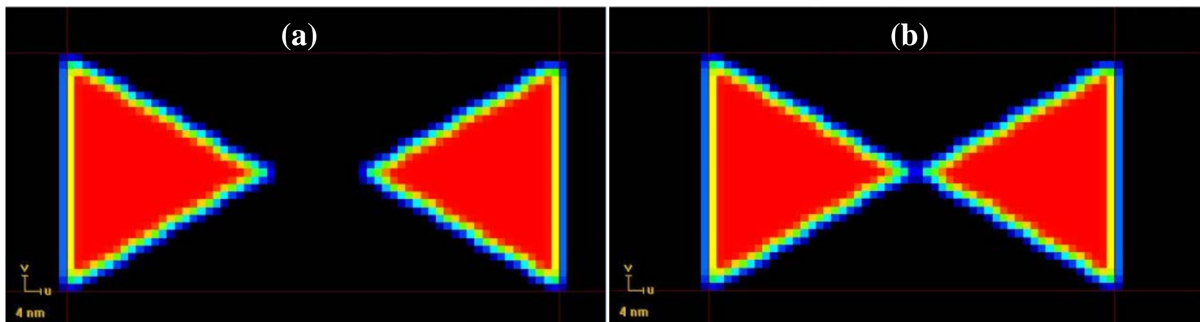

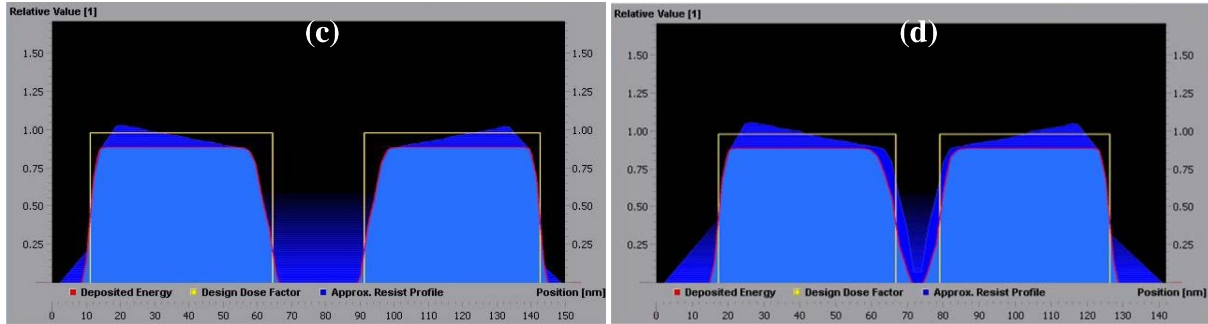

Figure 5.10 Top view of dose distribution of bowtie patterns on bulk wafer with the gap size of (a) 25 nm, (b) 6 nm. Cross-sectional view of proximity effects on bowtie with the gap size of (c) 25 nm, (d) 6 nm.

5.5.2. Bowtie nano-antenna fabrication

A 4 inch silicon wafer with 150 nm Si_3N_4 on both sides was used as substrate. Photolithography was carried out on the backside of the substrate. The un-patterned area of Si_3N_4 was developed and removed by using CF_4 reactive ion etching (RIE) (Fig. 5.11 step (a)). The nitride membrane was first fabricated using wet chemical etching with hot KOH solution that etches silicon anisotropically at a rate of ~1 μm/min with negligible etching of the nitride film (Fig. 5.11 step (b)).

Next, the top surface of the membrane was cleaned by O_2 plasma, and a 100 nm PMMA layer as the resist and 10 nm Cr as the conductive charge dissipation layer were coated by spin-coating and electron beam evaporation, respectively (Fig. 5.11 step (c)). EBL was carried out using Raith 150^{TWO} system at 20 kV acceleration voltage and 0.33 nA beam current. The conductive layer was removed after exposure and the pattern was developed using methyl isobutyl ketone (MIBK): 2-propanol (IPA) = 1:3 and rinsed by fresh IPA (Fig. 5.11 step (d)).

Finally, 1 nm Cr as the adhesive layer and a 25 nm gold or silver were deposited by e-beam evaporation (Fig. 5.11 step (e)). The metal film was deposited at rate of 0.2 Å/s to reduce the surface roughness. The sample was soaked in anisole for several hours to liftoff the metal (Fig. 5.11 step (f)).

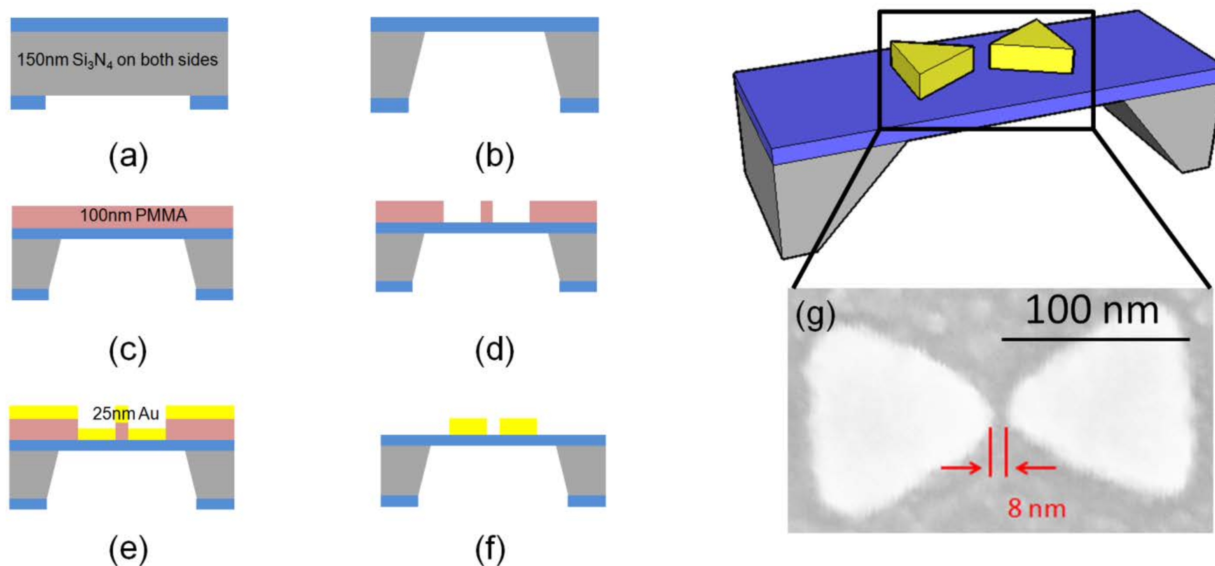

Figure 5.11 Schematic of the fabrication process of bowtie nano-antenna on Si_3N_4 membrane: (a) photolithography on backside Si_3N_4 and CF_4 reactive ion etching to remove the unpatterned Si_3N_4; (b) Si wet etch in KOH solution to form Si_3N_4 membrane; (c) spin-coating 100 nm PMMA layer and deposition 10 nm Cr for EBL; (d) e-beam lithography of bowtie array and development; (e) evaporation of 1nm Cr and 25nm Au or Ag; (f) liftoff in anisole and rinse the surface; (g) illustration of the final bowtie structure on Si_3N_4 membrane and SEM image of fabricated bowtie structure with gap size of 8 nm as an example of the fabricated structure.

Fig. 5.12a shows the SEM image of bowtie patterns with 6 nm gap exposed on bulk Si substrate. The gaps in bowties are exposed because of the proximity effect even after dose modification by NanoPECS. This kind of connected bowtie structure shown in Fig. 5.13 does not possess “hotpots”, shown in Fig. 5.13.

In contrast, Fig. 5.12b shows that bowtie nano-antenna with varied gaps from 3 nm to 25 nm could be fabricated on membrane. Considering the beam size of about 5 nm, the proximity effect was eliminated totally. The narrowest gap was obtained as 3 nm, though for this size the gap was not uniform with many gaps connected. Larger gaps were more uniform and reproducible. Both of the Au and Ag bowtie with narrow gap were achieved, as shown in Fig. 5.12c&d.

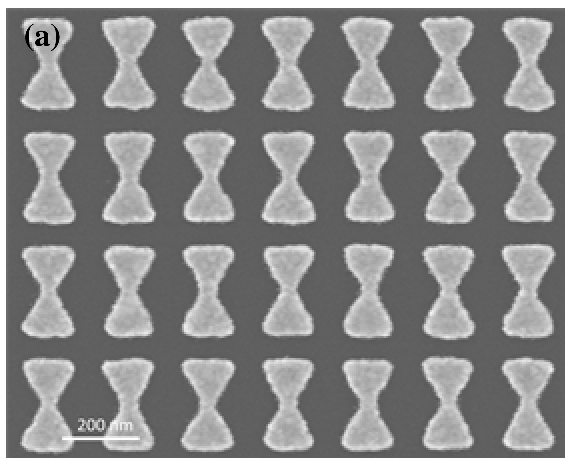

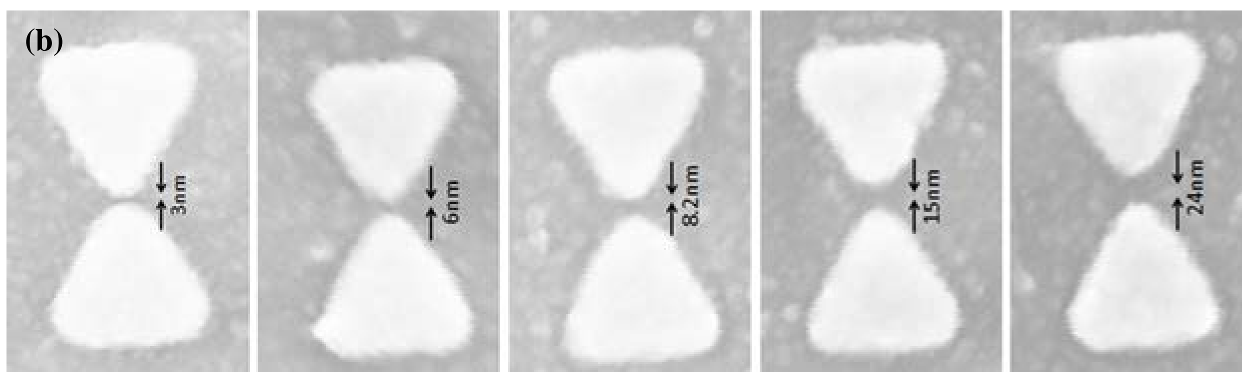

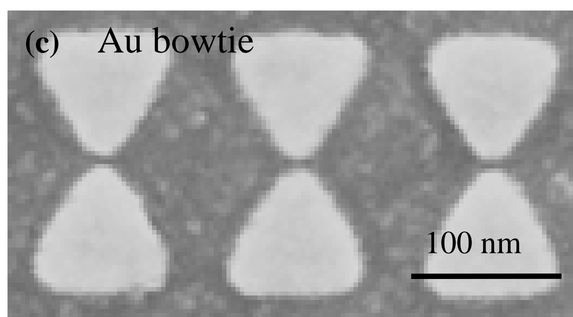

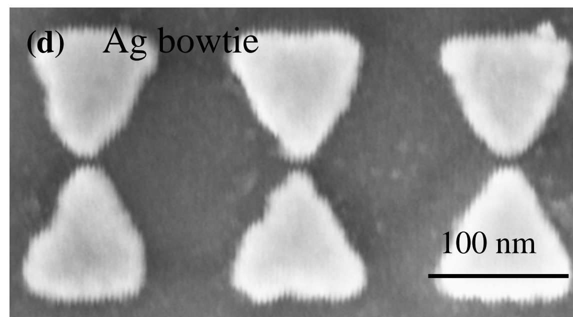

Figure 5.12 (a) SEM image of bowtie array exposed on Si wafer; (b) SEM image of bowtie array exposed on Si_3N_4 membrane, with the varied gap size from 3 nm to 24 nm. d) SEM image of gold bowtie array with 6 nm gap. (e) SEM image of silver bowtie array with 6 nm gap.

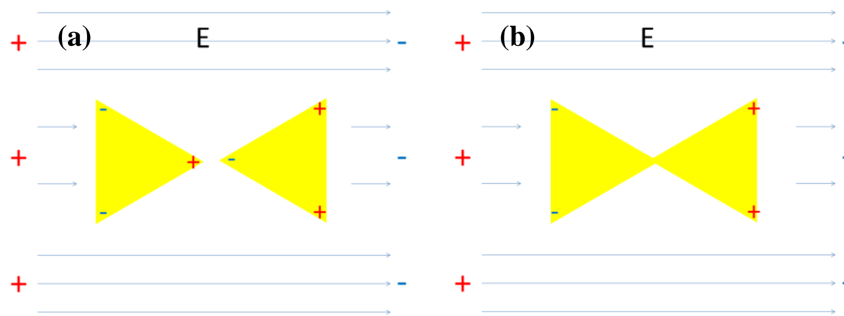

Figure 5.13 Corresponding electric field in bowtie pattern with (a) nano-gap and (b) connection.

5.6. Bowtie-shape nano-antenna for SERS sensors

5.6.1. The advantages of bowtie-shape nano-antenna in SERS

In this research, bowtie shape was selected for SERS applications. There are several advantages for bowtie-shape sensors:

(1) The gap size affects the enhancement factor sensitively since with certain wavelength the hotspots exist within the gap area. The gap size, shape, and sharpness, can be studied systematically based on bowtie antenna. Compared with gap-shape antenna, tip-shape antenna is also considered in SERS study. For tip-shape antenna, since the sharpness of the tips is very important, many reasons besides EBL resolution will affect the enhancement. For example, the grain size of the noble metal will changed greatly when the temperature and evaporation rate varies. And smaller grain size is more desirable for smooth metal film and sharp structure. So gap-shape antenna such as bowtie is more robust for SERS application.

(2) The enhancement based on bowtie-shape antenna is generated from electric dipole, compared with the enhancement generated from single point in tip-shape antenna. So the enhancement factor will be higher in bowtie with the same experimental condition.

5.6.2. Numerical modeling

The electrical near field profile in gold bowtie nano-antenna was simulated using the 3D full wavevector finite difference time domain (FDTD) method, which is a reliable technique in solving Maxwell's equations in dispersive media. Each media was specified by a relative permittivity $\varepsilon(\omega)$. For the substrate layer permittivity was assumed as n^2, and for the gold layer the Lorentz-Drude model was utilized to describe its permittivity.[156,157] The FDTD was carried out using the Lumerical FDTD from Lumerical Solutions, Inc. The planewave source, sub-wavelength hole and monitors were co-planar with boundary conditions that made them effectively infinite. In this study, a plane wave of linearly polarized light along Y-axis (λ_{centre}=680 nm, time offset of 0.8×10^{-14} s and half width of 0.1×10^{-14} s) which propagates along Z-axis was used. The simulation background was taken as air (n=1.0). The gap in the bowtie structure was varied in the range of 6 nm to 25 nm. Metal film with 25 nm thickness was selected corresponding to the fabrication process. The simulation cell was considered as 400×400×400 nm^3 and the periodic boundary condition (PBC) was used in the X- and Y- directions. Anisotropic perfect matching layer (APML) was used in the Z-direction as absorbing boundary condition. The calculation grid resolution was as high as 5 nm (grid point-to-point distance) in the simulation cell. The calculation time was set as 100 fs, with calculation step size of 0.00834 fs for a total of about 12000 time steps per simulation. The transmission spectra were calculated using an X-Y monitor at 150 nm away from the bowtie nano-antenna surface as it is shown in Fig.5.14.

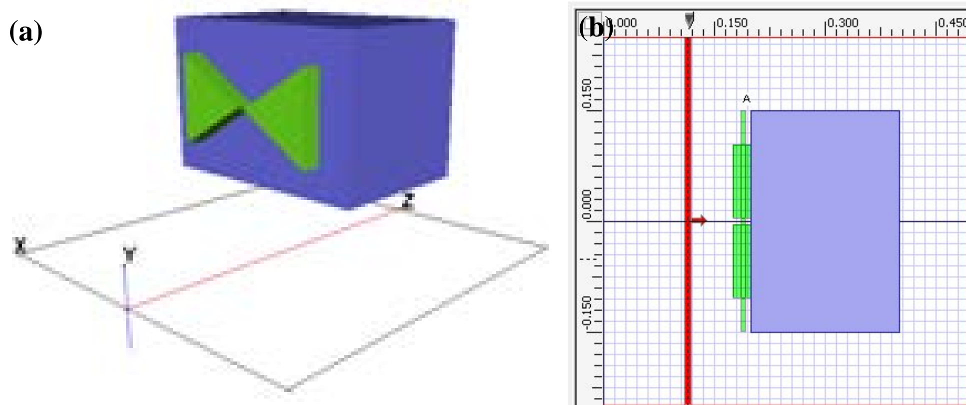

Figure 5.14 Schematic of the simulated bowtie structure with 25 nm thickness on 150 nm Si_3N_4 membrane in (a) 3D view and (b) cross-sectional view at bowtie centre on x/z plane.

5.6.3. Surface enhanced Raman spectroscopy (SERS) measurement

The Raman spectrum was recorded by using Bruker Senterra Raman spectrometer equipped with confocal microscope and a nitrogen-cooled multichannel CCD detector. A He-Ne laser with wavelength of 632.8 nm and a diode laser with wavelength of 785 nm were used as the excitation sources. The light source was focused on the sample using a 100× objective lens to obtain a spot size of ~4 μm^2, and the acquisition time was set as 100 s. The laser power was chosen as low as 1 mW to avoid burning effect and surface carbonization of the adsorbed organic molecules.

1,2-di(4-pyridyl)ethylene (BPE) (Sigma-Aldrich), of which the chemical structure and Raman spectrum are shown in Fig 5.15, was selected as the molecule to be detected. A BPE solution in ethanol with the concentration of 100 mM was diluted to a series of different concentrations in the range of 10^{-1} to 10^{-6} mM. The diluted solution was dropped on the bowtie nano-antenna samples and dried at room temperature before each experiment. It was found that a brief O_2 plasma cleaning of Au bowtie nano-antenna structures led to more reproducible Raman measurement, whereas the same surface treatment led to very poor results for Ag bowtie structures. Hence the Au bowtie structure was cleaned by O_2 plasma right before BPE application.

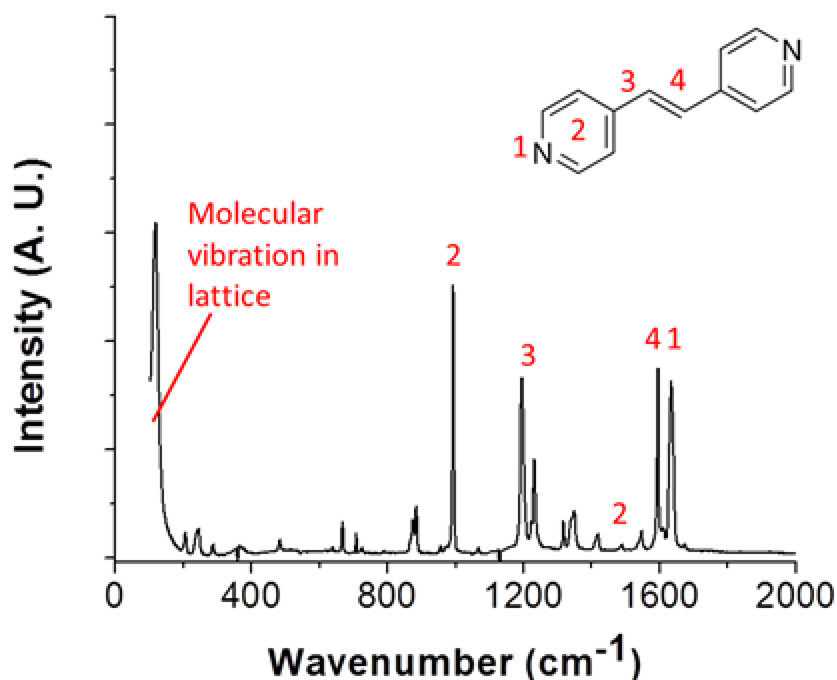

Figure 5.15 Molecular structure of 1,2-di(4-pyridyl)ethylene (BPE) and its Raman spectroscopy.

5.7. Results and discussion

5.7.1. Numerical analysis

Fig. 5.16a shows the FDTD calculated electric field profile, $|E|^2$, of gold bowtie of gap size of 8 nm at excitation wavelength of 785 nm. As can be seen from this figure the electric field was highly confined in the gap area. It was also found that on changing the excitation wavelength from 785 nm to 632.8 nm, the electric field confinement in the gap area was eliminated and more electric field propagation was observed on the triangles sides of the bowtie structures as it is clear from Fig. 5.16b. This indicates that 785 nm is close to the wavelength for the surface plasmon resonance at the gap of the gold bowtie. Also, longer wavelength is preferred to reduce the background fluorescence effects during exposure of organic sample.

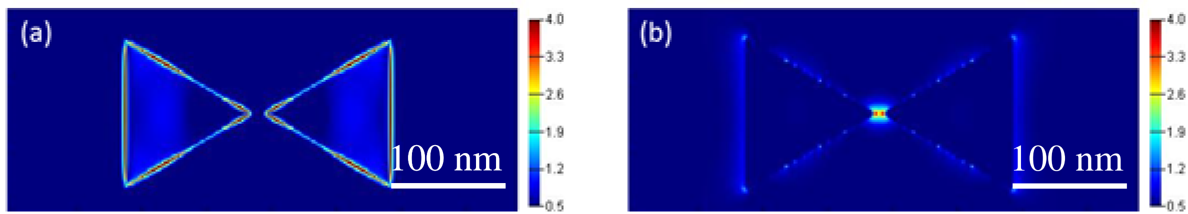

Figure 5.16 FDTD calculated electric field intensity , $|E|^2$, on gold bowtie structure with 8 nm gap illuminated by excitation wavelength of (a) 632.8 nm and (b) 785 nm.

Fig. 5.17 shows the FDTD calculated 3D electric field intensity,$|E|^2$, of both gold and silver bowtie nano-antenna at excitation wavelengths of 785 nm with the gap size of 8 nm. The later experiment conforms that the maximum obtained electric field enhancement for the gold and silver bowtie at wavelength of 785 nm was 10^7 and 10^8, respectively.

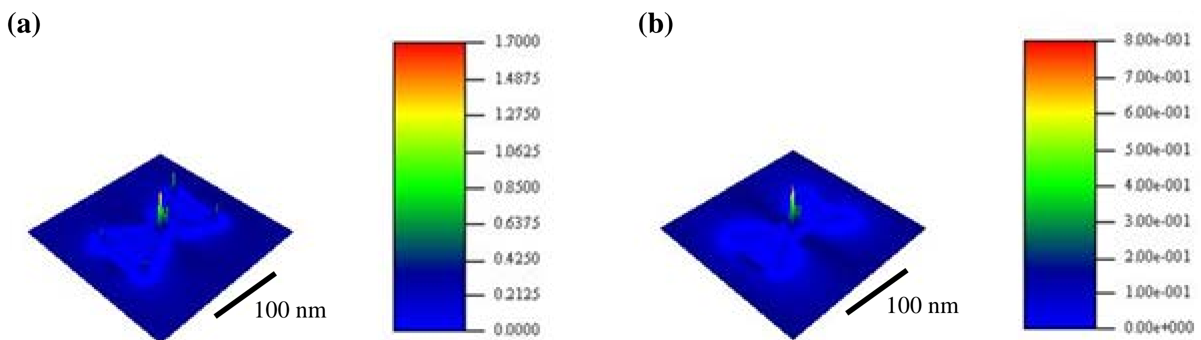

Figure 5.17 FDTD simulations of the electrical field intensity $|E|^2$ on the (a) gold and (b) silver bowtie.

5.7.2. SERS chemical sensors

Nobel metals such as gold and silver are usually employed in SERS applications because of their inert activity, absorbability to amino/thiol group, low energy absorption and high reflectivity in the visible range of electromagnetic field.[158] It is more interesting to use gold than silver due to the higher stability of gold nanostructure in atmosphere conditions and recycling by O_2 plasma cleaning, whereas silver bowtie nano-antenna is not stable in atmospheric conditions.

A series of bowtie nano-antenna structures with different periods in the range of 550 nm to 1000 nm with step of 150 nm were fabricated to study the impact of bowtie density on the SERS signal enhancement. The effects of varying structural periodicity on the Raman signal intensity of the gold bowtie nano-antenna of gap size of 6 nm is shown in Fig.5.18a. As it is clear in Fig.5.18b, on reducing the periodicity from 1000 nm to 550 nm the recoded Raman intensity at wavenumber of 1610 cm^{-1} (i.e. C=N bond) increased linearly, and bowtie array of 6 nm gap and 1000 nm period can still support a large Raman signal.

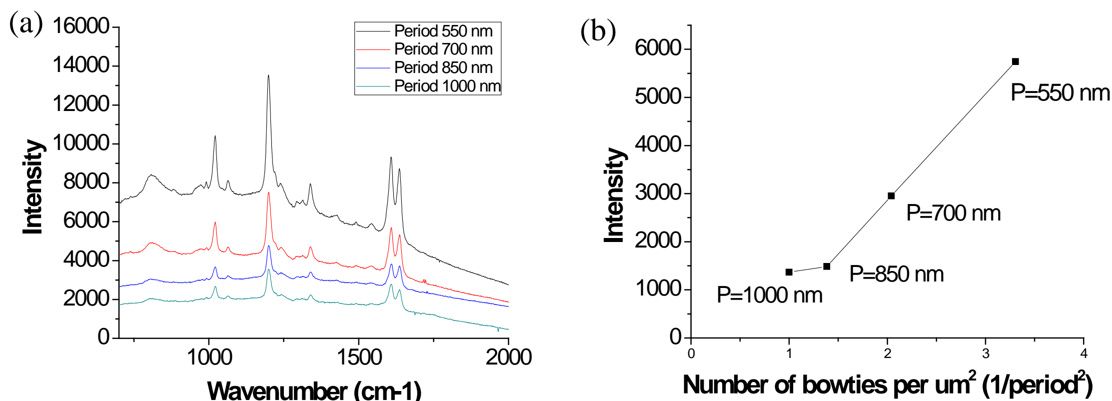

Figure 5.18 (a) Recorded SERS Raman signal of 0.1 mM BPE from bowtie array of a) gap size of 6 nm and different period in the range of 550 nm to 1000 nm, (b)The relationship between recorded Raman intensity of C=N bond and the bowtie period.

The effects of varying the gap size and excitation wavelength on the recorded SERS signal are compared in Fig. 5.19a&b. As it is clear from Fig. 5.19a, in case of using excitation wavelength of 785 nm, on reducing the gap size from 25 nm to 6 nm, Raman intensity of BPE molecules was increased by up to two orders of magnitude. However, in case of using the excitation wavelength of 632.8 nm, there was no significant changes in the Raman intensity of BPE molecules in the bowtie nano-antenna structures with different gap sizes.

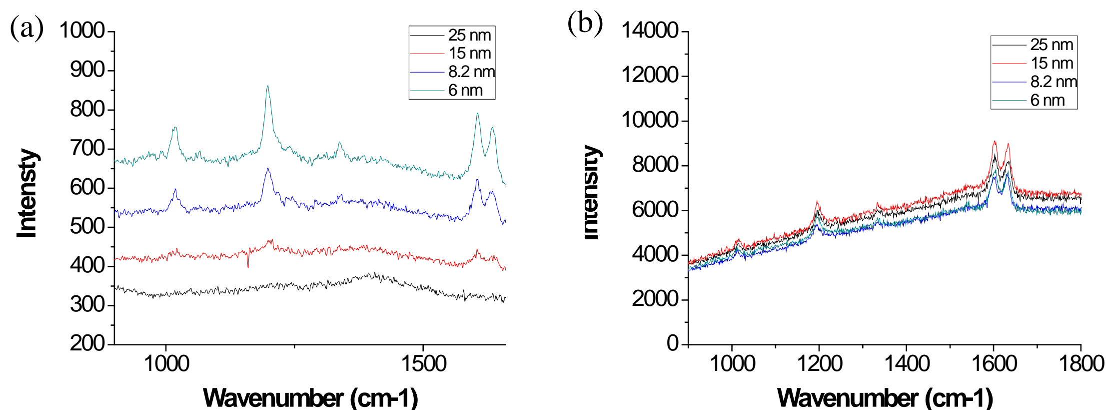

Figure 5.19 Recorded SERS Raman signal of 0.1 mM BPE from bowtie array of (a) period of 550 nm, excitation wavelength of 785 nm and different gap size, and (b) period of 550 nm, excitation wavelength of 632.8 nm and different gap sizes.

The effects of varying the BPE concentration on the recorded Raman signal at wavenumber of 1610 cm^{-1} (i.e. C=N bond) of gold and silver bowtie of different gap sizes at excitation wavelength of 785 nm are compared in Fig.5.20. As it is clear from this figure, the recorded sensitivity of C=N bond was reduced on reducing the concentration of BPE for both gold and silver bowties. Below 10^{-1} mM BPE, Raman signal of silver bowtie nano-antenna was recorded larger than that of gold bowtie nano-antenna of same gap size. Based on Fig. 5.20, the EF enhancement of the gold bowtie with 8 nm gap was achieved at 10^{7} with the BPE concentration of 10^{-5}; whereas the EF enhancement of silver bowtie was achieved at 10^{8} with the BPE concentration of 10^{-6}. Silver owns higher SERS enhancement because of its larger $|\varepsilon_1|$ and smaller $|\varepsilon_2|$. The non-ideal vibration of the decreasing Raman intensity from silver bowtie might be due to higher roughness of the silver film surface compared to gold one which leads to more absorption of target molecules, as compared in Fig. 5.12c-d. For the highest BPE concentration of 10^{-1} mM, the Raman intensity of Au bowtie is abnormally higher than the silver one, which is probably because of the uncontrolled agglomeration of BPE.

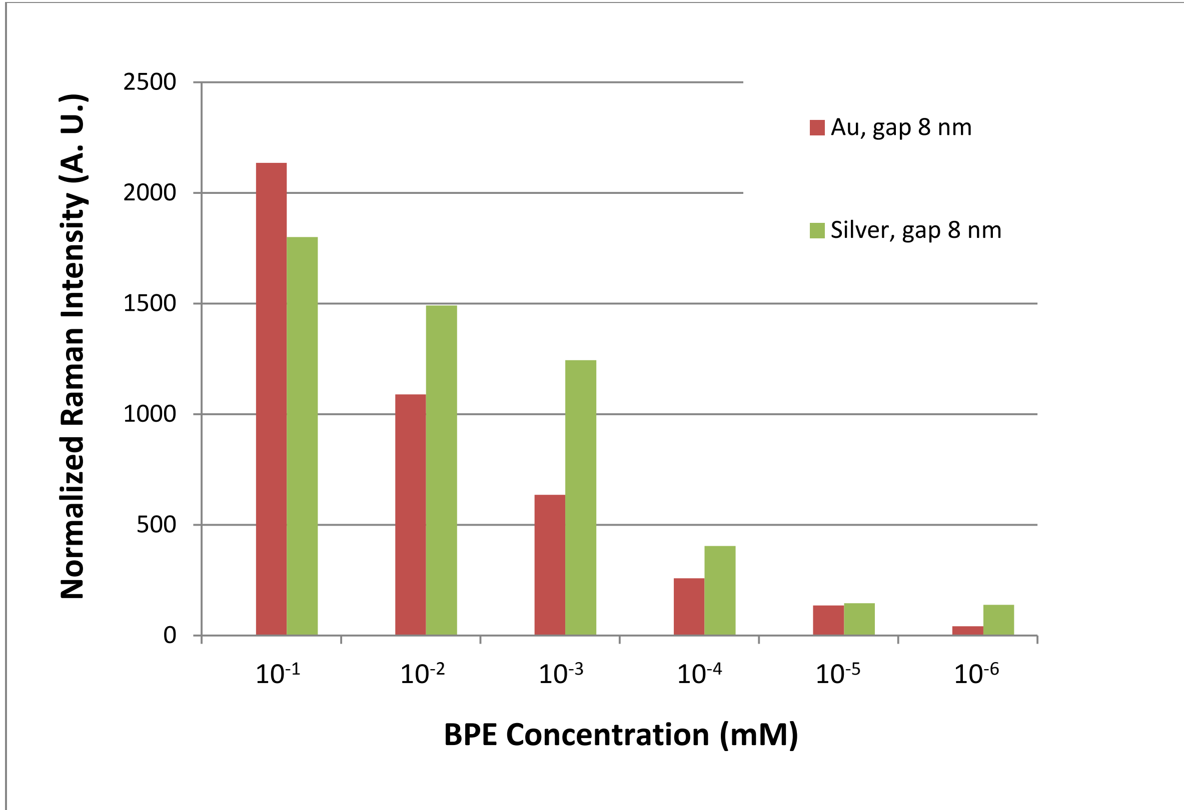

Figure 5.20 Recorded Raman intensity of C=N bond from gold and silver bowtie nano-antenna with 8 nm gap, period of 550 and excitation wavelength of 785 nm for gold and silver bowtie nano-antenna.

From Fig. 5.20, it is clear that the sensitivity of gold bowtie nano-antenna at BPE concentration of 10^{-6} mM and lower was recorded as nearly zero at excitation wavelength of 785 nm, however, the silver bowtie nano-antenna of the same small gap size was still sensitive to diluted BPE solution as high as 10^{-6} mM at excitation wavelength of 785 nm.

The enhancement factor (EF) is one of the most important parameters in SERS application which is given by:[159]

$$EF = \frac{I_{SERS}}{I_{CON}} \frac{M_{CON} \cdot A_{CON}}{M_{SERS} \cdot A_{SERS}} \qquad (5.20)$$

where I_{SERS}, I_{CON}, M_{SERS} and M_{CON} are the measured Raman intensities of the SERS sample and the reference samples, the molar concentration of the SERS sample and reference samples, respectively, A_{SERS} is the actual normalized area of the gold pattern and A_{CON} is the reference

area which is 1 μm^2 in this work. Since in the bowtie nano-antenna the hotspot only exists within the area of several nanometers around the gaps, the actual effective area is much smaller than the whole bowtie area and hence the corresponding EF is much larger than calculated one.

Raman spectroscopy is a simple way to direct understanding of the enhancement change affected by varied bowties structures. The gap size plays an important role in the enhancement of SERS. Fig. 5.21a show the Raman spectra of bowtie nano-antenna of gap size of 6 nm at different BPE concentrations in the range of 10^{-1} to 10^{-6} mM. It was found that the bowtie nano-antenna of gap size of 6 nm achieved at EF of 10^7 at BPE concentration of 10^{-5} mM. Whereas on using nano-antenna of gap size of 25 nm, the highest sensitivity was recorded at BPE concentration of 10^{-3} mM with an EF of 10^5 as shown in Fig. 5.21b. This confirms that the hotspots are only obtained in nano gap between facing tips of the bowtie structure and the amplitude of the local electric field was significantly increased by reducing the gap size, which is in good agreement with numerical results.

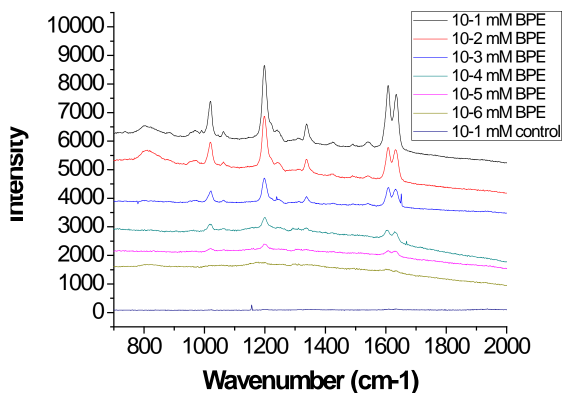

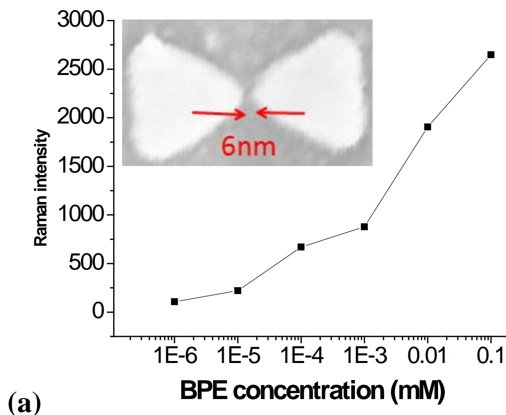

(a)

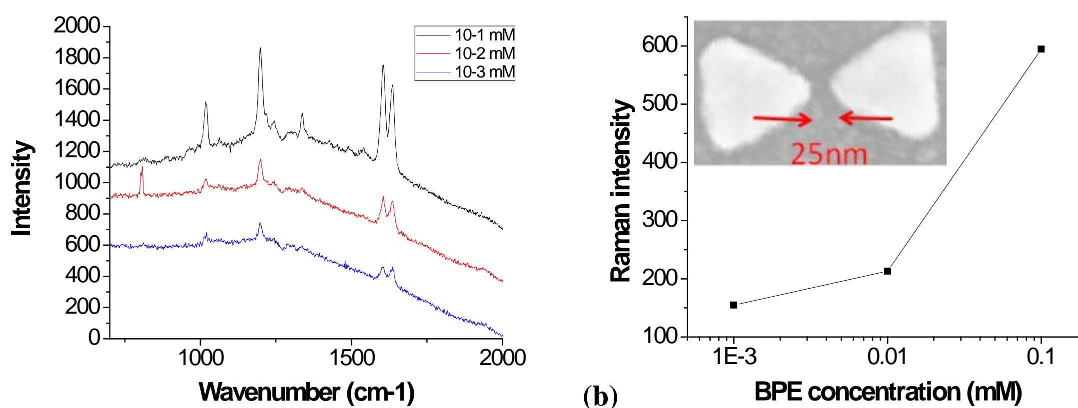

Figure 5.21 Comparison of SERS spectra of BPE with varied concentration from 10^{-1} mM to 10^{-6} mM on bowtie array with (a) 6 nm gap and (b) 25 nm gap.

5.8. Conclusion

An efficient method was developed to achieve large-area electron beam lithography with a breakthrough of the resolution from 10s nm to 3 nm. A bowtie nano-antenna structure of sub-10 nm gap was fabricated and SERS measurements were carried out. The effect of different structures including different gap sizes, different period, different metals and different excitation wavelengths on the SERS performance were studied experimentally and numerically. On using excitation wavelength of 785 nm, the SERS signal intensity shows a strong dependence on the gap size, which proves the localized hotspots and confirmed by numerical analysis. Different BPE concentrations were used for SERS measurements. It was shown that silver bowtie nano-antenna performs higher sensitivity than gold one as was confirmed by FDTD calculation. However, on using the excitation wavelength of 633 nm, the electric field profile scatters along the triangle edges which reduces the SERS signal intensity.

Chapter 6

Extraordinary optical transmission (EOT) for chemical and bio-sensors

6.1. Introduction to existing sensors based on propagating SP

The SP momentum ($\hbar k_{SP}$) is always greater than a free-space photon ($\hbar k_0$) of the same frequency ω. So the SP mode is always lying beyond the light line, leading to the challenge of coupling light and SP modes together. By providing an additional momentum, SPs become electromagnetic waves that can propagate along the metal/dielectric interface. To excite propagative SP mode, different methods are developed to provide this additional momentum.

6.1.1. Kretschmann configuration of attenuated total reflection (ATR)

Most of the commercial SPR sensors use the so-called Kretschmann configuration, where a prism with high refractive index is employed to excite SPR by attenuated total reflection (ATR) (see Fig. 6.1(left)).[160] This method including a phase-matching mechanism which can be achieved by a sandwich structure consisting of a thin metal layer and two insulating layers of different dielectric constants (ε). Normally, one of the insulating layers is air and its dielectric constants is 1. An incident beam from prism side is reflected on the interface between the metal and insulator of higher dielectric constants with in-plant momentum $k_x = k\sqrt{\varepsilon}\sin\theta$. Obviously,

this wave vector is higher than the incident light from air side, so it is sufficient to excite SP polarization at the metal/air interface. Thus such prism can overcome the momentum mismatch between air and metal/air interface. The difference between wave vectors of air, prism, metal/air interface and metal/prism interface is shown in Fig. 6.2. The value of the wave vector in prism crosses the one on metal/air interface which proves that SP resonance can be excited by ATR in prism.

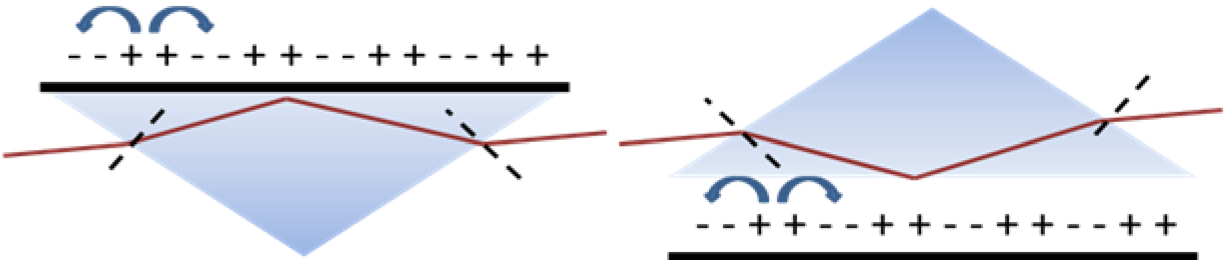

Figure 6.1 Prism coupling to surface plasmon polarizations (SPPs) using attenuated total internal reflection in the Kretshmann (left) and Otto (right) configuration.

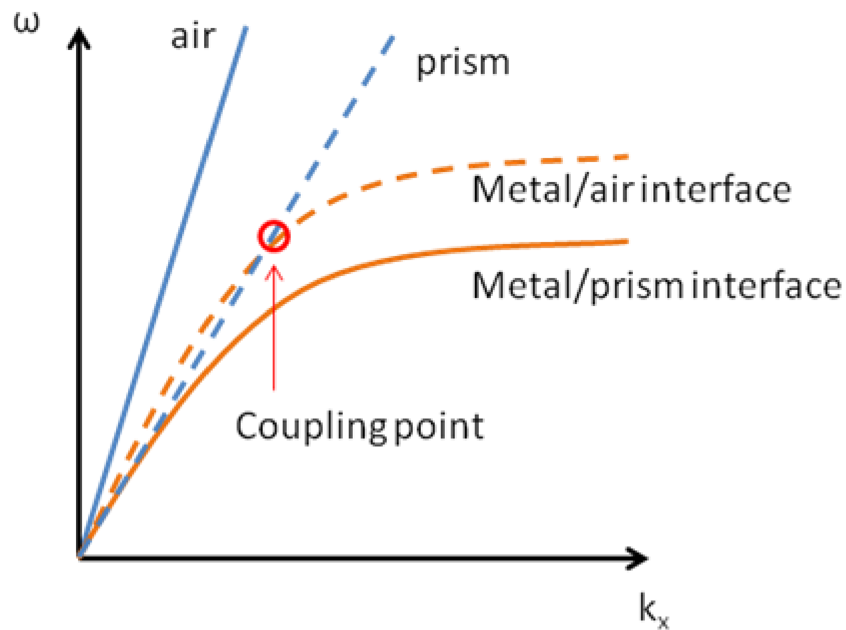

Figure 6.2 Prism coupling and SPP dispersion.

Similar to Kretschmann configuration,[161] another method of prism coupling is Otto configuration.[162] The metal and prism surface is separated by an air gap. Total internal reflection occurs at prism/air interface, exciting and coupling with the SP polarizations on air/metal interface. Compared to Kretschmann configuration, which is the commercially employed, this method is preferred only when direct contact between metal layer and target molecules is not desirable. And the gap needs to be controlled exactly.

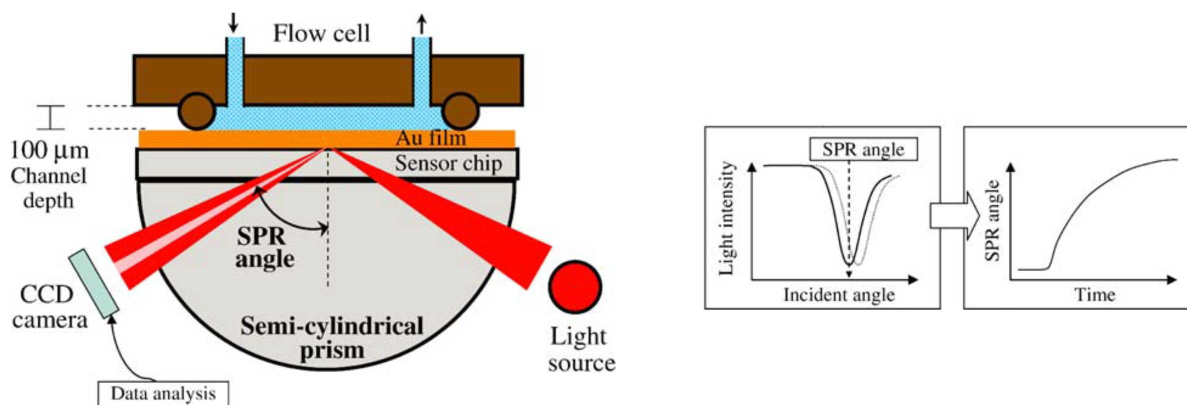

Figure 6.3 (left) Schematic of the commercial SPR device with Kretschmann configuration; (right) surface plasma resonance curves of silver film and the same film coated with a monolayer of p-4-BCMU. Copyright 2007 by the Springer.

In commercial SPR device of Kretschmann configuration (see in Fig. 6.3), a p-polarized laser beam is incident into one side of prism. A microscope is set on the other side to monitor the total reflection angle (θ_{SP}). The electromagnetic field will couple with SP on the interface at certain θ_{SP}, exciting an evanescent field propagating along the interface. At the same time, the ATR signal drops. Prasad firstly published the work of SPR and showed the dip in the curve of reflectivity.[163] The relationship for the wave vector SPs (k_{SP}), the wave vector of incident wave (k), the refractive index of the prism (n_p) and θ_{SP} is expressed as:

$$k_{SP} = kn_p \sin\theta_{SP} \qquad (6.1)$$

And the wave vector of SPs (k_{SP}) is already expressed in Equation (4.13):

$$k_x = \frac{\omega}{c}(\frac{\varepsilon_1\varepsilon_2}{\varepsilon_1 + \varepsilon_2})^{1/2} \qquad (4.13)$$

Based on this, the change of dielectric constant of dielectric layer can be calculated for further inspection. In Kretschmann configuration, the angle shifts after SPR coupling is utilized for sensing target molecule.[164]

6.1.2. Grating coupling

Periodic nanostructures such as grating[165-168] and holes (2D gratings)[169,170] can also offer additional momentum for SP polarization. Take grating for example, the lattice constant *a* is equal to the period, and the additional momentum is expressed as:

$$|\boldsymbol{k}_{grating}| = \frac{2\pi}{a} \qquad (6.2)$$

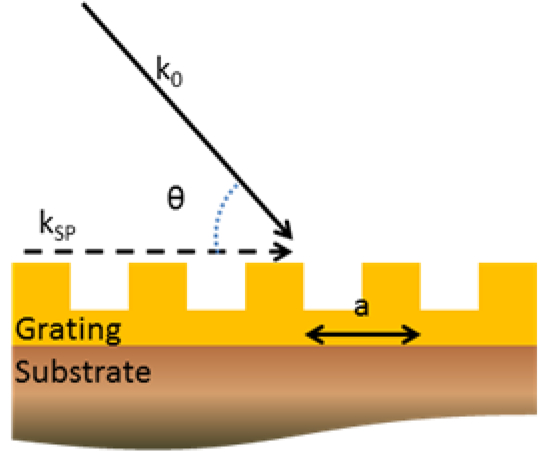

Figure 6.4 Phase-matching of light to SPPs using a grating.

The mismatch between k_{SP} and k_0 can be overcome by:

$$\boldsymbol{k}_{SP} = \boldsymbol{k}_0 + n\boldsymbol{k}_{grating} \qquad (6.3)$$

where θ is incident angle, $|\boldsymbol{k}_0| = \frac{2\pi}{\lambda}$ and $n = (\pm1, \pm2, \pm3 \ldots)$.

Considering the diffraction in 3D condition, Equation 6.3 can be expressed as:

$$\boldsymbol{k}_{SP} = \boldsymbol{k}_0 + n\boldsymbol{k}_{grating} = \begin{pmatrix} k_x \\ 0 \\ k_z \end{pmatrix} + \begin{pmatrix} n\frac{2\pi}{a} \\ 0 \\ 0 \end{pmatrix} \qquad (6.4)$$

Since $k_x = |\boldsymbol{k}_0|cos\theta$, θ is the incident angle and k_z is the imaginary part, the relation between $\boldsymbol{k}_{SP}$ and θ can be expressed as:

$$|\boldsymbol{k}_{SP}|^2 - (|\boldsymbol{k}_0|cos\theta + n\frac{2\pi}{a})^2 = k_z^2 < 0 \qquad (6.5)$$

The imaginary part of k_z approaches to zero at the angle θ_{SP} given by:

$$k_{SP} = k_0 cos\theta_{SP} + n\frac{2\pi}{a} \qquad (6.6)$$

6.1.3. Surface plasmonic waveguide

Unlike planar propagation in planar metal/insulator (M/I) or insulator /metal/ insulator (I/M/I) interfaces, structured metals such as stripe, groove, wire and metal dot array, can route SPs in 1D direction, resulting surface plasmonic waveguide. By adjusting the geometries of metal structures, the lateral dispersion of SP propagation can be confined properly. The first kind of SP waveguide is 2D nano-structure array. SP propagation can be achieved by reflection via structures like Bragg mirrors[81,171,172] or focus via lateral confinement[173,174]. Different from the first SP waveguide, the second kind of SP waveguide is based on the structures of I/M/I multi layers with $w \ll l$.[175-177] Specially, when $w < \lambda_0$, the SP waveguide is considered as nanowire type.[178-180]

Considering the propagation of SP following *z* direction within a dielectric waveguide of ε_{core} at core and $\varepsilon_{cladding}$ at cladding, the phase constant β, wave vector k_x , k_y , and the angular frequency ω should satisfy:

$$\beta^2 + k_x^2 + k_y^2 = \varepsilon_{core}\frac{\omega^2}{c^2} \qquad (6.7)$$

For metal nanowire $\varepsilon_{core} < 0$ in visible and near-infrared wavelength, so at least one of k_x and k_y must be imaginary. This means that SP propagation can be realized.

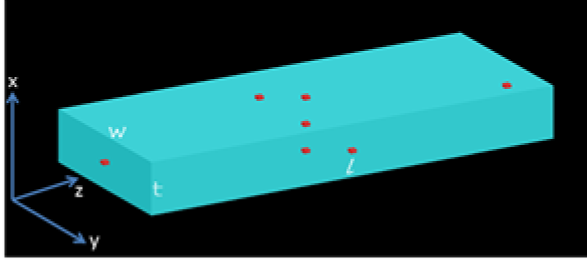

Figure 6.5 Schematic of a symmetric waveguide with width w, thickness t and length l, where $l >> w, t$.

6.2. Extraordinary optical transmission (EOT)

In 1998, T. W. Ebbesen found that the coupling of light with SPs also happens in transmission instead of reflection,[87] in contrast with previous work on SPs in Section 1.1-13. This strong enhancement of transmitted light can be one order higher than predicted by Bethe's theory (see Equation 6.8), by the contribution from the coupling of the light with the SP of the two-dimensional array of sub-wavelength holes (see Fig. 6.6, hole diameter << wavelength).

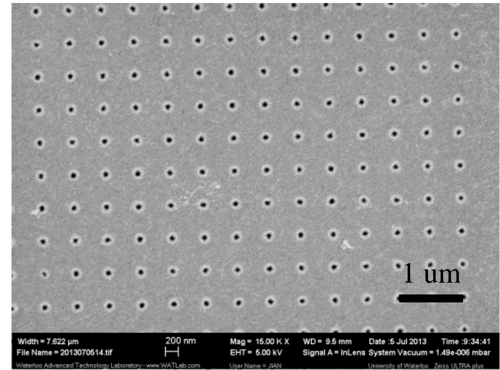

Figure 6.6 SEM image of EOT-based SPR biosensor. Here 500 nm period hole array with the diameter of 150 nm in 100nm-thick Au film is fabricated by EBL and liftoff.

$$\eta_B = \frac{64(kd)^4}{27\pi^2} \qquad (6.8)$$

where $k = \frac{2\pi}{\lambda}$, η_B is the transmission efficiency, and d is the diameter of the nano-hole.

Similar to SP in grating, the matching for the wave vector of SPs (k_{SP}) and the wave vector of incident wave (k_0) can be achieved by:

$$\boldsymbol{k}_{SP} = \boldsymbol{k}_0 \pm i\boldsymbol{G}_x \pm j\boldsymbol{G}_y \qquad (6.9)$$

where $\boldsymbol{G}_x$ and $\boldsymbol{G}_y$ are lattice vectors in x and y direction[87]. For the condition of 2D dot array in square lattice with period P, $|\boldsymbol{G}_x| = |\boldsymbol{G}_y| = \frac{2\pi}{P}$, and the peak for surface plasmonic enhancement can be estimated as:

$$\lambda_{max} = \frac{P}{\sqrt{(i^2 + j^2)}}\sqrt{\frac{\varepsilon_m \varepsilon_d}{\varepsilon_m + \varepsilon_d}} \qquad (6.10)$$

where *i, j* is the integers, and ε_m, ε_d are the dielectric constant for metal and the dielectric material, respectively.

Unlike slits, no direct transmission mode exists for sub-wavelength holes, and light has to pass through the holes through "tunneling" of which the amplitude decays exponentially. Different from aforementioned prism- or grating-coupled SPR, in EOT the disturbance from light and the environment from incident side can be minimized. EOT spectrum is extremely sensitive to the dielectric environment near the metal surface, thus it can be used as bio-sensor. Fig. 6.7 shows one typical EOT device for bio-sensor.[181] EOT cannot be simply attributed to interference effect for that this repeated sub-wavelength structures enable much higher transmission efficiency to occur, up to several orders of magnitude greater than that predicted by classical aperture theory.

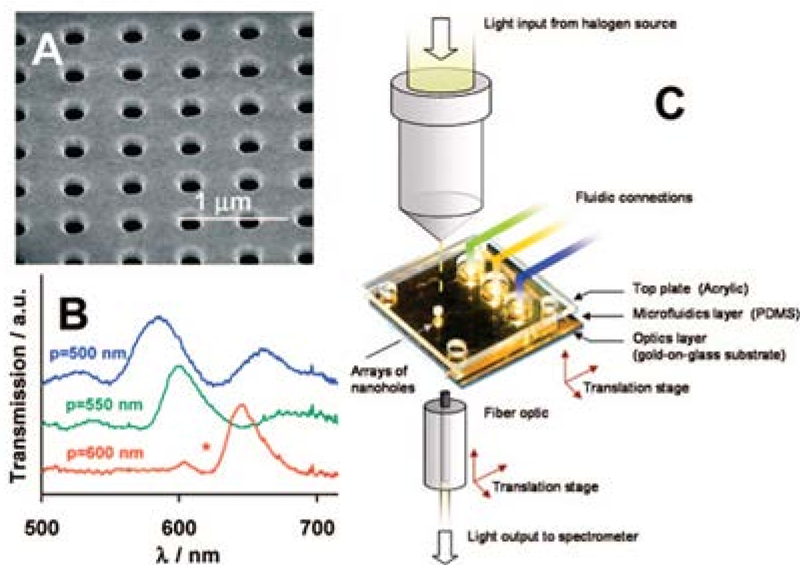

Figure 6.7 (A) SEM image of an array of nano-holes in a gold film. (B) EOT spectra for three hoe arrays with different periodicities. (C) Schematic of EOT device. Copyright 2008 by the American Chemical Society.

Compared to sensors based on Kretshmann configuration, advantages of EOT bio-sensor includes: 1) transmission mode operation at normal incidence makes low cost portable tools possible; 2) the footprint of EOT device, i.e. the area covered by the hole array, can be as small as ~5 μm, over one order smaller than that for prism-coupled SPR sensor (~200 μm), enabling detection of thousands of targets in the same chip without sacrifice of sensitivity; (Note: in principle, a prism-coupled SPR sensor is also capable of parallel detection, but at the expense of sensitivity due to the optical constrains at non-normal incidence); 3) the intrinsic sensitivity, in term of resonant wavelength shift/mass of attached biomaterial over device area (nm/pg), is 2-3 orders higher, again due to its much smaller device area, thus making trace amount detection possible; 4) the non-contact optical measurement obviates the need for a prism and index-matching fluids, and greatly facilitates high-resolution imaging for highly parallel arrayed measurement.

6.3. Nanofabrication techniques for EOT structures

Up to now almost all EOT devices were fabricated by focused ion beam (FIB) milling of nano holes array (NHA) into the metal film because: 1) it is rather straightforward to mill nano-holes into a metal film by a focused energetic beam; 2) it is challenging to pattern noble metal by lithography plus reactive ion etching because metal is difficult to etch; 3) it is also challenging to fabricate the device by liftoff because the film is too thick for ordinary liftoff process. However, the throughput of FIB is extremely low, taking months to pattern a nano-hole array over a 4" wafer. Here, several novel techniques were developed and examined in the application of EOT sensors.

6.3.1. Nano-hole array (NHA) fabrication through double liftoff process and its characterization

6.3.1.1. Fabrication process

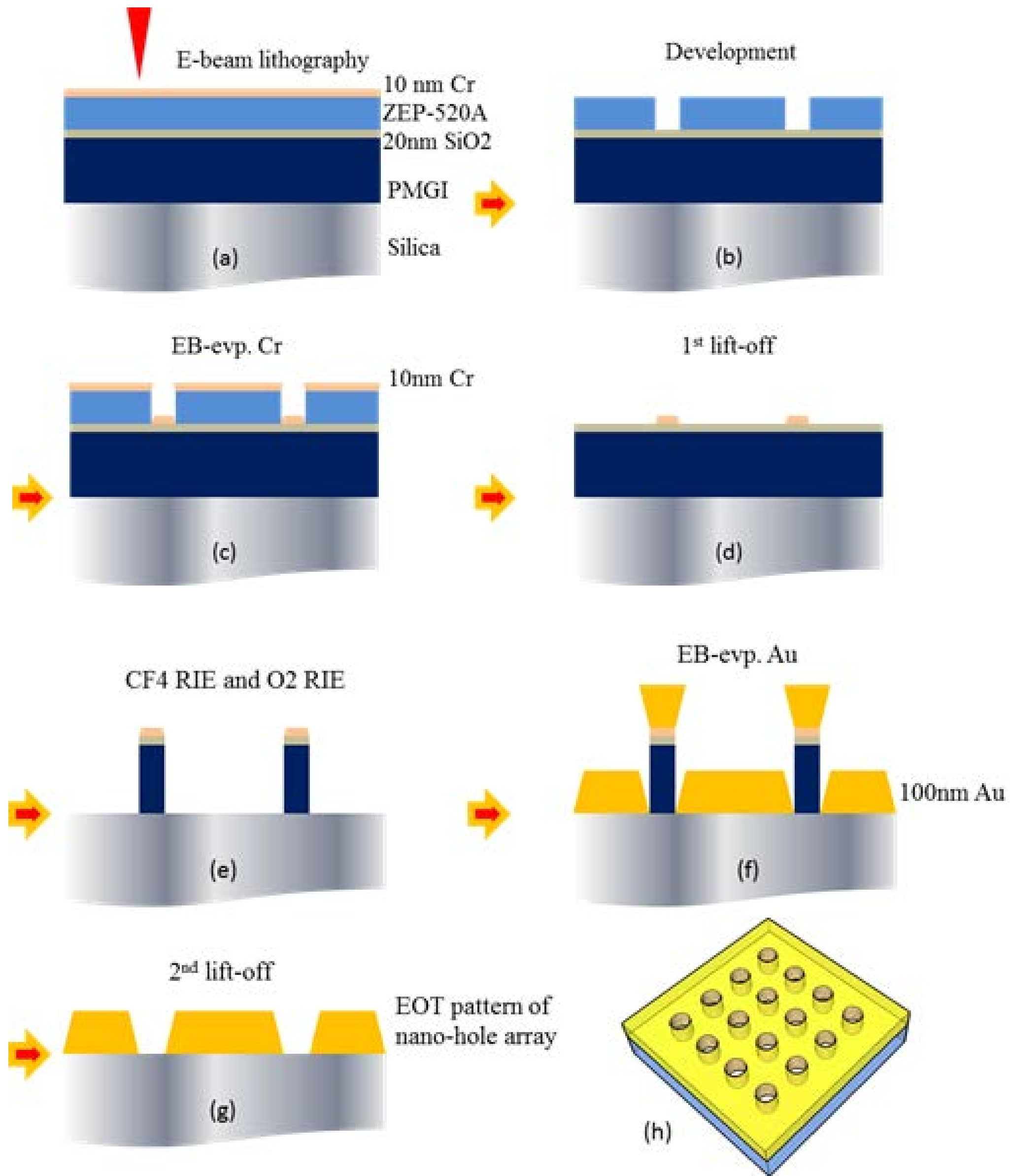

Figure 6.8 Schematic diagram of the nano-hole array fabrication process which includes (a) EBL process, (b) resist development, (c) Cr deposition, (d) first liftoff, (e) RIE, (f) gold deposition and (g) second liftoff process, and (h) final structure.

In the normal manufacturing process through electron beam lithography (EBL), metal deposition and single liftoff is not suitable for the metal thickness over 100 nm (discussed in the following Section 3.1.2). Here, the nano-hole array fabrication was carried out using EBL followed by double liftoff process on 2 in. fused silica substrate as shown in Fig. 6.8. Cleaned 2” silica wafer was coated by 400 nm poly(dimethyl glutarimide) (PMGI, MicroChem Corp.) as the sacrificial layer, 20 nm SiO_2 by electron beam evaporation as the separating layer, 90 nm ZEP-520A (ZEON Inc.) as the resist, and 10 nm Cr as the conductive charge dissipation layer, respectively. EBL was carried out using Raith 150^{TWO} system at 20 kV acceleration voltage and 0.33 nA beam current. Dot array pattern with the period of 500 nm and the write field of 100 μm^2 was exposed with the typical dose from 10 to 100 fC/dot. The Cr layer was removed by etchant after EBL, and the patterns were developed using amyl acetate (Sigma-Aldrich) for 1 min and rinsed by fresh IPA. For the first liftoff step, the sample was coated by 10 nm Cr and soaked in anisole for 4 hours. By using the Cr as the RIE mask, the unexposed area of SiO_2 and PMGI was etched to bottom by CF_4 RIE (20 sccm CF_4, 20 mTorr, 100 w) and O_2 RIE (20 sccm O_2, 20 mTorr, 20 w) respectively. 1 nm Cr and 100 nm Au were deposited by electron beam evaporation with the rate of 0.2 Å/s and lifted off by AZ-300 for the second liftoff step.

The fabrication process is monitored by atomic force microscopy (AFM). Fig. 6.9 shows the profile of EOT pattern after (a) first liftoff, (b) O_2 RIE to bottom, and (c) second liftoff scanned by AFM. The changed color and scale bar indicates the changes of pattern height.

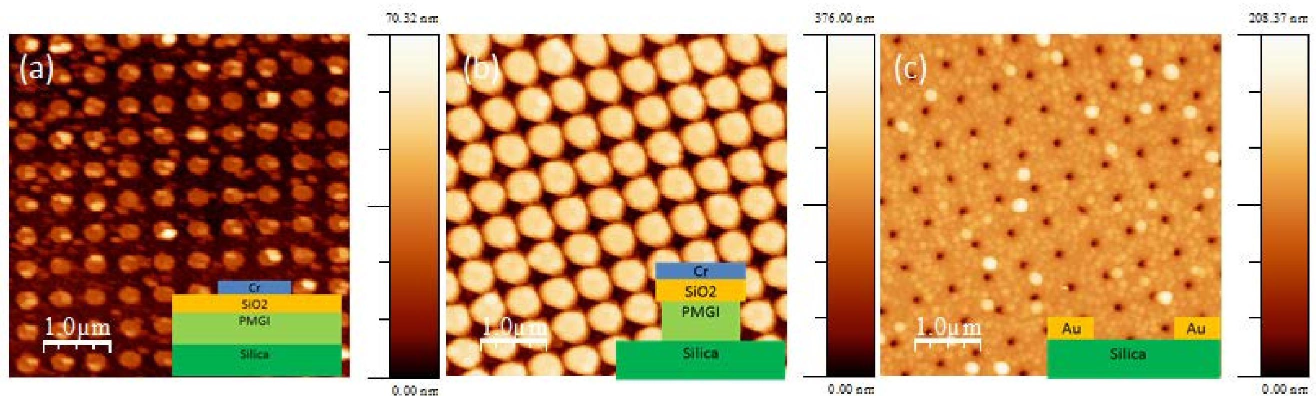

Figure 6.9 AFM images of fabrication of EOT structure after three intermediate steps: (a) after first lift-off; (b) after CF_4 and O_2 RIE to silica; (c) after second liftoff.

6.3.1.2. Comparison to single liftoff process

For comparison, the normal process of EBL, metal deposition and liftoff was tested to prove the advantage of double liftoff process. 300 nm ma-N 2403 (Micro Resist Technology GmbH.) as the negative resist was spin-coated on cleaned silica wafer and baked at 90°C for 1 min (Fig. 6.10a). Electron beam lithography was carried out by using Raith 150^{TWO} system at 20 kV acceleration voltage and 0.33 nA beam current with varied dot dose from 10-200 fc/dot. The sample was developed in MF-319 (Rohm and Haas Electronic Materials LLC.) for 90 sec and rinsed by DI water for twice (Fig. 6.10b). 1 nm Cr and 100 nm gold was deposited by electron beam evaporation with the rate of 0.2 Å/s and lifted off in Remover PG (MicroChem Corp.) Three problems by single liftoff process are shown in Fig. 5.10c:

(1) Normally, the exposed resist pillars are tapered, unlike Fig 6.9(b) with under-cutting, so the sidewall of the pillars is easily covered with metal by lateral deposition, which will prevent the dissolution of resist during liftoff (see Fig. 6.10c-1).

(2) For the same reason as above, the metal on sidewall is remained after lift-off. Thus chimney-shape structures are formed instead of flat hole array (see Fig. 6.10c-2).

(3) For ideal liftoff process, the thickness of resist is required to be more than three times of the deposited metal. But pillars with high aspect ratio collapse frequently during development because of capillary force (see Fig. 6.10c-3).

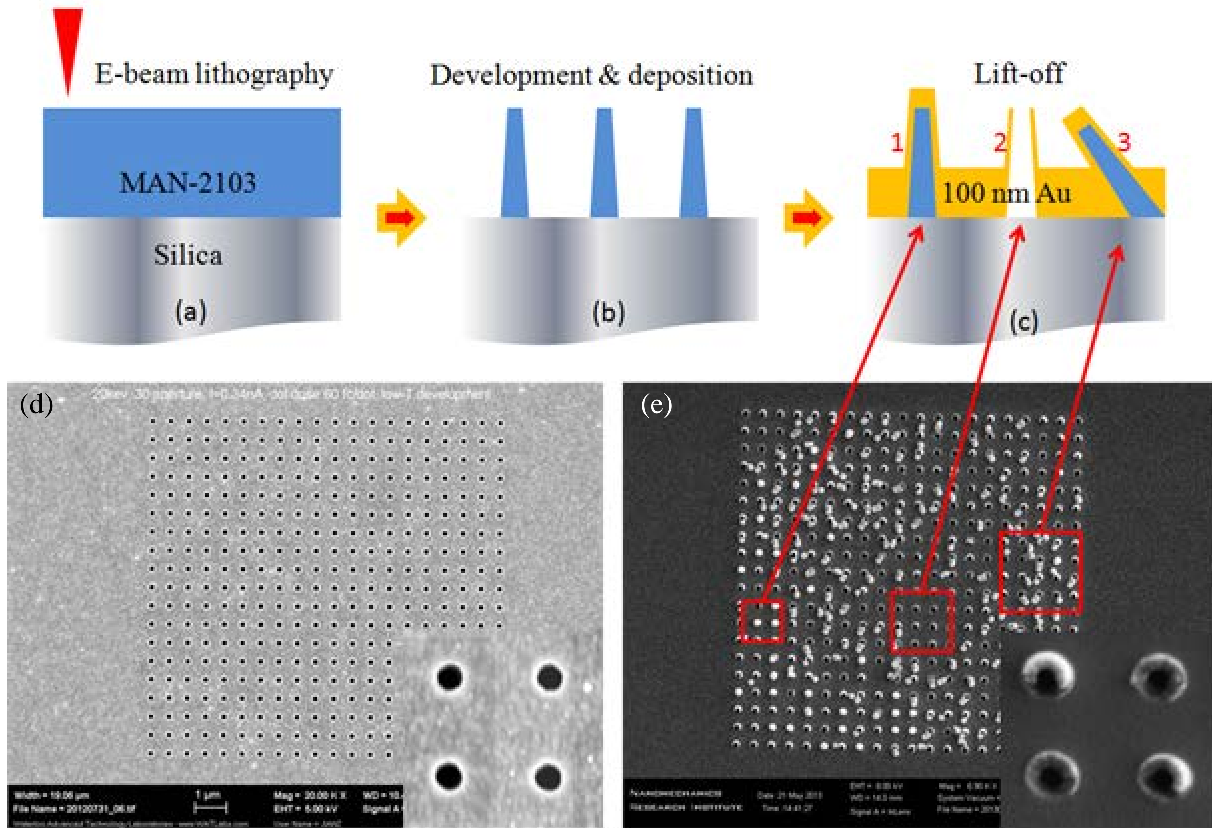

Figure 6.10 (a)-(c) The schematic of fabrication process through single liftoff step. In (c) the mechanism of three types of defects are described: 1. pattern covered by metal blocking dissolution; 2. chimney-shape holes; 3. collapse of structures. (d) SEM image of final EOT pattern through double liftoff process. (e) SEM image of final EOT pattern through single liftoff process.

Fig. 6.10d&f compare the final results through single and double liftoff process. Three types of defects formed in single liftoff are marked in the SEM image corresponding to the mechanism described in Fig. 6.10c.

6.3.1.3. The effect of exposure dose

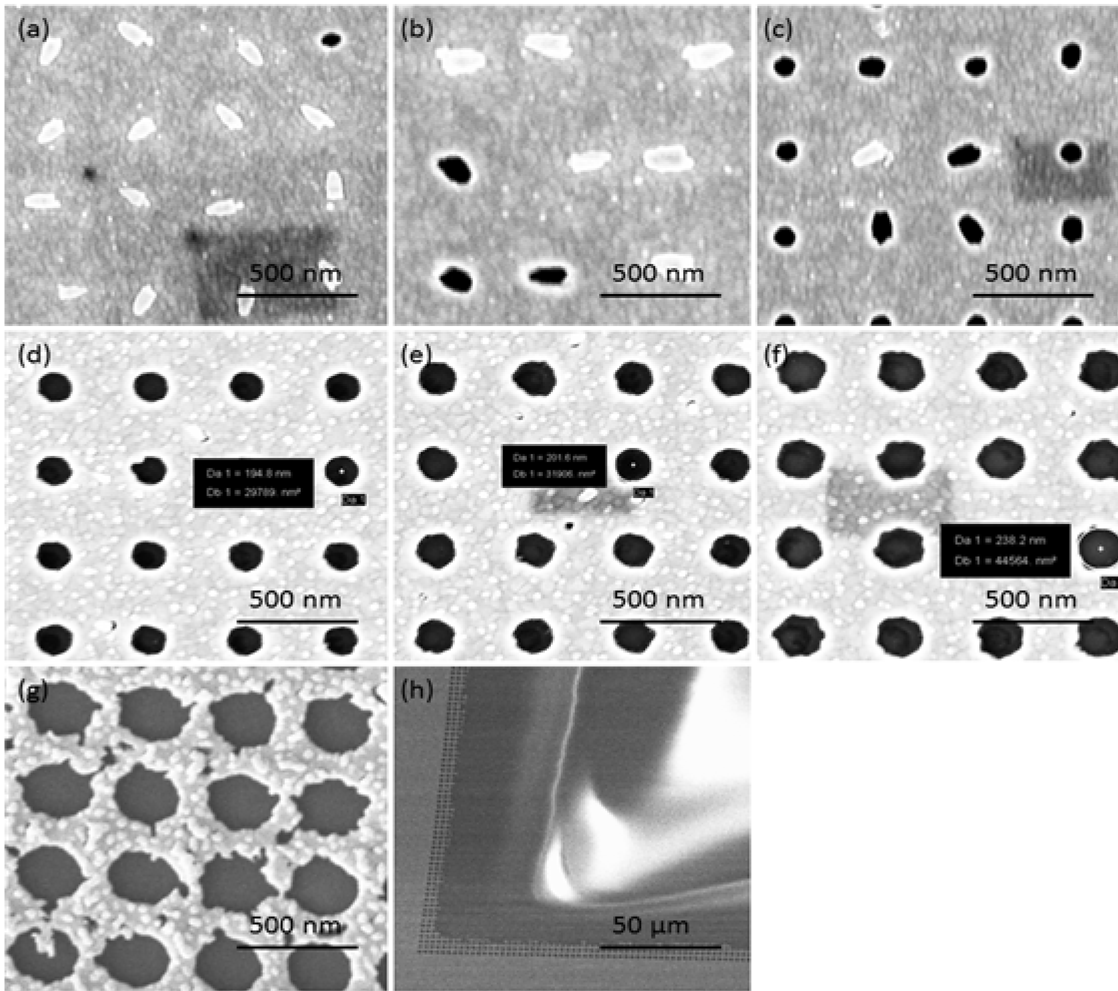

Figure 6.11 SEM images of final EOT hole array with the dot dose of (a) 10 fc/dot, (b) 20 fc/dot, (c) 30 fc/dot, (d) 40 fc/dot, (e) 50 fc/dot, (f) 60 fc/dot, (g) 80 fc/dot, (h)100 fc/dot. Fewer pillars fall with increasing exposure dose of 10-30 fc/dot. Higher exposure dose over 60 fc/dot leads to obvious noise. After 100 fc/dot, central area was over exposed totally because of dose overlap.

During electron beam exposure, dot dose was varied from 10-100 fc/dot for different hole size. As shown in Fig. 6.11, the relationship between the hole size and the dose was examined by SEM after final liftoff step. Too low or too high doses caused problems, other than the change of hole size. After O_2 RIE to bottom, PMGI pillars were formed. The pillars with smaller diameter could not stand firmly and will collapsed in the step of RIE or Au deposition, leading to the distorted hole shape. SEM images of Fig. 6.11 a-c prove the collapse of pillars with dose of 10-30 fc/dot. Exposure with higher dose required longer exposure time. SEM image of Fig. 6.11e

shows the final pattern with dose of 80 fc/dot, with the obvious distortion of the hole shape. Higher dose also increased the proximity effect. In the SEM image of Fig. 6.11h, the central area is completely exposed with no hole structure by dose of 100 fc/dot, while the edge area is in hole-shape because of less proximity effect. Therefore, the correction between dose and hole size was considered. Nano-hole array pattern was normally exposed with dot dose of 40-60 fc/dot.

6.3.1.4. The effect of facing-up and facing-down during the second liftoff

The effect of position of samples during second liftoff was also noticed here. For thicker metal layer (Au film with 100 nm thickness here), liftoff is more difficult. The second liftoff steps by facing-up and facing-down were carried out under the same exposure dose and compared by SEM. From Fig. 6.12, it is noticeable that during liftoff with wafer facing-up, once the pillars falled onto nearby surface they could not be removed easily by repeated rinse and ultrasonic cleaning. In comparison, the surface of samples through liftoff with wafer facing-down is much cleaner as shown in Fig. 6.11 d-f above.

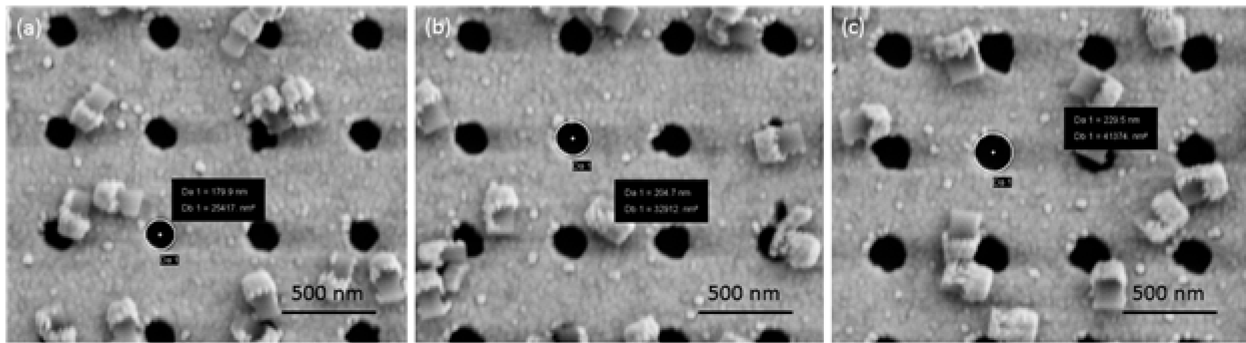

Figure 6.12 SEM images of final EOT hole array by facing up position during the second liftoff step. The patterns were exposed with the dot dose of (a) 40 fc/dot, (b) 50 fc/dot, (c) 60 fc/dot, respectively.

6.3.1.5. The effect of low-temperature development

The resolution of the same resist can be improved by low-temperature development, since the dissolvability of the developer is reduced at lower temperature. Finer features can be achieved by limiting the dissolution of partially-exposed polymer fragments at the edges of exposed area. In

our consideration, the noise of the pattern can also be averaged out by decreasing the sensitivity thus increasing exposure time at the same time. In the experiment, the sample was exposed with the same dose range from 10 to 100 fc/dot and developed in amyl acetate (Sigma-Aldrich Corp.) for 1 min at 5°C controlled by a cold plate (Echo Therm IC20 Chilling/heating Plate, Torrey Pines Scientific Inc.), then followed by the same process of double liftoff method.

It is found from Fig. 6.13 that the sizes of the series of holes were reduced obviously, in agreement with the mechanism of reduced sensitivity at lower temperature. Also, the smaller pillars with the dose below 30 fc/dot collapsed easily like in room-temperature development. During longer exposure with the dose over 60 fc/dot, the noise was reduced significantly and smoother pattern with maximum dose of 100 fc/dot was achieved.

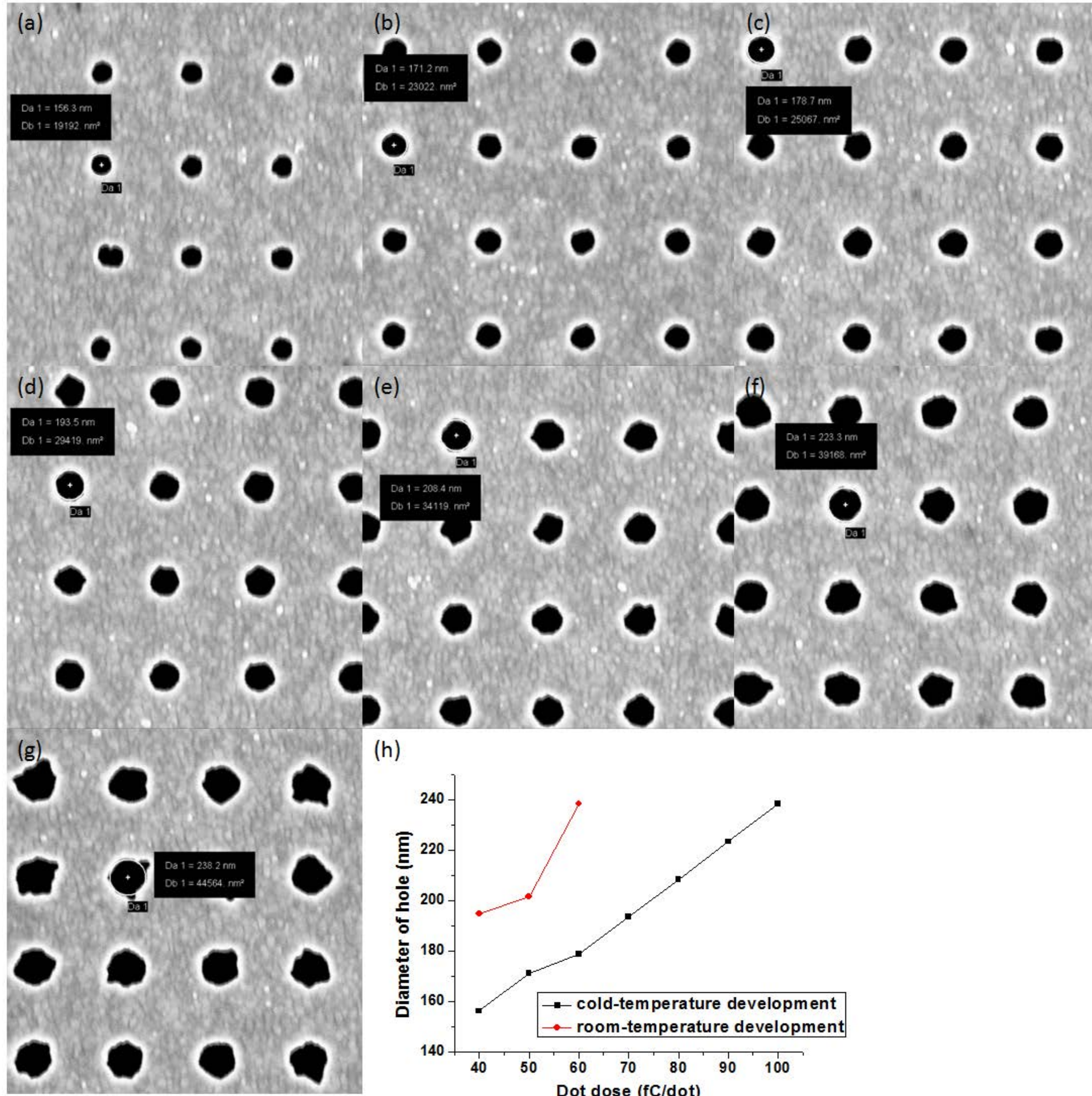

Figure 6.13 (a)-(g) SEM images of EOT hole array with the dot dose of 30, 40, 50, 60, 70, 80, 90 and 100 fc/dot, developed in low temperature, respectively. (h) The relationship between exposure dose and the diameter of holes with the development at room temperature and low temperature (5 ^{o}C).

6.3.2. Methods to improve the smoothness of Au films

Nobel metal film by physical vapor deposition (evaporation and sputtering) is inherently rough due to low surface energy and polycrystallinity even though a Ti or Cr adhesive layer is used. The rough surface leads to absorption, scattering and limited SP propagation (propagation length

reduced by nearly 10 times).[182,183] which all reduce the sensitivity of the EOT-based bio-sensor. Fig. 6.14 describes the brief mechanism of the effect from evaporated metal film on silica:

(1) The rough surface causes random reflection of part of the incident light that reduces the transmission intensity;
(2) The gaps of grains and particles increase the scattering and absorption, reducing the transmission intensity.

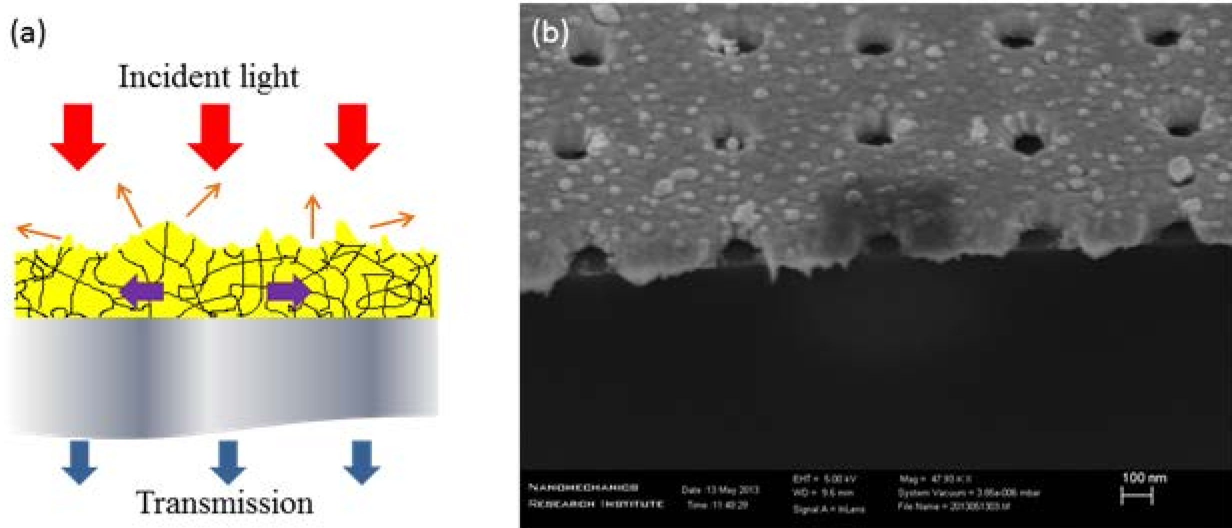

Figure 6.14 (a) Schematic of mechanism for reduced transmission by random scattering on rough surface and gaps of grains and particles within the noble metal film. (b) Cross-sectional SEM image of the rough surface of the nano-hole array in evaporated Au film.

It was reported that super-smooth silver and gold films with both thickness of 20 nm were achieved by utilizing 1 nm germanium[184] and a self-assemble monolayer of (3-mercaptopropyl)trimethoxysilane (MPTMS, SAM layer) [185] as a seed layer respectively. However, for 100 nm thick noble metal films in EOT, the improvement is not significant compared with that using the common adhesive layer of 1 nm chromium or titanium (as shown in Fig. 6.15). Film stripping method was also applied widely in EOT fabrication[186-189], for which the smooth gold film can only exist on the resin as shown in Fig. 6.16. Chemical polishing is another possible way to achieve the smooth surface, but the film and nanostructures will be attacked during chemical reaction.[190] In comparison of all the above methods based on physical vapor deposition (PVD), single-crystalline Au film through chemical synthesis was also applied

in surface plasmonic study.[178,191,192] To be pointed out, it is difficult to form Au film by chemical synthesis onto patterned template. As a result only FIB milling on synthesized Au film was used for EOT patterning.

Here, in the Fig. 6.15a-b, 1 nm Cr and Ge layer were electron beam evaporated at 0.5 Å/s and 100 nm Au was electron beam evaporated with 0.2 Å/s. In the Fig. 6.15c, the wafer was treated with $HCl:HNO_3:H_2O=1:6:60$ for 10min to induce active hydroxyl groups on the wafer surface and then treated with one drop of MPTMS (Sigma-Aldrich Corp.) in vacuum desiccator for overnight to form a self-assembled monolayer of MPTMS on wafer surface. The treated wafer was coated by 100 nm Au by electron beam evaporation at 0.2 Å/s. The roughness of the Au films was examined by AFM. The final EOT patterns were observed in SEM. The RMS roughness for the films of Cr/Au, Ge/Au and MPTMS/Au are 6.4 nm, 6.9 nm and 7.4 nm, respectively. The results are very close and show that the smoothness of the Au film with over 100 nm thickness is less impacted by adhesion layers.

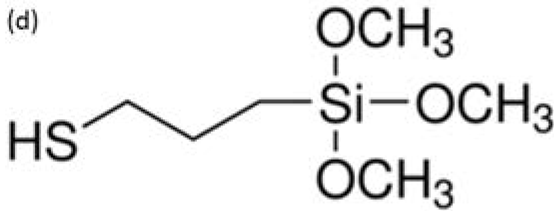

Figure 6.15 Comparison of the roughness of (a) 1 nm Cr/100 nm Au, (b) 1 nm Ge/100 nm Au, and (c) MPTMS/100 nm Au by AFM (left) and SEM (right). The RMS roughness for the three types of Au films is 6.4 nm, 6.9 nm and 7.4 nm, respectively. (d) Chemical structure of MPTMS.

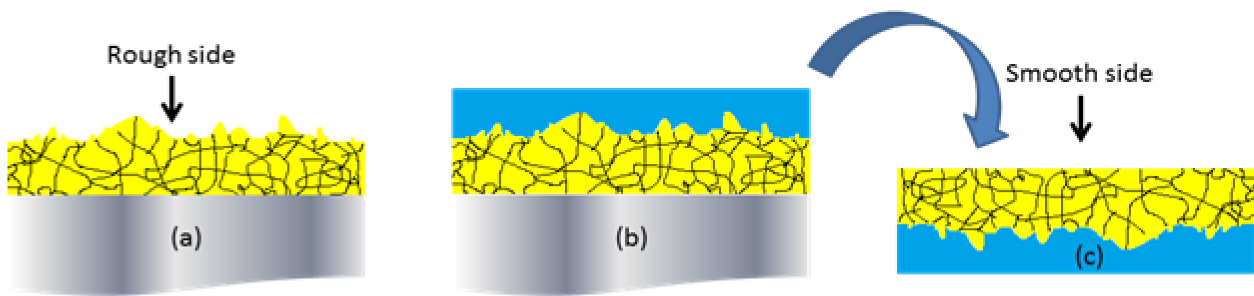

Figure 6.16 Schematic of "Template stripping" method: (a) film deposition or pattering; (b) resin casting; (c) template stripping.

Recently, annealing procedure was applied in surface plasmonic study, such as surface plasmon enhanced solar cell[193], metal-enhanced fluorescence[194] and nanodisk surface plasmon resonance sensor[195]. In this work, thermal annealing under Ar atmosphere was carried out to improve the film quality. The optical transmission spectra and sensitivity of the nano-hole arrays were compared for both annealed and as-fabricated structures.

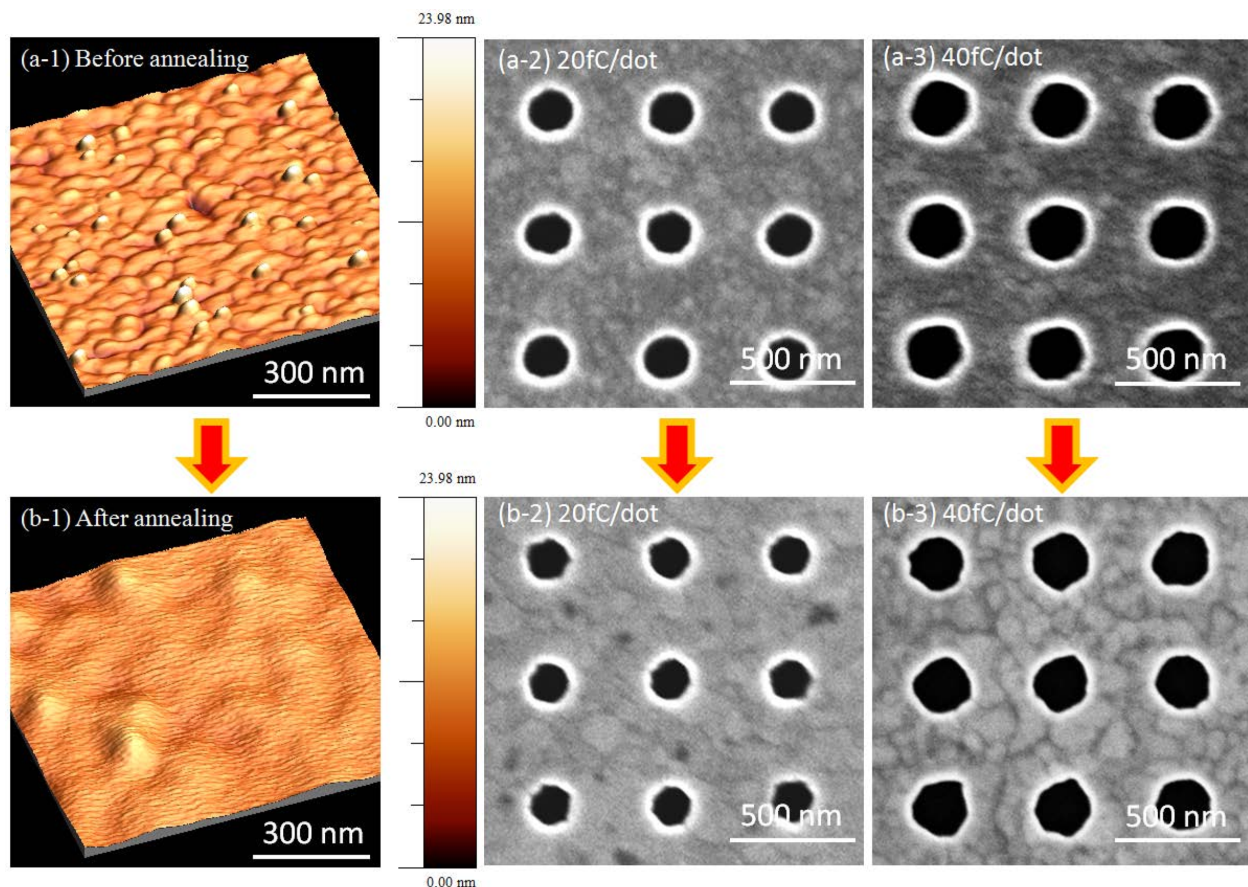

Figure 6.17 Comparison of the same EOT samples (a) before and (b) after annealing with the exposure dose of 40 and 60 fc/dot, respectively.

For annealing method, EOT sample with the film of 1 nm Cr and 100 nm Au was fabricated through double liftoff process shown previously. The sample was annealed in a tube furnace at 600°C with the protection of Ar atmosphere for one hour. The annealed samples were examined by AFM and SEM as shown in Fig. 6.17. The RMS roughness after annealing was obviously reduced from 1.87 nm to 0.89 nm. Interestingly, the SEM images show the shrinkage of hole size after annealing from 178.6 nm to 148.9 nm and from 256.8 nm to 208.4 nm. Another interesting change from the SEM images is that the small grains disappeared after annealing.

6.3.3. Other fabrication methods for EOT structures

6.3.3.1. Fabrication of EOT structure on Si_3N_4 membrane

The fabrication process of nanostructures on Si_3N_4 membrane has been discussed in Chapter 5. This technique shows competence for varous free-standing nanostructures and received increasing interests.[196-198] Various metal patterns can be obtained by deposition on etched-through free-standing membrane. On one hand, continuous metal patterns can be achieved directly by deposition on free-standing membranes with etched-through apertures.[199] On the other hand, isolated metal structures can be deposited through membrane as shadow mask onto the wafer below (named as stencil lithography).[200] The fabrication process of double liftoff discussed previously shows the limitation of exposure dose. Lower dose leads to smaller PMGI pillar which is apt to collapse. Higher dose leads to rougher patterns and greater proximity effect. The maximum dose is limited by proximity effect. Based on this, the designed hole size of EOT pattern is limited between 100 nm and 280 nm with the dose of 30-70 fc/dot. In comparison, by using membrane the proximity effect is eliminated. So higher dose can be utilized without the problem of the total areal exposure. Also, there is no issue of the collapse of pillars.

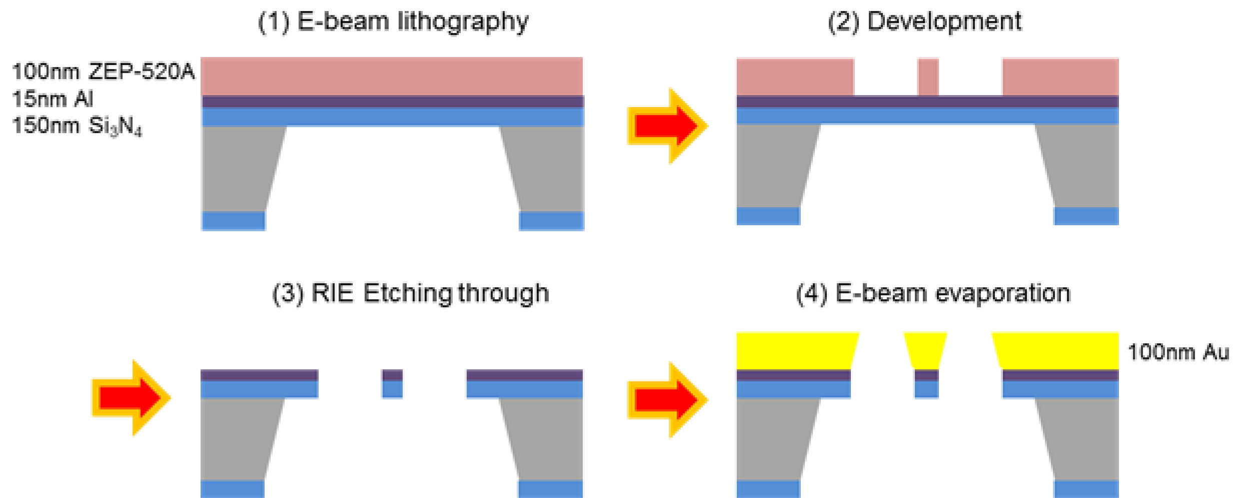

Figure 6.18 Schematic of the fabrication process of EOT pattern on Si_3N_4 membrane: (1) coating 15 nm Al/100 nm ZEP-520A on cleaned Si_3N_4 membrane and EBL; (2) development in amyl acetate; (3) etching through by BCl_3 and CF_4 RIE; (4) deposition of 1 nm Cr and 100 nm Au.

The fabrication process is shown in Fig. 6.18. The free-standing Si_3N_4 membrane was prepared through the same process described in Chapter 5, Section 5.2. The cleaned Si_3N_4 membrane was coated with 15 nm Al layer by electron beam evaporation and 100 nm ZEP-520A (ZEON Inc., the resist was diluted by anisole to reduce to the target thickness) (step-1). Electron beam lithography was carried out by using Raith 150^{TWO} system at 20 kV acceleration voltage and 0.33 nA beam current with varied dot dose from 10-200 fc/dot for various hole size. The pattern was developed using amyl acetate (Sigma-Aldrich Corp.) for 1 min at room temperature and rinsed by fresh IPA (step-2). The uncovered Al was etched by BCl_3 RIE (50 sccm, 5 mTorr, ICP 800 W, RF 200 W, V_{DC} -360 V, Oxford III-V & Metals Etch) for 20 sec. Then the Si_3N_4 membrane was etched through by CF_4 RIE (20 sccm, 20 mTorr, RF 100 W, Oxford Si Etch) with the etched Al as mask (step-3). The residual layers were cleaned by O_2 RIE (20 sccm, 20 mTorr, RF 20 W), Al etchant (the mixture of H_3PO_4 : HNO_3 : DI water = 30 : 1: 10), and DI water. Finally, 1 nm Cr and 100 nm Au were deposited by electron beam evaporation with the rate of 0.2 Å/s (step-4). The final samples were examined by AFM and SEM.

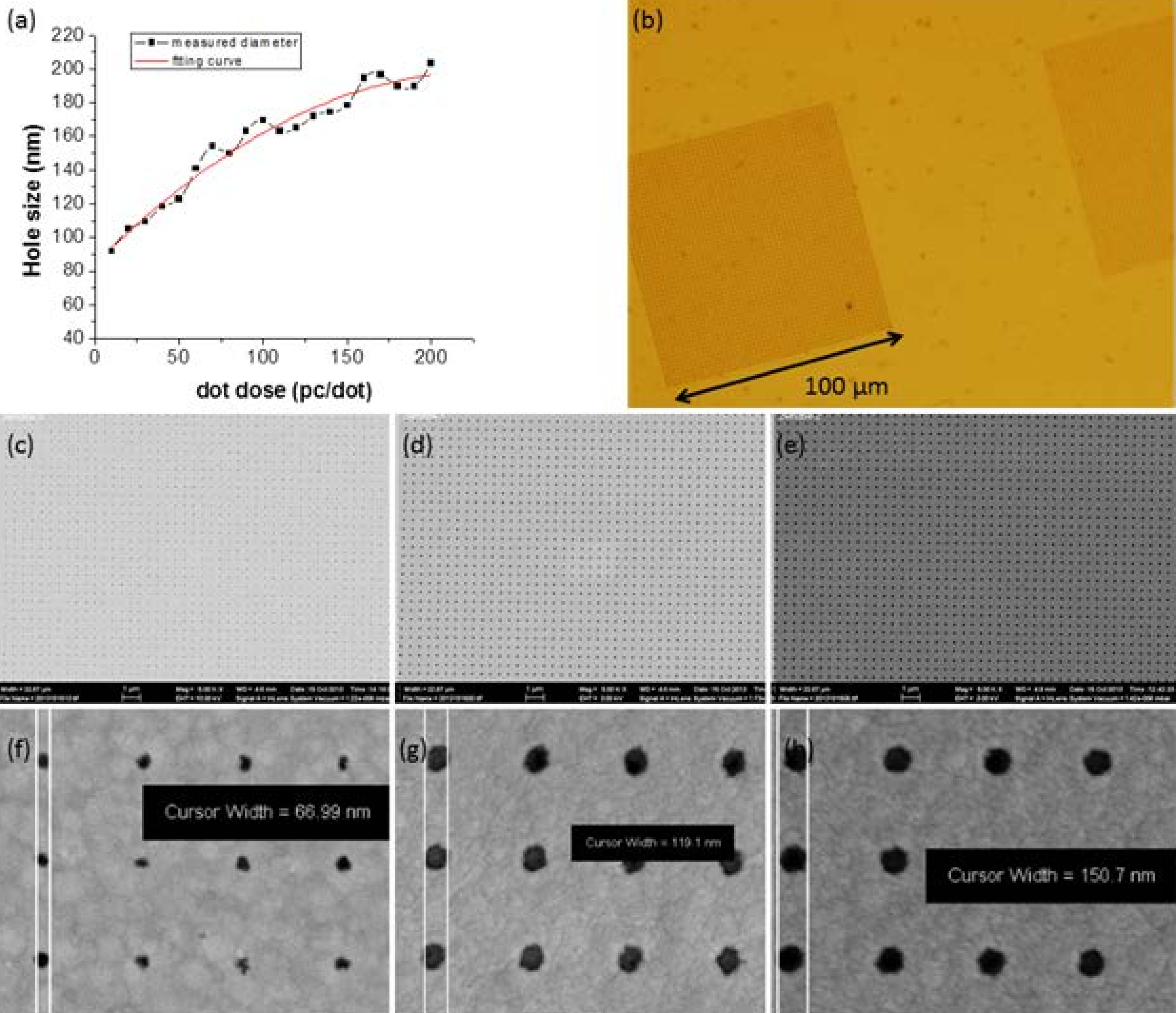

Figure 6.19 (a) The relationship between dot dose and the diameter of the final hole array. (b) Top-view by microscope of the Au nano-hole array patterns. SEM images of the nano-hole arrays with varied diameters exposed by (c)&(f) 10 pC/dot, (d)&(g) 40 pC/dot, (e)&(h) 70 pC/dot.

Fig. 6.19 shows the top view of the final Au structures on Si_3N_4 membrane. The relationship between the diameter of Au hole array and the exposure dose was concluded in Fig. 6.19a.

A remarkable aspect here is that, because of the lateral agglomeration on the sidewall during Au deposition, the hole size will shrink and the sidewall will be tapered, as shown in Fig. 6.18(4).

Observed by top-view SEM imaging, the diameter of the hole array was reduced from 216 nm to 179 nm by the shrinkage of 17.3% (see in Fig. 6.20). Tapered nanostructures have been studied by many researchers about its optical transmission properties.[201-203] In this work, the effects of the tapered angle on the EOT sensor through non-vertical cylindrical nano-hole (i.e. the geometries which were shown in Fig. 6.18) were considered. The work on simulation and optical characterization is discussed in later part.

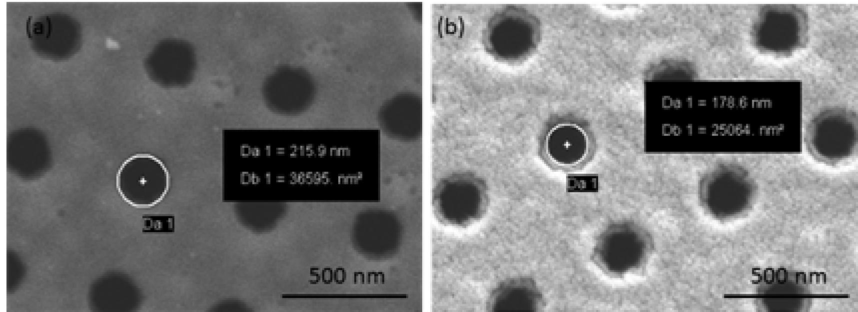

Figure 6.20 Top-view SEM images of (a) bare Si_3N_4 membrane with etched-through nano-hole array, (b) the same membrane with 100nm-thick Au by electron beam evaporation.

6.3.3.2. Fabrication of EOT structures by electroplating of Au

Gold is one of the most popular metals for surface plasmon devices due to its unique optical properties, stability and adsorbility with amino/thiol groups.[204,205] Importantly, the topography of the Au film, including the film quality and surface roughness, affects the applications in surface plasmon,[105,206] superhydrophobicity[207] and chemical activity.[208] Until now the manufacturing process of gold film is mainly based on physical vapor deposition (PVD), including thermal/electron beam evaporation, sputtering and molecular beam epitaxy. For EOT application, a thicker Au film (>100 nm) is normally required, for which the simple liftoff process is not competent as described previously.

Here, electroplating is investigated as an alternative technique to prepare thick Au film. Compared with PVD process, electroplating process requires no high vacuum or cleanroom environment, so it is lower cost, faster, more efficient and commercially available. More importantly, there is no concern about the liftoff issue since Au only forms within the patterned resist as the template.

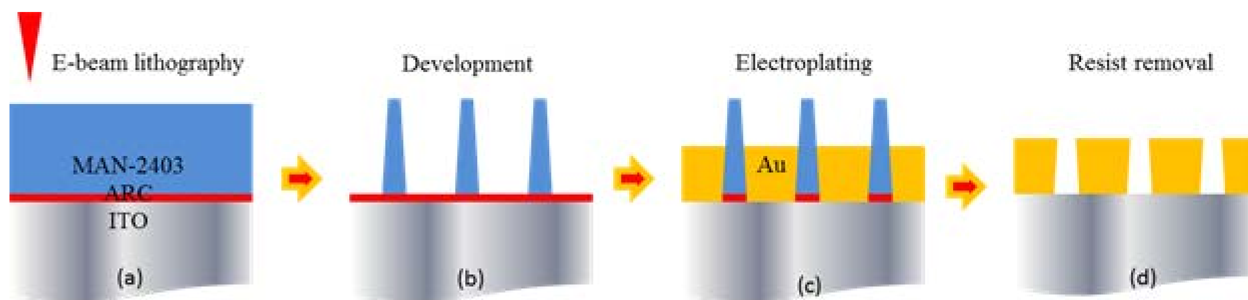

Figure 6.21 Schematic of the fabrication process of EOT pattern by electroplating: (a) coating 20 nm ARC/300 nm ma-N 2403 on cleaned ITO and EBL; (b) development in MF-319; (c) electroplating of Au film; (d) resist removal by O_2 RIE.

The fabrication process by electroplating is shown in Fig. 6.21. As the plating substrate needs to be conductive and transparent, indium tin oxide on glass (ITO, 15 Ω/sq., from Luminescene Technology Corp.) was cleaned by ultrasonic washing and O_2 RIE. For ideal electrochemical reactivity, a thin layer of 1 nm Cr and 5 nm Pt was deposited by electron beam evaporation. at the rate of 0.2 Å/s. 20 nm anti-reflective coating layer (ARC, from Brewer Sciences) as the adhesion layer and 300 nm ma-N 2403 (Microresist Technology GmbH.) as the negative resist was spin-coated and baked at 90°C for 1 min (step-a). The glass was cut into pieces with the size of 0.5 cm × 1 cm before future steps. Electron beam lithography was carried out using Raith 150^{TWO} system at 20 kV acceleration voltage and 0.33 nA beam current with varied dot dose from 10-200 fc/dot. The sample was developed in MF-319 (Rohm and Haas Electronic Materials LLC.) for 90 seconds and rinsed by DI water for twice (step-b). Before electroplating, the developed sample was briefly cleaned by O_2 RIE for 10 seconds to remove the thin ARC layer. The cleaned sample was then set as the working cathode combined with a bare Cr/Pt on ITO piece of the size of 2 cm × 4 cm as the balancing cathode, and a piece of Pt-coated steel mesh as the anode in the electrolyte of potassium aurocyanide solution (434 HS RTU, Technic Canada Inc.) (step-c). The plating was carried out at 60°C with the applied potential between 2.8V and 3.6 V without stirring. After plating, the sample was rinsed with DI water and the resist was removed by O_2 RIE (step-d). The surface roughness of the deposited Au films was examined by AFM and SEM. To test the plating rate, the samples with varied plating time and potential were partially removed with aqua regia (mixture of HNO_3 : HCl = 1 : 3) to create a step to be tested by Dektak 8 Stylus Profilometer.

There are two issues identified for the fabrication of EOT structures by electroplating:

(1) The surface roughness is affected by the plating rate, which is decided by the applied current. A faster growth process may introduce the higher stress of the metal grain, leading to rough surface.[209] By AFM scanning (Fig. 6.22a&b), the RMS roughness increases from 5.9 nm to 11.5 nm with the increasing current from 2.8 mA to 3.6 mA. Fig. 6.22c shows the cross-sectional images of Au film prepared by various electroplating current for 6 minutes.

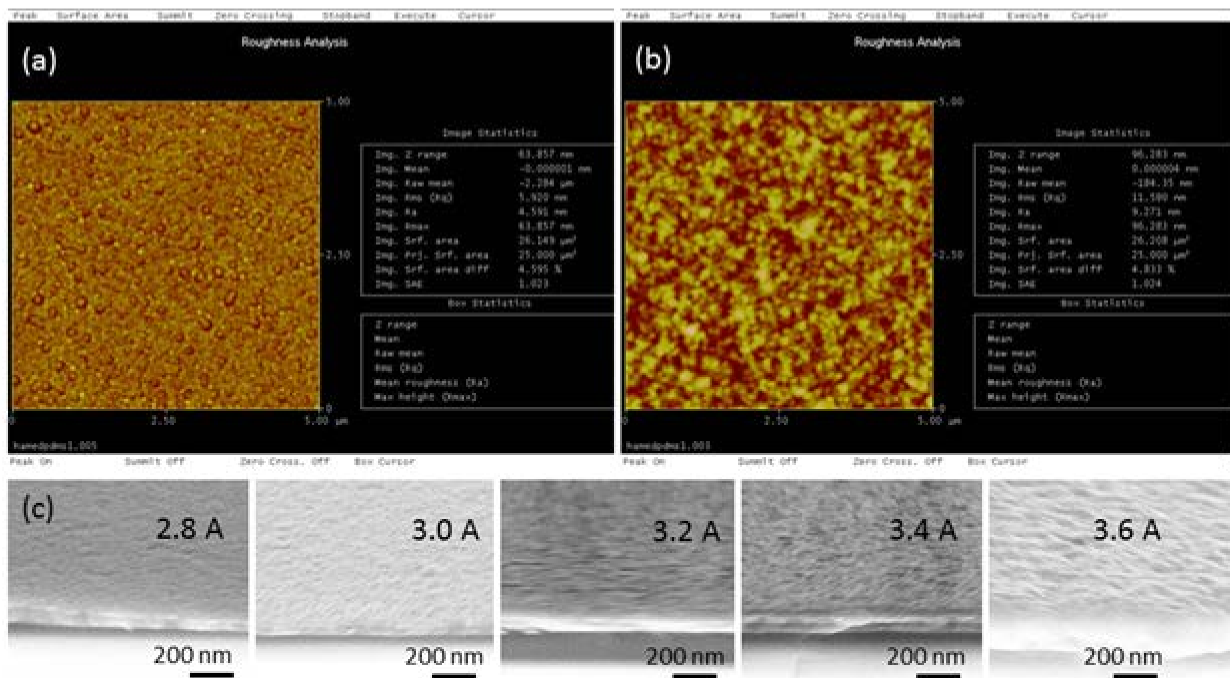

Figure 6.22 AFM imaging of Au film by electroplating current of (a) 2.8 mA and (b) 3.6 mA. (c) SEM cross-sectional view of Au film by electroplating current of 2.8 – 3.6 mA.

(2) In the previous work as described in Chapter 3, periodic tilted Au pillar array was fabricated by electroplating into hole-array pattern in resist film directly. Considering the tone-reversed structures here, the resist pillars were extruded frequently, probably caused by the much greater stress from the surrounding growing Au film (see Fig 6.23a). To overcome this problem, a thin ARC layer was coated before spin-coating ma-N 2403 resist to improve the adhesion (see Fig 6.23b). Fig. 6.23c shows the final EOT hole array with the diameter of 128

nm after removal of ma-N 2403. SEM images in Fig. 6.23e shows the uniform final result of EOT pattern in large area based on the EBL result shown in Fig. 6.23d.

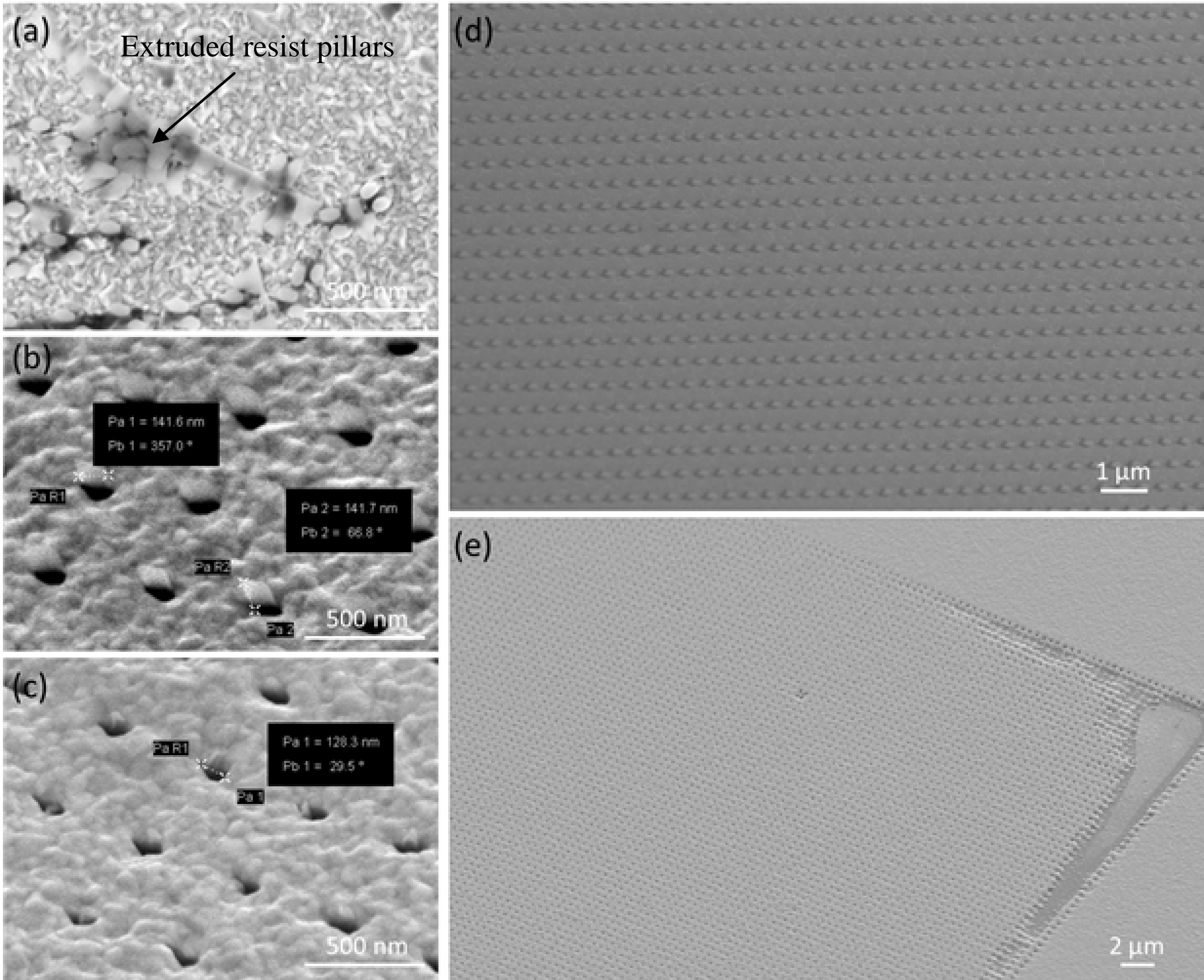

Figure 6.23 SEM image of (a) electroplating result without ARC adhesive layer; (b) electroplating result with ARC adhesive layer; (c) final EOT pattern after resist removal; (d) uniform resist pillar array after EBL in large area; (e) uniform final EOT pattern in large area.

6.3.3.3. Fabrication of EOT structure using nanoimprint lithography (NIL)

NIL is a high throughput (~1 min/wafer), high resolution (<5 nm) parallel patterning method in which a surface pattern of a mold (stamp) is replicated into a polymer by mechanic contact-induced material displacement.[210] As described in Chapter 2, hybrid nanoimprint-soft

lithography through sacrificial PMGI mold was developed by us as a versatile duplication technique especially on non-flat surface. Here, EOT nano-hole array was fabricated by hybrid nanoimprint soft-lithography.

The fabrication process of hybrid imprint mold through sacrificial PMGI master mold was already described in Chapter 2.[211] For imprinting using the hybrid mold, cleaned silica was first coated with 300 nm PMMA as adhesive and liftoff layer, then with 140 nm UV-curable resist onto which the mold was laid down and the mold-substrate stack was exposed to UV light of 365 nm wavelength. The mold was peeled off the substrate after the resist was fully cured (Fig. 5.21a). The imprinted sample was etched by CF_4 RIE for 1 minute to remove residual UV-resist layer and O_2 RIE for 2 minutes (Fig. 5.21b). The sample was coated with 1 nm Cr as adhesion layer and 100 nm Au by evaporation and soaked in PG remover for lift-off (Fig. 5.21c). Fig. 5.21d shows the SEM image of final nano-hole array with the diameter of 116 nm. To be pointed out, the hole array was not uniform probably because of the deformation of the soft mold during imprinting.

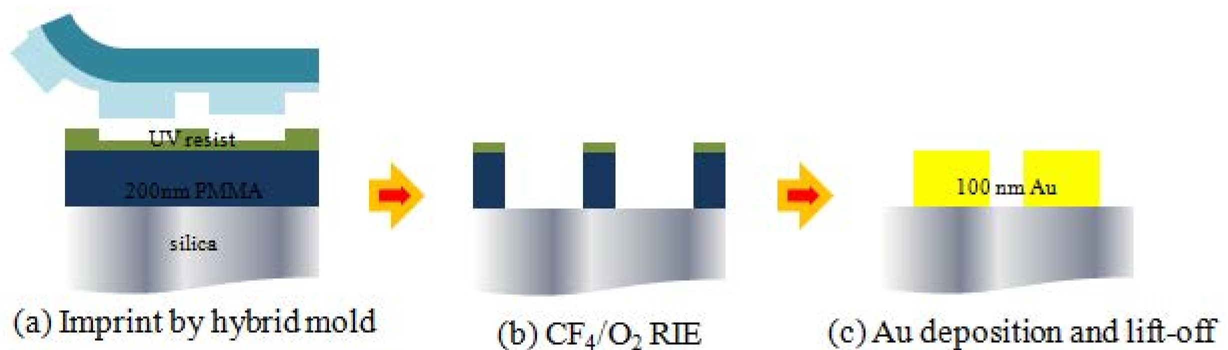

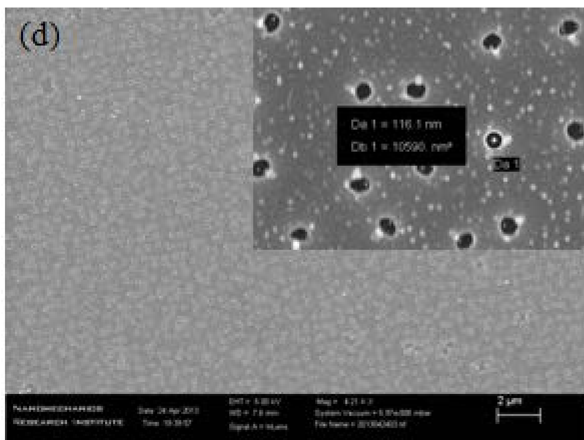

Figure 6.24 Schematic of the fabrication process of EOT pattern by hybrid nanoimprint-soft lithography: (a) coating 200 nm PMMA/140 nm UV-curable resist on cleaned silica and imprinting by hybrid mold; (b) CF_4/O_2 RIE to bottom; (c) electron beam evaporation of 1 nm Cr and 100 nm Au, followed by liftoff. (d) SEM image of final EOT hole array.

6.4. Numerical analysis

Optical behavior of the incident EM field through the nano-hole arrays were analyzed using the 3D full wavevector FDTD method, which is a reliable method in solving Maxwell's equations in dispersive media like gold and silver. Each media was specified by relative permittivity, $\varepsilon(\omega)$. For glass substrate and superstratum (i.e. target molecule) layers $\varepsilon(\omega)$ were assumed respectively as $n^2(=1.45^2)$ and $n_1^2 =(1.48^2)$. The Lorentz-Drude model was employed in calculating the permittivity of metal film layer.[212]

The FDTD was carried out using the commercial software package (FDTD solution 8) from Lumerical Inc. The plane wave source, nano-hole structure and monitor were co-planar with boundary conditions that made them effectively infinite. In this study, a plane wave of wavelength in the range of 400 nm to 900 nm with electric field amplitude of 1V/m which propagates in the Z-axis was used. The asymmetric boundary condition in the X-direction and symmetric boundary condition in the Y-direction and perfect matching layer (PML) in the Z-direction was used as absorbing boundary condition to study the transmission properties at normal incidence of electromagnetic wave through the subwavelength hole structure. The asymmetric and symmetric boundary conditions were considered in order to reduce the calculation time.[213] The calculation grid resolution was as high as 5 nm (grid point-to-point distance) in the simulation cell and the conformal mesh method was used to calculate the electric and magnetic field at the corner and rounded region of the nano-holes. Although this method gives better convergence than staircasing method for small enough mesh sizes, at larger mesh sizes it could results in worst results. In case of using metal and surface plasmon phenomena the 5 nm mesh gird is sufficient. The calculation time was set to 150 fs, and the transmission spectra were calculated using an X-Y monitor at 200 nm away from the film/air interface.

Based on this, surface plasmon excitation and propagation on the surface of hole-structured metal film and its transmission into air was studied systematically. The numerical analysis was applied for the optimization of the EOT pattern design in order to improve its sensitivity.

6.4.1. Effect of hole diameter

In this simulation, hole array structure with the period of 500 nm in 100 nm-thick Au film was investigated by changing the hole diameter between 140 nm and 300 nm. The transmittance was calculated based on broad-band white light with the wavelength from 0.4 to 0.9 μm.

$$\lambda_{max} = \frac{P}{\sqrt{(i^2 + j^2)}}\sqrt{\frac{\varepsilon_m \varepsilon_d}{\varepsilon_m + \varepsilon_d}} \quad (6.10)$$

Based on the approximate Equation 6.10, peak position will not shift by only changing the diameter since the period is fixed. However, with the increasing hole size the simulation result of transmittance in Fig. 6.25 shows the redshift for the first peak (i=1, j=0) and stable location for the second peak (i=1, j=1). The reason for this is that the holes in the (1, 0) direction are closer and the increasing diameter will shorten the distance of the two edges of the neighboring holes with greater ratio than the change in the (1, 1) direction. The positions of the first peaks and second peaks are summarized in Table 6.1.

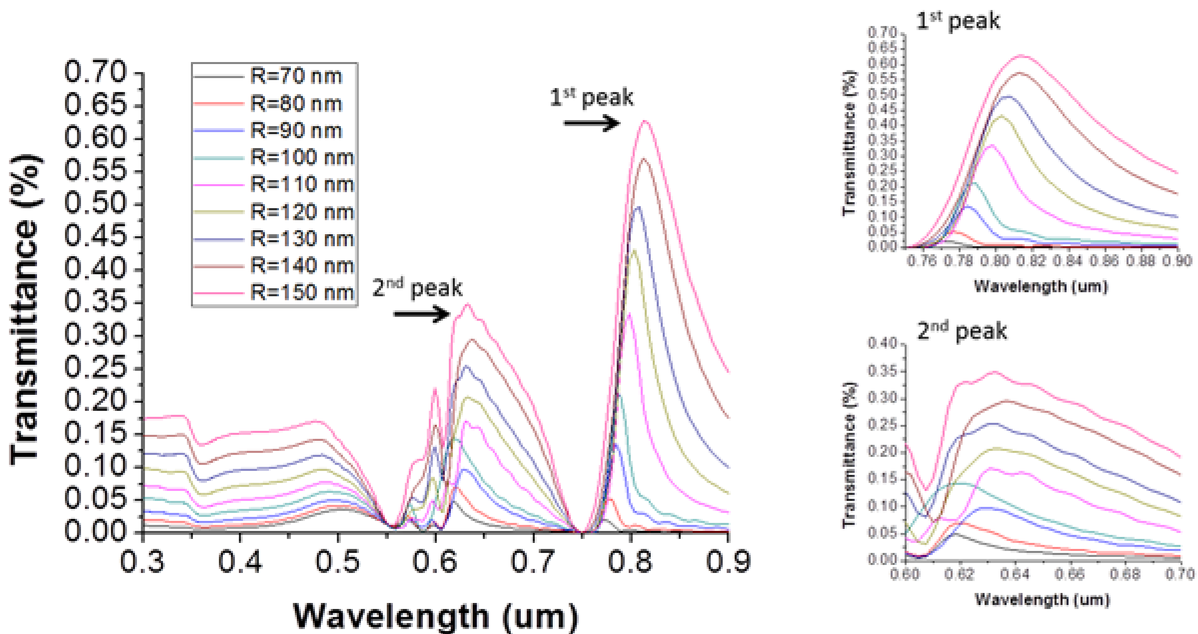

Figure 6.25 Simulated optical transmission spectrum of the EOT hole array fabricated on silica with varied diameter from 140 nm to 300 nm, Au film thickness of 100 nm, and periodicity of 500 nm.

Radius (nm)	70	80	90	100	110	120	130	140	150
1st peak (nm)	773.8	777.6	784.4	788.3	798.4	803.2	806.8	813.3	814.9
2nd peak (nm)	618.4	619.2	629.0	618.8	630.3	633.1	630.7	636.1	632.2

Table 6.1 Positions for the first and second peaks with varied radius.

6.4.2. Effect of Au film thickness

In this simulation, Au film with varied thickness from 60 nm to 200 nm was investigated, on which the period of hole array was 500 nm and the hole diameter was 140 nm. The transmittance was calculated based on broad-band white light with the wavelength from 0.4-0.9 μm.

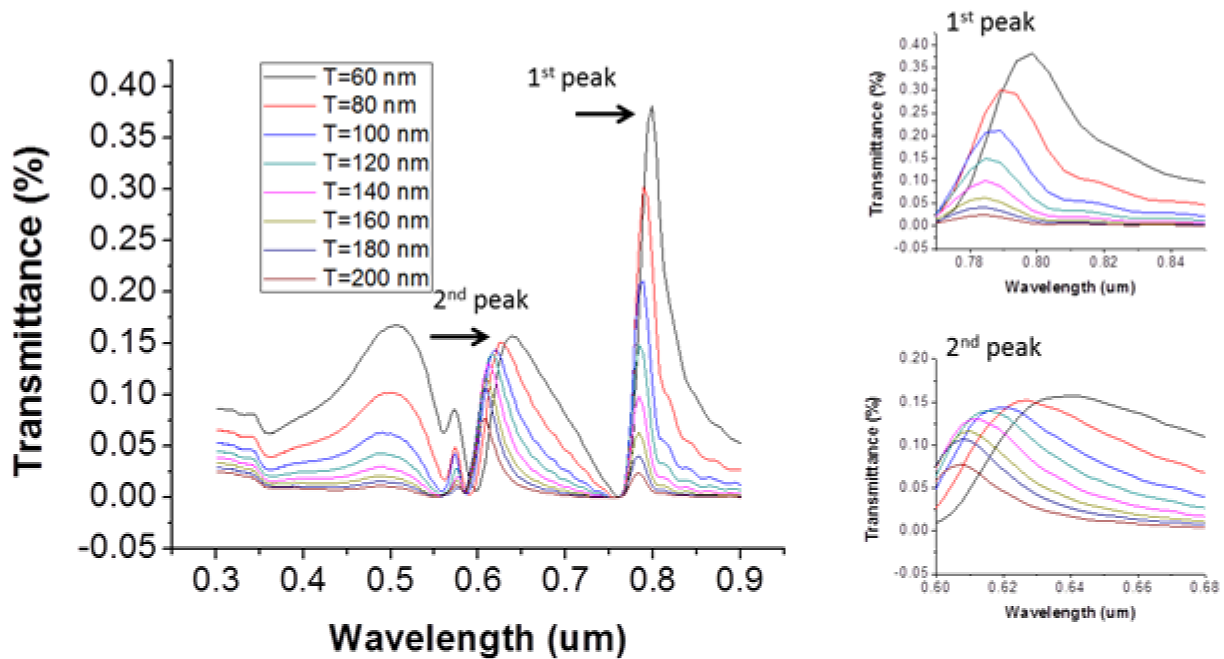

Figure 6.26 Simulated optical transmission spectrum of the EOT hole array fabricated on silica with varied film thickness from 60 nm to 200 nm, diameter of 140 nm, and periodicity of 500 nm.

Again, based on the approximate Equation 6.10, peak position will not shift by changing the film thickness since only the period is related. However, with the increasing thickness the simulation result of transmittance in Fig. 6.26 shows the blueshift for both of the peaks. There are two conclusions based on simulated result for different thickness:

(1) This indicates that surface plasmon on both sides of the Au film takes charge of the enhanced transmission, which is totally different from the SPP based on grating reflection and Kretschmann configuration. Since for propagating surface plasmon the momentum mismatch is provided by periodic structures and the increasing thickness of Au film causes longer distance between the coupling surface plasmon on top and back sides of the Au film, the changing LSPR within the individual tunnel leads to the shift as shown in Table 6.2.

(2) A thicker Au film reduces the extraordinary optical transmission. By increasing Au film from 60 nm to 200 nm, the intensity of the 2nd peak (1,1 mode) decreases dramatically from 1.2% to 0.1% (as shown in Fig. 6.26). The trade-off should be considered since thinner Au film will lead greater direct transmission, as shown in the transmission spectrum with the wavelength range of 0.3-0.5 μm in Fig. 6.27.

Thickness (nm)	60	80	100	120	140	160	180	200
1st peak (nm)	813.6	809.6	805.7	805.7	805.7	805.7	805.7	805.7
2nd peak (nm)	648.6	643.6	638.7	638.7	636.2	636.2	636.2	636.2

Table 6.2 Positions for the first and second peaks with varied Au film thickness.

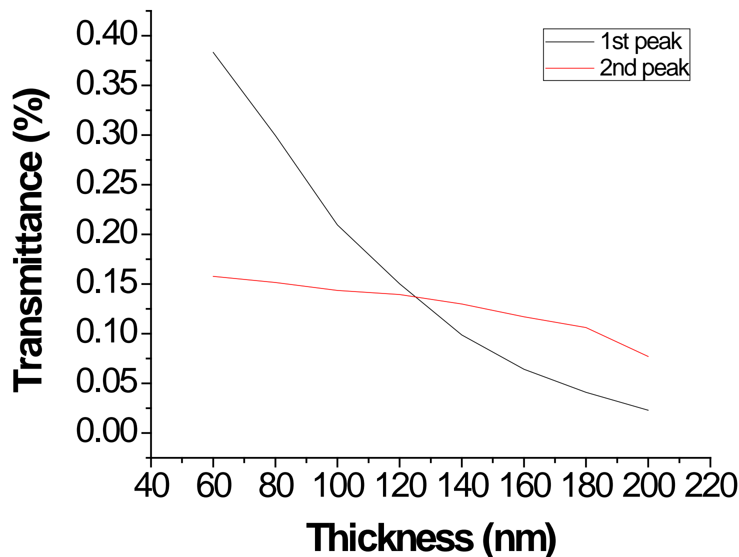

Figure 6.27 Effects of film thickness on EOT transmission intensity at the first peak (1,0) and the second peak (1,1).

6.4.3. Effect of hole array period

The effect of period (the center-to-center distance) was examined by simulation of nnao-hole array with the diameter of 140 nm on 100 nm-thick Au film. Since the diameter and thickness were fixed, their effects on LSPR were eliminated. Period, as the only long-range parameter, was varied from 400 nm to 550 nm in the calculation (see Fig. 6.28).

The location of the first peak (1,0 mode) and the second peak (1,1 mode) was summarized in Table. 6.3. The simulated transmission spectrum shows redshift with increasing period, which matches the simple Equation 6.10:

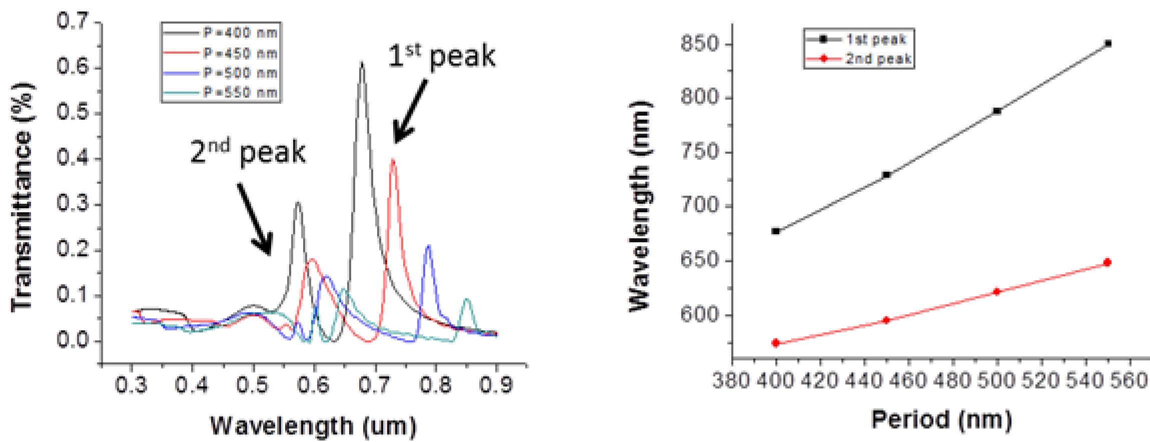

Figure 6.28 (a) Simulated optical transmission spectrum of the EOT hole array fabricated on silica with varied period from 400 nm to 600 nm, diameter of 140 nm, and 100 nm Au film. (b) The position of the first and second peaks impacted by changing period from 400 nm to 600 nm.

Period	400	450	500	550	600
1st peak (nm)	700.5	751.1	805.7	805.7	873.4
2nd peak (nm)	586.8	12.8	638.7	638.7	672.2

Table 6.3 Positions for the first and second peaks with varied period.

6.4.4. Effect of tapered angle

Figure 6.29 Schematic of a periodic array of tapered nan-hole array in Au film fabricate by (a) double lift-off process and (b) evaporation of Au onto the hole array patterned on a free standing membrane. The structures are illuminated by TM polarized light from glass side.

As seen in Fig. 6.29, the tapered angle of nano-hole array is unavoidable because of the lateral agglomeration during Au deposition. However, this effect from fabrication process is normally ignored in theoretical simulation. In this part of work, the nano-hole array is patterned in 100 nm-thick gold film with a periodic array of 500 nm, tapered angle α in the range of 0 to 16°, hole radius R of 75 nm to 125 nm, and tapered radius, R_{tap}, which is given by:

$$R_{tap} = R + 100 \times tan(\alpha) \qquad 6.11$$

The effect of increasing the tapered angle on the near-field electric near field of the output surface was shown in Fig. 6.30 for hole period of 500 nm. A broad peak around 490 nm with a transmission of 7-10% (at different tapered angle) was observed in nano-hole array. This peak was attributed to the direct transmission of gold film and occurs regardless of the hole array structure and incident EM wave polarization.[214,215] Another broad peak at wavelength of 656 nm with a transmission of 17% was also observed in the tapered hole array of structural periodicity of 500 nm at tapered angle of 0°. This broad peak was attributed to the surface plasmon resonance mode of (1,1). An anti-symmetric sharp peak was recorded at wavelengths of 807 nm with transmission intensity of 50-48 % in the nano-hole array with tapered angle of 0 and structural periodicity of 500 nm, which was attributed to the SPP resonance mode of (1,0). The anti-symmetric peaks were indicative of Fano resonances[216] which were characteristics of interference between a resonant transmission and non-resonant one and have been reported elsewhere.[216-219] The near-filed profile of the FDTD calculated $|E|^2$ of the (1,0) resonance mode in the glass/film interface of tapered nano-hole profile at different tapered angle in the range of 0° to 16° with step of 4° and periodicity of 500 nm are shown in Fig. 6.30c.

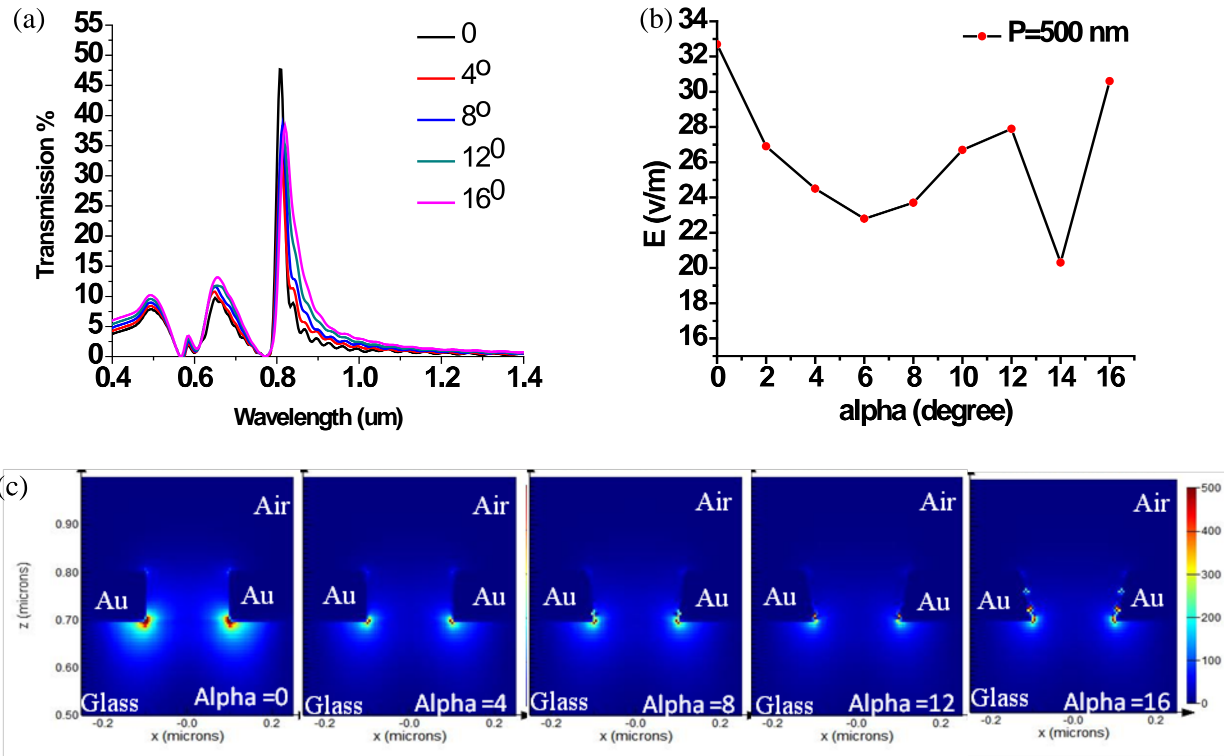

Figure 6.30 (a) FDTD simulated near filed transmission spectrum of non-vertical profile of nano-hole structure at different tapered angle of nano-hole array with radius of 100 nm, hole depth of 100 nm, and structural periodicity of 500nm. (b) Effect of tapered angle on the normalized electric field of the nano-hole array with radius of 100 nm, hole depth of 100 nm, and period of 500 nm at wavelength of 820 and 200 nm away from the air/Au interface. (c) The FDTD calculated $|E|^2$ profile of the $(1,0)_{film/glass}$ resonance mode. The raw shows the cross section across middle of the tapered nano-holes of period 500 nm at wavelength of λ= 807 nm and α=0, λ= 810 nm and α=4, λ= 814 nm and α=8, λ= 817 nm and α=12, and λ= 820 nm and α=16, respectively. The hole radius and hole depth were 100 nm. Light incident from the substrate medium through the nano-hole array.

6.5. Optical Characterization

6.5.1. Transmission measurement

The optical transmission spectra were recorded using a fiber optical spectrometer (Ocean Optics - USB4000), with spectral resolution of 1nm. The fabricated nano-hole array were illuminated using a tungsten halogen lamp which provides broadband radiation in the wavelength range of 200 nm to 900 nm and a 10× objective lens of numerical aperture (NA) of 0.15 was used as

collimator. The transmitted spectrum was collected using a 40× objective lens of NA of 0.4 and coupled to the fiber which is connected to the spectrometer. All spectra were recorded by average of 100 accumulations and an integration time of 100 ms.

Both of the annealed and as-fabricated samples were treated by O_2 plasma and RCA1 cleaning before each measurement. The 16-mercaptohexadecanoic acid (16-MHA, Sigma-Aldrich) was utilized as the target molecule. A drop of 1 mM 16-MHA in ethanol was coated on the EOT sample surface area followed by rinse with fresh ethanol for three times and baked at room temperature to form a self-assemble monolayer of target molecule. The spectrum was recorded *in situ* before and after each coating.

6.5.2. The effect of nano-hole array period and diameter on EOT result

For periodic Au hole array with the square lattice P at normal incident light, the SPP wavelength (λ_{SP}) of maximum intensity at the resonance mode (i, j) can be calculated by Equation 6.10. Fig. 6.31 shows the normalized transmission spectrums of nano-hole arrays with the hole diameters of 153.3, 174.9, 184.2, 198.2, 209.3, 234.5 nm, respectively. For each diameter, both of the (1,0) and (1,1) resonance modes shows redshift with the increasing period from 400 nm to 550 nm. When reducing the period or increasing the diameter of the hole array, the transmission increases which can be explained by the increasing effective transmission area.

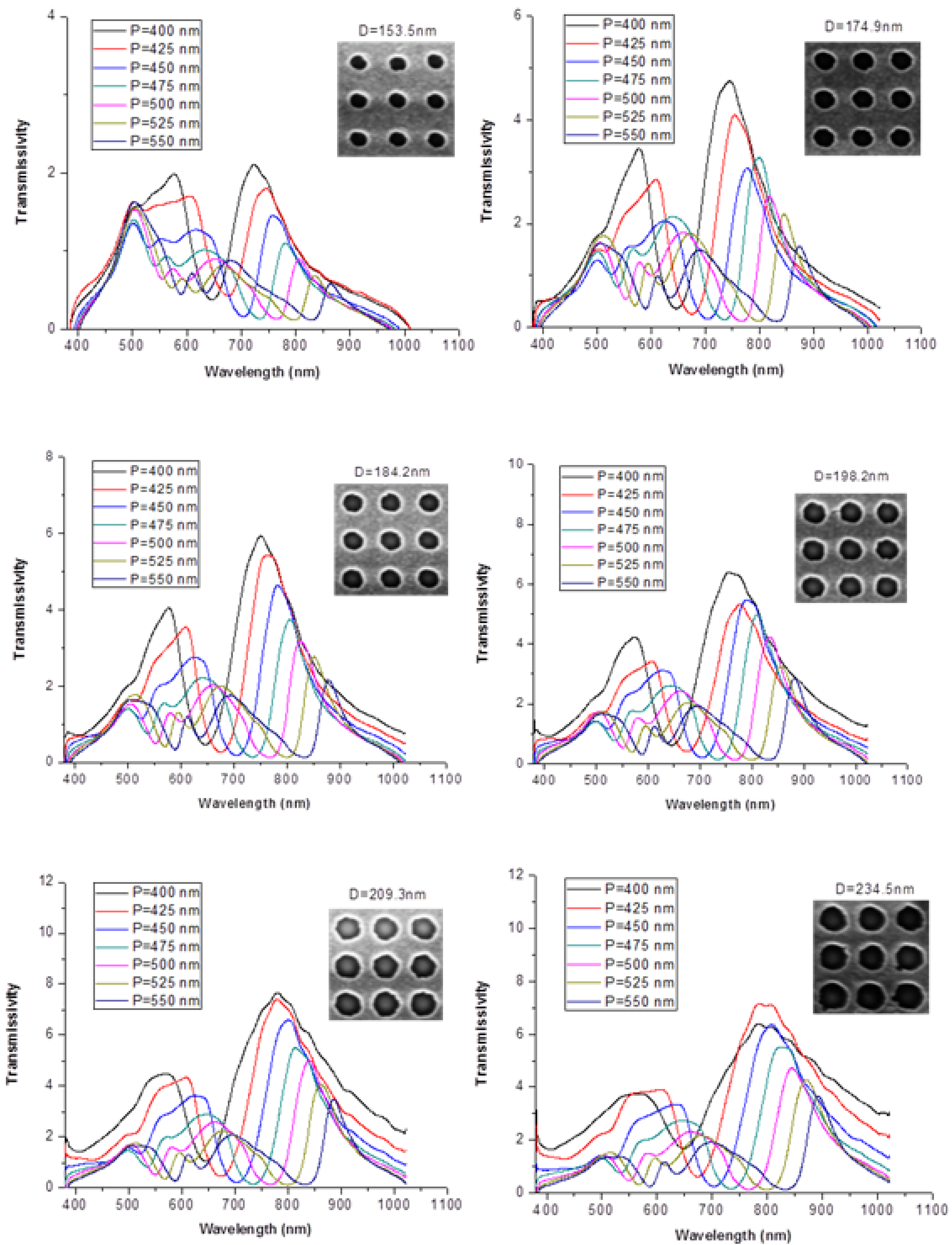

Figure 6.31 Transmission spectrum of nano-hole arrays with varied periods and diameters. The thickness f Au film is 100 nm. The diameters are 153.6 nm, 174.9 nm, 184.2 nm, 198.2 nm, 209.3 nm, and 234.5 nm, with the changing period from 400 nm to 550 nm with step of 25 nm.

6.5.3. The effect of tapered angle on EOT performance

The tapered angle of hole array is unavoidable because of the lateral agglomeration during Au deposition. However, this effect from fabrication process is normally ignored in theoretical simulation. In this part of work, the tapered nano-hole profile was considered and compared. Fig. 6.32a shows the SEM image of non-vertical nano-hole with hole depth and radius of 100 nm and periodicity of 500 nm, which were fabricated via double liftoff process on a silica substrate. Measured and FDTD simulated far-field transmission of tapered nano-hole with tapered angle of 10° (Fig. 6.32a) is shown in Fig. 6.32b. As can be seen in this figure, except the transmission amplitude, a very good agreement in terms of peak position and overall trend between the FDTD result (red) and experimental one (black) was observed. The difference between the transmission amplitude of FDTD and measured values for un-annealed sample might be due to the imperfection in the fabricated nano-hole structures such as roughness of the surface and edges which increases the light scattering and reduces the transmission intensity. The film roughness was reduced by annealing at 600 °C for 1 h, as described in Chapter 6, Section 3.2. The EOT measurement of the annealed nano-hole array and non-annealed one were also compared with FDTD in Fig. 6.32b. As can be seen from this figure, the transmission of the NHA after annealing (green) was improved, and the discrepancy between the FDTD and measurements was reduced.

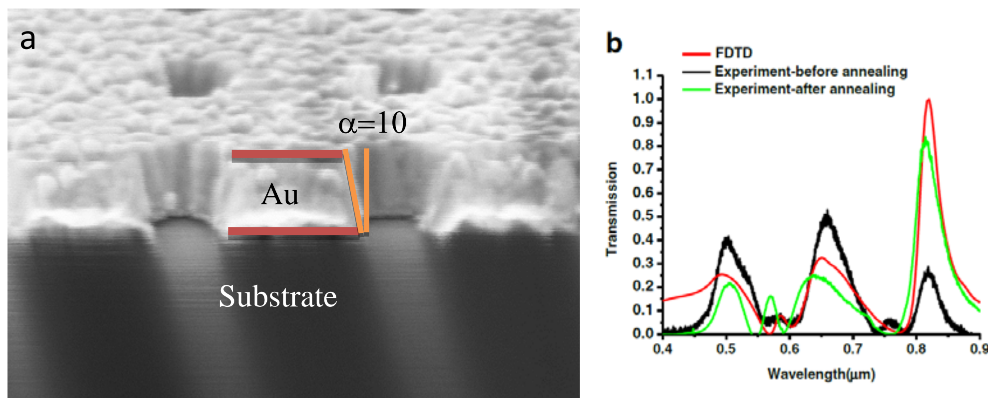

Figure 6.32 (a) SEM micrograph of the positive profile NHA before annealing. The inset shows the positive profile NHA after annealing. (b) FDTD simulated transmission spectrum of the positive profile NHA and measured one before and after annealing at 600 °C.

6.5.4. The effect of annealing on Au EOT sample

Here, the transmission enhancement was compared with the annealed and non-annealed samples with the similar diameter. The optical transmission of the annealed and as-fabricated samples of hole diameter in the range of 149 nm to 235 nm and period of 500 nm were compared in Fig. 6.33a&b. It was found that the (1,0) resonance mode of the annealed samples shows a blueshift of 19 nm and 23 nm which can be attributed to the hole diameter shrinkage from 185 to 149 nm and 235 nm to 208 nm, respectively, as it is shown in the red and black lines in Fig.6.33a-b. To understand the effect of annealing on the quality of fabricated samples, the optical transmission of both annealed and as-fabricated hole array structures of hole diameter of 149 nm and 208 nm are compared in the blue and black lines in Fig. 6.33. As can be seen from these figures, the optical transmissions of annealed EOT structures of both diameters were enhanced. This enhancement was attributed to the surface roughness reduction of the gold film.

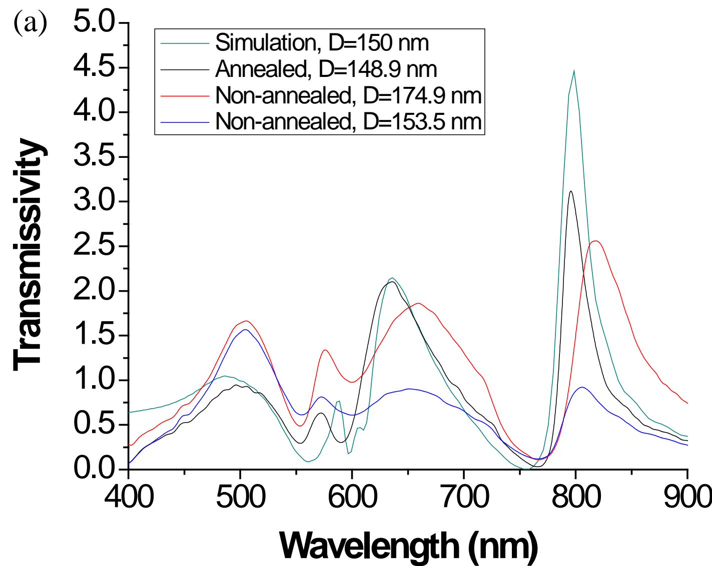

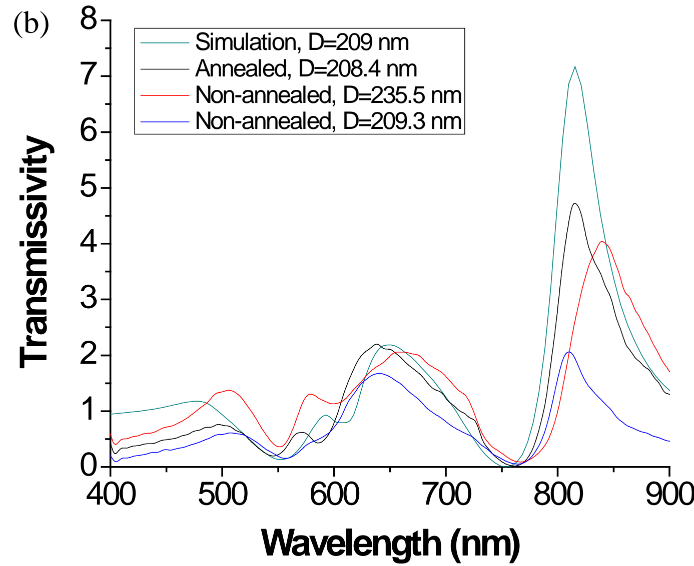

Figure 6.33 Comparison of optical transmission spectrum of NHAs with the diameters of (a) —148.9 nm after annealing, —174.9 nm before annealing, —153.5 nm as-fabricated, —150 nm in simulation; (b) —208.4 nm after annealing, —235.5 nm before annealing, —209.3 nm as-fabricated, —209 nm in simulation.

6.5.5. Transmission of the hole array structure in free-standing gold film

Hole array structures were patterned on Si_3N_4 membrane as described in Chapter 5, Section 2. After coating Au onto the hole array in Si_3N_4 membrane, the Si_3N_4 membrane was removed by CF_4 RIE, resulting in free-standing Au EOT structure. In the case of hole array in free-standing Au film, the surface plasmon resonance is excited uniformly on both Air/Au sides. Both the simulation and experimental measurement show that there is only single peak for transmission spectrum. Fig. 6.34 shows the peak is at 817 nm for simulation and 842 nm for experimental measurement, based on the same parameters of 178 nm diameter, 100 nm film thickness, 500 nm period. The slight shift between theoretical and experimental results is caused probably by the non-ideal fabrication process, such as lateral deposition, shift in real thickness, and the roughness of Au film. To be pointed out, since the Au film is only 100 nm and there is no absorption from substrate, the interaband transition (direct transmission) of gold film causes a broad and intense peak around 490 nm which overlaps the EOT peak partly. This can be resolved by using larger period of nano-hole array, of which the transmission intensity will be reduced significantly.

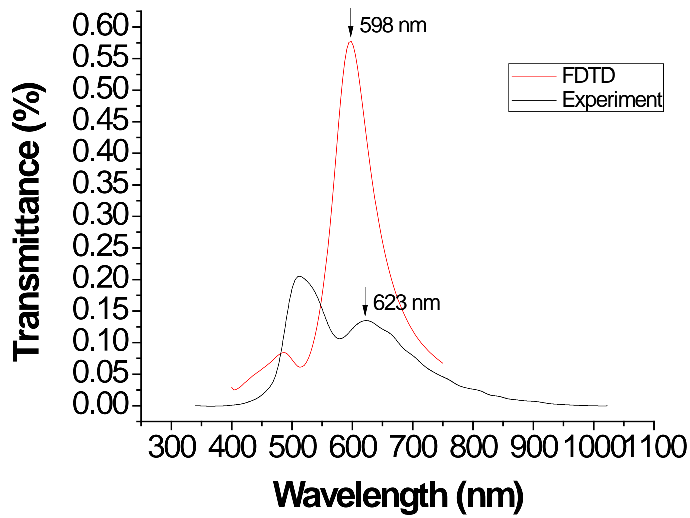

Figure 6.34 Recorded and FDTD simulated far field transmission spectrum of the nano-hole array patterned on free-standing Au film. The hole diameter, hole depth and period is 178 nm, 100 nm, and 500 nm respectively.

6.6. Application of annealed nano-hole array in bio-sensing

The effect of annealing on the sensitivity of the fabricated samples on the silica glass was studied by using the 16-MHA as the target molecule. The optical transmission of the target-coated annealed and as-fabricated EOT structures of the hole diameter of 150 nm are compared in Fig. 6.35. The sensitivity was defined as:

$$Sensitivity = {}^{\Delta\lambda}/_{(n_{target} - n_0)} \qquad (6.11)$$

where $\Delta\lambda$ is the peak shift before and after coating target, n_{target} and n_0 are the index of the target molecule and media (air here, $n_0 = 1.0$). It was found that on using the 16-MHA molecule (n=1.48) as sensing medium in the EOT structure with the diameter of 150 nm and period of 500 nm, the (1,0) resonance mode sensitivity was measured as 6.7 nm/RIU and 6.0 nm/RIU respectively for as-fabricated EOT sample with the diameter of ~150 nm (Fig. 6.35b) and ~200 nm (Fig. 6.35d). However, on using annealed EOT samples, the sensitivity of 16.77 nm/RIU for ~150 nm (Fig. 6.35a) diameter and 40 nm/RIU for ~200 nm diameter (Fig. 6.35c) were measured respectively.

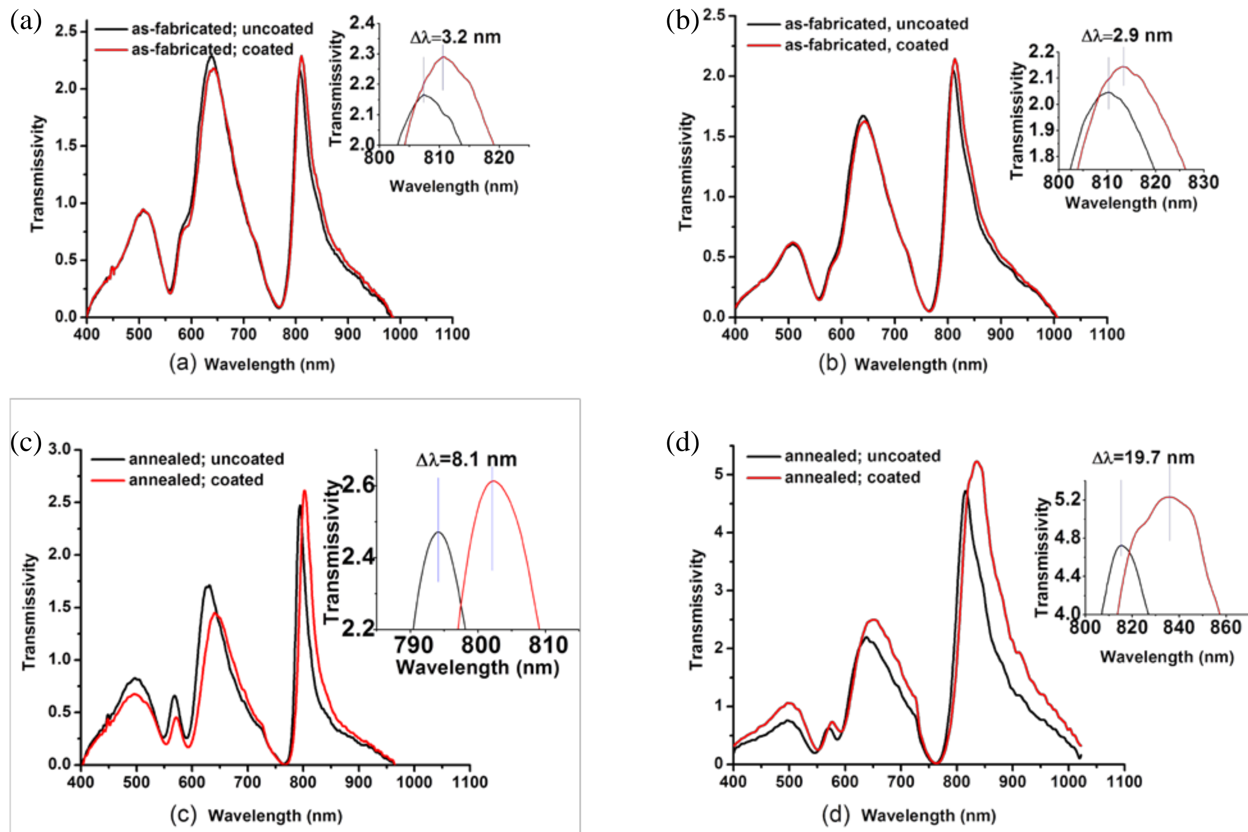

Figure 6.35 Measured transmission spectrum of a) annealed hole array of diameter of 149 nm; b) as-fabricated hole array of diameter of 153 nm; c) annealed hole array of diameter of 208nm and d)as-fabricated hole array of diameter of 209 nm.

6.7. Conclusion

The double liftoff process technique was developed for nano-hole arrays fabrication on a thick layer (100 nm) of gold utilizing the technique of electron beam lithography. This process is versatile for the fabrication of many kinds of high-aspect-ratio noble metal structures. The fabricated samples were annealed at 600°C under Ar atmosphere for 1h to improve the gold film quality. It was found that the roughness of the deposited film surface was reduced by 72 % and the sensitivity was increased by 32 nm/RIU as a result of annealing. It was also found that the optical transmission intensity of the annealed hole array of similar hole diameter was increased more than twice which is due to smaller absorption/scattering of the incident light and surface

waves from the gold film surface. Furthermore, imprint method, electroplating method, and patterning on membrane were applied for the fabrication of nano-hole arrays.

Chapter 7

Conclusions of Completed Works

This thesis is focused on the nanofabrication and its application in plasmonic chemical and bio-sensors. The contribution thus is the development of novel nanofabrication techniques and nanostructures for the sensors based on surface plasmon (SP).

For the first part on nanofabrication, several projects have been done:

(1) Fabrication of flexible mold for hybrid nanoimprint-soft lithography through sacrificial PMGI master mold was developed in this work. By a sacrificial PMGI master mold, the problems of resist wetting and mold release was avoided. By this method, the record of pattern replication by soft mold with sub-10 nm resolution was achieved.

(2) Charging effect reduction in electron beam lithography with nA beam current was studied. Charging effect is a serious issue when performing electron beam lithography using high beam current. Several aspects were examined in this work, including the exposure sequence, the sensitivity of resists, and the conductivity of the substrates.

(3) Large-area tilted nanostructure array was fabricated by electron beam exposure. The fabrication of large-area tilted nanostructures is a challenge in nanofabrication. In this work, the function of dynamic focus during electron beam scanning was utilized to overcome this problem. Metal plating and PDMS casting can be used for pattern transfer.

(4) Resists and the development conditions were studied for higher resolution and higher sensitivity.

(5) Electron beam lithography on irregular surfaces with evaporated polystyrene was demonstrated. By evaporation instead of traditional spin-coating method, AFM tips and optical fibers were patterned successfully.

For the second part on surface plasmonic sensor, two projects have been done:

(1) Bowtie-shape nano-antenna structure of sub-10 nm gap for SERS sensor was fabricated with the resolution down to 3 nm by exposing resist on Si_3N_4 membrane. By controlling the gap size during electron beam lithography, the surface plasmon enhancement was tuned accurately. High sensitivity of Au bowties nano-antenna with sub-10 nm gap was achieved at low concentration of the target molecule (10^{-7} mM 1,2-di(4-pyridyl)ethylene in ethanol solution) and the SERS enhancement of 10^7 was resulted from the corresponding bowtie structure.

(2) Nano hole array as extraordinary optical transmission (EOT) sensor was studied. Double liftoff process was demonstrated as a versatile method for the fabrication of high-aspect-ratio Au nanostructures. Annealing method was utilized in this work to improve the smoothness of Au film. The sensitivity of EOT sensor was increased by 32 nm/RIU as a result of annealing. Beside the double liftoff process, several techniques were developed for EOT structures, including electro-plating, nanoimprint method and deposition on membrane.

Appendix A: List of publication

(1) **Zhang J.**, Irannejad M. and Cui B. “Bowtie nano-antenna with single digit nanometer gap for surface enhanced Raman scattering (SERS)”, *Nano Photonics*, submitted

(2) **Zhang J.**, Irannejad M. and Cui B. “Sensitivity enhancement of extraordinary optical transmission sensor by annealed gold nano-hole array”, under preparation

(3) **Zhang J.**, Con C., and Cui B. “Electron beam lithography on irregular surfaces using evaporated resist”, *ACS Nano*, revised manuscript submitted

(4) Con C., **Zhang J.** and Cui B. “Nanofabrication of high aspect ratio structures using evaporated resist containing metal”, *Nanotechnology*, accepted

(5) Zhang W., Yang K. F., Pan Z.**, Zhang J.**, and Zhao B. “Bio-inspired dopamine functionalization of polypyrrole for improved adhesion and conductivity”, *Macromol. Rapid Commun.* **35**, 350-354 (2014)

(6) Irannejad M., **Zhang J.**, Yavuz M., and Cui B. “Numerical study of optical behavior of nano-hole array with non-vertical sidewall profile”, *Plasmonics*, in process

(7) **Zhang J.**, Shokouhi B. and Cui B. “Tilted nanostructure fabrication by electron beam lithography” *J. Vac. Sci. Technol. B*, 30, 06F302 (2012).

(8) Con C., **Zhang J.**, Jahed Z., Tsui T. Y., Yavuz M. and Cui B. “Thermal nanoimprint lithography using fluoropolymer mold”, *Microelectron. Eng.*, 98, 246–249, (2012).

(9) Zhang J., Hu X., **Zhang J.**, Cui Y., Yuan C., Ge H., Chen Y., Wu W., and Xia Q. “A fast thermal-curing nanoimprint resist based on cationic polymerizable epoxysiloxane”, *Nanoscale Research Letter*, 7(1), 380-392, (2012).

(10) Con C., Dey R., Ferguson M., **Zhang J.**, Mansour R., Yavuz M. and Cui B. “High molecular weight polystyrene as very sensitive electron beam resist”, *Microelectron. Eng.*, 98, 254–257, (2012).

(11) **Zhang J.**, Fouad M., Yavuz M. and Cui B. “Charging effect reduction in electron beam lithography with nA beam current”, *Microelectron. Eng.*, 88(8), 2196-2199 (2011).

(12) **Zhang J.**, Cui B. and Ge H. “Fabrication of flexible mold for hybrid nanoimprint-soft lithography”, *Microelectron. Eng.*, 88(8), 2192-2195 (2011).

(13) Shokouhi B., **Zhang J.** and Cui B. “Very high sensitivity ZEP resist using MEK:MIBK developer”, *Micro & Nano Lett.*, 6(12), 992–994 (2011).

Appendix B: Conference presentations

(1) **Zhang J.**, Irannejad M. and Cui B. "Smooth Au film by annealing for enhanced extraordinary optical transmission", 58th International Conference on Electron, Ion and Photon Beam Technology and Nano-fabrication (EIPBN), Washington DC, US, 2014 (submitted)

(2) **Zhang J.**, Cao K., Wang X. S. and Cui B. "Metal-containing polymer as electron beam resist with high resolution and high etching resistivity ", 58th International Conference on Electron, Ion and Photon Beam Technology and Nano-fabrication (EIPBN), Washington DC, US, 2014 (submitted)

(3) Irannejad M., **Zhang J.**, Yavuz M. and Cui B. "Numerical investigation of optical behavior of nano-hole array with non-vertical sidewall profile", 58th International Conference on Electron, Ion and Photon Beam Technology and Nano-fabrication (EIPBN), Washington DC, US, 2014 (submitted)

(4) Irannejad M., **Zhang J.**, Yavuz M. and Cui B. "Sensitivity enhancement of gold nano-hole array“, 6th International Conference on Optical, Optoelectronic and Photonic Materials and Applications, Leeds, UK, 2014 (accepted)

(5) **Zhang J.**, Irannejad M. and Cui B. "Fabrication of gold bowtie nano-antenna by E-beam Lithography on Si3N4 membrane for SERS", 57th International Conference on Electron, Ion and Photon Beam Technology and Nano-fabrication (EIPBN), Nashville, US, May 2013.

(6) (invited talk) **Zhang J.** and Cui B. "Nanofabrication on non-flat surface using evaporated electron beam resist", 8th IEEE international Conference on Nano/Micro Engineered and Molecular Systems, Suzhou, PR China, April 2013

(7) **Zhang J.**, Shokouhi B. and Cui B. "Fabrication of tilted nano-pillar and nano-hole arrays by electron beam exposure", 3rd International Conference on Nanotechnology: Fundamentals and Applications, Montreal, Canada, August 2012.

(8) **Zhang J.** and Cui B. "Electron beam lithography with evaporated resist", 56th International Conference on Electron, Ion and Photon Beam Technology and Nano-fabrication (EIPBN), Waikoloa, US, May 2012.

(9) **Zhang J.**, Shokouhi B. and Cui B. "Periodic tilted Au structure fabrication by electron beam exposure", 56th International Conference on Electron, Ion and Photon Beam Technology and Nano-fabrication (EIPBN), Waikoloa, US, May 2012.

(10) Con C., **Zhang J.**, Ferguson M., Yavuz M. and Cui B. “High molecular weight polystyrene as very sensitive electron beam resist", 37th International Conference on Micro- and Nano-Engineering, Berlin, Germany, September 2011.

(11) **Zhang J.**, Shokouhi B. and Cui B. "Periodic tilted structure fabrication by electron beam exposure", 37th International Conference on Micro- and Nano-Engineering, Berlin, Germany, September 2011.

(12) **Zhang J.**, Shokouhi B. and Cui B. “High sensitivity electron beam lithography using ZEP resist and MEK:MIBK developer”, 55th International Conference on Electron, Ion and Photon Beam Technology and Nano-fabrication (EIPBN), Las Vegas, US, June 2011.

(13) **Zhang J.** and Cui B. "Fabrication of flexible mold for hybrid nanoimprint-soft lithography", 36th International Conference on Micro- and Nano-Engineering, Genoa, Italy, September 2010.

(14) **Zhang J.** and Cui B. "Electron beam lithography using nA beam current with reduced charging effect", 36th International Conference on Micro- and Nano-Engineering, Genoa, Italy, September 2010.

Reference

1 Feynman, R. P. There's plenty of room at the bottom. *Engineering and Science* **23**, 22-36 (1960).

2 Ethan, M. Establishing Moore's Law. *IEEE Annales* **28**, 62-75 (2006).

3 Nishinaga, T., Nishioka, Y., Ito, H. & Hiraki, A. ISCSI-3 - Proceedings of the Third International Symposium on the Control of Semiconductor Interfaces. *Appl Surf Sci* **159**, Xiii-Xiii (2000).

4 Born, M. & Wolf, E. *Principles of optics: electromagnetic theory of propagation, interference and diffraction of light*. (CUP Archive, 1999).

5 Mizutani, U. *et al.* Fabrication of Mo/Si multilayer mirrors for extreme ultraviolet lithography by means of superconducting bulk magnet magnetron sputtering. *Physica C* **468**, 1456-1460 (2008).

6 Grigorescu, A. E., van der Krogt, M. C., Hagen, C. W. & Kruit, P. 10 nm lines and spaces written in HSQ, using electron beam lithography. *Microelectron Eng* **84**, 822-824 (2007).

7 Chou, S. Y., Krauss, P. R. & Renstrom, P. J. Imprint of Sub-25 Nm Vias and Trenches in Polymers. *Appl Phys Lett* **67**, 3114-3116 (1995).

8 Schulz, H. *et al.* Impact of molecular weight of polymers and shear rate effects for nanoimprint lithography. *Microelectron Eng* **83**, 259-280 (2006).

9 Guo, L. J. Recent progress in nanoimprint technology and its applications. *J Phys D Appl Phys* **37**, R123-R141 (2004).

10 Parikh, A. N., Allara, D. L., Azouz, I. B. & Rondelez, F. An Intrinsic Relationship between Molecular-Structure in Self-Assembled N-Alkylsiloxane Monolayers and Deposition Temperature. *J Phys Chem-Us* **98**, 7577-7590 (1994).

11 Tredgold, R. H. An Introduction to Ultrathin Organic Films - from Langmuir-Blodgett to Self-Assembly - Ulman,A. *Nature* **354**, 120-120 (1991).

12 Wu, W. *et al.* Cross-linked polymer replica of a nanoimprint mold at 30 nm half-pitch. *Nano Lett* **5**, 179-182 (2005).

13 Hirai, Y. Polymer science in nanoimprint lithography. *J Photopolym Sci Tec* **18**, 551-558 (2005).

14 Muhlberger, M. *et al.* A Moire method for high accuracy alignment in nanoimprint lithography. *Microelectron Eng* **84**, 925-927 (2007).

15 Chou, S. Y., Keimel, C. & Gu, J. Ultrafast and direct imprint of nanostructures in silicon. *Nature* **417**, 835-837 (2002).

16 Ruchhoeft, P. *et al.* Patterning curved surfaces: Template generation by ion beam proximity lithography and relief transfer by step and flash imprint lithography. *J Vac Sci Technol B* **17**, 2965-2969 (1999).

17 Szuromi, P. D. Handbook of nanostructured materials and nanotechnology. *Science* **288**, 1596-1596 (2000).

18 Schift, H. & Kristensen, A. *Nanoimprint lithography, Ch. 8, 239-278* (Springer Berlin Heidelberg, 2007).

19 Austin, M. D. *et al.* Fabrication of 5 nm linewidth and 14 nm pitch features by nanoimprint lithography. *Appl Phys Lett* **84**, 5299-5301 (2004).

20 Kehagias, N. *et al.* Reverse-contact UV nanoimprint lithography for multilayered structure fabrication. *Nanotechnology* **18** (2007).

21 Kumar, A. & Whitesides, G. M. Features of Gold Having Micrometer to Centimeter Dimensions Can Be Formed through a Combination of Stamping with an Elastomeric Stamp and an Alkanethiol Ink Followed by Chemical Etching. *Appl Phys Lett* **63**, 2002-2004 (1993).

22 Whitesides, G. M. & Xia, Y. N. Soft lithography. *Angew Chem Int Edit* **37**, 551-575 (1998).

23 Ge, H. X. *et al.* Hybrid Nanoimprint-Soft Lithography with Sub-15 nm Resolution. *Nano Lett* **9**, 2306-2310 (2009).

24 Cheng, X., Guo, L. J. & Fu, P. F. Room-temperature, low-pressure nanoimprinting based on cationic photopolymerization of novel epoxysilicone monomers. *Adv Mater* **17**, 1419-1424 (2005).

25 Whitesides, G. M., Lee, J. N. & Park, C. Solvent compatibility of poly(dimethylsiloxane)-based microfluidic devices. *Anal Chem* **75**, 6544-6554 (2003).

26 Odom, T. W., Love, J. C., Wolfe, D. B., Paul, K. E. & Whitesides, G. M. Improved pattern transfer in soft lithography using composite stamps. *Langmuir* **18**, 5314-5320 (2002).

27 Duan, X. R. *et al.* Preliminary results of ELMy H-mode experiments on the HL-2A tokamak. *Nucl Fusion* **50** (2010).

28 Mayadas, A. F. & Laibowit.Rb. One-Dimensional Superconductors. *Phys Rev Lett* **28**, 156-& (1972).

29 Yamazaki, K. & Namatsu, H. 5-nm-order electron-beam lithography for nanodevice fabrication. *Jpn J Appl Phys 1* **43**, 3767-3771 (2004).

30 Cui, Z. *Nanofabrication : principles, capabilities, and limits*. 1st edn, (Springer, 2008).

31 Mohsin, M. A. & Cowie, J. M. G. Enhanced Sensitivity in the Electron-Beam Resist Poly(Methyl Methacrylate) Using Improved Solvent Developer. *Polymer* **29**, 2130-2135 (1988).

32 Bernstein, G. H., Hill, D. A. & Liu, W. P. New High-Contrast Developers for Poly(Methyl Methacrylate) Resist. *J Appl Phys* **71**, 4066-4075 (1992).

33 Yasin, S., Hasko, D. G. & Ahmed, H. Comparison of MIBK/IPA and water/IPA as PMMA developers for electron beam nanolithography. *Microelectron Eng* **61-2**, 745-753 (2002).

34 Hoole, A. C. F., Welland, M. E. & Broers, A. N. Negative PMMA as a high-resolution resist - the limits and possibilities. *Semicond Sci Tech* **12**, 1166-1170, doi:Doi 10.1088/0268-1242/12/9/017 (1997).

35 Ma, S. Q., Con, C., Yavuz, M. & Cui, B. Polystyrene negative resist for high-resolution electron beam lithography. *Nanoscale Res Lett* **6**, 446 (2011).

36 Bentley, S., Li, X., Moran, D. A. J. & Thayne, I. G. Two methods of realising 10 nm T-gate lithography. *Microelectron Eng* **86**, 1067-1070 (2009).

37 Bonam, R., Verhagen, P., Munder, A. & Hartley, J. Performance characterization of negative resists for sub-10-nm electron beam lithography. *J Vac Sci Technol B* **28**, C6c34-C36c40 (2010).

38 Veres, T. & Cui, B. High resolution electron beam lithography of PMGI using solvent developers. *Microelectron Eng* **85**, 810-813 (2008).

39 Chen, C. C., Hsieh, P. C. H., Wang, G. M., Chen, W. C. & Yeh, M. L. The influence of surface morphology and rigidity of the substrata on cell motility. *Mater Lett* **63**, 1872-1875, doi:DOI 10.1016/j.matlet.2009.05.073 (2009).

40 Ou, F. S. *et al.* Hot-Spot Engineering in Polygonal Nanofinger Assemblies for Surface Enhanced Raman Spectroscopy. *Nano Lett* **11**, 2538-2542 (2011).

41 Murphy, M. P., Aksak, B. & Sitti, M. Adhesion and anisotropic friction enhancements of angled heterogeneous micro-fiber arrays with spherical and spatula tips. *J Adhes Sci Technol* **21**, 1281-1296 (2007).

42 Kim, T. I., Jeong, H. E., Suh, K. Y. & Lee, H. H. Stooped Nanohairs: Geometry-Controllable, Unidirectional, Reversible, and Robust Gecko-like Dry Adhesive. *Adv Mater* **21**, 2276-2281 (2009).

43 Boesel, L. F., Greiner, C., Arzt, E. & del Campo, A. Gecko-Inspired Surfaces: A Path to Strong and Reversible Dry Adhesives. *Adv Mater* **22**, 2125-2137 (2010).

44 Zheng, Y. M., Gao, X. F. & Jiang, L. Directional adhesion of superhydrophobic butterfly wings. *Soft Matter* **3**, 178-182 (2007).

45 Kwak, M. K., Jeong, H. E., Kim, T. I., Yoon, H. & Suh, K. Y. Bio-inspired slanted polymer nanohairs for anisotropic wetting and directional dry adhesion. *Soft Matter* **6**, 1849-1857 (2010).

46 Fang, H., Li, X. D., Song, S., Xu, Y. & Zhu, J. Fabrication of slantingly-aligned silicon nanowire arrays for solar cell applications. *Nanotechnology* **19**, 255703 (2008).

47 Aksak, B., Murphy, M. P. & Sitti, M. Adhesion of biologically inspired vertical and angled polymer microfiber arrays. *Langmuir* **23**, 3322-3332 (2007).

48 del Campo, A. & Greiner, C. SU-8: a photoresist for high-aspect-ratio and 3D submicron lithography. *J Micromech Microeng* **17**, R81-R95 (2007).

49 Jeong, H. E., Lee, J. K., Kim, H. N., Moon, S. H. & Suh, K. Y. A nontransferring dry adhesive with hierarchical polymer nanohairs. *P Natl Acad Sci USA* **106**, 5639-5644 (2009).

50 Con, C. *et al.* High molecular weight polystyrene as very sensitive electron beam resist. *Microelectron Eng* **98**, 254-257 (2012).

51 Xia, Y. N. & Whitesides, G. M. Soft lithography. *Annu Rev Mater Sci* **28**, 153-184 (1998).

52 Ko, H. C. *et al.* A hemispherical electronic eye camera based on compressible silicon optoelectronics. *Nature* **454**, 748-753 (2008).

53 Murphy, M. P., Kim, S. & Sitti, M. Enhanced Adhesion by Gecko-Inspired Hierarchical Fibrillar Adhesives. *Acs Appl Mater Inter* **1**, 849-855 (2009).

54 Zamarreno, C. R., Matias, I. R. & Arregui, F. J. Nanofabrication Techniques Applied to the Development of Novel Optical Fiber Sensors Based on Nanostructured Coatings. *Ieee Sens J* **12**, 2699-2710 (2012).

55 Bailey, T. *et al.* Step and flash imprint lithography: Template surface treatment and defect analysis. *J Vac Sci Technol B* **18**, 3572-3577 (2000).

56 Kou, J. L. *et al.* Microfiber-Based Bragg Gratings for Sensing Applications: A Review. *Sensors-Basel* **12**, 8861-8876 (2012).

57 Bell, D. C., Lemme, M. C., Stern, L. A., RWilliams, J. & Marcus, C. M. Precision cutting and patterning of graphene with helium ions. *Nanotechnology* **20**, 455301 (2009).

58 Pedersen, R. H. *et al.* Electron beam lithography using plasma polymerized hexane as resist. *Microelectron Eng* **87**, 1112-1114 (2010).

59 Kelkar, P. S. *et al.* Nano patterning on optical fiber and laser diode facet with dry resist. *Journal of Vacuum Science & Technology A* **22**, 743-746 (2004).

60 Lavallee, E. *et al.* in *Microprocesses and Nanotechnology Conference, 2003. Digest of Papers. 2003 International.* 152-153.

61 Awad, Y. *et al.* Arrays of holes fabricated by electron-beam lithography combined with image reversal process using nickel pulse reversal plating. *Journal of Vacuum Science & Technology A* **22**, 1040-1043 (2004).

62 King, G. M., Schürmann, G., Branton, D. & Golovchenko, J. A. Nanometer Patterning with Ice. *Nano Lett* **5**, 1157-1160 (2005).

63 Han, A., Kuan, A., Golovchenko, J. & Branton, D. Nanopatterning on Nonplanar and Fragile Substrates with Ice Resists. *Nano Lett* **12**, 1018-1021 (2012).

64 Gardener, J. A. & Golovchenko, J. A. Ice-assisted electron beam lithography of graphene. *Nanotechnology* **23**, 185302 (2012).

65 Bahlke, M. E., Mendoza, H. A., Ashall, D. T., Yin, A. S. & Baldo, M. A. Dry Lithography of Large-Area, Thin-Film Organic Semiconductors Using Frozen CO2 Resists. *Adv Mater* **24**, 6136-6140 (2012).

66 Muray, A., Isaacson, M. & Adesida, I. AlF3—A new very high resolution electron beam resist. *Appl Phys Lett* **45**, 589-591 (1984).

67 Macaulay, J. M., Allen, R. M., Brown, L. M. & Berger, S. D. Nanofabrication using inorganic resists. *Microelectron Eng* **9**, 557-560 (1989).

68 Pennelli, G., Totaro, M. & Piotto, M. Selective Doping of Silicon Nanowires by Means of Electron Beam Stimulated Oxide Etching. *Nano Lett* **12**, 1096-1101 (2012).

69 Svorcik, V., Rybka, V., Efimenko, K. & Hnatowicz, V. Deposition of polystyrene films by vacuum evaporation. *J Mater Sci Lett* **16**, 1564-1566 (1997).

70 Dey, R. K. & Cui, B. Effect of molecular weight distribution on e-beam exposure properties of polystyrene. *Nanotechnology* **24**, 245302 (2013).

71 Kashyap, R. Fiber Bragg Gratings Second Edition Preface. *Fiber Bragg Gratings, 2nd Edition*, Xv-Xvi (2010).

72 Xu, Q. B. *et al.* Fabrication of large-area patterned nanostructures for optical applications by nanoskiving. *Nano Lett* **7**, 2800-2805 (2007).

73 Paul, K. E., Zhu, C., Love, J. C. & Whitesides, G. M. Fabrication of mid-infrared frequency-selective surfaces by soft lithography. *Appl Optics* **40**, 4557-4561 (2001).

74 Kneipp, K., Kneipp, H., Itzkan, I., Dasari, R. R. & Feld, M. S. Surface-enhanced Raman scattering and biophysics. *J Phys-Condens Mat* **14**, R597-R624 (2002).

75 Muskens, O. L. *et al.* Large Photonic Strength of Highly Tunable Resonant Nanowire Materials. *Nano Lett* **9**, 930-934 (2009).

76 Kang, S. *et al.* Subwavelength plasmonic lens patterned on a composite optical fiber facet for quasi-one-dimensional Bessel beam generation. *Appl Phys Lett* **98**, 241103 (2011).

77 Liu, Y. X., Xu, H., Stief, F., Zhitenev, N. & Yu, M. Far-field superfocusing with an optical fiber based surface plasmonic lens made of nanoscale concentric annular slits. *Opt Express* **19**, 20233-20243 (2011).

78 Wang, H. X., Zhou, W., Cui, Y., Wang, G. H. & Shum, P. P. Focused Ion Beam Nanoscale Patterned Transmission-Enhanced Fiber-Optic Tips. *J Nanosci Nanotechno* **13**, 4581-4586 (2013).

79 Jia, P. P., Jiang, H., Sabarinathan, J. & Yang, J. Plasmonic nanohole array sensors fabricated by template transfer with improved optical performance. *Nanotechnology* **24**, 195501 (2013).
80 Ashcroft, N. W. & Mermin, N. D. *Solid state physics*. (Saunders College, 1976).
81 Barnes, W. L., Dereux, A. & Ebbesen, T. W. Surface plasmon subwavelength optics. *Nature* **424**, 824-830 (2003).
82 Nuzzo, R. G. *et al.* Nanostructured plasmonic sensors. *Chem Rev* **108**, 494-521 (2008).
83 Raether, H. Surface-Plasmons on Smooth and Rough Surfaces and on Gratings. *Springer Tr Mod Phys* **111**, 1-133 (1988).
84 Henzie, J., Lee, J., Lee, M. H., Hasan, W. & Odom, T. W. Nanofabrication of Plasmonic Structures. *Annu Rev Phys Chem* **60**, 147-165 (2009).
85 Daniel, M. C. *et al.* Gold nanoparticles containing redox-active supramolecular dendrons that recognize H2PO4-. *Chem Commun*, 2000-2001 (2001).
86 Tripp, R. A., Dluhy, R. A. & Zhao, Y. P. Novel nanostructures for SERS biosensing. *Nano Today* **3**, 31-37 (2008).
87 Ebbesen, T. W., Lezec, H. J., Ghaemi, H. F., Thio, T. & Wolff, P. A. Extraordinary optical transmission through sub-wavelength hole arrays. *Nature* **391**, 667-669 (1998).
88 Yee, K. S. Numerical Solution of Initial Boundary Value Problems Involving Maxwells Equations in Isotropic Media. *Ieee T Antenn Propag* **Ap14**, 302 (1966).
89 Kumar, C. S. *Raman spectroscopy for nanomaterials characterization*. (Springer Verlag, 2012).
90 Jeanmaire, D. L. & Vanduyne, R. P. Surface Raman Spectroelectrochemistry .1. Heterocyclic, Aromatic, and Aliphatic-Amines Adsorbed on Anodized Silver Electrode. *J Electroanal Chem* **84**, 1-20 (1977).
91 Albrecht, M. G. & Creighton, J. A. Anomalously Intense Raman-Spectra of Pyridine at a Silver Electrode. *J Am Chem Soc* **99**, 5215-5217 (1977).
92 Fleischmann, M., Hendra, P. J. & McQuillan, A. J. Raman spectra of pyridine adsorbed at a silver electrode. *Chem Phys Lett* **26**, 163-166 (1974).
93 Kerker, M. Estimation of Surface-Enhanced Raman-Scattering from Surface-Averaged Electromagnetic Intensities. *J Colloid Interf Sci* **118**, 417-421 (1987).
94 Gersten, J. & Nitzan, A. Electromagnetic Theory of Enhanced Raman-Scattering by Molecules Adsorbed on Rough Surfaces. *J Chem Phys* **73**, 3023-3037 (1980).
95 Metiu, H. & Das, P. The Electromagnetic Theory of Surface Enhanced Spectroscopy. *Annu Rev Phys Chem* **35**, 507-536 (1984).
96 Böttcher, C. J. F. *Theory of electric polarisation*. (Elsevier Pub. Co., 1952).
97 Stoner, E. C. XCVII. The demagnetizing factors for ellipsoids. *Philosophical Magazine Series 7* **36**, 803-821 (1945).
98 Yang, W. H., Schatz, G. C. & Vanduyne, R. P. Discrete Dipole Approximation for Calculating Extinction and Raman Intensities for Small Particles with Arbitrary Shapes. *J Chem Phys* **103**, 869-875 (1995).
99 Yin, L. *et al.* Surface plasmons at single nanoholes in Au films. *Appl Phys Lett* **85**, 467-469 (2004).
100 Schatz, G. C. & Hao, E. Electromagnetic fields around silver nanoparticles and dimers. *J Chem Phys* **120**, 357-366 (2004).
101 Kneipp, K., Kneipp, H., Moskovits, M. & SpringerLink (Online service). in *Topics in applied physics,* (Springer-Verlag Berlin Heidelberg, Berlin, Heidelberg, 2006).

102 Cui, L. *et al.* Orientation change of adsorbed pyrazine on roughened rhodium electrodes as probed by surface-enhanced Raman spectroscopy. *J Phys Chem B* **109**, 17597-17602 (2005).

103 Lin, X. F., Ren, B. & Tian, Z. Q. Electrochemical and surface-enhanced Raman spectroscopic studies on the adsorption and electrooxidation of C-1 molecules on a roughened Rh electrode. *J Phys Chem B* **108**, 981-986 (2004).

104 Zheng, J. Z., Ren, B., Wu, D. Y. & Tian, Z. Q. Thiourea adsorption on a Pt surface as detected by electrochemical methods and surface-enhanced Raman spectroscopy. *J Electroanal Chem* **574**, 285-289 (2005).

105 Kneipp, K. *et al.* Single Molecule Detection Using Surface-Enhanced Raman Scattering (SERS). *Phys Rev Lett* **78**, 1667-1670 (1997).

106 Le Ru, E. C., Meyer, M. & Etchegoin, P. G. Proof of Single-Molecule Sensitivity in Surface Enhanced Raman Scattering (SERS) by Means of a Two-Analyte Technique. *The Journal of Physical Chemistry B* **110**, 1944-1948 (2006).

107 Michaels, A. M., Jiang & Brus, L. Ag Nanocrystal Junctions as the Site for Surface-Enhanced Raman Scattering of Single Rhodamine 6G Molecules. *The Journal of Physical Chemistry B* **104**, 11965-11971 (2000).

108 Xu, H. X., Bjerneld, E. J., Kall, M. & Borjesson, L. Spectroscopy of single hemoglobin molecules by surface enhanced Raman scattering. *Phys Rev Lett* **83**, 4357-4360 (1999).

109 Dieringer, J. A., Lettan, R. B., Scheidt, K. A. & Van Duyne, R. P. A frequency domain existence proof of single-molecule surface-enhanced Raman Spectroscopy. *J Am Chem Soc* **129**, 16249-16256 (2007).

110 Qian, X. M. & Nie, S. M. Single-molecule and single-nanoparticle SERS: from fundamental mechanisms to biomedical applications. *Chem Soc Rev* **37**, 912-920 (2008).

111 Camden, J. P. *et al.* Probing the structure of single-molecule surface-enhanced Raman scattering hot spots. *J Am Chem Soc* **130**, 12616-12617 (2008).

112 Fleischm.M, Hendra, P. J. & Mcquilla.Aj. *Raman-Spectra of Pyridine Adsorbed at a Silver Electrode* (thesis, 1974).

113 Albrecht, M. G. & Creighton, J. A. Anomalously intense Raman spectra of pyridine at a silver electrode. *J Am Chem Soc* **99**, 5215-5217 (1977).

114 Moskovits, M. IMAGING Spot the hotspot. *Nature* **469**, 307-308 (2011).

115 Cang, H. *et al.* Probing the electromagnetic field of a 15-nanometre hotspot by single molecule imaging. *Nature* **469**, 385-388 (2011).

116 Hartschuh, A., Anderson, N. & Novotny, L. Near-field Raman spectroscopy using a sharp metal tip. *J Microsc-Oxford* **210**, 234-240 (2003).

117 Pazos-Perez, N. *et al.* Growth of Sharp Tips on Gold Nanowires Leads to Increased Surface-Enhanced Raman Scattering Activity. *J Phys Chem Lett* **1**, 24-27 (2010).

118 Aldeanueva-Potel, P. *et al.* Spiked Gold Beads as Substrates for Single-Particle SERS. *Chemphyschem* **13**, 2561-2565 (2012).

119 Song, H. M., Deng, L. & Khashab, N. M. Intracellular surface-enhanced Raman scattering (SERS) with thermally stable gold nanoflowers grown from Pt and Pd seeds. *Nanoscale* **5**, 4321-4329 (2013).

120 Vitol, E. A. *et al.* In Situ Intracellular Spectroscopy with Surface Enhanced Raman Spectroscopy (SERS)-Enabled Nanopipettes. *Acs Nano* **3**, 3529-3536 (2009).

121 Hinde, R. J., Sepaniak, M. J., Compton, R. N., Nordling, J. & Lavrik, N. Surface-enhanced resonance Raman scattering of adsorbates under liquid nitrogen. *Chem Phys Lett* **339**, 167-173 (2001).

122 Speed, J. D. *et al.* SERS from molecules bridging the gap of particle-in-cavity structures. *Chem Commun* **47**, 6335-6337 (2011).

123 Merk, V., Kneipp, J. & Leosson, K. Gap Size Reduction and Increased SERS Enhancement in Lithographically Patterned Nanoparticle Arrays by Templated Growth. *Adv Opt Mater* **1**, 313-318 (2013).

124 Kwon, S. H. Plasmonic Ruler With Angstrom Distance Resolution Based on Double Metal Blocks. *Ieee Photonic Tech L* **25**, 1619-1622 (2013).

125 Wu, W., Hu, M., Ou, F. S., Li, Z. Y. & Williams, R. S. Cones fabricated by 3D nanoimprint lithography for highly sensitive surface enhanced Raman spectroscopy. *Nanotechnology* **21**, 255502 (2010).

126 Hu, M. *et al.* Gold Nanofingers for Molecule Trapping and Detection. *J Am Chem Soc* **132**, 12820-12822 (2010).

127 Veres, T., Cui, B. & Clime, L. Fabrication of nanostar arrays by nanoimprint lithography. *Journal of Vacuum Science & Technology B* **28**, C6O26-C26O29 (2010).

128 Fromm, D. P., Sundaramurthy, A., Schuck, P. J., Kino, G. & Moerner, W. E. Gap-Dependent Optical Coupling of Single “Bowtie” Nanoantennas Resonant in the Visible. *Nano Lett* **4**, 957-961 (2004).

129 Kinkhabwala, A. *et al.* Large single-molecule fluorescence enhancements produced by a bowtie nanoantenna. *Nat Photonics* **3**, 654-657 (2009).

130 Fromm, D. P. *et al.* Exploring the chemical enhancement for surface-enhanced Raman scattering with Au bowtie nanoantennas. *J Chem Phys* **124**, 061101 (2006).

131 Qin, L. *et al.* Designing, fabricating, and imaging Raman hot spots. *Proceedings of the National Academy of Sciences* **103**, 13300-13303 (2006).

132 Hatab, N. A. *et al.* Free-Standing Optical Gold Bowtie Nanoantenna with Variable Gap Size for Enhanced Raman Spectroscopy. *Nano Lett* **10**, 4952-4955 (2010).

133 Dhawan, A., Gerhold, M. & Vo-Dinh, T. Theoretical Simulation and Focused Ion Beam Fabrication of Gold Nanostructures for Surface-Enhanced Raman Scattering (SERS). *Nanobiotechnol* **3**, 164-171 (2007).

134 Lin, Y. Y., Liao, J. D., Ju, Y. H., Chang, C. W. & Shiau, A. L. Focused ion beam-fabricated Au micro/nanostructures used as a surface enhanced Raman scattering-active substrate for trace detection of molecules and influenza virus. *Nanotechnology* **22**, 185308 (2011).

135 Melli, M. *et al.* Reaching the Theoretical Resonance Quality Factor Limit in Coaxial Plasmonic Nanoresonators Fabricated by Helium Ion Lithography. *Nano Lett* **13**, 2687-2691 (2013).

136 Li, W. D., Ding, F., Hu, J. & Chou, S. Y. Three-dimensional cavity nanoantenna coupled plasmonic nanodots for ultrahigh and uniform surface-enhanced Raman scattering over large area. *Opt Express* **19**, 3925-3936 (2011).

137 Zou, S. L., Janel, N. & Schatz, G. C. Silver nanoparticle array structures that produce remarkably narrow plasmon lineshapes. *J Chem Phys* **120**, 10871-10875 (2004).

138 Thomas, S. *et al.* Raman, infrared, SERS and DFT calculations of a triazole derivative (akacid). *Chem Phys Lett* **402**, 361-366 (2005).

139 Popp, J., Baia, M., Baia, L. & Kiefer, W. Surface-enhanced Raman scattering and density functional theoretical study of anthranil adsorbed on colloidal silver particles. *J Phys Chem B* **108**, 17491-17496 (2004).
140 Chang, T. H. P. Proximity Effect in Electron-Beam Lithography. *J Vac Sci Technol* **12**, 1271-1275 (1975).
141 Lee, S. Y. & Anbumony, K. Analysis of three-dimensional proximity effect in electron-beam lithography. *Microelectron Eng* **83**, 336-344 (2006).
142 Webster, M. N. *et al.* Proximity Effect in High-Voltage Electron-Beam Lithography on Ti/Pt/Au Metallization. *Microelectron Eng* **17**, 29-32 (1992).
143 Kim, S. *et al.* High-harmonic generation by resonant plasmon field enhancement. *Nature* **453**, 757-760 (2008).
144 Ils, P. *et al.* Fabrication of Ultrasmall Ingaas/Inp Nanostructures by High-Voltage Electron-Beam Lithography and Wet Chemical Etching. *Nato Adv Sci Inst Se* **264**, 77-80 (1994).
145 Gibbons, F. P., Robinson, A. P. G., Palmer, R. E., Manickam, M. & Preece, J. A. Ultrathin fullerene films as high-resolution molecular resists for low-voltage electron-beam lithography. *Small* **2**, 1003-1006 (2006).
146 Grigoresecu, A. E., van der Krogt, M. C. & Hagen, C. W. Sub-10 nm structures written in ultra-thin HSQ resist layers, using electron beam lithography - art. no. 65194A. *Advances in Resist Materials and Processing Technology XXIV* **6519**, A5194-A5194 (2007).
147 Hu, W. C., Bernstein, G. H., Sarveswaran, K. & Lieberman, M. Low temperature development of PMMA for sub-10-nm electron beam lithography. *2003 Third Ieee Conference on Nanotechnology, Vols One and Two, Proceedings*, 602-605 (2003).
148 Hu, W. C., Sarveswaran, K., Lieberman, M. & Bernstein, G. H. Sub-10 nm electron beam lithography using cold development of poly(methylmethacrylate). *J Vac Sci Technol B* **22**, 1711-1716 (2004).
149 Haffner, M. *et al.* Influence of temperature on HSQ electron-beam lithography. *J Vac Sci Technol B* **25**, 2045-2048 (2007).
150 Yasin, S., Hasko, D. G. & Ahmed, H. Comparison of MIBK/IPA and water/IPA as PMMA developers for electron beam nanolithography. *Microelectron Eng* **61–62**, 745-753 (2002).
151 Shokouhi, B., Zhang, J. & Cui, B. Very high sensitivity ZEP resist using MEK:MIBK developer. *Micro Nano Lett* **6**, 992-994 (2011).
152 Zhang, J., Fouad, M., Yavuz, M. & Cui, B. Charging effect reduction in electron beam lithography with nA beam current. *Microelectron Eng* **88**, 2196-2199 (2011).
153 Frye, R. C., Rietman, E. A. & Cummings, K. D. Computation of Proximity Effect Corrections in Electron-Beam Lithography by a Neural Network. *Ieee Ijcnn*, A7-A14 (1990).
154 Seo, E. & Kim, O. Dose and shape modification proximity effect correction for forward-scattering range scale features in electron beam lithography. *Microprocesses and Nanotechnology 2000, Digest of Papers*, 158-159 (2000).
155 Manheller, M., Trellenkamp, S., Waser, R. & Karthauser, S. Reliable fabrication of 3 nm gaps between nanoelectrodes by electron-beam lithography. *Nanotechnology* **23**, 125302 (2012).

156 Vial, A. & Laroche, T. Description of dispersion properties of metals by means of the critical points model and application to the study of resonant structures using the FDTD method. *Journal of Physics D: Applied Physics* **40**, 7152 (2007).
157 Rakic, A. D., Djuri?ic, A. B., Elazar, J. M. & Majewski, M. L. Optical Properties of Metallic Films for Vertical-Cavity Optoelectronic Devices. *Appl. Opt.* **37**, 5271-5283 (1998).
158 Astilean, S. Noble-metal nanostructures for controlling surface plasmons and sensing molecules. *Radiat Phys Chem* **76**, 436-439 (2007).
159 Hatab, N. A.; Hsueh, C. H.; Gaddis, A. L.; Retterer, S. T.; Li, J. H.; Eres, G.; Zhang, Z. Y.; Gu, B. H. Free-Standing Optical Gold Bowtie Nanoantenna with Variable Gap Size for Enhanced Raman Spectroscopy (support information). *Nano Lett* **2010**, *10*, 4952.
160 Maier, S. A. *Plasmonics : fundamentals and applications*. (Springer, 2007).
161 Kretschm.E & Raether, H. Plasma Resonance Emission in Solids. *Z Naturforsch Pt A* **A 23**, 615 (1968).
162 Otto, A. Excitation of Nonradiative Surface Plasma Waves in Silver by Method of Frustrated Total Reflection. *Z Phys* **216**, 398 (1968).
163 Prasad, P. N. *Introduction to biophotonics*. (Wiley-Interscience, 2003).
164 Gobi, K. V., Matsumoto, K., Toko, K., Ikezaki, H. & Miura, N. Enhanced sensitivity of self-assembled-monolayer-based SPR immunosensor for detection of benzaldehyde using a single-step multi-sandwich immunoassay. *Anal Bioanal Chem* **387**, 2727-2735 (2007).
165 Gazzola, E. *et al.* Coupled SPP Modes on 1D Plasmonic Gratings in Conical Mounting. *Plasmonics*, 1-10 (2013).
166 Kan, T., Matsumoto, K. & Shimoyama, I. Tunable gold-coated polymer gratings for surface plasmon resonance coupling and scanning. *J Micromech Microeng* **20**, 085032 (2010).
167 Fu, H. K., Chen, C. W., Wang, C. H., Chen, T. T. & Chen, Y. F. Creating optical anisotropy of CdSe/ZnS quantum dots by coupling to surface plasmon polariton resonance of a metal grating. *Opt Express* **16**, 6361-6367 (2008).
168 Balci, S., Kocabas, A., Kocabas, C. & Aydinli, A. Slowing surface plasmon polaritons on plasmonic coupled cavities by tuning grating grooves. *Appl Phys Lett* **97**,131103 (2010).
169 Fehrembach, A. L., Enoch, S. & Sentenac, A. Highly directive light sources using two-dimensional photonic crystal slabs. *Appl Phys Lett* **79**, 4280-4282 (2001).
170 Harris, J. B., Preist, T. W., Sambles, J. R., Thorpe, R. N. & Watts, R. A. Optical response of bigratings. *J Opt Soc Am A* **13**, 2041-2049 (1996).
171 Gonzalez, M. U. *et al.* Analysis of the angular acceptance of surface plasmon Bragg mirrors. *Opt Lett* **32**, 2704-2706 (2007).
172 Weeber, J. C. *et al.* Near-field characterization of Bragg mirrors engraved in surface plasmon waveguides. *Phys Rev B* **70**, 235406 (2004).
173 Yin, L. L. *et al.* Subwavelength focusing and guiding of surface plasmons. *Nano Lett* **5**, 1399-1402 (2005).
174 Liu, Z. W. *et al.* Focusing surface plasmons with a plasmonic lens. *Nano Lett* **5**, 1726-1729 (2005).
175 Zia, R., Selker, M. D., Catrysse, P. B. & Brongersma, M. L. Geometries and materials for subwavelength surface plasmon modes. *J Opt Soc Am A* **21**, 2442-2446 (2004).
176 Berini, P. Plasmon-polariton waves guided by thin lossy metal films of finite width: Bound modes of symmetric structures. *Phys Rev B* **61**, 10484-10503 (2000).

177 MacDonald, K. F., Samson, Z. L., Stockman, M. I. & Zheludev, N. I. Ultrafast active plasmonics. *Nat Photonics* **3**, 55-58 (2009).

178 Ditlbacher, H. *et al.* Silver nanowires as surface plasmon resonators. *Phys Rev Lett* **95**, 257403 (2005).

179 Wei, H., Zhang, S. P., Tian, X. R. & Xu, H. X. Highly tunable propagating surface plasmons on supported silver nanowires. *P Natl Acad Sci USA* **110**, 4494-4499 (2013).

180 Song, M. *et al.* Electron-induced limitation of surface plasmon propagation in silver nanowires. *Nanotechnology* **24**, 095201 (2013).

181 Brolo, A. G., Gordon, R., Leathem, B. & Kavanagh, K. L. Surface plasmon sensor based on the enhanced light transmission through arrays of nanoholes in gold films. *Langmuir* **20**, 4813-4815 (2004).

182 Norris, D. J., Nagpal, P., Lindquist, N. C. & Oh, S. H. Ultrasmooth Patterned Metals for Plasmonics and Metamaterials. *Science* **325**, 594-597 (2009).

183 Conforti, M. & Della Valle, G. Derivation of third-order nonlinear susceptibility of thin metal films as a delayed optical response. *Phys Rev B* **85**, 245423 (2012).

184 Islam, M. S. *et al.* Ultrasmooth Silver Thin Films Deposited with a Germanium Nucleation Layer. *Nano Lett* **9**, 178-182 (2009).

185 Mahapatro, A. K., Scott, A., Manning, A. & Janes, D. B. Gold surface with sub-nm roughness realized by evaporation on a molecular adhesion monolayer. *Appl Phys Lett* **88**, 151917 (2006).

186 Im, H. *et al.* Template-Stripped Smooth Ag Nanohole Arrays with Silica Shells for Surface Plasmon Resonance Biosensing. *Acs Nano* **5**, 6244-6253 (2011).

187 Nagpal, P., Lindquist, N. C., Oh, S. H. & Norris, D. J. Ultrasmooth Patterned Metals for Plasmonics and Metamaterials. *Science* **325**, 594-597 (2009).

188 Lee, K. L. *et al.* Enhancing Surface Plasmon Detection Using Template-Stripped Gold Nanoslit Arrays on Plastic Films. *Acs Nano* **6**, 2931-2939 (2012).

189 Jia, P. P. & Yang, J. Integration of large-area metallic nanohole arrays with multimode optical fibers for surface plasmon resonance sensing. *Appl Phys Lett* **102**, 243107 (2013).

190 Nowicka, A. M., Hasse, U., Hermes, M. & Scholz, F. Hydroxyl Radicals Attack Metallic Gold. *Angew Chem Int Edit* **49**, 1061-1063 (2010).

191 Huang, J. S. *et al.* Atomically flat single-crystalline gold nanostructures for plasmonic nanocircuitry. *Nat Commun* **1**, 150 (2010).

192 Nelayah, J. *et al.* Mapping surface plasmons on a single metallic nanoparticle. *Nat Phys* **3**, 348-353 (2007).

193 Temple, T. L., Mahanama, G. D. K., Reehal, H. S. & Bagnall, D. M. Influence of localized surface plasmon excitation in silver nanoparticles on the performance of silicon solar cells. *Sol Energ Mat Sol C* **93**, 1978-1985 (2009).

194 Aslan, K., Leonenko, Z., Lakowicz, J. & Geddes, C. Annealed Silver-Island Films for Applications in Metal-Enhanced Fluorescence: Interpretation in Terms of Radiating Plasmons. *J Fluoresc* **15**, 643-654 (2005).

195 Chang, Y.-C., Chung, H.-C., Lu, S.-C. & Guo, T.-F. A large-scale sub-100 nm Au nanodisk array fabricated using nanospherical-lens lithography: a low-cost localized surface plasmon resonance sensor. *Nanotechnology* **24**, 095302 (2013).

196 Klein, M. J. K. *et al.* in *Solid-State Sensors, Actuators and Microsystems Conference (TRANSDUCERS), 2011 16th International.* 610-613.

197 Klein, M. J. K. *Wafer-Scale Fabrication of Thin SiN Membranes and Au Films and Membranes with Arrays of Sub-um Holes Using Nanosphere Lithography*, EPFL, (2010).
198 Penn, M. A., Drake, D. M. & Driskell, J. D. Accelerated Surface-Enhanced Raman Spectroscopy (SERS)-Based Immunoassay on a Gold-Plated Membrane. *Anal Chem* **85**, 8609-8617 (2013).
199 Turkmen, M. *et al.* U-shaped nano-apertures for enhanced optical transmission and resolution. Proc. SPIE 2011, 80340H-80346.
200 Aksu, S. *et al.* High-Throughput Nanofabrication of Infrared Plasmonic Nanoantenna Arrays for Vibrational Nanospectroscopy. *Nano Lett* **10**, 2511-2518 (2010).
201 Stockman, M. I. Nanofocusing of Optical Energy in Tapered Plasmonic Waveguides. *Physical Review Letters* **93**, 137404 (2004).
202 Gramotnev, D. K., Pile, D. F. P., Vogel, M. W. & Zhang, X. Local electric field enhancement during nanofocusing of plasmons by a tapered gap. *Physical Review B* **75**, 035431 (2007).
203 Søndergaard, T. *et al.* Extraordinary optical transmission with tapered slits: effect of higher diffraction and slit resonance orders. *J. Opt. Soc. Am. B* **29**, 130-137 (2012).
204 Zhang, Y. *et al.* Suspended hybrid films assembled from thiol-capped gold nanoparticles. *Nanoscale Res Lett* **7**, 1-5 (2012).
205 Elghanian, R., Storhoff, J. J., Mucic, R. C., Letsinger, R. L. & Mirkin, C. A. Selective Colorimetric Detection of Polynucleotides Based on the Distance-Dependent Optical Properties of Gold Nanoparticles. *Science* **277**, 1078-1081 (1997).
206 Bechelany, M. *et al.* Simple Synthetic Route for SERS-Active Gold Nanoparticles Substrate with Controlled Shape and Organization. *Langmuir* **26**, 14364-14371 (2010).
207 Yu, X., Wang, Z., Jiang, Y., Shi, F. & Zhang, X. Reversible pH-Responsive Surface: From Superhydrophobicity to Superhydrophilicity. *Adv Mater* **17**, 1289-1293 (2005).
208 Bond, G. C. & Thompson, D. T. Catalysis by gold. *Catal Rev* **41**, 319-388 (1999).
209 Elias, J. *et al.* Electrodeposition of gold thin films with controlled morphologies and their applications in electrocatalysis and SERS. *Nanotechnology* **23**, 255705 (2012).
210 Chou, S. Y., Krauss, P. R. & Renstrom, P. J. Imprint lithography with 25-nanometer resolution. *Science* **272**, 85-87 (1996).
211 Zhang, J., Cui, B. & Ge, H. X. Fabrication of flexible mold for hybrid nanoimprint-soft lithography. *Microelectron Eng* **88**, 2192-2195 (2011).
212 Rakic, A. D., Djurisic, A. B., Elazar, J. M. & Majewski, M. L. Optical Properties of Metallic Films for Vertical-Cavity Optoelectronic Devices. *Appl. Opt.* **37**, 5271-5283 (1998).
213 <http://docs.lumerical.com/en/fdtd/user_guide_symmetric_anti_symmetric.html>
214 Gao, H., Henzie, J. & Odom, T. W. Direct Evidence for Surface Plasmon-Mediated Enhanced Light Transmission through Metallic Nanohole Arrays. *Nano Letters* **6**, 2104-2108 (2006).
215 Irannejad, M. & Cui, B. Effects of Refractive Index Variations on the Optical Transmittance Spectral Properties of the Nano-Hole Arrays. *Plasmonics* **8**, 1245-1251 (2013).
216 Miroshnichenko, A. E., Flach, S. & Kivshar, Y. S. Fano resonances in nanoscale structures. *Reviews of Modern Physics* **82**, 2257-2298 (2010).
217 Francescato, Y., Giannini, V. & Maier, S. A. Plasmonic Systems Unveiled by Fano Resonances. *ACS Nano* **6**, 1830-1838 (2012).

218 Luk'yanchuk, B. *et al.* The Fano resonance in plasmonic nanostructures and metamaterials. *Nature Materials* **9**, 707-715 (2010).

219 Rahmani, M. *et al.* Generation of pronounced Fano resonances and tuning of subwavelength spatial light distribution in plasmonic pentamers. *Opt. Express* **19**, 4949-4956 (2011).